To the Graduate Council:

I am submitting herewith a dissertation written by Davis C. Easley entitled "Prompt vs Local Redeposition: Model Refinement and Experimental Design for Understanding High-Z Net Erosion in Magnetic Confinement Fusion." I have examined the final paper copy of this dissertation for form and content and recommend that it be accepted in partial fulfillment of the requirements for the degree of Doctor of Philosophy, with a major in Energy Science and Engineering.

David Donovan, Major Professor

We have read this dissertation
and recommend its acceptance:

Theodore Biewer

Livia Casali

Ezekial Unterberg

Accepted for the Council:

Dixie Thompson

Vice Provost and Dean of the Graduate School

To the Graduate Council:
I am submitting herewith a dissertation written by Davis C. Easley entitled "Prompt vs Local Redeposition: Model Refinement and Experimental Design for Understanding High-Z Net Erosion in Magnetic Confinement Fusion." I have examined the final electronic copy of this dissertation for form and content and recommend that it be accepted in partial fulfillment of the requirements for the degree of Doctor of Philosophy, with a major in Energy Science and Engineering.

David Donovan, Major Professor

We have read this dissertation
and recommend its acceptance:

Theodore Biewer

Livia Casali

Ezekial Unterberg

Accepted for the Council:

Dixie Thompson

Vice Provost and Dean of the Graduate School

(Original signatures are on file with official student records.)

Prompt vs Local Redeposition: Model Refinement and Experimental Design for Understanding High-Z Net Erosion in Magnetic Confinement Fusion

A Dissertation Presented for the

Doctor of Philosophy

Degree

The University of Tennessee, Knoxville

Davis C. Easley

August 2024

© by Davis C. Easley, 2024
All Rights Reserved.

For Liz...

By any metric of blood, sweat, or tears,

this dissertation is as much yours as it is mine.

Acknowledgements

If the reader will forgive a brief moment of philosophizing on my part, I would posit that no one's achievements are their own. Although our own effort is no small component of every failure and success, means and circumstances set the gradient of difficulty and are often as much to blame for each achievement. The people who affect those circumstances, for good or for ill, have helped make each of us what we are. In this way, the achievement this dissertation represents would not be possible without the cumulative support of people too numerous to mention. Indeed, if I know you, I owe this work in some part to you. With the utmost sincerity, I thank you.

Of course, I would like to take up some space here to thank those who have been particularly impactful in helping me reach this accomplishment, which is still a very long list. First, none of my academic achievements would have been possible without the support and guidance of the educational systems that delivered me to this point in my career. From the custodial staff to the administrative leadership, the team behind every school and university I have attended has provided me with the tools I have used to succeed. If you were employed in the Dickson, Tennessee school system at SBES (2001-2007), DMS (2007-2010), or DCHS (2010-2014) while I attended, thank you for every facilitation of student success that you gave me. In particular, I would like to thank Teresa Fussell, Dawn Crosman, and Patricia Manley from each of these respective institutions. These educators uniquely instilled a love of learning that has carried me throughout my education. One doesn't stay in academia for over two decades without encountering dozens of brilliant instructors, but I would

like to highlight that Mrs. Manley's course in Algebra II remains the most edifying and ambitious of my career to date. I am profoundly indebted to her excellence in teaching.

Next, I would like to equally thank those at Sewanee: The University of the South (2014-2018) and The University of Tennessee, Knoxville (2018-2024) for their support throughout my undergraduate and graduate education. The faculty of the chemistry, mathematics, and physics departments at Sewanee have my gratitude for their instruction, guidance, and patience as I spread myself thin trying to triple major. Each of these departments provided a staggering quality of instruction given their size and budget; their combined education gave me many of the tools I needed to succeed in an interdisciplinary Ph.D. program. Also, I would especially like to mention Eugenii Donev for his work as an undergraduate academic advisor and research mentor; his mentorship instilled critical research skills early in my education that have immensely aided my career. He encouraged me to take an internship at ORNL, and my career has never been the same.

Similarly, I want to commend the faculty in the mathematics, nuclear engineering, and physics departments at UTK for the caliber of their instruction. In the best possible way, these professors demanded excellence while fostering the means to achieve it. As I conclude my career as a full-time student, I am very grateful for every lecture I heard, assignment I untangled, and lesson I now apply to my life and career. I want to give special thanks to Lee Riedinger and Wanda Davis for developing the Bredesen Center into a place I wanted to grow as a graduate student and for giving my application a chance; additionally, I would like to thank Allie Burns for walking me through every step of the graduate process and cultivating a climate of mentorship and community among BC students. Thanks also to Gale Hauck for her words of encouragement. Outside the BC, I am very appreciative of Livia Casali's contributions to my dissertation. Although our paths never met in the classroom, she was willing to join my doctoral committee and provided insightful suggestions

throughout the twists and turns of my research. I greatly value the time she was able to find for me amidst her noteworthy career.

Tightly coupled to this final stage of my formal education are the people of Oak Ridge National Laboratory (2016-2024) and the broader Department of Energy who each went above and beyond their job descriptions to mentor my early career. In many ways I never could have written this dissertation without the investment of the SULI and SCGSR programs and the people I met therein. Thanks are due to the Fusion Energy Division of ORNL and especially the members of the Power Exhaust and Particle Control group who encouraged my involvement, built my skills, and co-authored my work. Special thanks goes to Ken Herwig, Ben Lawrie, and Yingzhong Ma for getting me started; Ted Biewer and Elijah Martin for bringing me to UTK; and John Caughman, Abdou Diaw, Curt Johnson, and Chris Klepper for helping me cross the finish line. Ted in particular has been an incredible mentor since my undergraduate days, and I am profoundly grateful for his continued investment in my career as a member of my doctoral committee. His encouragement and generosity speaks highly of ORNL staff, and I look forward to working with him again.

Now, my research and dissertation would not be possible without the contributions of David Donovan and Zeke Unterberg, whose mentorship have most shaped my education. During my time as a student, Zeke has been an exceptional group leader at ORNL who continually stretches himself to the limits of his time and energy for the sake of the fusion effort. Somehow, amidst all that his schedule entails, he managed consistently to advise, correct, and mentor my research every step of the way. I am very thankful for the long hours invested in my education, the facilitation of my involvement with ORNL, and the fact that he always treated me like a valued member of his PEPC group, despite the fact that I was neither experienced nor an employee. Meanwhile, David has been an excellent academic advisor and mentor who keeps himself far too busy with too many students yet somehow finds the time for all of them. When my funding was in jeopardy during my second year and I was unable to continue with my original group and project, I am deeply grateful that

David convinced me to stay and grafted me a position into his group. His teaching, mentorship, and advice are of the highest academic caliber, and my professional growth has been dramatically improved as a result of it.

While educational systems are important, the network of support I have received from friends and family throughout my career has been indispensable; their kindness has made the difficulties bearable and the successes gratifying. Thanks to Beau, Daniel, Diah, Ethan, Gennaro, Greg, Jacob, Matt, Miah, Michael, Noah, and Trent for their early support of my career ambitions and their blessings of friendship and fellowship; I still think of them often, and I would be a much different person without their impact. Thanks also to Aidan, Daniel, Drew, Tilly, Tyler, Will, and Xin for the small community of physics majors at Sewanee; when morale was low, it was better to lock arms. Further thanks to Alec, Alex, Bingzhe, Brian, Elizabeth, Jaker, Jeremy, Jonah, Jun, Katie, Kirtan, Lee, Mason, Sean, Seth, and Shawn for their camaraderie and collaboration during the work of this dissertation; I very much look forward to my next opportunity to work with each of them. Additional thanks to Elysabeth, Hunter, Kelly, Meagan, Robert, and Zach for their encouragement; the sense of community they each provided meant more than they know and will not be forgotten. Thanks also to Rick Dunn and Greg Pinkner for feeding my soul and keeping me moving throughout my higher education.

In particular, I would like to thank Matt, Jacob, Evan, and Tilly directly. These people have been the very definition of friendship; despite leading busy lives in other cities, they never failed to encourage, laugh, commiserate with me. Every visit was a treasure, and I will never be able to repay their kindness. To each of you, know that I could not have written this dissertation without your help. I would also like to especially thank Kirtan, Monica, Katie, and Andrew for the many invigorating words of support they lent me over my final three years as a student; this crew made the mezzanine a little less lonely and a lot more hopeful. Kirtan walked side-by-side with me through every fire, and his friendship has been invaluable.

Most importantly, I would like to thank my wonderful extended family, without whom this document would not exist. As the first in my family to pursue a doctorate, it was not easy to reach this moment of my educational career, but they have championed my every ambition and lightened all burdens. Their kindnesses and prayers have sustained me for over two decades as a full-time student and carried me to the finish line of my Ph.D. program. I cannot list all of them here, but they know who they are, and they have my utmost gratitude. Words cannot express how much they have fortified and deepened my life, from aunts and uncles down to cousins once removed. Specifically, my grandparents have been a profound source of wisdom and strength throughout my life, and I have pursued this career in no small part thanks to their efforts. I hope that this dissertation and the degree it represents is a source of pride for each of them and a small measure of return on the priceless investments they've made in me. Carl, Marilyn, Leslie, and Barbara, you are much loved.

Penultimately, I want to thank my in-laws, my sister, and my parents. The Estes family and their extend relatives have all been nothing but welcoming, generous, and supportive of my career; they have each lessened the challenge of being a full-time student and gone out of their way to help me work on my degree. Next, my sister has forever been my biggest cheerleader; I am greatly indebted to her selfless compassion and her strength of character. Michaela, you inspire me, and I wish I were more like you. Lastly, my parents have been my quintessential supporters from the very start; Michael and Leslie are two of the most generous people I know, and I will never be able to repay all they have sacrificed to help me reach this achievement. My mother taught me to love to learn, and my father taught me to give everything my best effort. To both of you, I owe everything I've written here to the values you instilled; I will always cherish you and everything you have done for me.

Lastly, I want to thank the person who was my strength throughout the entire, tumultuous path every graduate student must take. My wife patiently bore every delay and continuously sacrificed her time and energy to keep us afloat during these humble days of graduate education. She restored my spirit and emboldened my

dreams with her wit and her heart. Arguably, she worked harder to manifest this document than I did, and I owe every word in it to her. Liz, I could never have completed this program without you; I will never forget all that you have done for us. I love you more than life itself, now and always.

As I conclude these acknowledgements and the dissertation begins in earnest, I once more want to thank everyone mentioned for their support in this endeavour. I am sure I missed naming some important people during the tumult that was the final months of feverish dissertation writing, but I meant them no slight; to those that I will think about after this work is published and slap my forehead with embarrassment, thank you also. Finally, I thank God for the infinite graces, mercies, and blessings provided by bringing so many amazing people into my life. I stand amazed and confused. Here, as in all things, every failure was my own and every success His glory.

Science, like nature, must also be tamed
With a view towards its preservation
Given the same state of integrity
It will surely serve us well...

Let the truth of love be lighted
Let the love of truth shine clear
Sensibility, armed with sense and liberty
With our hearts and minds united in a single perfect sphere

-Neil Peart

Abstract

The economic and engineering success of magnetic confinement fusion reactors significantly depends upon the optimization of plasma facing component (PFC) design. For high-Z PFCs, the critical engineering condition is minimal net erosion (i.e. gross erosion – redeposition). Here, we present a high-Z net erosion model discriminating three primary redeposition mechanisms: **prompt** (geometric-driven), **local** (sheath-driven), and **far** (scrape-off-layer-driven). Using these distinctions, we show modeling for high-Z net erosion in magnetic-confinement fusion over a matrix of key plasma parameters. With Sobol' methods we assess the sensitivity of each mechanism and show that prompt-vs-local trade-off critically explains underprediction in redeposition losses of up to two orders of magnitude across magnetic-field-to-PFC pitch angles. Finally, we report a "design-of-experiment" study exploring the measurability of prompt vs local distinctions in current experimental facilities. We use a combination of synthetic diagnostics and plasma-parameter optimization to propose an isotopic method of measurement by exploiting robust *in situ* and *ex situ* techniques. In principle, this approach provides a ready path forward for improving and validating PFC models needed to target optimal regimes of PFC design in future reactors.

Table of Contents

1 The Approach to Fusion Energy **1**

1.1 Energy Needs and the Future 1

1.2 Basics of Fusion Energy 5

1.3 The Divertor Tokamak 10

1.4 SOL Modeling with OEDGE 15

1.5 Net Erosion and the ITEP Gap 20

1.6 Executive Summary 25

2 Fundamental Aspects of the Plasma Sheath **27**

2.1 The Debye Sheath 27

2.2 The Chodura Sheath 34

2.3 The Brooks and Borodkina Sheath Models 38

2.4 Executive Summary 44

3 Model of Gross Erosion **45**

3.1 Physical Sputtering 45

3.2 Erosion of High-Z Materials 50

3.3 Incident Ion Energy and Angle Distributions and PYEAD 56

3.4 Neutral Energy and Angle Distributions and RustBCA 66

3.5 Executive Summary 73

4 Model of Redeposition **74**

4.1 Current Models of High-Z Redeposition 74
4.2 A Model Refinement of High-Z Redeposition 87
4.3 Discrimination of High-Z Redeposition Mechanisms and GITR 92
4.4 Executive Summary 97

5 Importance of the $\vec{B}$-to-PFC Pitch Angle in Net Erosion 98
5.1 Motivation and Methodology 98
5.2 Sensitivity of Gross Erosion to Pitch Angle α 106
5.2.1 Incident Ion Energy and Angle Distributions 106
5.2.2 Sputtered Neutral Energy and Angle Distributions 115
5.3 Sensitivity of Redeposition to Pitch Angle α 122
5.3.1 Prompt Redeposition Sensitivity to α 122
5.3.2 Local Redeposition Sensitivity to α 126
5.3.3 Far Transport Sensitivity to α 127
5.4 Refinement of Predictive Net Erosion 128
5.5 Executive Summary 132

6 An Uncertainty Quantification of Net Erosion Trends 135
6.1 Motivation and Methodology 135
6.2 Sobol' Sensitivity of PYEAD-RustBCA-GITR 144
6.2.1 Sobol' analysis of PYEAD 152
6.2.2 Sobol' analysis of PYEAD-RustBCA 157
6.2.3 Sobol' analysis of PYEAD-RustBCA-GITR 166
6.3 Executive Summary 186

7 A "Design-of-Experiment" for Assessing Net Erosion 188
7.1 Motivation and Methodology 188
7.2 Spectroscopic Diagnostics and ColRadPy 192
7.3 Microtrench Diagnostics and MPR 207
7.4 Surface Characterization Diagnostics and GITR 211

7.5 Experimental Predictions for mm-Scale Deformation 219
7.5.1 ColRadPy Spectroscopy Simulations 219
7.5.2 GITR LAMS Simulations 224
7.5.3 MPR Microtrench Simulations 229
7.6 Experimental Predictions for μm-Scale Deformation 230
7.7 Executive Summary 234

8 Discussion of Key Results **237**

9 Summary and Future Work **249**

Bibliography **254**

Appendix **275**
A PYEAD Source Code 275

Vita **307**

List of Figures

1.1 Change in surface air temperature over land and sea for the past 140 years (left) (89) and world energy consumption by source for the past 25 years (right) (12). 2

1.2 Adapted plot of binding energy vs proton number (102), with increasing stability via fusion reactions in green and via fission reactions in red. 6

1.3 Cross-section of low-nucleon fusion reactions against kinetic energy of reacting nuclei (47). Deuterium and tritium reactions are circled in red, which may all contribute to thermonuclear energy production in a reactor using DT fuel. 8

1.4 Demonstration that fusion, against the metric of the triple product, outcompetes other fields in the rate of development (65). 11

1.5 Cross-sectional schematic of a general tokamak and stellarator design, showing the internal plasma flow within each (129). 13

1.6 Toroidal cross-section of a JET-sized plasma with a limiter in-vessel (109). 16

1.7 Difference in magnetic geometry between tokamaks with limiters (left) and divertors (center) with important regions of the divertor configuration labeled in an expanded figure (right) (109). 16

1.8 Cross-section of a computational grid used in OEDGE interpretation of a DIII-D discharge, with tungsten (W) metal rings labeled in purple, the Divertor Material Evaluation Station (DiMES) in red, filterscope spectroscopy (FS) view chord in green, filtered camera (FC) view chord in dark blue, LPs in light blue, and divertor TS (DTS) cross-section in orange (91). 19
1.9 Example profiles of pressure (a), density (b), and temperature (c) demonstrating the presence of the pedestal region in H-mode (with labeled dimensions) but not L-mode at Alcator C-Mod (Mossessian et al.) 21
1.10 Characteristic H-α emission during H-mode at ASDEX with example continuous (a) and discrete (b) bursts of ELMs highlighted in red (109) 22
1.11 Ignition curves with different concentrations of tungsten impurities C_W, showing the decreased operational space of increased impurity contamination in the core (95). 24
1.12 Generalized PMI impurity pathway from material surface to plasma core, with lifetime-extending PFC redeposition pathways in yellow (Unterberg). 24

2.1 A one-dimensional cartoon showing the variation of electric potential across the sheath region and its ambipolar effect on particles. Here, $V = \psi$ (109). 29
2.2 Cartoon of the three distinct regions at the plasma-material surface: the DS, the MPS, and the main plasma (i.e. the pre-sheath). Here, Ψ is the angle complementary to α, and $n_i = n_{ip}$ in the text (109). . . . 35
2.3 Comparison between the Brooks and Borodkina models of potential drop through the sheath as a function of above-PFC height. The MPS and DS thicknesses (here, we approximate the DS at $\sim 10\lambda_D$) are marked for different values of α. 43

3.1 Generalize geometry of a sputtering event in a tokamak, including the $\vec{B}$-to-PFC pitch angle (α), the polar (θ) and azimuthal (ϕ) ion impact angles for incident ion i, and the forward-scattering angle (δ) for sputtered neutral s. 47
3.2 Cartoon of physical sputtering, using D and W as example incident ion and PFC neutrals, respectively. Grayscale represents increasing kinetic energy of the D ion. Represented are (a) a D reflection, (b) a D embedment, and (c) D sputtering of a W neutral. 47
3.3 Sputtering yields for D on typical PFCs vs impact energy of D ions ($E_o = E_{ii}$ above) using the TRIM code (109). 51
3.4 Physical sputtering yield vs W impact energy E_{ii} on W PFCs using the Bohdansky formula, highlighting the threat of avalanche at sufficiently high impact energies (23). 53
3.5 W erosion work (71) at JET showing: (a) W erosion measurements in ITER-like divertor via spectroscopic W-I emission lines (see Chapter 7) in inter- and intra-ELM H-mode, (b) Calculated W erosion fluxes in ITER-like divertor via ERO (72) simulations in inter- and intra-ELM H-mode showing good agreement with the data in (a), (c) BCA-calculated W sputter yields based on D^+ and Be^{2+} conditions in inter-ELM H-mode, (d) BCA-calculated W sputter yields based on D^+ and Be^{2+} conditions in intra-ELM H-mode. Note that, at 0.5% Be expected at JET, D sputter yields will exceed Be yields in the intra-ELM case of (d) but not the inter-ELM case of (c). 55
3.6 SEM images of W exposed to (a) 0.050 keV He and (b) 12 keV He fluxes, highlighting the increased growth of W fuzz with increasing He incident energy (126). 55
3.7 Spectroscopic emission line ratio between WD and W inter-ELM (blue) and intra-ELM (red) against distance from strike point Δs (16). . . . 57
3.8 Workflow of core functions within PYEAD. 60

3.9 Auto-generated figures from PYEAD using the default inputs with 10000 test particles. The subfigure numbers refer to the individualized figure descriptions in the text. 64
3.10 Comparison of PYEAD (Python) and ieadrk3 (IDL) default input calculations for subfigures (4), (5), and (6) in Figure 3.9, as well as computational runtime (*) using ***pal***=10. 65
3.11 Generalized scattering event (99), with labeled parameters highlighted in the text. 68
3.12 Benchmark study comparing silicon sputtering yields in RustBCA to other TRIM-style codes F-TRIDYN and SRIM as well as empirical Yamamura and Thomas formulations and experimental results (37). . 72

4.1 The original cartoon (90) of the prompt redeposition process when p is unity, emphasizing the geometric interplay between λ_{s+} and ρ_{s+}. . 77
4.2 Contour plots of p (a) and f_{red} (b) as a function of sheath-entrance density and temperature, held constant throughout the sheath here for illustrative purposes. 79
4.3 Simulated orbit of multiply-ionized W impurity, with distances above and along the surface in relative units to the singly-ionized W Larmor radius. Note that multiply-ionized W does not geometrically intersect with the PFC surface (23). 79
4.4 Simulated orbit of multiply-ionized W redeposition as a refinement of Figure 4.3 including Chodura sheath electric fields (23). 83
4.5 Redeposition geometric redistribution for surface-scale and global-scale redeposition processes (84). 84
4.6 Figure of merit for non-redeposition fraction against T_e and maximum normalized sputtering ion energy $\sim R_E$ (85). 86

4.7 Simulated figures of merit for approximating surface-scale redeposition by the concentration of sputtered, multiply-ionized W ions (53). On the left, sputtered fractions of W charge states are compared with the fraction of non-promptly deposited W ($\chi_{non-prompt} = f_{non}$ above). On the right, the charge state of W that best approximates f_{non} is plotted against T_e and n_e. Characteristic regions for DIII-D and predicted regions for ITER are highlighted. 88

4.8 Cartoons of prompt (geometric-driven), local (sheath-driven), and far (SOL-driven) redeposition, with trajectories avoiding each redeposition mechanism in gray for comparison. 91

4.9 Example PDF contours of (a) f_{prompt}, (b) f_{local}, and (c) f_{far} onto the PFC surface for a 1 mm radius source spot centered at the origin, assuming $\alpha = 3°$, $B = 2.25$ T, and D plasma at $\approx 4.5{\times}10^{19}$ m^{-3} density and ≈ 19 eV temperature. The PDF of the maximum displacement above vs. along the PFC surface is respectively shown in (d), (e), and (f). 96

5.1 Potential distribution through the sheath as a function of above-PFC height using the Borodkina sheath model (see Section 2.3). The impact to the L_{MPS} thickness is noted, with $L_{DS} = 10\lambda_D$ held fixed. 101

5.2 Workflow diagram of physics model coupling used to study the entire net erosion physics of high-Z PFCs. 103

5.3 Incident C-EAD for $|\vec{B}| = 2.25$ T and D plasma across the full range of simulated α. Normalized particle fraction means particle count normalized to $E_{ii} - \theta$ bin size and total number of particles. 107

5.4 Incident C-EAD for $|\vec{B}| = 2.25$ T and D plasma at different α extremes ($\alpha = 1°$ in (a) and $\alpha = 60°$ in (b)), with integrated distributions in E_{ii} (right) and θ (top). Normalized particle fraction means particle count normalized to $E_{ii} - \theta$ bin size and total number of particles. 109

5.5 Incident C-EAD for $|\vec{B}| = 2.25$ T and D plasma across the full range of simulated α. Normalized particle fraction means particle count normalized to $E_{ii} - \phi$ bin size and total number of particles. 110
5.6 Incident C-EAD for D plasma at shallow and steep α across the full range of simulated $|\vec{B}|$. Normalized particle fraction means particle count normalized to $E_{ii} - \theta$ bin size and total number of particles. . . 112
5.7 Incident C-EAD for D plasma at shallow and steep α across the full range of simulated $|\vec{B}|$. Normalized particle fraction means particle count normalized to $E_{ii} - \phi$ bin size and total number of particles. . . 113
5.8 Incident C-EADs for D vs He plasma at shallow and steep α and $|\vec{B}| =$ 2.25 T. Normalized particle fraction means particle count normalized to $E_{ii} - \theta$ (a-b) or $E_{ii} - \phi$ (c-d) bin size and total number of particles. 114
5.9 Sputtered W^0-EADs for $|\vec{B}| = 2.25$ T and D plasma across a representative subset of simulated α conditions. Normalized particle fraction means particle count normalized to $E_s - \delta$ bin size and total number of particles. 116
5.10 Sputtered W^0-EAD for $|\vec{B}| = 2.25$ T and D plasma at different α extremes ($\alpha = 1°$ in (a) and $\alpha = 60°$ in (b)), with integrated distributions in E_s (right) and δ (top). Normalized particle fraction means particle count normalized to $E_s - \delta$ bin size and total number of particles. Also shown is an analytic cosine distribution in δ, for comparison. 116
5.11 Sputtered W^0-EADs for $|\vec{B}| = 2.25$ T and D plasma across a representative subset of simulated α conditions. Normalized particle fraction means particle count normalized to E_s-azimuthal sputtering angle bin size and total number of particles. 117

5.12 Sputtered-W^0EAD for D plasma at shallow and steep α across the full range of simulated $|\vec{B}|$, which appear ∼invariant. Normalized particle fraction means particle count normalized to $E_s - \delta$ bin size and total number of particles. 119
5.13 Sputtered-W^0EAD for D plasma at shallow and steep α across the full range of simulated $|\vec{B}|$, which appear ∼invariant. Normalized particle fraction means particle count normalized to E_s-azimuthal sputtering angle bin size and total number of particles. 120
5.14 Sputtered W^0-EADs for D vs He plasma at shallow and steep α and $|\vec{B}| = 2.25$ T, which appear ∼invariant. Normalized particle fraction means particle count normalized to $E_s - \delta$ (a-b) or E_s-azimuthal sputtering angle (c-d) bin size and total number of particles. 121
5.15 Prompt (a), local (b), and far (c) particle fractions as a function of p. In (c), α- and plasma-ion-averaged f_{far} ($\langle f_{far} \rangle$) is compared with f_{non} in Eq. 4.7. 123
5.16 Illustrations (not to scale) of gyro-orbits avoiding prompt re- deposition for different α values and otherwise identical conditions. Shallow α conditions favor sheath escape (a), while sharp α conditions favor sheath containment (b), so long as magnetic field conditions yield sufficient L_{MPS} thickness. 125
5.17 Far transport fraction vs $\hat{\lambda}$, with comparisons to the ERO model in $\hat{\lambda}$ shown in Figure 4.7. We show results for the analytic (a) and numerical (b) treatments of W^0-EADs, as discussed in the text. 130
5.18 Far transport fraction as function of p and α (a). Slices $\alpha = 60°$ (b) and $\alpha = 1°$ (c) are shown, showing different f_{prompt} vs f_{local} scaling. . 133

6.1 Prompt, local, and far particle fractions as a function of p with an incorrect (linear) density model, discussed further in the text, in comparison with the correct (rational) density model. For the far fraction, α- and plasma-ion-averaged f_{far} ($\langle f_{far} \rangle$) is compared with f_{non} in Eq. 4.7. Note that the subfigures associated with the rational model are a direct reproduction of Figure 5.15, provided again here to facilitate comparison with the linear model. 137
6.2 An example 2D LHC with D=8 parameter subdivisions of generic Variables 1 and 2. 143
6.3 Total-effect sensitivity index for the first-ionization mean-free path output λ_{s+} against input PMI parameters n_e, T_e, $|\vec{B}|$, α, m_{ii}, and Z_{ii}. 145
6.4 Histograms of raw λ_{s+} data (normalized to the maximum bin count) vs input PMI parameters (a) n_e, (b) T_e, (c) $|\vec{B}|$, (d) α, (e) m_{ii}, and (f) Z_{ii}. The bin-averaged trend is shown in red, with the range of averaging shaded in pink for clarity. 146
6.5 Total-effect sensitivity index for the first-ionization Larmor radius output ρ_{s+} against input PMI parameters n_e, T_e, $|\vec{B}|$, α, m_{ii}, and Z_{ii}. 148
6.6 Histograms of raw ρ_{s+} data (normalized to the maximum bin count) vs input PMI parameters (a) n_e, (b) T_e, (c) $|\vec{B}|$, (d) α, (e) m_{ii}, and (f) Z_{ii}. The bin-averaged trend is shown in red, with the range of averaging shaded in pink for clarity. 149
6.7 Total-effect sensitivity index for the magnetic pre-sheath thickness output L_{MPS} against input PMI parameters n_e, T_e, $|\vec{B}|$, α, m_{ii}, and Z_{ii}. 150
6.8 Histograms of raw L_{MPS} data (normalized to the maximum bin count) vs input PMI parameters (a) n_e, (b) T_e, (c) $|\vec{B}|$, (d) α, (e) m_{ii}, and (f) Z_{ii}. The bin-averaged trend is shown in red, with the range of averaging shaded in pink for clarity. 151

6.9 Total-effect sensitivity index for the average sputtering ion impact energy output E_{ii} against input PMI parameters n_e, T_e, $|\vec{B}|$, α, m_{ii}, and Z_{ii}. 153
6.10 Histograms of raw E_{ii} data (normalized to the maximum bin count) vs input PMI parameters (a) n_e, (b) T_e, (c) $|\vec{B}|$, (d) α, (e) m_{ii}, and (f) Z_{ii}. The bin-averaged trend is shown in red, with the range of averaging shaded in pink for clarity. 154
6.11 Total-effect sensitivity index for the average polar inclination angle output θ against input PMI parameters n_e, T_e, $|\vec{B}|$, α, m_{ii}, and Z_{ii}. . 155
6.12 Histograms of raw θ data (normalized to the maximum bin count) vs input PMI parameters (a) n_e, (b) T_e, (c) $|\vec{B}|$, (d) α, (e) m_{ii}, and (f) Z_{ii}. The bin-averaged trend is shown in red, with the range of averaging shaded in pink for clarity. 156
6.13 Total-effect sensitivity index for the average azimuthal impact angle output ϕ against input PMI parameters n_e, T_e, $|\vec{B}|$, α, m_{ii}, and Z_{ii}. . 158
6.14 Histograms of raw ϕ data (normalized to the maximum bin count) vs input PMI parameters (a) n_e, (b) T_e, (c) $|\vec{B}|$, (d) α, (e) m_{ii}, and (f) Z_{ii}. The bin-averaged trend is shown in red, with the range of averaging shaded in pink for clarity. 159
6.15 Total-effect sensitivity index for the average sputtered neutral energy output E_s against input PMI parameters n_e, T_e, $|\vec{B}|$, α, m_{ii}, and Z_{ii}. 160
6.16 Histograms of raw E_s data (normalized to the maximum bin count) vs input PMI parameters (a) n_e, (b) T_e, (c) $|\vec{B}|$, (d) α, (e) m_{ii}, and (f) Z_{ii}. The bin-averaged trend is shown in red, with the range of averaging shaded in pink for clarity. 161
6.17 Total-effect sensitivity index for the average sputtered yield output Y against input PMI parameters n_e, T_e, $|\vec{B}|$, α, m_{ii}, and Z_{ii}. 163

6.18 Histograms of raw Y data (normalized to the maximum bin count) vs input PMI parameters (a) n_e, (b) T_e, (c) $|\vec{B}|$, (d) α, (e) m_{ii}, and (f) Z_{ii}. The bin-averaged trend is shown in red, with the range of averaging shaded in pink for clarity. 164
6.19 Total-effect sensitivity index for the average sputtered forward-scattering angle δ against input PMI parameters n_e, T_e, $|\vec{B}|$, α, m_{ii}, and Z_{ii}. . . 165
6.20 Histograms of raw δ data (normalized to the maximum bin count) vs input PMI parameters (a) n_e, (b) T_e, (c) $|\vec{B}|$, (d) α, (e) m_{ii}, and (f) Z_{ii}. The bin-averaged trend is shown in red, with the range of averaging shaded in pink for clarity. 167
6.21 Total-effect sensitivity index for the prompt redeposition fraction f_{prompt} against input PMI parameters n_e, T_e, $|\vec{B}|$, α, m_{ii}, and Z_{ii}. . . 168
6.22 Histograms of raw f_{prompt} data (normalized to the maximum bin count) vs input PMI parameters (a) n_e, (b) T_e, (c) $|\vec{B}|$, (d) α, (e) m_{ii}, and (f) Z_{ii}. The bin-averaged trend is shown in red, with the range of averaging shaded in pink for clarity. 170
6.23 Total-effect sensitivity index for the local redeposition fraction f_{local} against input PMI parameters n_e, T_e, $|\vec{B}|$, α, m_{ii}, and Z_{ii}. 171
6.24 Histograms of raw f_{local} data (normalized to the maximum bin count) vs input PMI parameters (a) n_e, (b) T_e, (c) $|\vec{B}|$, (d) α, (e) m_{ii}, and (f) Z_{ii}. The bin-averaged trend is shown in red, with the range of averaging shaded in pink for clarity. 172
6.25 Total-effect sensitivity index for the far redeposition fraction f_{far} against input PMI parameters n_e, T_e, $|\vec{B}|$, α, m_{ii}, and Z_{ii}. 174
6.26 Histograms of raw f_{far} data (normalized to the maximum bin count) vs input PMI parameters (a) n_e, (b) T_e, (c) $|\vec{B}|$, (d) α, (e) m_{ii}, and (f) Z_{ii}. The bin-averaged trend is shown in red, with the range of averaging shaded in pink for clarity. 175

6.27 Total-effect sensitivity index for $Y * f_{prompt}$ against input PMI parameters n_e, T_e, $|\vec{B}|$, α, m_{ii}, and Z_{ii}. 177
6.28 Histograms of raw $Y * f_{prompt}$ data (normalized to the maximum bin count) vs input PMI parameters (a) n_e, (b) T_e, (c) $|\vec{B}|$, (d) α, (e) m_{ii}, and (f) Z_{ii}. The bin-averaged trend is shown in red, with the range of averaging shaded in pink for clarity. 178
6.29 Total-effect sensitivity index for $Y * f_{local}$ against input PMI parameters n_e, T_e, $|\vec{B}|$, α, m_{ii}, and Z_{ii}. 179
6.30 Histograms of raw $Y * f_{local}$ data (normalized to the maximum bin count) vs input PMI parameters (a) n_e, (b) T_e, (c) $|\vec{B}|$, (d) α, (e) m_{ii}, and (f) Z_{ii}. The bin-averaged trend is shown in red, with the range of averaging shaded in pink for clarity. 180
6.31 Total-effect sensitivity index for $Y * f_{far}$ against input PMI parameters n_e, T_e, $|\vec{B}|$, α, m_{ii}, and Z_{ii}. 182
6.32 Histograms of raw $Y * f_{far}$ data (normalized to the maximum bin count) vs input PMI parameters (a) n_e, (b) T_e, (c) $|\vec{B}|$, (d) α, (e) m_{ii}, and (f) Z_{ii}. The bin-averaged trend is shown in red, with the range of averaging shaded in pink for clarity. 183
6.33 Far redeposition fraction as function of p and α, using a simple curve fit to the entire Sobol' analysis dataset. 185

7.1 Cartoon of idealized DiMES head design. (a) shows the isotopic probe surface with SEM imaging close-ups of early bench-testing of the microtrench design. (b) shows the probe side-view for the mm-scale experiment (not to scale). (c) shows the probe side-view for the μm-scale experiment (not to scale). 191
7.2 Workflow diagram of the connection between the real-world experimental data and the synthetic data we model in this dissertation. . . 193

7.3 TEXTOR experimental setup for measuring S/XB ratios from known fluxes of puffed WF_6 (93). 201
7.4 Comparisons between simulation and experimental spectroscopy from the TEXTOR study (15), which cross-validates the S/XB results. . . 203
7.5 ColRadPy-computed PEC and SCD values for some W I emission lines (68). 208
7.6 Microtrench AFM data (a) and SEM image (b) showcasing the practical uses of microtrenches for determining EADs (1). Note that, here, $\theta = 90° - \theta$ as defined in Figure 3.1 and $I_\phi = \phi$ in the same figure. 210
7.7 SEM images of a Si_3C_2 microtrench pre- and post-exposure, with gross erosion interpretable from fiducial depth markers (29). 210
7.8 Geometry of the incident ion (a) and sputtered neutral (b) angles from the original MPR manual (77). Note the geometry and variables in this figure are different from what was established in Figure 3.1. We will convert all MPR outputs in this dissertation to the Figure 3.1 coordinates before discussing them. Note especially that $\alpha_{in} = \theta_{loc}$ in our formalism. 212
7.9 Schematic of the basic RBS setup (96). 214
7.10 Schematic of the PFC coupon used in the Hakola study (left), and its location (highlighted in red) in the divertor (right) (56). 216
7.11 Picture of a W/C DiMES head coupon (34). 216
7.12 Diagram of the major components of a LAMS system (4). 218
7.13 Analysis of W deposition on collector probes inserted into the mid-plane of DIII-D (40). (a) shows good agreement between RBS and LAMS data, while (b) shows the decomposition of LAMS data into W isotopes. 218
7.14 Determination of spectroscopic measurability, consisting of (a) maximum f_{local} charge state, (b) $f_{W^{4+}}$ fraction, and (c) overall gross erosion yield. The chosen range of measurement is emphasized in black. . . . 221

7.15 Comparison between the PYEAD-RustBCA-GITR charge state fractions f_{charge} and the weighted PEC line ratios from ColRadPy for the VUV lines of interest discussed in Table7.3. 223
7.16 Comparison between the PYEAD-RustBCA-GITR charge state fractions f_{charge} and the weighted PEC line ratios from ColRadPy for the revised far-UV lines of interest. 225
7.17 Comparison between the PYEAD-RustBCA-GITR charge state fractions $f_{prompt} + f_{local}$ and the fraction of particles within the average radial bound $f_{\leq\langle R\rangle}$. 228
7.18 Comparison between the PYEAD-RustBCA-GITR charge state fractions $f_{prompt} + f_{local}$ and the fraction of particles within the δ_{max} radial bound $f_{R_{max}}$. 228
7.19 MPR simulations varying microtrench depth d at each α of interest. Here, we show the normalized particle fraction (i.e. number of particles normalized to maximum particle count and bin size) of incident ions onto the surface. Little variation is observed in these simulations, and the reader is referred to the digital version of this document for optimal clarity. Our chosen conditions are highlighted in red. 231
7.20 Major summary figures generated within MPR, with average impact angle in the left-hand column and net erosion in the right-hand column. No net erosion figure is generated in MPR for $R_a = 0.02$ μm because no redeposition is calculated. 233

8.1 Pictures of cm-mm melting deformation to first-wall components during transient emulation studies in the ITER-like divertor at ASDEX Upgrade (75) (Subfigure (A)) and the ITER-like sacrificial limiter at T-10 (20) (Subfigure (B)). 239
8.2 Pictures of μm-nm surface morphology changes from melting, cracking, bubbling, etc. of ITER-like W PFCs at the IDTF-Russia facility (104). 240

8.3 Relationship between the electron density and the $\vec{B}$-to-PFC pitch angle in setting the particle fraction entering the SOL, f_{far}. 246

List of Tables

1.1 Table of important low-nucleon nuclear fusion reactions and their corresponding net energy outputs (36). 8

3.1 Table of PYEAD output files for .txt file format. 64

4.1 Table of f_{non} values from ERO, not including sheath electric fields but including multiple ionizations (23). 81

4.2 Table of f_{non} values from ERO including both sheath electric fields and multiple ionizations but only accounting for the material redepositing within the first gyro-orbit (23). 83

4.3 Table of f_{non} values from ERO including both sheath electric fields and multiple ionizations and allowing the material requiring multiple gyro-orbits within the sheath to redeposit (23). 84

5.1 Table of important OEDGE parameters used for the net erosion simulations in this chapter (91) 103

6.1 Range of values considered for each PMI parameter studied. We list the discrete range of impacting ions available in RustBCA as *ii*. . . . 143

7.1 Table of transition (or selection) rules for a few important transition types (76). 198

7.2 Tables of W I and W II lines identified in the TEXTOR spectra, potentially useful for analyzing surface-scale net erosion (93). Table (a) contains spectroscopic identifiers, including quantum configurations and wavelengths. Table (b) contains S/XB values for important W I and W II lines. 201
7.3 Emission lines measured at CTH against the NIST database or identified using ColRadPy without NIST-wavelength correction (66). 205
7.4 Emission lines producing good agreement between simulated experimental data and PYEAD-RustBCA-GITR outputs. 225
7.5 Current measurability of mm-scale and μm-scale experiments on the grounds of technological readiness and theoretic interpretability. Diagnostics with an experimental readiness in both categories are shaded for emphasis. 235

Chapter 1

The Approach to Fusion Energy

1.1 Energy Needs and the Future

To date, fossil fuels (delineated as coal, natural gas, and oil) remain the primary source of the world's energy supply. These resources have been invaluable tools in the technological evolution of humankind; however, atmospheric physics demonstrates that increased burning of fossil fuels drives global warming processes (82). Figure 1.1 visually demonstrates the link between the increase in fossil fuel consumption over the last 100 years and an increase in atmospheric temperature, driven by positive radiative forcing from increasing CO_2 gas in the atmosphere (82; 117). While some variation about the mean global temperature can be attributed to the cyclical behavior of glacial periods (58), ice core sampling verifies that ongoing abnormal and unseasonal temperature increases are anthropogenically driven by the burning of fossil fuels. Indeed, data from the International Energy Agency in 2019 shows that, while coal accounted for almost 40% of the world's energy consumption, it also accounted for over 40% of the world's global-warming CO_2 emissions (64). If unchecked, research anticipates dramatic ecological fall-out from global warming, reducing biodiversity and fresh water resources as well as limiting food production amid an exploding human population (118). To make matters worse, trends in modernization and

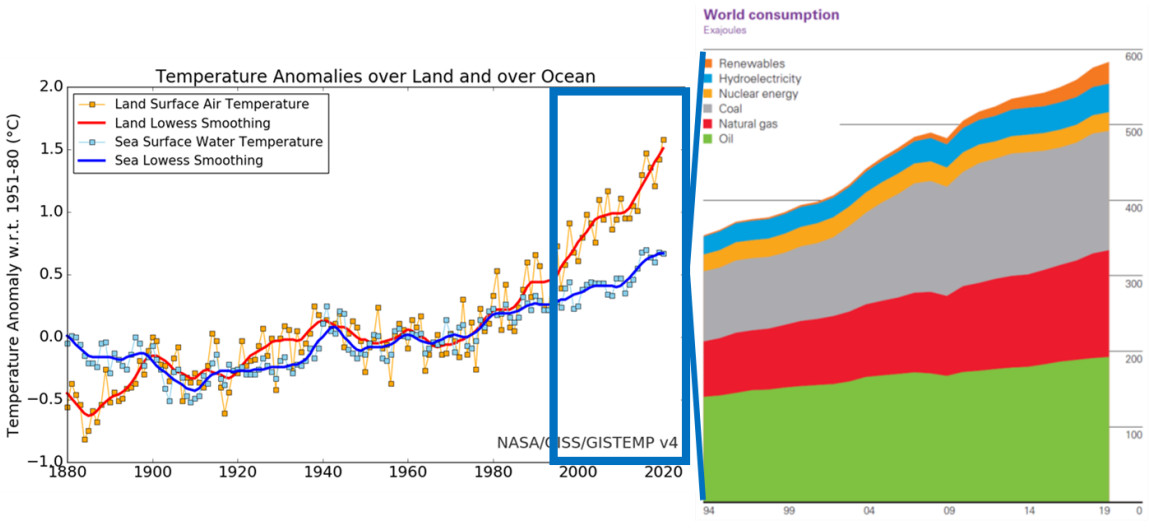

Figure 1.1: Change in surface air temperature over land and sea for the past 140 years (left) (89) and world energy consumption by source for the past 25 years (right) (12).

population growth suggest that the world's energy needs will increase almost 50% by mid-century (45), with much of the supply expected to come from fossil fuels (12).

As shown in Figure 1.1, the growth of coal is stabilizing, perhaps even diminishing, while natural gas and oil are filling the increasing global energy need. This fact is (partly) a positive one in the effort to reduce global warming because the latter two energy sources can produce down to almost half the CO_2 emissions of coal (117). However, the fact remains that total CO_2 levels emitted are more than enough to exponentially continue global warming due to rising energy demand. Carbon capture technology and other means of efficiently mitigating CO_2 emission from fossil fuels remain mostly undemonstrated. With these observations in mind, the logical choice is to turn to hydroelectric, nuclear (i.e. fission), and renewables (i.e. solar and wind) for salvation. Inspection of the ∼constant thickness of nuclear and hydroelectric resources over time in Figure 1.1 illustrates that these resources have stagnated in growth. Geographic constraints and wildlife conservation needs explain the stagnation of hydroelectric. Some increase in hydroelectric may be possible, but certainly not enough to supplant the energy demand of fossil fuels; moreover, global warming can further limit hydroelectric availability over time (117). On the other hand, public perception is largely to blame for the stagnation of nuclear energy. After high profile nuclear disasters such as Three Mile Island and Fukushima Daiichi, the "not-in-my-backyard" mentality and increased regulatory oversight has led to decreased economic returns from fission power; in turn, this cascade has led to the inability to build new fission plants in many cases and the closure of existing fission plants in others. Small modular reactors and other advances in nuclear technology may change public perception due to increased safeguards and modularity (62), but this outlook remains undemonstrated. Unless dramatic changes can be made, it is unlikely that fission will reach its full potential.

One positive observation over the last 10 years has been the increase of renewable energy sources in the world energy portfolio. Investment tax credits in the U.S. especially have motivated rapid growth of renewable technology; solar installations

are spreading predominantly in the Southwest and Florida where the variability of solar exposure is minimal. Similarly, the U.S. Midwest has high wind speeds ideal for the optimized extraction of wind energy, leading to large growth of this source in recent years. Outside of the U.S., Germany and its *Energiewende* policy are eschewing both nuclear power and fossil fuels in favor of renewable sources, though these efforts have been less successful in the cost-efficient reduction of carbon emissions compared to those of France, which has a strong nuclear baseload. Based on some predictions, these efforts may cause renewables to overtake natural gas and coal as the predominant single energy source before 2030 (45). However, it is worth pointing out that renewables have implicit restrictions which will limit their ability to completely replace fossil fuels. Chief among these restrictions is the limited efficiency of solar and wind farms in the majority of climates because of high variability in solar and wind exposure. To compensate for this variation, tremendous efficiencies in energy storage are needed, which may require significant technological advancement. Consequently, renewables currently pose a poor substitute to baseload power plants (which are predominantly fossil fuel sources) because of their high variability in power output. In other words, renewables can only form part of the dynamic and multifaceted solution to the global warming problem.

The above discussion only begins to touch the complexities of the energy-climate crisis. Important (but similarly limited) energy sources have been overlooked here for brevity such as biofuels and geothermal energy. Moreover, significant sociopolitical and economic complexities exist in mitigating global warming without harming the growth of "developing" countries or regressing the prosperity of "developed" countries. Research suggests that countries with low scores on the human development index (HDI, which aggregates national life expectancy, education, and gross income) may be dramatically aided by increased energy consumption, but HDI saturation with high energy consumption leads to diminishing returns in developing national prosperity (19). Importantly, historical and political exploitation of low HDI countries results in practice to little reordering of HDI even as global HDI continues to

increase (19). Indeed, even improving quality of life within a single country without intentional or implicit discrimination quickly becomes labyrinthine. While such topics are of profound importance, they are outside of the scope of this document and will be left for better-equipped minds to solve. We will now turn our discussion to a strong potential solution to the energy-climate crisis: nuclear fusion energy.

1.2 Basics of Fusion Energy

In simple terms we may think of nuclear fusion as the opposite process of nuclear fission: whereas the latter process generates smaller (by mass) nuclei from larger ones, the former generates larger nuclei from smaller ones. Fission reactions are driven by the weak fundamental force, and, while fission reactors accelerate this decay through neutron-induced reactions, spontaneous decay can occur significantly as a natural, ongoing process for large, unstable isotopes. Fusion reactions are driven by the strong fundamental force, and, while they can also be found in nature, they require extreme environments to occur beyond a statistically insignificant amount. In this way the analogs between fission and fusion essentially end with the above 10,000-foot view. Stars are the archetypical example of naturally occurring fusion reactors; in this case immense gravitational forces are required to achieve significant fusion. This necessity is attributed to the high kinetic energies needed for two nuclei to overcome Coulombic repulsion forces and pass close enough that the strong fundamental force dominates, causing a reaction to occur (108). Although fission reactor plants were operational shortly after the discovery of nuclear reactions, the difficulties associated with generating and controlling such extreme environments on Earth, without the aid of immense gravitation, are the primary reason why fusion remains a theoretical energy source to date.

To synthesize fusion at the power-plant level, we must first make a careful choice about the type of nuclear reaction to be used as fuel. Inspection of the binding-energy against nucleon number, shown in Figure 1.2, reveals the obvious: that the fusion

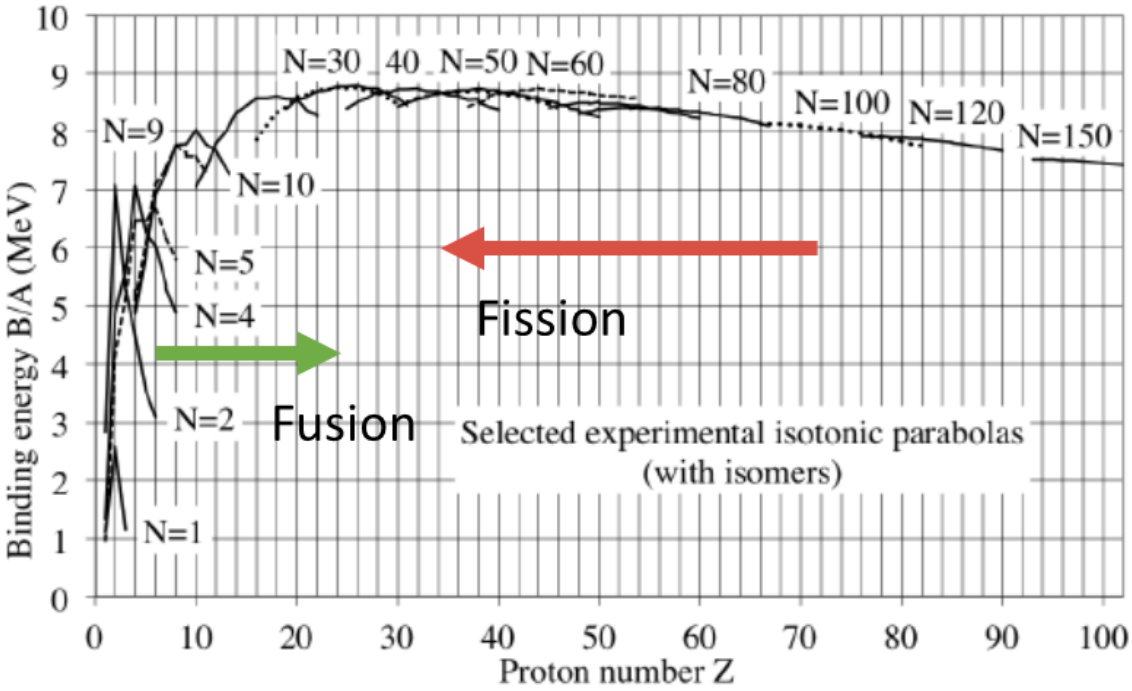

Figure 1.2: Adapted plot of binding energy vs proton number (102), with increasing stability via fusion reactions in green and via fission reactions in red.

reaction of smaller nuclei generally results in more tightly bound (i.e. stable) nuclei while the fission of larger nuclei generally results in more stable nuclei. Therefore, it is logical to select low nucleon fuel for fusion reactors. Several low nucleon candidates are shown below in Table 1.1. The DT (deuterium-tritium) fusion reaction is of particular interest as it releases an incredibly high 17.59 MeV of energy per reaction, split between its ^{4}He and neutron biproducts. Hence, DT fusion has the potential to produce massive amounts of energy compared to other energy sources. Also of note is the fact that D is in plentiful supply on Earth as an isotope in sea water; processes to extract D from sea water are readily available (108).

While it appears at first that the half-life of T (about 12.5 years) may inhibit this choice of fuel, note also in the last two lines of Table 1.1 that two neutron-lithium (Li) reactions exist to produce T and ^{4}He. Thus, by lining a fusion reactor with Li blankets, the reactor can use its neutron by-products to create its own T fuel: even doing so without theoretically introducing any impurities extrinsic to the main DT reaction (108). All that remains in principle is to show that reactor environments capable of reliably mass inducing DT fusion can be made, which is easier said than done. To this end, one considers the cross-section of the DT reaction (i.e. its likelihood) against fuel kinetic energy (i.e. the fuel temperature). Fortuitously, one can see in Figure 1.3 that DT fusion has the largest cross-section at the lowest projectile energy when compared to similar fusion reactions. This amazing fact suggests that DT fusion not only produces the most energy among similar fusion reactions but also occurs most frequently in the least extreme thermonuclear environment. In other words, DT fuel has the greatest chance for success in creating reliable fusion reactors (108; 36).

With the choice of fuel now established, it remains to discuss the means of generating an environment capable of optimizing DT fusion rates. Several schemes have been proposed, and we will not have the time to consider all of them here. However, one aspect is constant among all of them: generation of a DT plasma. Plasma, the fourth state of matter, occurs when gas becomes heated to the extreme that electrons disassociate from ions to form a "sea" of disparate electrons and

Table 1.1: Table of important low-nucleon nuclear fusion reactions and their corresponding net energy outputs (36).

Name	Abbreviation	Reaction (energy, MeV)	Total (MeV)	Energy (10^{-12} J)
DT	T(d,n)^{4}He	D + T → ^{4}He(3.54) + n(14.05)	17.59	2.818
DDn	D(d,n)^{3}He	D + D → ^{3}He(0.82) + n(2.45)	3.27	0.524
DDp	D(d,p)T	D + D → T(1.01) + p(3.02)	4.03	0.646
TT	T(t,2n) ^{4}He	T + T → n + n + ^{4}He	11.3	1.81
D-^{3}He	^{3}He(d,p) ^{4}He	D + ^{3}He → ^{4}He(3.66) + p(14.6)	18.3	2.93
p-^{6}Li	^{6}Li(p,α) ^{3}He	^{6}Li + p → ^{4}He + ^{3}He	4.02	0.644
p-^{11}B	^{11}B(p,2α)^{4}He	^{11}B + p → 3(^{4}He)	8.68	1.39
Reactions for breeding tritium (Natural lithium = 7.42 % ^{6}Li and 92.58 % ^{7}Li)				
n-^{6}Li	^{6}Li(n,α)T	^{6}Li + n(thermal) → ^{4}He(2.05) + T(2.73)	4.78	0.766
n-^{7}Li	^{7}Li(n,n′+α)T	^{7}Li + n(fast) → T + ^{4}He + n	−2.47 (endothermic)	−0.396

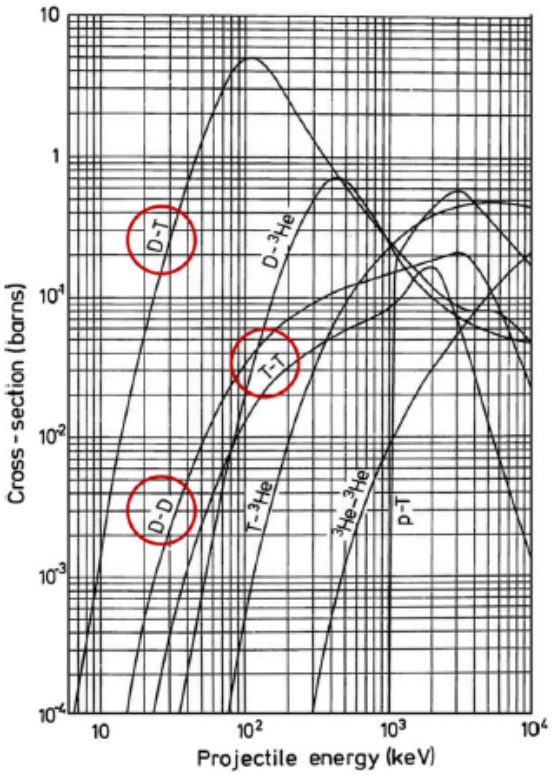

Figure 1.3: Cross-section of low-nucleon fusion reactions against kinetic energy of reacting nuclei (47). Deuterium and tritium reactions are circled in red, which may all contribute to thermonuclear energy production in a reactor using DT fuel.

ions (24). Plasmas can be characterized by the density and temperature of the disparate species with electron and ion components often assumed to be equal, but not always. The assumption of equal charge densities is called quasineutrality, and the assumption of equal temperatures is an assumption of thermal equilibrium (24). By assuming equalities, we may characterize plasmas purely by their electron density and temperature.

The Lawson criterion proposed in 1957 provides a metric using density and temperature characteristics for measuring fusion research's progress toward developing a functional reactor. In particular, we note that the power from fusion (P_f) is equal to the product of the density of both nuclei (n_D;n_T), the cross-section of the reaction (σ_{DT}), and the efficiency (Q). Meanwhile, power loss (P_l) is equal to the sum of kinetic energy components for the D, T, and electron gases (3/2 nkT) divided by the energy confinement time (τ_E). (Additional terms such as radiation losses can be counted as well.) Consequently, for a fusion reactor to be viable, it must be true to first order that (36):

$$n_D n_T \sigma_{DT} Q > \frac{1}{\tau_E}\left(\frac{3}{2}n_D k T_D + \frac{3}{2}n_T k T_T + \frac{3}{2}n_e k T_e\right) \tag{1.1}$$

If the produced alpha particles (i.e. ionized ^{4}He) provide enough energy to the fuel through collisions to overcome losses, the reactor is said to have reached "ignition." Hence, the above inequality may be rewritten after substitution and rearrangement as the generally recognized form of the Lawson criteria (78; 108), where U_{He} is the alpha particle energy:

$$nT\tau_E > \frac{12}{const * U_{He}} \equiv (nT\tau_E)_{lawson} \tag{1.2}$$

This so-called triple product $nT\tau_E$ has marked the progress toward fusion energy over the past century. A 2010 study of fusion research progression showed that, against the metric of the triple product, fusion development outperforms Moore's

law for transistors and the development of attained energies at accelerators, shown in Figure 1.4 (65). The gap between existing fusion technology and ITER, the world's first energy-positive fusion device, is closing fast but at a high cost. With this demonstration of progress in mind, we return to the discussion of generating thermonuclear environments in fusion reactors.

1.3 The Divertor Tokamak

As mentioned several potential reactor schemes have been proposed surrounding plasma-state DT fuel. The means of generating and controlling the plasma generally fall into two categories: inertial confinement fusion (ICF) and magnetic confinement fusion (MCF). In ICF, pellets of DT fuel are compressed rapidly and isotropically (e.g. by lasers) into rapid bursts of plasma (i.e. lower $n\tau_E$ and higher T) (32). The difficulties associated with ICF are quite different than those of MCF, as will be seen. In ICF, reactors must be able to produce extremely high firing rates (nanosecond scale) to efficiently generate electricity, which creates a technology obstacle in both rapidly introducing DT pellets and compressing them (i.e. firing rates of laser systems). Moreover, pellets must be compressed with almost perfect isotropy to successfully generate a reaction, which makes overcoming Rayleigh-Taylor instabilities during compression a challenge (32). Isotropic improvements have been demonstrated using laser hohlraums to indirectly compress pellets, but refinements with this technique are still ongoing (32; 133). For brevity, we will leave the discussion of ICF fusion here and turn to MCF: the main discussion for the rest of this work.

One of the features which distinguishes a plasma from weakly ionized gas is the fact that electromagnetic forces strongly outcompete hydrodynamic forces in determining the plasma's motion (24). In MCF this strong electromagnetic susceptibility of plasma fuel is exploited by controlling plasma confinement with external magnetic fields (i.e. lower T and higher $n\tau_E$). Several schemes (and variations on those schemes) of MCF have been proposed, but the general forerunners are the tokamak and stellarator

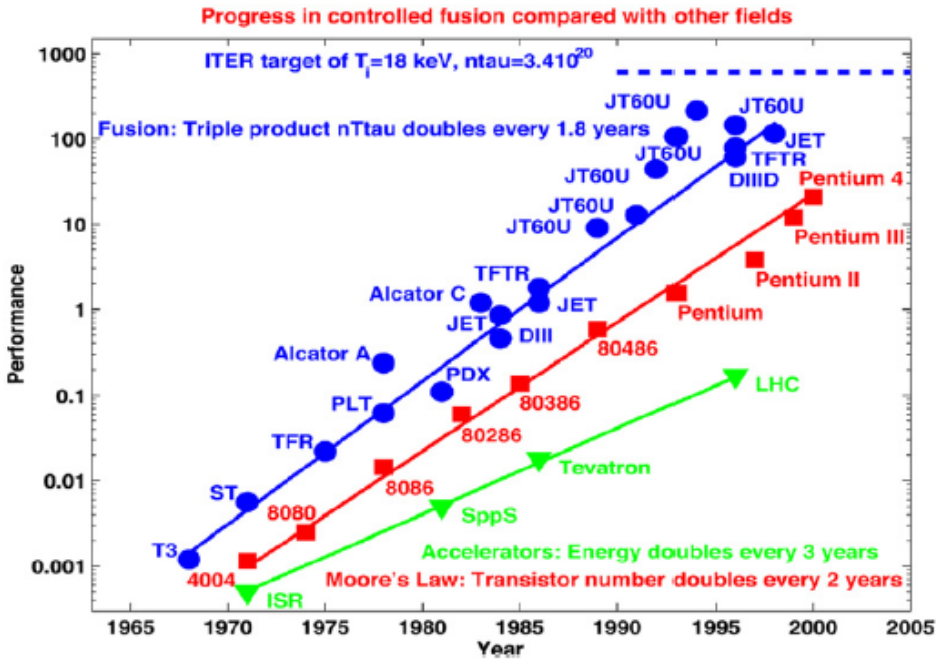

Figure 1.4: Demonstration that fusion, against the metric of the triple product, outcompetes other fields in the rate of development (65).

designs as these have the highest τ_E to date. We will largely focus on tokamaks in this document but, while the magnetic geometry techniques to resolve plasma confinement, transport, and magnetohydrodynamic instabilities differ in stellarators, much of the underlying physics is the same (129).

We begin by discussing the general tokamak design; note that a cross-section schematic can be seen in Figure 1.5 alongside a similar schematic of a stellarator design. The basic concept is relatively simple: both ions and electrons in a plasma will orbit in a gyromotion perpendicular to magnetic field lines under the Lorentz force. In principle, these particles are now locked onto magnetic "tracks" (i.e. field lines) which are arranged toroidally (meaning poloidal magnetic coils are required) so that the plasma forms a "donut" shape in the middle of the reactor. Inherently, the resulting plasma current generates its own poloidal magnetic field lines, resulting in the overall helical magnetic field lines shown in Figure 1.5. Conversely, explicit external magnetic fields are used to generate a helical path in stellarators (129). Initially, it may seem as though the plasma is very well contained (and it mostly is); nevertheless, such geometry also introduces drifts that allow the plasma to slowly escape confinement in addition to turbulent transport. Besides an inherent but usually negligible gravity drift, three drifts are of critical importance to plasma motion: the magnetic gradient drift, the curvature drift, and the ExB drift (108).

These drifts originate as follows. When the magnetic field lines are nonuniform in strength, the gradient induces a velocity perpendicular to both the magnetic field and its gradient:

$$\overrightarrow{v_{\nabla B}} = \frac{mv_{\perp}^2}{2q} \frac{\overrightarrow{B} \times \nabla \overrightarrow{B}}{|\overrightarrow{B}|^3} \tag{1.3}$$

where m is the particle's mass, q is the particle's charge, and $v_{\perp}$ is the speed of the particle perpendicular to the magnetic field $\overrightarrow{B}$ (108; 24). Similarly, the centripetal force from the tokamak curvature induces a velocity perpendicular to both the

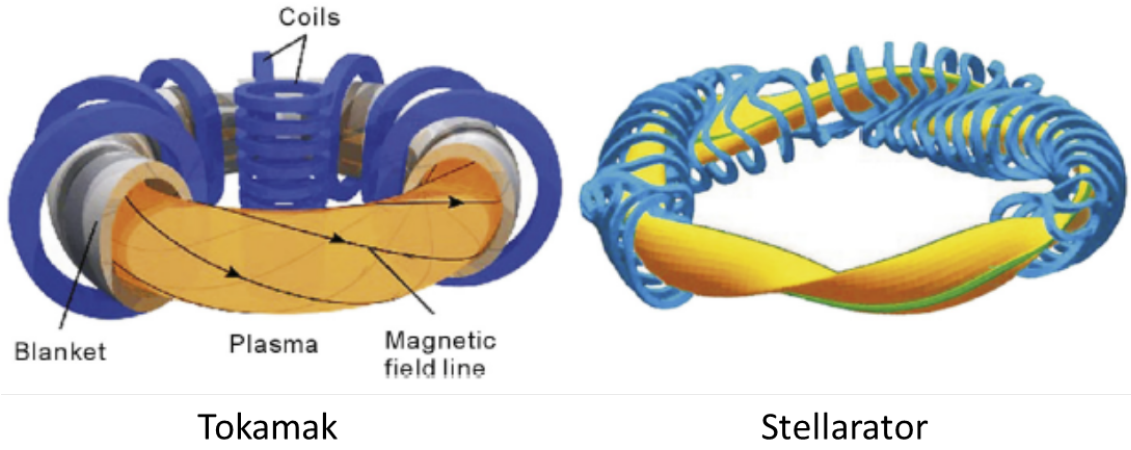

Figure 1.5: Cross-sectional schematic of a general tokamak and stellarator design, showing the internal plasma flow within each (129).

magnetic field and centripetal force (unit vector $\overrightarrow{n_F}$) directions:

$$\overrightarrow{v_F} = -\frac{mv_{\parallel}^2}{Rq}\frac{\overrightarrow{B} \times \overrightarrow{n_F}}{|\overrightarrow{B}|^2} \tag{1.4}$$

where $v_{\parallel}$ is the speed of the particle parallel to the curved arc of radius R (108; 24). The final drift, ExB, is the result of the Lorentz force when the electric field is perpendicular to the magnetic field; this electric field $\overrightarrow{E}$ will always be inherent in a tokamak because the gravity drift will slightly separate ions and electrons by mass, creating a potential difference further exacerbated by the ambipolar nature of the other drifts above (108; 24). The resulting velocity

$$\overrightarrow{v_{\overrightarrow{E}\times\overrightarrow{B}}} = \frac{\overrightarrow{E} \times \overrightarrow{B}}{|\overrightarrow{B}|^2} \tag{1.5}$$

is uniquely independent of the charge of the particle, meaning that the bulk plasma is always drifting uniformly.

Poloidal magnetic field lines from the plasma current partly correct for these drifts via the net-helical B-field shape discussed above, but additional toroidal coils not pictured in Figure 1.5 may be used to further line shaping and minimize the impact of drifts. Nonetheless, despite our best efforts, some drifting as well as more fundamental turbulent transport will always be inherent in tokamaks, which will prove detrimental to vessel walls. To this end, it is essential that a delineation be made between the bulk plasma in the middle of the tokamak and particles escaping the bulk plasma that are destined to impact the wall. The central, bulk plasma is toroidally symmetric, following closed B-field lines of concentric, nested toroids; the first poloidal field line to connect with a wall surface (i.e. first open field line) begins the scrape-off layer (SOL) (109). Escaping particles from the bulk plasma diffuse across poloidal field lines into the SOL via drifts and impact the wall. A first approach to minimizing SOL connection with the vessel wall is to insert a particularly durable material close to the last closed flux surface (LCFS) of the bulk plasma, aptly

called a "limiter." This action makes the SOL essentially equal the LCFS, as shown in Figure 1.6 (109). Consequently, the limiter will take the bulk of the particle and heat flux, reducing damage to the remaining walls of the vessel.

Unfortunately, the geometry of the impurity flux from the limiter will cause sputtered impurities to seed directly into the main plasma. In addition to damaging the limiter, these sputtered impurities will degrade reactor performance; efforts to heat DT fuel will parasitically heat these impurities as well (36). Hence, we consider a different technique to help control the mitigation of particle flux to the wall: the divertor. With this technique additional magnetic coils are installed to change the poloidal geometry of the SOL while preserving the nested-toroid geometry of the bulk plasma. The change to the SOL is shown in Figure 1.7. The main plasma now pinches to a null or x-point with a magnetically shielded (i.e. "private") plasma region below. In Chapter 2, we will see that different physics is now required to explain the SOL behavior (i.e. simple vs complex SOL), with strong behavioral dependence at the material surface upon the upstream density and temperature (109). Importantly, sputtered neutral impurity sources are displaced from the main plasma. While these impurities still can make their way into the bulk plasma eventually via impurity transport, the process is less immediate than in the limiter case. For this reason, the divertor tokamak design is expected to be the industry standard for tokamak reactors. Meanwhile, some experimental devices at present have both a limiter and divertor. Many variations of divertor designs exist across both tokamaks and stellarators. This dissertation will focus solely on the conventional lower-single-null tokamak divertor sketched in Figure 1.7, but we posit that many results are applicable across MCF concepts due to the similarity of the basic physics.

1.4 SOL Modeling with OEDGE

Naturally, the SOL is a critical region of study for MCF plasma physics: forming the bridge between the very different plasma requirements at the core vs the vessel

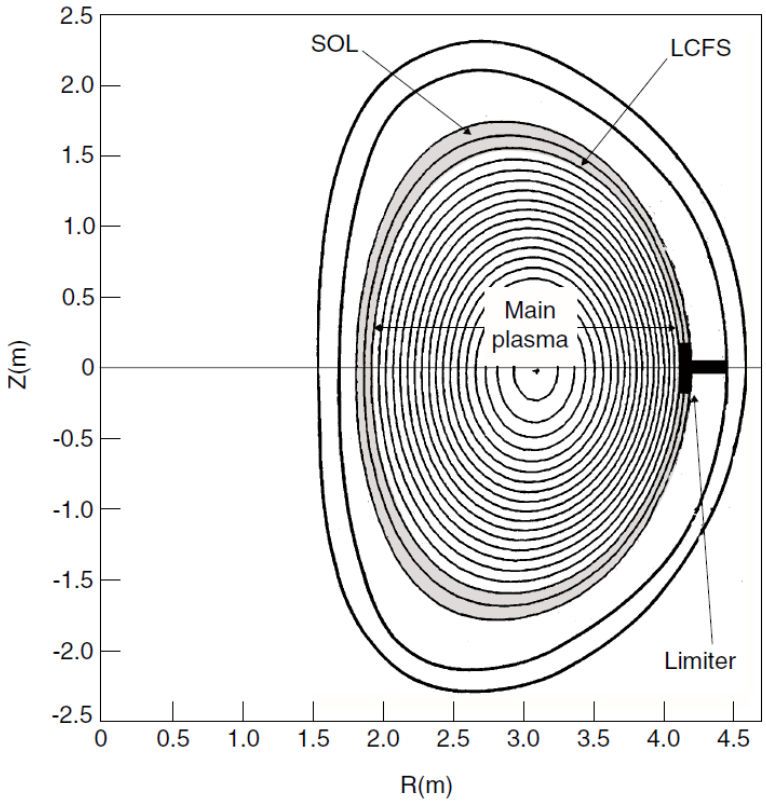

Figure 1.6: Toroidal cross-section of a JET-sized plasma with a limiter in-vessel (109).

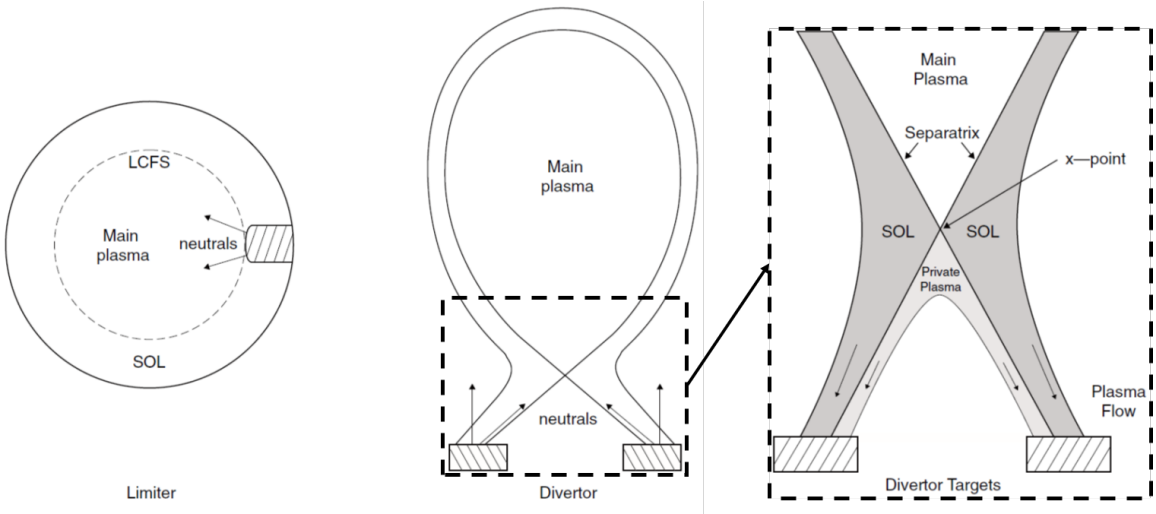

Figure 1.7: Difference in magnetic geometry between tokamaks with limiters (left) and divertors (center) with important regions of the divertor configuration labeled in an expanded figure (right) (109).

wall. However, knowledge of SOL conditions are practically limited by diagnostic coverage, which cannot encompass the entire SOL. Langmuir probes (LPs) and Thomson scattering (TS) diagnostics currently form the bulk of electron density and temperature measurements within the SOL (36). LPs are electrodes which are inserted into the plasma from the vessel wall and can be used to determine local plasma conditions based on current responses to changes in the potential difference between the plasma and the probe. Knowledge of SOL conditions via LPs is highly localized to the probe exposure area; moreover, these diagnostics perturb the plasma so require geometrically limited, methodologically careful application. Meanwhile, TS diagnostics use a high-power, pulsed laser to electromagnetically excite plasma particles, then measure the commensurate radiation at infrared-to-visible wavelengths with standard spectroscopy. The full-width-at-half-maximum of the spectroscopic emission lines inform electron temperature and density within the diagnostic field-of-view. Once again, these SOL measurements are localized, here by the constraints of spectroscopic coverage for a given device.

Nonetheless, theoretic and computational models must overcome these experimental constraints to account for the full SOL picture. Predictive models like SOLPS are highly computationally expensive (127); this fact makes them less useful for informing large sets of plasma discharge experiments. A sound alternative is interpretive modeling; interpretive modeling uses experimental measurements (e.g. LPs and TS diagnostics) as boundary conditions before iterating on free parameters in the model to propose a SOL that reproduces the entire physics picture available from experimental data. Now, we will undertake neither predictive nor interpretive SOL modeling during this dissertation; however, we will use outputs from OEDGE, an interpretive model, to inform the work in Chapter 5. Thus, it is worth describing a few key points about OEDGE as an aside (112; 91).

OEDGE defines a SOL by solving 1-D fluid equations across flux tube coordinates. These coordinates are defined by nested poloidal magnetic flux toroids

$$\Psi_N = \frac{\Psi - \Psi_{(axis)}}{\Psi_{(separatrix)} - \Psi_{(axis)}} \tag{1.6}$$

where $\Psi_N = 0$ is at the center of the magnetic cross-section (i.e. the magnetic axis) and $\Psi_N = 1$ is at the separatrix (see Figure 1.7). For each Ψ_N, s defines the coordinate along the poloidal magnetic field line in the SOL ($s = 0$ is the inner target and $s = s_{max}$ is the outer target), and we typically assume the rotation around the torus is axisymmetric. Hence, the 1D fluid equations solved at each Ψ_N are as follows:

$$\overrightarrow{\nabla} \cdot \overrightarrow{\Gamma} = \frac{d}{ds} n(s)v(s) = S_p(s) \tag{1.7}$$

$$\overrightarrow{\nabla} \cdot \overrightarrow{P} = \frac{d}{ds}(n(s)(kT_e(s) + kT_i(s)) + n(s)m_i v(s)^2) = S_m(s) \tag{1.8}$$

$$\overrightarrow{\nabla} \cdot \overrightarrow{Q_e} = \frac{d}{ds}\left(\frac{5}{2} n(s)v(s)kT_e(s) - \kappa_{0e} kT_e s^{5/2} \frac{dkT_e(s)}{ds}\right) = S_{e,e}(s) \tag{1.9}$$

$$\overrightarrow{\nabla} \cdot \overrightarrow{Q_i} = \frac{d}{ds}\left(\frac{5}{2} n(s)v(s)kT_i(s) + \frac{1}{2} m_i n(s)v(s)^3 - \kappa_{0i} kT_i s^{5/2} \frac{dkT_i(s)}{ds}\right) = S_{e,i}(s) \tag{1.10}$$

Here, Γ is particle flux density, P is pressure, Q_e is electron energy, Q_i is ion energy, and each of $S_p, S_m, S_{e,e}, S_{e,i}$ are volumetric source/sink free parameters. Hence, Equations 1.7-1.10 represent conservation of particles, mass, electron energy, and ion energy, respectively. These fluid equations form an initial value problem over a grid-cell geometry, with boundary conditions set by experimental measurement conditions. Figure 1.8 shows an example OEDGE grid at DIII-D with important diagnostics setting the boundary conditions labeled. The code solves four unknowns $(n(s), v(s), T_e(s), T_i(s))$ based on the boundary conditions and free parameter settings,

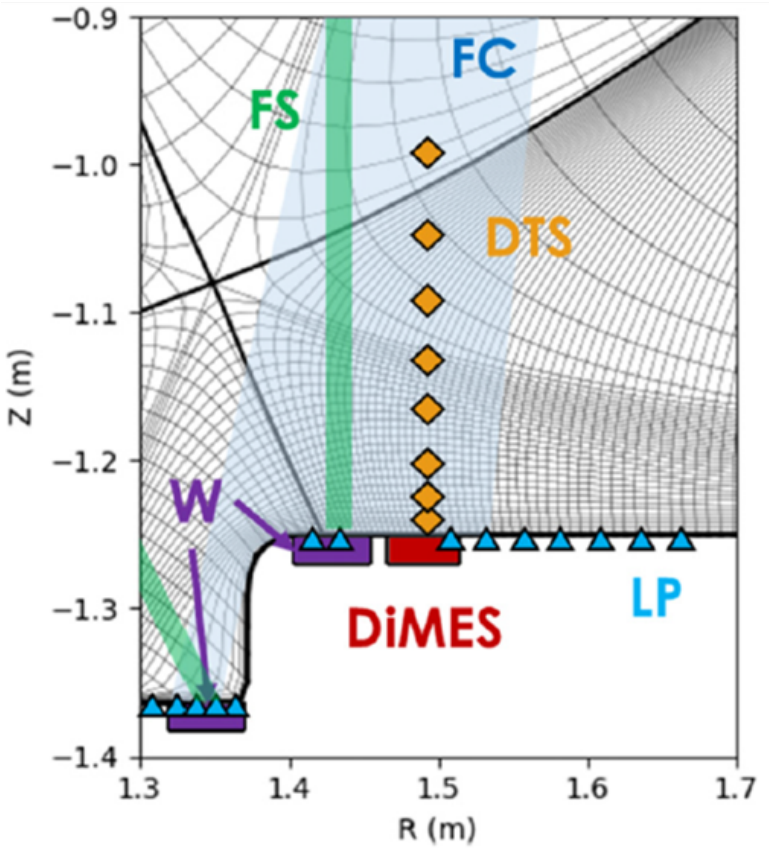

Figure 1.8: Cross-section of a computational grid used in OEDGE interpretation of a DIII-D discharge, with tungsten (W) metal rings labeled in purple, the Divertor Material Evaluation Station (DiMES) in red, filterscope spectroscopy (FS) view chord in green, filtered camera (FC) view chord in dark blue, LPs in light blue, and divertor TS (DTS) cross-section in orange (91).

the last of which are iterated until agreement is reached with all experimental data. In this way, OEDGE can reveal the "full" SOL for a given plasma discharge. We will use its outputs in Chapter 5.

1.5 Net Erosion and the ITEP Gap

A significant boundary to MCF is the integration of the energy-production requirements of the core plasma with the wall-lifetime constraints of the edge plasma. We refer to this problem as closing the Integrated Tokamak Exhaust and Performance (ITEP) gap (21). Obviously, SOL engineering plays an important role here as the bridge between the two plasma condition extremes, but overcoming the ITEP gap will require full-device optimization.

For example, optimized confinement regimes may partially lower the SOL restrictions from the core. Up until 1982, plasma operations persisted in what is now called L-mode or low-confinement mode, characterized by a confinement time that decreases strongly with auxiliary power (5). Then, a new mode of sudden, enhanced confinement time was discovered beyond a threshold power value by Friedrich Wagner that year (5), subsequently called H-mode or high-confinement mode. H-mode is further characterized by the steep gradient descent of electron density and temperature radially outward beyond a so-called pedestal region in the bulk plasma (61). Figure 1.9 shows example pedestal profiles, demonstrating the emergence of this phenomenon in H-mode but not L-mode. While understanding H-mode from first principles is still an ongoing research topic, H-mode has been observed now at all major fusion devices, including DIII-D and JET (116). However, there is a trade-off to H-mode in the form of short but strong bursts of particle (microsecond) and energy (nanosecond) expulsion from the core, typically measured experimentally in the form of the H-α spectroscopic Balmer line as shown in Figure 1.10 (109). These bursts are referred to as edge localized modes (ELMs). Despite ELMs, H-mode is intended to be the operating regime for tokamak reactors, with investigation into

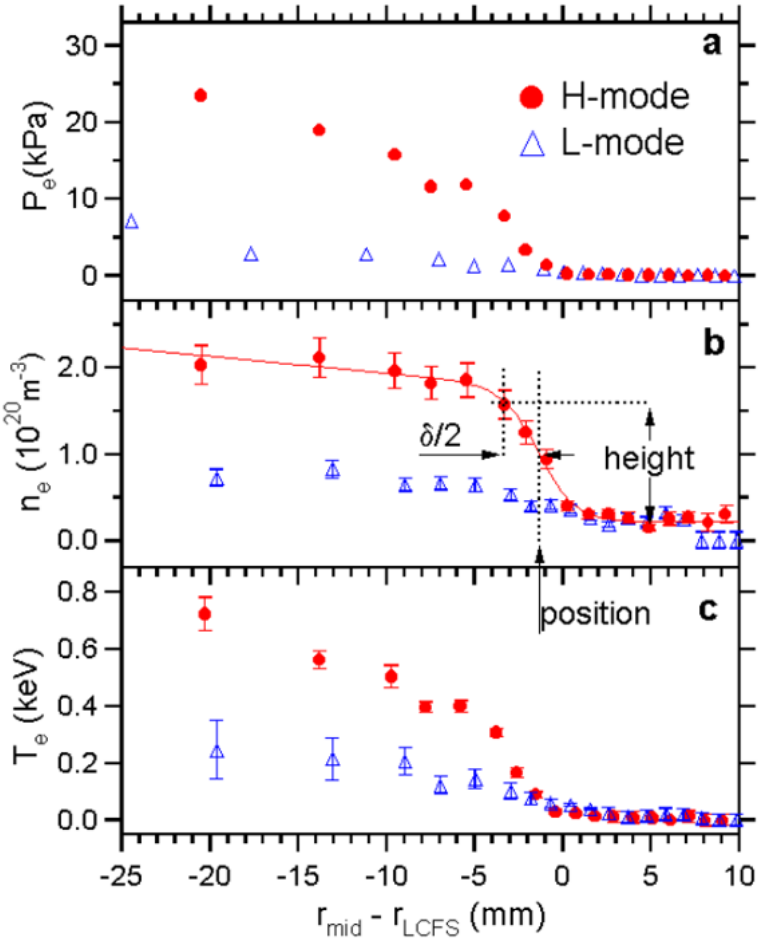

Figure 1.9: Example profiles of pressure (a), density (b), and temperature (c) demonstrating the presence of the pedestal region in H-mode (with labeled dimensions) but not L-mode at Alcator C-Mod (Mossessian et al.)

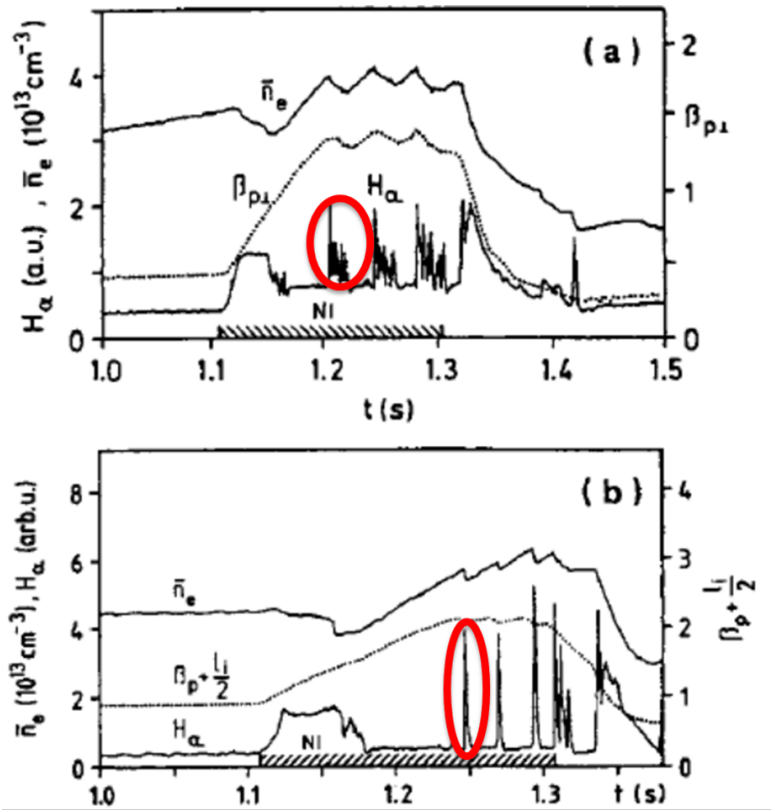

Figure 1.10: Characteristic H-α emission during H-mode at ASDEX with example continuous (a) and discrete (b) bursts of ELMs highlighted in red (109)

mitigating ELM devastation on vessel walls ongoing. We may subsequently define parts of an H-mode discharge as inter- or intra-ELM while L-mode is entirely without ELMs.

Now, the motivation of this work will be the need to seek partial solutions to closing the ITEP gap from the other extreme: the constraints of the vessel wall. For economical reasons, vessel walls must exhibit long (∼years) lifetimes in order for MCF to be viable; moreover, as mentioned in Section 1.3, impurity contamination in the core significantly degrades reactor performance. If the SOL transports impurities into the edge (Chapter 4, they can destabilize the pedestal performance and increase disruptions (86). The further transport of these impurities into the core from the edge will decrease the efficiency of heating efforts and collapse the operational space of ignition (86), as shown in Figure 1.11.

Consequently, minimizing the net erosion of vessel wall plasma-facing components (PFCs) is critical to closing the ITEP gap. We will define net erosion as gross erosion (the amount of wall material initially leaving a PFC surface) minus redeposition (the amount of eroded wall material returning to a PFC surface); hence, net erosion minimization may occur through both minimizing the gross erosion and maximizing the redeposition of PFCs. The plasma-material interaction (PMI) impurity pathway between wall net erosion and core performance is shown in Figure 1.12; PFC-saving redeposition can come through favorable impurity transport properties from both the "global" and "surface" scale. The plasma region touching the PFC surface is called the sheath; this region has very different physics from the rest of the bulk plasma and will be discussed in greater detail in Chapter 2.

As will be seen in Chapter 3-4, different physical scaling is expected for net erosion of low-Z and high-Z PFC materials. Some arguments suggest that low-Z materials make ineffectual PFCs because of their high sputtering rate and the rapid build-up of tritium co-deposits (101). On the other hand, high-Z materials are largely without these issues but come at a high cost of core-radiation losses when impurities seep into the bulk plasma (95). At present, we expect tungsten (W) or a similar high-Z material

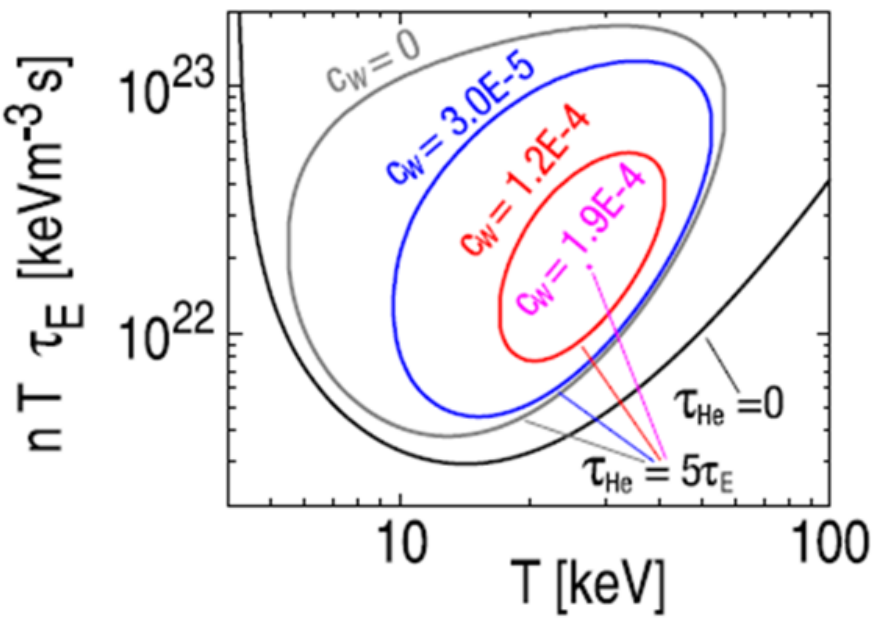

Figure 1.11: Ignition curves with different concentrations of tungsten impurities C_W, showing the decreased operational space of increased impurity contamination in the core (95).

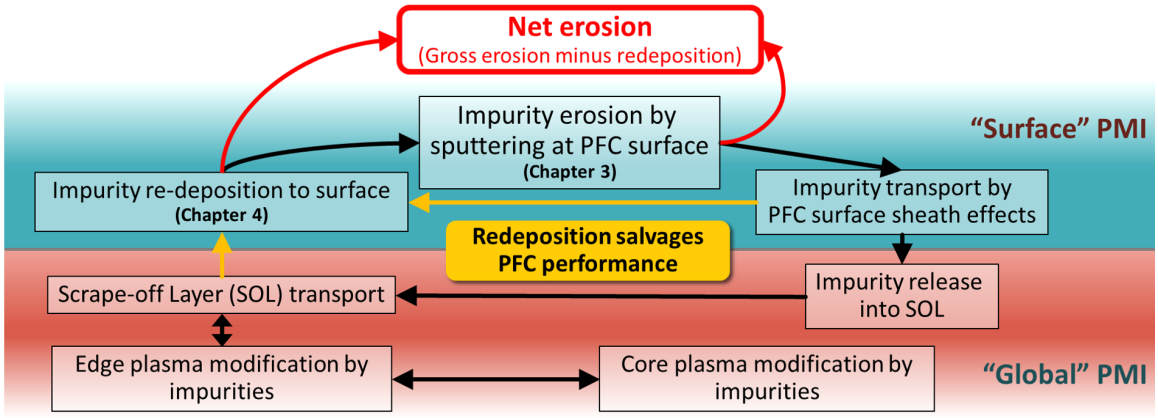

Figure 1.12: Generalized PMI impurity pathway from material surface to plasma core, with lifetime-extending PFC redeposition pathways in yellow (Unterberg).

to be a PFC in at least the divertor of both ITER and future tokamak reactors due its general ability to withstand high heat fluxes and energetic neutrons (92). Hence, it is critical that we understand net erosion mechanisms of high-Z material to high fidelity in order to improve reactor performance towards an ITEP solution.

In this dissertation, we will outline a refined model of high-Z net erosion physics in the context of divertor PFCs under L- or inter-ELM H-mode. Because of the characteristics of the energetic particles expelled during an ELM event, net erosion scaling intra-ELM is distinct from that of either inter-ELM H-mode or L-mode; we will restrict our focus in this dissertation to net erosion in the latter two schemes for conciseness. Chapter 2 will outline the physics of the sheath. Chapter 3 will discuss the physics and trends of high-Z gross erosion; it will show a new Monte Carlo code used for estimating incident ion conditions onto the PFC surface that in turn improves estimation of the sputtered PFC distribution as it exits the surface. Chapter 4 will outline the details of high-Z redeposition, using W as a representative PFC, and put forth an improved model of redeposition that discriminates between the mechanistic pathways involved. In Chapter 5, we show the scaling trends of different redeposition mechanisms against key underlying net erosion drivers in the sheath. In Chapter 6, we reassess the results of Chapter 5 in the context of a larger set of plasma-material parameters using Sobol' indices. Finally, we will design an experiment to test these new findings in Chapter 7.

1.6 Executive Summary

- Fusion energy may be a necessary part of the baseload energy portfolio needed to curtail climate change.
- Deuterium-tritium plasma forms the basis of fusion pilot plant design.
- Magnetic confinement fusion requires plasma and material engineering capable of long first-wall lifetimes in extreme environments.

- High-Z plasma facing components require manageable net erosion (gross erosion - redeposition) to maintain a functioning reactor.

Chapter 2

Fundamental Aspects of the Plasma Sheath

2.1 The Debye Sheath

In this chapter, we will discuss the physics of the plasma sheath, an inherent aspect of vessel plasma confinement that contributes to impurity net erosion. We will discuss aspects of the sheath that determine both gross erosion and redeposition in subsequent chapters. We begin by discussing the most basic of sheaths: the Debye sheath. In simple terms this sheath is a thin region of plasma at a plasma-material surface with distinct dynamics that electrically insulates the main plasma from the material (24). We may think of the sheath creation in the following steps (109). First, a plasma discharge is created by inducing high electromagnetic fields on a fill gas. Immediately, displaced electrons are attracted to the relative ground of the vessel walls and begin to negatively charge the material surface (within microseconds) via collisions. Note that ions also interact with the wall but are much slower moving that electrons by mass. Consequently, a potential difference develops between the main plasma and the wall surface with plasma electrons repelled from the material surface and ions accelerated toward it. The sheath is defined as precisely this plasma region,

characterized by strong ambipolar electric fields from the potential difference; this sheath is much smaller than the main plasma volume. Additionally, the sheath varies in thickness until loss rates from surface collisions are equivalent between electrons and ions. A cartoon to guide the understanding is shown in Figure 2.1.

In the simplest form, we may estimate the size of the sheath (24) by assuming a 1-D Maxwell-Boltzmann distribution of electrons, perturbed by an electric potential difference ψ. We further assume that the ion density forms a constant, uniform background charge at the electron timescale due to inertia. Thus, the electron distribution f in velocity v goes like:

$$f(v) \propto e^{\frac{\frac{1}{2}m_e v^2 + q_e \psi}{k_B T_e}} \tag{2.1}$$

Here, m_e, q_e, and T_e are the mass, charge, and temperature of the electrons, respectively, with k_B as the Boltzmann constant. Integrating f results in the following electron density, where n_e and n_{ip} are the electron and constant plasma ion densities, respectively:

$$n_e = n_{ip} e^{\frac{q_e \psi}{k_B T_e}} \tag{2.2}$$

So, the Poisson equation (1-D) above the material surface (where z is the height and ϵ is the electrical permittivity) becomes:

$$\frac{d^2\psi}{dz^2} = \frac{q_e}{\epsilon}(n_e - n_{ip}) = \frac{q_e}{\epsilon} n_{ip}(e^{\frac{q_e \psi}{k_B T_e}} - 1) \tag{2.3}$$

Due to the rapid potential decay expected across the sheath, we may approximate this equation by a linearized one from the Taylor expansion, i.e.:

$$\frac{d^2\psi}{dz^2} = \frac{q_e^2}{\epsilon} \frac{n_{ip}\psi}{k_B T_e} \tag{2.4}$$

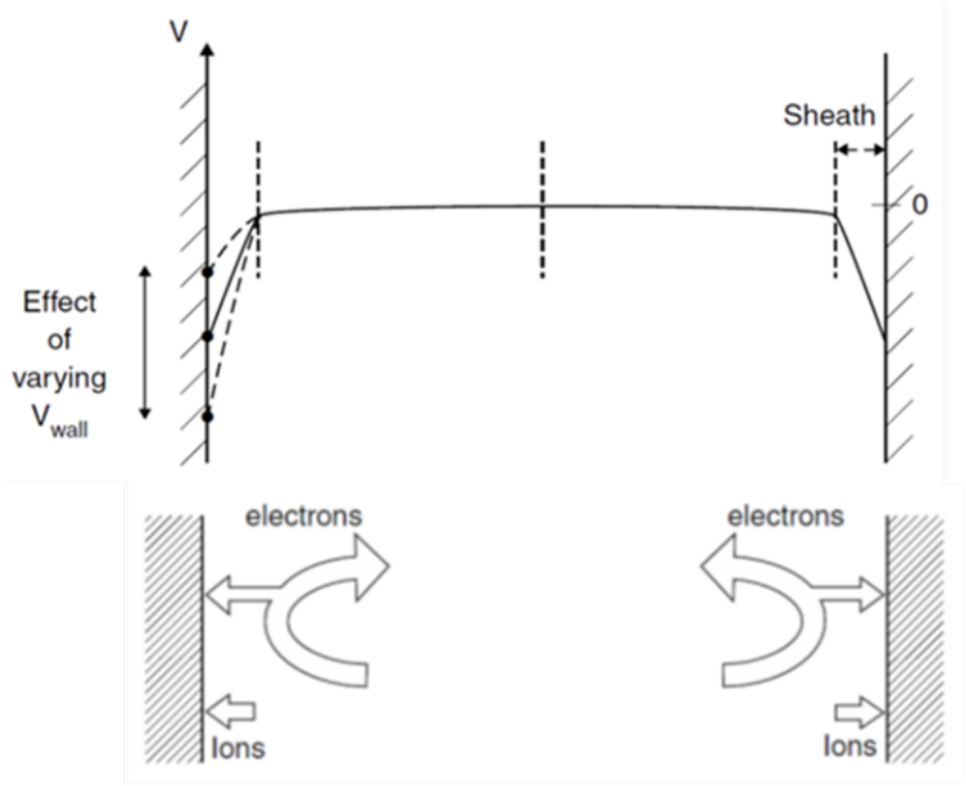

Figure 2.1: A one-dimensional cartoon showing the variation of electric potential across the sheath region and its ambipolar effect on particles. Here, $V = \psi$ (109).

The solution to this equation decays as given by:

$$\psi(z) \propto e^{-z/\lambda_D} \tag{2.5}$$

where

$$\lambda_D = \sqrt{\frac{\epsilon k_B T_e}{n_{ip} q_e^2}} \tag{2.6}$$

is called the Debye length and represents the effective shielding distance of the sheath. Hence, although the sheath has no precisely defined boundary, we may think of the Debye length as its effective thickness to first order. In reality, the sheath may be a few ($\sim$ 10) Debye lengths wide. The potential shielding accomplished on the order of the Debye length is called the Debye shield. As stated in Chapter 1, a feature distinguishing plasma from lightly ionized gas is the dominance of electromagnetic forces (as opposed to collisions) in determining the plasma's motion. A rigorous definition of a plasma includes, in addition to this qualifier, that λ_D must be much smaller than the length of the plasma and N_D, the number of particles in a sphere of radius λ_D, must be much larger than unity (24).

Having introduced the basic Debye sheath, we now discuss some of its implications (109). We first note that Debye shielding is not perfect. A small electric field $|\vec{E}| \approx \frac{k_B T_e}{2 q_e L}$ extends the length of the plasma L and draws ions in the SOL toward the material surface, commensurately repelling electrons. This electric field is sometimes called the pre-sheath electric field. Competing forces from (1) this electric repulsion and (2) fluid pressure gradients toward the wall essentially (but imperfectly) balance the electron acceleration; this justifies the so-called Boltzmann factor relation given for n_e in Equation 2.2 above. Meanwhile, electric attraction only compounds with fluid pressure gradients to accelerate ions toward the wall. Quasineutrality implies that the electron and ion fluxes to the surface are equivalent; therefore, electrons must be almost perfectly force-balanced to compensate for their small size relative to ions. Indeed, it is important to point out that, while the pre-sheath $\vec{E}$-field affects

both ions and electrons, it has no net effect on the overall plasma because of the quasineutrality. Nevertheless, we note that ions are especially accelerated through the sheath which may increase PFC sputtering (see Chapter 3).

We note similarly that electrons are more cooled thermally by the sheath than ions (109). Subsequently, ion temperatures usually exceed electron temperatures in the SOL; hence, the isothermal or thermal equilibrium assumption discussed in Chapter 1 is technically no longer valid when sheath effects are considered. Now, temperature gradients are normally small due to the high thermal conductivity of plasmas (109). However, when collisionality is high, we require corrections to the SOL model in order to account for these temperature variations. We may formally define collisionality within the SOL as (109)

$$\nu^*_{col} = L/\lambda \tag{2.7}$$

where L is the connection length and $\lambda \approx 10^{16}T^2/n$ is either the electron or ion self-collisionality. For tokamaks with a limiter (where connection lengths are smaller), an isothermal approximation may still be valid in modeling the SOL, called the simple (or sheath-limited) SOL. However, divertor tokamaks (where connection lengths are longer) may have significant temperature differences between the upstream and downstream ends of the SOL; this model is called the complex (or conduction-limited) SOL. We refer the reader to the book by Stangeby (109) for further details.

A final topic that we will discuss here regarding traditional Debye sheaths is the so-called Bohm criterion. We will reproduce here for clarity an argument for the Bohm criterion made in (109) for the case $T_{ip} = 0$ (i.e. plasma ion temperature is 0), which is simpler to derive than the isothermal $T_e = T_{ip}$ case. Interestingly, this result will still provide insight into the $T_e = T_{ip}$ case, as we will explain. We will assume here without proof that particles in the SOL enter the sheath at a velocity less than

or equal to the plasma sound speed c_s:

$$c_s = \sqrt{\frac{k_B(T_e + T_{ip})}{m_{ip}}} \tag{2.8}$$

where m_{ip} is the plasma ion mass. In other words, $v_{se} \leq c_s$, where v_{se} is the sheath edge velocity. This assumption is justified in (109) using an isothermal fluid model that assumes smooth solutions (i.e. no singularities). The Bohm criterion will bound v_{se} from below using the flow of plasma on the sheath side. We start with some assumptions from the derivation of the Debye length, namely that $n_e \neq n_{ip}$ within the sheath; moreover, n_e obeys the Boltzmann factor. That is,

$$n_e(z) = n_{se} e^{\frac{q_e(\psi(z) - \psi_{se})}{k_B T_e}} \tag{2.9}$$

where $\psi(z)$ is the local electric potential at above-PFC height z, n_{se} is the Debye sheath entrance electron density, and ψ_{se} is the Debye sheath entrance electric potential. We seek to find ψ_{se}, which determines the pre-sheath electric field. In this way, we may know v_{se} under conservation of energy, assuming that $\psi = 0$ upstream from the sheath edge. We further assume that ions originate from a single upstream point-source with zero initial velocity and that ions are only electrostatically accelerated through the potential drop ψ_{se} (i.e. ions pass collisionlessly through this region). Consequently, $n_{ip} = n_{se}\sqrt{\psi_{se}/\psi(z)}$ by combining particle conservation with conservation of energy.

Now, we again recover from Poisson's equation (in 1-D) an expression of the form:

$$\frac{d^2\psi}{dz^2} = \frac{q_e}{\epsilon}(n_e - n_{ip}) = \frac{q_e}{\epsilon} n_{se} \left(e^{\frac{q_e(\psi - \psi_{se})}{k_B T_e}} - \sqrt{\frac{\psi_{se}}{\psi}} \right) \tag{2.10}$$

After a variable substitution for the positive potential difference just inside the sheath ($\hat{\psi} = \psi_{se} - \psi$), we may approximate:

$$\sqrt{\frac{\psi_{se}}{\psi}} \approx 1 + \frac{1}{2}\frac{\hat{\psi}}{\psi_{se}} = 1 - \frac{1}{2}\frac{\hat{\psi}}{|\psi_{se}|} \tag{2.11}$$

Combined with a Taylor expansion of the exponential term, the Poisson equation may be approximated to first order as:

$$\frac{d^2\hat{\psi}}{dz^2} \approx \frac{q_e n_{se}}{\epsilon}\left(\frac{q_e}{k_B T_e} - \frac{1}{2|\psi_{se}|}\right)\hat{\psi} \tag{2.12}$$

Considering this equation as an eigenvalue equation, a negative eigenvalue would imply oscillations which are unobserved experimentally. Thus, assuming a nontrivial equation, we may conclude that the eigenvalue is positive. Thus, $\frac{q_e}{k_B T_e} \geq \frac{1}{2|\psi_{se}|} \implies m_{ip} v_{se}^2 \geq k_B T_e \implies$

$$v_{se} \geq \sqrt{\frac{k_B T_e}{m_{ip}}} = \sqrt{\frac{k_B(T_e + 0)}{m_{ip}}} = \sqrt{\frac{k_B(T_e + T_{ip})}{m_{ip}}} = c_s \tag{2.13}$$

Hence, we may bound v_{se} from below with c_s. This relationship, $v_{se} \geq c_s$ is the Bohm criterion. Combined with the assumption above from the fluid model that $v_{se} \leq c_s$, we may say that $v_{se} = c_s$. However, in general, it may only be the case that $v_{se} \geq c_s$ (i.e. the velocity at the sheath entrance may be supersonic). Regardless, we see that the ions at the sheath entrance are traveling at least at the sound speed, meaning vessel walls are bombarded by very high-speed particles (see Chapter 3). A generalized Bohm criterion may be given as follows, with $\gamma = 1$ for isothermal conditions:

$$v_{se} \geq \sqrt{\frac{k_B(T_e + \gamma T_{ip})}{m_{ip}}} \tag{2.14}$$

2.2 The Chodura Sheath

Now, we will discuss a different type of sheath structure: the Chodura pre-sheath or magnetic pre-sheath (MPS). This Chodura sheath will play a critical role in determining redeposition, to be discussed in Chapter 4. The primary difference between a sheath with a MPS or without one (i.e. just the Debye sheath (DS) discussed before) is the incidence angle of magnetic field lines onto the material surface. The above DS analysis has ignored this effect, implicitly assuming either the absence of magnetic fields or magnetic fields normal to the material surface. However, particularly in divertor tokamaks, glancing toroidal $\vec{B}$-field angles at material surfaces are expected to minimize heat flux, hence minimize material erosion (36). We will now consider a heuristic approach to the effect of oblique angles, which induce a MPS in addition to the DS discussed above.

We may intuitively think of the MPS as a region of heightened electric fields between the main plasma and the DS which functions to correct the incident ion flow from a parallel-to-$\vec{B}$ direction to a surface-normal direction (109; 103). As shown in Figure 2.2, this feature implies an effective depth of the MPS on the order of a few ion Larmor radii, which will generally be thicker than the DS depth (a few Debye lengths). This implication will be shown more rigorously below. In the DS, electron density is far lower than ion density due to rapid accumulation of electrons on the wall and subsequent ambipolar electric fields. In contrast, the plasma in the MPS is much closer to quasineutral; the reason is that the much smaller Larmor radius of the electrons allow electrons to pass through the MPS essentially unaffected (109). Nevertheless, some disparity between ion and electron concentration still exists in this region, contributing to a potential difference stronger than the electric field of the background plasma.

Based on the new geometry, we may summarize a few important features of the MPS (109). To begin, we consider changes induced by the MPS on the surface flux density of plasma ions (Γ_{ip}) and electrons (Γ_e). For the traditional DS, $\Gamma_{ip} = n_{se}c_s$

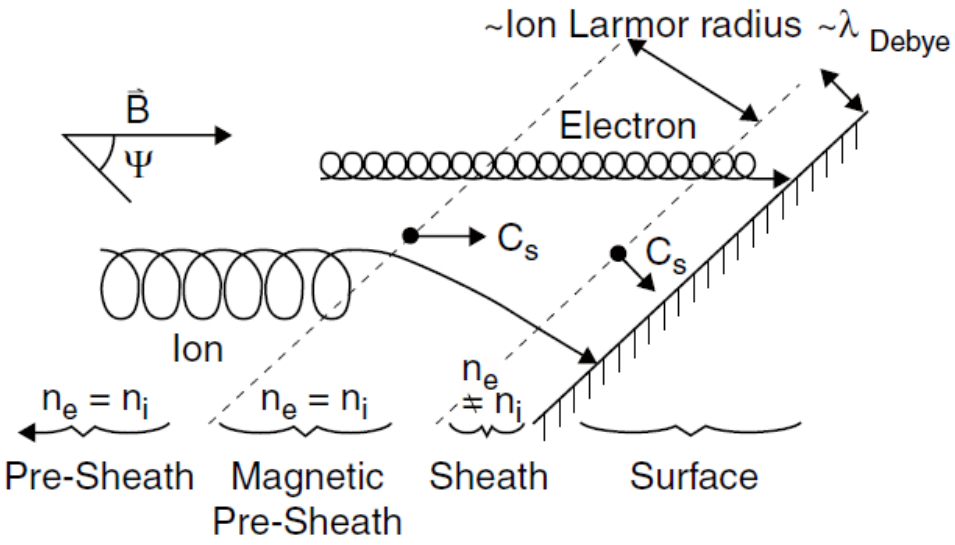

Figure 2.2: Cartoon of the three distinct regions at the plasma-material surface: the DS, the MPS, and the main plasma (i.e. the pre-sheath). Here, Ψ is the angle complementary to α, and $n_i = n_{ip}$ in the text (109).

based on the Bohm criterion. Considering additional effects from the Boltzmann relation, we may further say that $\Gamma_e = (1/4)n_{se}c_e e^{(q_e\psi_w)/(k_B T_e)}$, where c_e denotes the electron sound speed and ψ_w denotes the potential difference between wall and bulk plasma at the sheath edge. Because the pre-sheath electric fields do not affect the overall particle balance, we may set $\Gamma_{ip} = \Gamma_e$ and rearrange to find that

$$\psi_w = \frac{0.5 k_B T_e}{q_e} \ln\left[\left(2\pi \frac{m_e}{m_{ip}}\right)\left(1 + \frac{T_{ip}}{T_e}\right)\right] \tag{2.15}$$

Here, ψ_w can also be interpreted as the floating potential at the wall surface. Now considering the MPS, the geometry at oblique angles changes $\Gamma_{ip} = n_{MPSE} c_s \sin(\alpha)$, where $n_e = n_{ip} = n_{MPSE}$ at the MPS edge and α is complementary to the oblique angle in Figure 2.2. Similarly, $\Gamma_e = (1/4)n_{MPSE}c_e e^{(q_e\psi_w)/(k_B T_e)} \sin(\alpha)$. Interestingly, setting $\Gamma_{ip} = \Gamma_e$ we see that the angle effects cancel out so ψ_w is independent of the incidence angle. In other words, despite the fact that the individual fluxes to the surface are changed, this occurrence bears no effect on the overall potential drop, and the above relation for ψ_w remains valid. It turns out that the Bohm criterion also remains valid. Now, we note that the total potential ψ_w is split between a DS and MPS component, the proportions of which have angular dependence. Because electrons are less affected by the Chodura sheath than ions, we may assume a Boltzmann relationship in both sheath regions. This fact and particle conservation of ions allow us to generate two analytic expressions that may be used to calculate the MPS potential drop (ψ_{MPS}):

$$n_{se} = n_{MPSE} e^{\frac{q_e \psi_{MPS}}{k_B T_e}} \tag{2.16}$$

and

$$n_{se} c_s = n_{MPSE} c_s \sin\alpha \tag{2.17}$$

Combining Equations 2.16 and 2.17, we see that:

$$\psi_{MPS} = \frac{k_B T_e}{q_e} \ln\left[\sin\alpha\right] \tag{2.18}$$

We may conclude from this expression that the ψ_{MPS} magnitude increases with incidence angle α. This distribution of ψ_{MPS} and ψ_{DS} (the DS potential drop) within ψ_w will play a key factor in understanding net erosion in Chapter 5. As an aside, we note that approaches to analytically ascribing the potential distribution across the sheath (MPS+DS) from these boundary conditions are not straightforward, as will be discussed further in the next section. Nonetheless, the above theory is heuristically informative of the important sheath features for understanding net erosion.

Lastly, we can approximate the width of the MPS by exploiting the Lorentz-force balance in this region (109). Setting $q_e c_s|\vec{B}| \approx q_e|\vec{E_{MPS}}|$ and noting the MPS electric field magnitude $|\vec{E_{MPS}}| \approx (k_B T_e)/(q_e L_{MPS})$ in a capacitor-like model, we may see the sheath thickness

$$L_{MPS} \approx \frac{c_s}{\omega_i} = \rho_{ip} \tag{2.19}$$

where $\omega_i = (q_e|\vec{B}|)/m_{ip}$ is the ion cyclotron resonance and ρ_{ip} is the corresponding plasma ion Larmor radius as a function of c_s. In other words,

$$\rho_{ip} = \frac{m_{ip} c_s}{q_e|\vec{B}|} \tag{2.20}$$

Thus, our intuitive understanding of the scale length of the MPS is validated, as promised.

As it turns out, this pedagogical approach to the sheath thickness is fairly accurate. More explicitly, maintaining electron and ion flux balance at the wall requires normal ion incidences at the Debye sheath entrance; otherwise geometrically driven differences in ion flight times through the sheath would result in regions of nonuniform charge distribution on the surface. The magnetic pre-sheath arises as a transition of the dominance between the plasma fluid mechanics outside the sheath (at a non-normal PFC incidence) and the electrostatic kinetics within the Debye sheath (at normal PFC incidence). Integral equation solutions resolving the various equations of motion within the MPS region reveal that a few gyrokinetic rotations of plasma ions are needed to complete this transition in order to maintain the Bohm

criteria (25). A thicker transition region is required for shallow α, where greater momentum correction is required. Hence, in practice and experiment (27; 1), we find that

$$L_{MPS} = k\rho_{ip}\cos\alpha \tag{2.21}$$

where k is the number of plasma ion gyro-orbits completed within the sheath. The value of k may vary across experimental devices and conditions but is typically treated as $\sim$ 2-3 (1; 2). We will see in Chapter 4 that the sheath thickness is especially important to this work as it critically determines redeposition fractions of high-Z PFCs.

2.3 The Brooks and Borodkina Sheath Models

The careful reader of Section 2.2 may note that calculating the potential drop throughout the sheath as a function of above-PFC height is now a complicated problem; even though we have developed a good understanding of the potential at important locations (i.e. sheath entrance, MPS-to-DS boundary, PFC surface), these boundary conditions in turn dramatically increase the complexity of finding a solution to the Poisson equation. Typically, this fact necessitates using numerically derived solutions to the integral equation in order to ascribe $\psi(z)$ rigorously (110), which can pose an undue computational burden. Instead, it is beneficial to use analytic approximations of the potential by assuming a form similar to that of Equation 2.5. The Brooks model (17) is a commonly used example of this approach, which may be summarized by the following equations:

$$\psi(z) = \psi_w \left[f_D \left(e^{-z/2\lambda_D} \right) + (1 - f_D) \left(e^{-z/\rho_{ip}} \right) \right] \tag{2.22}$$

where two Debye lengths are here used as the DS decay length, f_D is an arbitrary function of α such that $|f_D| < 1$ and

$$\psi_w = \psi_{DS} + \psi_{MPS} \tag{2.23}$$

forms the total potential drop through the sheath. Although ψ_w and $(1 - f_D)$ were originally set using empirically derived inputs, these parameters can be reconciled, respectively, with the definition used in Equation 2.15 and ψ_{MPS}/ψ_w as in Equation 2.18 (110). We will update the definition of f_D later in this section. However, we note that this Brooks model, while seemingly effective, is largely *ad hoc*.

As an alternative, the work in (11) derives the Borodkina sheath model to maintain a self-consistent, analytic approach throughout while still circumventing the need for repeated numerical calculations. We will reproduce this derivation here for completeness (11; 10). We start with the Poisson equation for the MPS, employing (a) a variable substitution $\xi = z/\lambda_D$, (b) a density normalization to the sheath-entrance value, and (c) a potential expression in dimensionless units of $k_B T_e/q_e$. That is:

$$\frac{d^2\psi}{d\xi^2} = n_e - n_{ip} \tag{2.24}$$

We further take ψ_{MPS} as given in Equation 2.18 and note that, using a first-order approximation, we expect the solution in the MPS to go like:

$$\psi \approx \frac{\psi_{MPS}}{\Delta n_{MPS}}(n_{ip} - n_e) \tag{2.25}$$

where Δn_{MPS} is the difference between ion and electron densities at the MPS-to-DS boundary. Lastly, we assume that the MPS reaches its average electric field magnitude at $\psi_{MPS}/2$. Hence, the Poisson equation in the MPS transforms to:

$$\frac{d^2\psi}{d\xi^2} = -\frac{\Delta n_{MPS}\psi}{\psi_{MPS}} \tag{2.26}$$

which can be integrated (via variable substitution) to give the equation for the MPS electric field:

$$\frac{d\psi}{d\xi} = \sqrt{-\Delta n_{MPS} \frac{\psi^2}{\psi_{MPS}}} \tag{2.27}$$

Note that combining Equations 2.18, 2.21, and 2.27 with the boundary condition at $\psi_{MPS}/2$ reveals that

$$\Delta n_{MPS} = -\frac{\psi_{MPS}}{(L_{MPS})^2} = -\frac{\ln\left[\sin\left(\alpha\right)\right]}{(k\rho_{ip}\cos\alpha)^2} \tag{2.28}$$

so that $d\psi/d\xi$ is well-defined by α up to 90°. Thus, Equation 2.27 can be solved directly so that the potential drop through the MPS $\psi_{mps}(\xi)$ is given as

$$\psi_{mps}(\xi) = \psi_{MPS} e^{-2(\xi - \xi_{MPS})/L_{MPS}} \tag{2.29}$$

where ξ_{MPS} represents the normalized height that defines the MPS-to-DS boundary (see Equation 2.37).

Meanwhile, deriving the DS potential drop requires us to exploit the ion flux and energy conservation. Assuming sonic ions, we have that:

$$n_{ip,MPS} c_s = n_{ip} \sqrt{c_s^2 - \frac{2k_B T_e(\psi - \psi_{MPS})}{m_{ip}}} \tag{2.30}$$

where $n_{ip,MPS}$ is the ion density at the MPS-to-DS boundary. We note that this normalized density can be estimated by $\sin\alpha$ as it is roughly the density at the MPS entrance by the quasineutrality condition within the MPS. Hence, we have that

$$n_{ip} = \frac{\sin\alpha}{\sqrt{1 - \frac{2(\psi - \psi_{MPS})}{1 + T_{ip}/T_e}}} \tag{2.31}$$

On the other hand, the electron concentration may be assumed to be as given by the Boltzmann factor so that $n_e = e^{\psi}$. Therefore, the Poisson equation through the DS

may be integrated (through the same variable substitution as before) and find

$$\frac{d\psi}{d\xi} = \sqrt{2e^{\psi} + 4\sin(\alpha)\sqrt{1 - \frac{2(\psi - \psi_{MPS})}{1 + T_{ip}/T_e}} + C} \tag{2.32}$$

where C is a constant resolving the MPS-to-DS boundary condition so that

$$C = -\Delta n_{MPS}\psi_{MPS} - 6\sin\alpha \tag{2.33}$$

This differential equation is quite tricky to solve; in fact, it requires a numerical solution using the boundary condition at the wall as in Equation 2.15; however, the numerical solution may be approximated so that the potential drop through the DS ψ_{ds} is given by

$$\psi_{ds}(\xi) = \psi_w + Q - Qe^{-a\xi} \tag{2.34}$$

Here, a and Q are expression-simplifying constants given, respectively, by:

$$a = \frac{\sqrt{-\Delta n_{MPS}\psi_{MPS}} - \sqrt{2e^{\psi_w} + 4\sin(\alpha)\sqrt{1 - (\psi_w - \psi_{MPS})} + C}}{\psi_w - \psi_{MPS}} \tag{2.35}$$

$$Q = \frac{1}{a}\sqrt{2e^{\psi_w} + 4\sin(\alpha)\sqrt{1 - (\psi_w - \psi_{MPS})} + C} \tag{2.36}$$

where C is the integration constant given by Equation 2.33. Lastly, this expression can be matched at the MPS-to-DS boundary layer with Equation 2.29 to find that

$$\xi_{MPS} = \frac{-1}{a}\ln\left[\frac{\psi_w - \psi_{MPS} + Q}{Q}\right] \tag{2.37}$$

With the derivation concluded, the Brooks model (i.e. Equations 2.22 and 2.23) and the Borodkina model (i.e. Equations 2.29 and 2.34) clearly result in different potential drops for the same sheath conditions. As a final note, there exists a physics inconsistency within both of these models. In particular, Equation 2.18 suggests that the potential drop through the MPS component becomes infinite as $\alpha \searrow 0$ but

the total potential drop through the entire MPS+DS is fixed to the finite value of Equation 2.15 (110). We can reconcile this discrepancy by noting that, when $\alpha = \alpha^*$,

$$\alpha^* = \arcsin\left[2\pi\left(\frac{m_e}{m_{ip}}\right)\left(1+\frac{T_{ip}}{T_e}\right)\right] \tag{2.38}$$

the DS potential drop $(\psi_w - \psi_{MPS})$ goes to 0 (110). Beyond this point, the DS vanishes. For the Borodkina model, we may easily couple a separate sheath model without a DS for $\alpha \leq \alpha^*$ to resolve the inconsistency; whenever $\alpha < \alpha^*$, we simply ignore Equation 2.34 (ψ_{ds}) and replace Equation 2.29 (ψ_{mps}) with the following expression (10):

$$\psi_{mps}(\xi) = \psi_w e^{-2\xi/L_{MPS}} \tag{2.39}$$

This step is not as straightforward in the Brooks model. On the one hand, this problem restricts the value of f_D such that $(1 - f_D)$ cannot diverge as $\alpha \searrow 0°$ (i.e. $(1 - f_D) \neq \psi_{MPS}/\psi_w$ as before); on the other hand, it does not provide a ready substitute for what f_D should be instead. For simplicity, we may choose f_D to be $\sin\alpha$ so that the DS disappears as $\alpha \searrow 0°$ (see Chapter 4). We will use this value of f_D when referring to the Brooks model for the remaining duration of this work, and we choose a $k = 2$ value for the Borodkina MPS in order to get a consistent treatment between the two models of the MPS decay length. A comparison for both models at different α values is shown in Figure 2.3; as can be readily seen, these formulations tend to exhibit stronger agreement as $\alpha \nearrow 90°$. As α becomes more shallow, the differences in emulating the disappearing DS become more important, resulting in more noticeable residuals between the two sheath models. Nonetheless, we calculate only a 12% difference between the Brooks and Borodkina models at most; a more selective choice for f_D in future work may improve this agreement further. We will use both the Borodkina and Brooks models at different stages of this work, beginning with the next chapter.

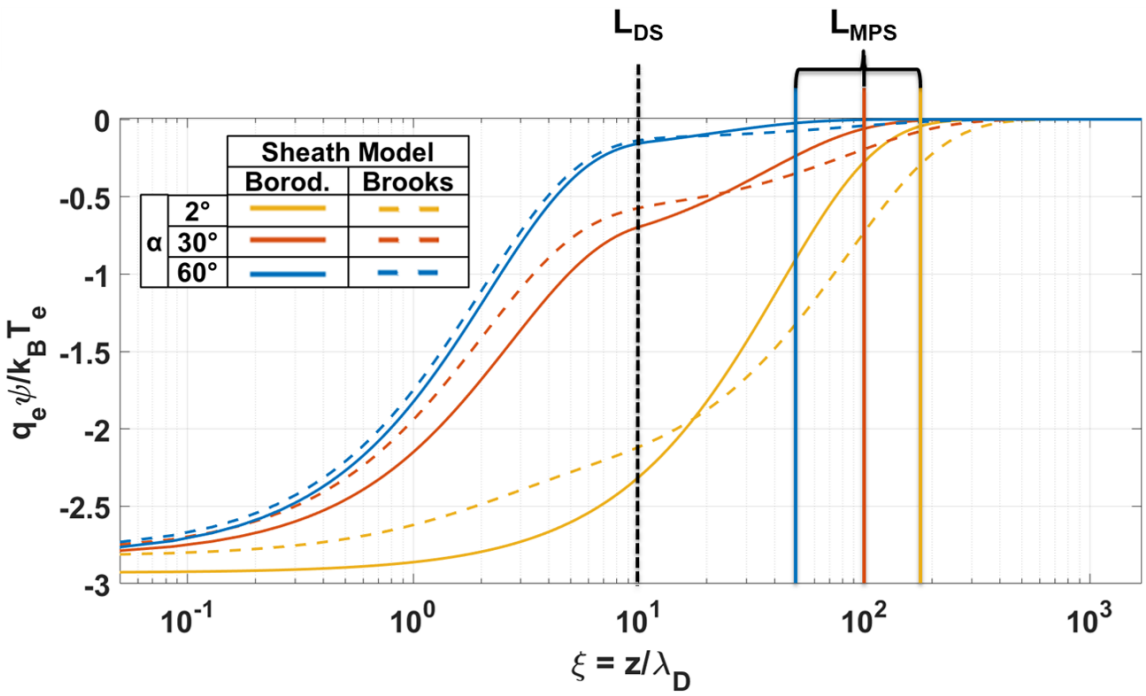

Figure 2.3: Comparison between the Brooks and Borodkina models of potential drop through the sheath as a function of above-PFC height. The MPS and DS thicknesses (here, we approximate the DS at $\sim 10\lambda_D$) are marked for different values of α.

2.4 Executive Summary

- Population imbalance between electron and plasma ion species forms a thin region of high electrostatic fields near the first-wall surface, called the sheath.
- At glancing magnetic field angles to the first-wall surface, the sheath splits into a thick magnetic pre-sheath and a thin Debye sheath.
- The Brooks and Borodkina sheath models provide two different analytic approximations for the potential and density distribution throughout the sheath, split between magnetic pre-sheath and Debye sheath components.

Chapter 3

Model of Gross Erosion

3.1 Physical Sputtering

In this chapter we will discuss the first component of the net erosion process determining PFC leakage into the SOL: gross erosion. The second component of net erosion, redeposition, will be discussed next in Chapter 4. Although we will start by presenting erosion physics that applies generally to all solid-state PFCs, our interest will increasingly narrow to high-Z PFCs and especially W as a representative species. As mentioned in Chapter 1, W is of particular importance because its ability to withstand high heat fluxes and energetic neutrons has made it the PFC of choice for ITER (92); these capabilities will likely cause W (or a very similar high-Z material) to remain a PFC in some aspect of all fusion reactors. In this section we will focus on the most important erosion source for this work: physical sputtering.

We will view the plasma outside the sheath, whenever possible, as little more than either a particle source of fluxes impinging onto the PFC surface or a particle sink for eroded, sheath-exiting PFC particles. In other words, we will be minimally concerned with the specifics of ion transport within the SOL, though we will touch on this physics a bit more in Chapter 4 in the context of redeposition. Our scope will be largely limited to localized PMI within the sheath. The generalized geometry of a sputtering

event is shown in Figure 3.1. An incident ion impinges the surface at polar (θ) and azimuthal (ϕ) angles of incidence, and the sputtered neutral travels ballistically with some forward-scattering angle (δ). At a high level, the physics of physical sputtering is dominated by the energies and angles of incident ions and the binding energy of the PFC (109). Sheath electrons have little-to-no effect on gross sputtering. Although these electrons have very high energies in the core, the deceleration of electrons across the sheath combined with their very small size relative to PFC atoms makes their contribution negligible, especially for high-Z species. Hence, we will focus only on incident ion energies and angles to understand physical sputtering, treating binding energies of singe-species PFCs as fixed by their composition. Any secondary electron effects and surface composition changes will be ignored here.

In some sense we may understand physical sputtering as an extension of the classic two-body energy transfer problem: the PFC atom is held at rest by some lattice threshold energy, and the sheath ion transfers a portion of its energy to the PFC atom via collisions. If the energy transfer is sufficient (i.e. greater than the threshold energy), the atom may sputter from the surface; otherwise, the atom remains at the PFC by definition. An illustration of this behavior is shown in Figure 3.2. As reported in (109), this paradigm allows us to take advantage of simple momentum transfer physics to conclude that the maximal energy fraction γ is:

$$\gamma = \frac{4 m_{ii} m_s}{(m_{ii} + m_s)^2} \tag{3.1}$$

Here, m_{ii} is the mass of the incident ion, and m_s is the mass of the sputtered PFC atom. Intuitively, we expect the threshold energy to be essentially the binding energy. A more rigorous description is presented in (109) by considering the three-step process through which the energy transfer typically occurs for light ions (e.g. D). First, the ion strikes the PFC surface, penetrating into the material. Second, the lower atomic layers of the PFC collisionally repel the ion, returning it toward the surface. Third, as the ion returns toward the surface, it strikes surface PFC atoms from below,

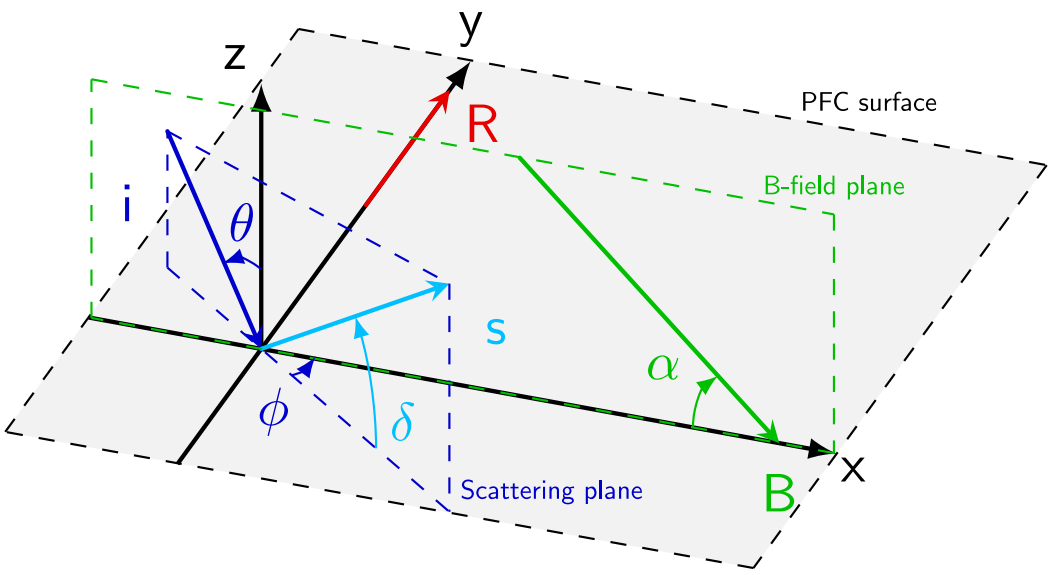

Figure 3.1: Generalize geometry of a sputtering event in a tokamak, including the $\vec{B}$-to-PFC pitch angle (α), the polar (θ) and azimuthal (ϕ) ion impact angles for incident ion i, and the forward-scattering angle (δ) for sputtered neutral s.

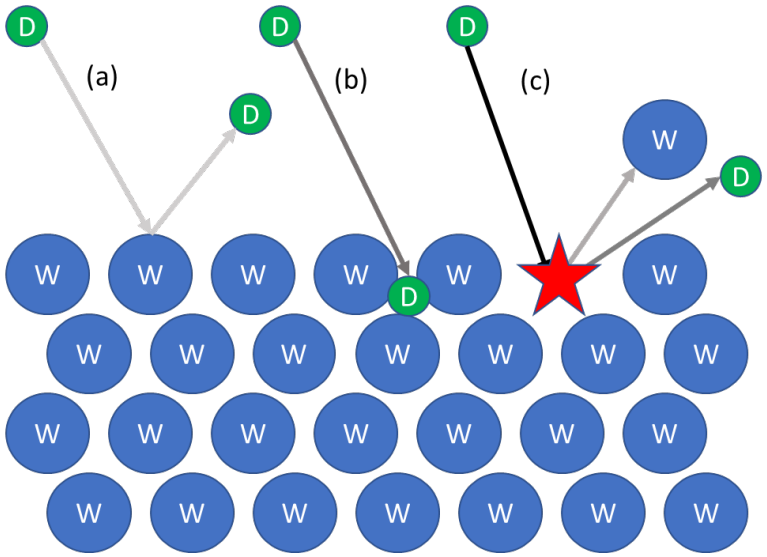

Figure 3.2: Cartoon of physical sputtering, using D and W as example incident ion and PFC neutrals, respectively. Grayscale represents increasing kinetic energy of the D ion. Represented are (a) a D reflection, (b) a D embedment, and (c) D sputtering of a W neutral.

potentially expelling them. The collisions in the last two steps result in the following energy balance equation at normal incidence (i.e. $\theta = 0$), where E_{ii} is the incident energy of the ion, E_s is the ejected energy of the PFC atomic neutral, and E_B is the PFC binding energy:

$$E_s = E_{ii}\gamma(1-\gamma) - E_B \tag{3.2}$$

Now, if $E_{ii} = E_{th}$, where E_{th} is the threshold energy, we have $E_s = 0$ by definition and we may rearrange this expression to find:

$$E_{th} = \frac{E_B}{\gamma(1-\gamma)} \tag{3.3}$$

Consequently, the actual threshold energy required to sputter a PFC neutral is implicitly limited by the incident ion mass once the PFC material is set. Heavier ions require lower energy to sputter a PFC surface than do lighter ions. For example, $E_B \approx 8.8$ eV for W (109), so $E_{th} \approx 214$ eV under an influx of D ions using the equation above while $E_{th} \approx 42$ eV under an influx of oxygen (O) ions.

As an important aside, ions completing the three-step energy transfer process may then [1] immediately escape the surface in an effective momentum reflection, [2] be temporarily trapped near the PFC surface before escaping as a thermal particle, or [3] become embedded in the PFC so that further ion collisions are essentially required to allow its escape (109). Accumulation of embedded ions in the PFC surface from [3] may weakly change the binding energy of the material over time, but high redeposition rates (see Chapter 4) for high-Z materials like W may keep this change negligible. Meanwhile, momentum transfer should typically reduce the speed of escaping ions in [1] and [2] above, but these ions may still return with energies relevant to the PFC energy threshold after plasma collisions and electrostatic acceleration through the sheath (This acceleration is discussed further in Section 3.3.). We will neglect these secondary effects here, for simplicity.

Returning to the original discussion, we note that in the third step of the energy transfer process the ion may eject one or more PFC atoms in its return toward the

surface, depending on its net energy with respect to the threshold energy. The yield at normal incidence (i.e. $\theta = 0$), Y_0, can be modeled by the Bohdansky formula (8; 50):

$$Y_0(m_{ii}, m_s, E_B, E_{ii}, E_{th}) = \bar{Q}(m_{ii}, m_s, E_B) S_n \left(\frac{E_{ii}}{E_{TF}}\right) \left(1 - \left(\frac{E_{th}}{E_{ii}}\right)^{2/3}\right) \left(1 - \frac{E_{th}}{E_{ii}}\right)^2 \tag{3.4}$$

Here, $\bar{Q}$ is the so-called "yield-factor," S_n is the nuclear stopping cross section, and E_{TF} is the Thomas-Fermi energy. Typically, $\bar{Q}$ is a fitting parameter, and we may express S_n and E_{TF} as follows (50), where Z_{ni} is the ion nuclear charge and Z_{ns} is the PFC nuclear charge:

$$S_n(\zeta) \approx \frac{3.441\sqrt{\zeta}\ln(\zeta + 2.718)}{1 + 6.355\sqrt{\zeta} + \zeta(6.882\sqrt{\zeta} - 1.708)} \tag{3.5}$$

$$E_{TF} \approx 30.74 \frac{m_{ii} + m_s}{m_s} Z_{ni} Z_{ns} \sqrt{Z_{ni}^{2/3} + Z_{ns}^{2/3}} \tag{3.6}$$

Normal-incidence approximations like the Bohdansky formula can be reasonably effective at predicting experimental sputtering yields since real-world surface roughness can complicate making a precise analysis of θ and ϕ, but good agreement may require heavy manipulation of free-parameters like $\bar{Q}$ or even E_B. Alternatively, we may use angle-dependent corrections (130) of the Bohdansky formula as follows (50):

$$Y(..., \theta) = Y_0(...)(\cos\theta)^{-f} \left(e^{f[1-(\cos\theta)^{-1}]\cos\theta_{max}}\right) \tag{3.7}$$

Here, Y_0 is as in Equation 3.4, θ_{max} is the angle that maximizes the sputtering yield, and f is a fitting parameter.

Although the semi-empirical approach above can be beneficial for guiding intuition and roughly predicting experimental yields in ideal conditions, Monte Carlo codes using binary collision approximation (BCA) theory provide a more rigorous treatment of physical sputtering. These codes are often more reliable at non-normal incidence

angles and better assess other aspects of erosion like the sputtered energy and angle distribution (99). We will discuss one such BCA code in more detail in Section 3.4. For now, we note that sputtering yields from the Bohdansky formula have good agreement with yields from BCA codes in the normal-incidence limit (i.e. $\theta = 0$) (44). In Figure 3.3 we may see example physical sputtering yields for a few species of interest using the BCA code TRIM (7; 88; 38). Note from the figure that tremendous E_{ii} is required for D on W to have a significant sputtering yield.

Within this section, we have introduced some of the important physics concepts involved in physical sputtering using a semi-empirical approach. We can immediately see that sputtering is sensitive to the incident ion species and concentration impinging from the SOL; the OEDGE code discussed in Section 1.4 may be used to determine these factors. Meanwhile, we also note that physical sputtering is sensitive to the energy and angle distribution of the incident ion, which are largely determined by sheath physics discussed in Chapter 2; we must use different computational models to account for these sheath effects. In the next section, we will take a brief aside to look at other important sources and conditions contributing to the gross erosion of high-Z materials in reactor-relevant scenarios. Importantly, we present this physics largely for completeness of the discussion and will not study erosion sources outside of non-ELM physical sputtering further in this work. Afterward, we will spend the final two sections discussing two codes that, when coupled, complete the physical sputtering picture.

3.2 Erosion of High-Z Materials

For completeness, we now consider particular cases of high-Z PFC erosion, especially W erosion, that are practically important when implementing these materials in a reactor environment. To begin, we consider further implications from the energy threshold and yield formulae in the previous section. In particular, it is important to call out "intrinsic" impurities within a fusion reactor. While DT fuel

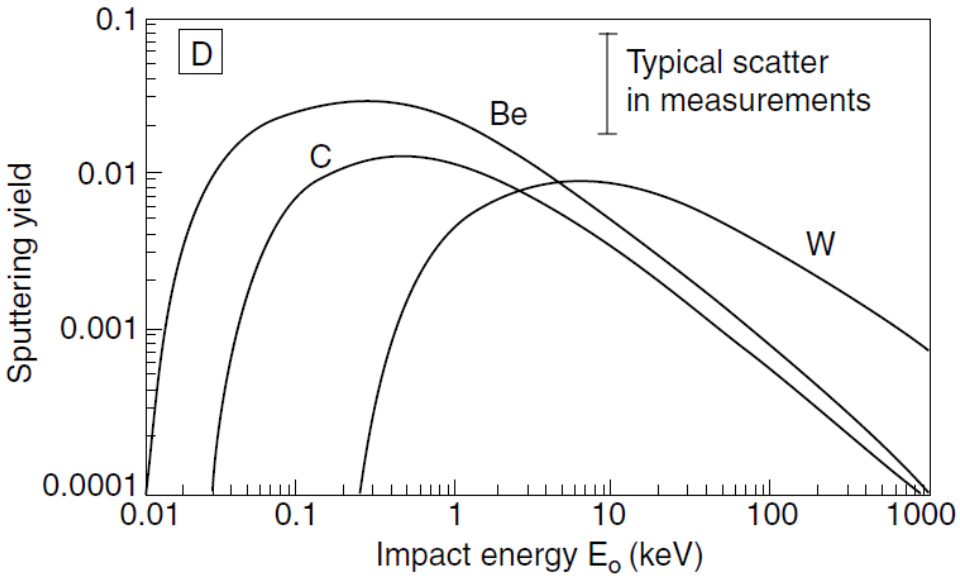

Figure 3.3: Sputtering yields for D on typical PFCs vs impact energy of D ions ($E_o = E_{ii}$ above) using the TRIM code (109).

should make up the overwhelming majority of plasma particles, no vacuum system will perfectly extract all the atmospheric gas before DT fuel is pumped into the vessel. Hence, larger impurities such as nitrogen, carbon, and oxygen will always exist in a reactor to sputter PFC surfaces. In addition to these intrinsic impurities, sputtered neutrals may become ionized in the sheath or SOL and return to the PFC surface; if the energies upon return are sufficient, self-sputtering will occur. This possibility suggests a risk for a runaway self-sputtering avalanche because of the high yield within Equation 3.7 for high-Z incident ions; Figure 3.4 shows an example of the exponential yield for W-on-W sputtering. Fortuitously, localized W avalanches are ruled out by magnetic pre-sheath effects (23). Recent work (23) shows that, even at the maximum possible ejected energy E_s within fusion-relevant conditions, energy amplification via electrostatic acceleration through the sheath results in a final energy that is actually reduced from the original impact energy by a factor of ~ 2.4. However, long-range W ions that first made their way into the SOL or even the core will have significantly higher energies than the sheath-localized ions considered in this study; this fact means that self-sputtering avalanches from long-range high-Z ions are not completely ruled out at this time. We will briefly consider W self-sputtering in Chapter 6, but we will incompletely consider the contribution from plasma transport in setting this self-sputtering in this document.

Direct inspection of the formulae in Section 3.1 reveals that sputtering via intrinsic impurities and self-sputtering will typically have a much greater yield on W PFCs than D sputtering by mass. Indeed, as demonstrated experimentally and computationally, impurities drive the global behavior of W gross erosion in divertor tokamaks (56; 33; 71); the primary driver of this gross erosion depends upon the impurities present in the device considered. For all-W PFC devices such as ASDEX Upgrade and WEST, light intrinsic impurities such as nitrogen (N) (56) and O (28; 49) drive W physical sputtering. Conversely, at devices with multiple PFC materials such as JET and DIII-D, light PFC impurities such as beryllium (Be) (71) and carbon (C) (33) drive W physical sputtering. It is important to keep in mind that, as discussed in Chapter 1,

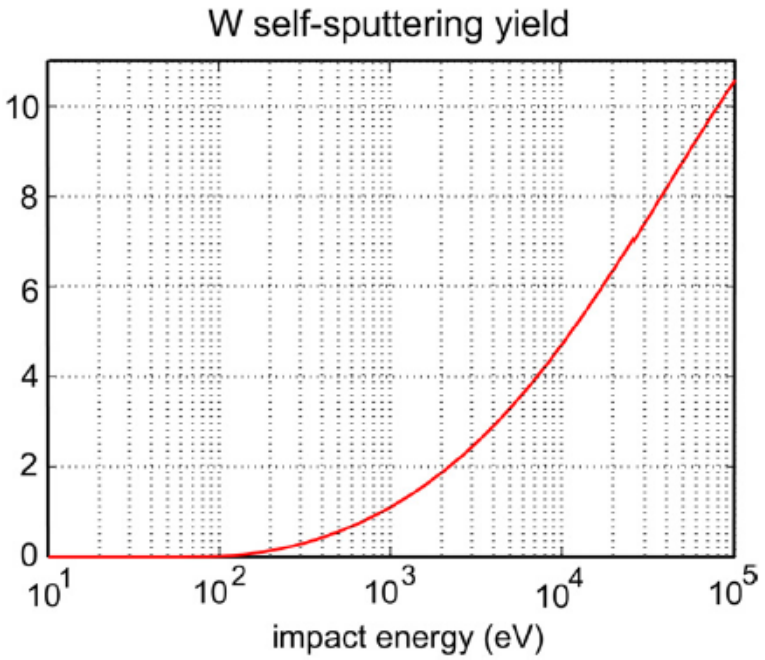

Figure 3.4: Physical sputtering yield vs W impact energy E_{ii} on W PFCs using the Bohdansky formula, highlighting the threat of avalanche at sufficiently high impact energies (23).

we are limiting our study to L-mode and inter-ELM H-mode confinement; if we were discussing intra-ELM H-mode, it is actually D fluxes that drive the gross erosion (71) due to their extremely high energies. Nevertheless, we emphasize that light impurities drive high-Z PFC sputtering in the cases we consider here, as the particles in the DT flux will largely have insufficient energy by mass to overcome the threshold energy of the PFC. Note an example of this relationship at JET in Figure 3.5; although intra-ELM gross erosion is greater here than the inter-ELM case, this extreme will be left to its experts as the techniques we will discuss in this work are not applicable to an intra-ELM study. Here, we assume techniques for significant mitigation of ELMs will exist by the time a net-energy positive divertor tokamak is operational.

Now, an important process distinguishable from physical sputtering is the interaction of W and He. It is well established that He ions incident on W PFCs produce a so-called "fuzz" of W nanotendrils above the PFC. The specific mechanism is still being researched, but it is generally understood (126) that Frenkel defects (i.e. lattice gaps) form over time in the W structure from physical sputtering and are filled by clusters of He atoms, causing bubbles to form in the surface. As these bubbles expand, they cause dislocation loops to expel from the PFC surface and return back to the surface as fuzz. A scanning electron microscope image of W exposure to different incident energies of He flux is shown in Figure 3.6. Now, until fusion technology is ready to handle net-energy production, research tokamaks usually run with only D plasmas, leaving the radioactive and expensive T aside; hence, no He is introduced into the plasma via fusion reactions at these facilities. Meanwhile, fuzz growth has been seen to actually reduce sputtering in *in situ* measurements (35). For these reasons, we will overlook the effect of He fuzz on W gross erosion in the present work; nonetheless, this physics will become more important in next-step devices and should receive further investigation.

Lastly, we will discuss chemical sputtering: another important facet of gross erosion. While chemical sputtering is significantly important to the gross erosion model of low-Z PFCs (e.g. formation of organic compounds between C PFCs and

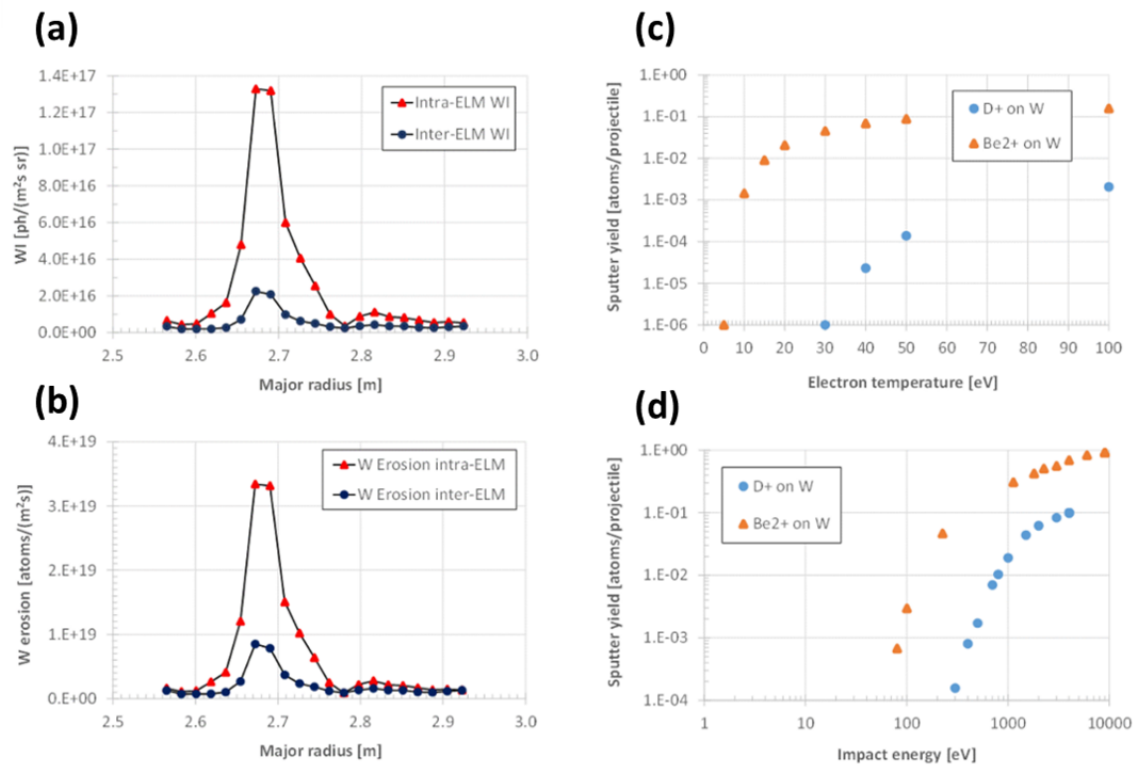

Figure 3.5: W erosion work (71) at JET showing: (a) W erosion measurements in ITER-like divertor via spectroscopic W-I emission lines (see Chapter 7) in inter- and intra-ELM H-mode, (b) Calculated W erosion fluxes in ITER-like divertor via ERO (72) simulations in inter- and intra-ELM H-mode showing good agreement with the data in (a), (c) BCA-calculated W sputter yields based on D^+ and Be^{2+} conditions in inter-ELM H-mode, (d) BCA-calculated W sputter yields based on D^+ and Be^{2+} conditions in intra-ELM H-mode. Note that, at 0.5% Be expected at JET, D sputter yields will exceed Be yields in the intra-ELM case of (d) but not the inter-ELM case of (c).

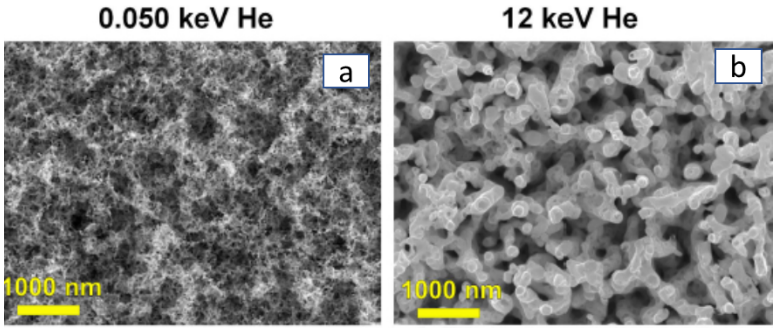

Figure 3.6: SEM images of W exposed to (a) 0.050 keV He and (b) 12 keV He fluxes, highlighting the increased growth of W fuzz with increasing He incident energy (126).

DT fuel), physical sputtering dominates the model for high-Z PFCs (109). Because our primary focus is W PFCs, we will not dwell long on this fascinating topic. Indeed, chemical sputtering processes are unique to the species involved, so it is difficult to discuss the topic in any generality. Regardless, one reactions are worth introducing for W: the reaction of W with D.

Recent work (16) shows a chemical formation of WD molecules during W sputtering measurements in TEXTOR and ASDEX Upgrade. It is worth emphasizing that this observation is unique to PFC surfaces; spectroscopic measurements (see Chapter 7) of seeded W from WF_6 puffing injections do not detect any WD presence, signifying that the W+D reaction occurs locally at the PFC. Thus, this molecule may form from D ions chemically combining with W on impact or from ions (D or impurity) expelling PFC WD that has formed from fuel retention in the walls. The WD production demonstrably scales with T_e (indicating an E_{ii} dependence similar to the physical sputtering theory above) and with D flux (emphasizing the chemical nature of the sputtering). In addition, WD production exhibits poloidal dependency in the work (see Figure 3.7); at the strike points of the SOL, the WD/W ratio is minimized due to high temperatures while the WD/W ratio increases away from the strike point where greater D retention occurs. While these factors are interesting and should undergo further study, we will assume that WD contribution to erosion is negligible, leaving a more extensive study of WD contributions to those experts.

3.3 Incident Ion Energy and Angle Distributions and PYEAD

With an overview of gross erosion now concluded, we want to narrow our focus to the physics of net erosion for high-Z PFCs, in which the DS and MPS will play critical roles. To begin, we must examine the effect that the sheath has on the energy and angle distribution of incoming ions of mass m_{ii}, whether plasma (i.e. $m_{ii} = m_{ip}$)

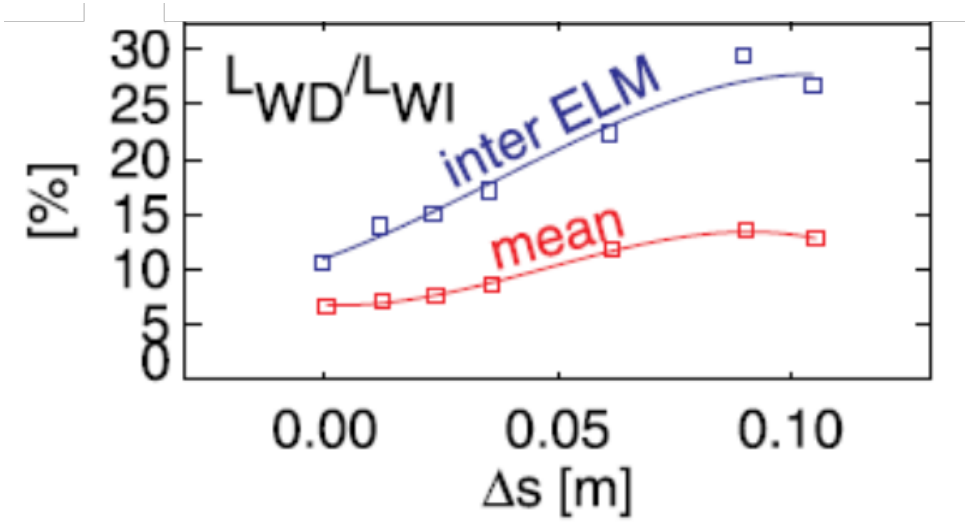

Figure 3.7: Spectroscopic emission line ratio between WD and W inter-ELM (blue) and intra-ELM (red) against distance from strike point Δs (16).

or impurity species. While it is reasonable to assume, per the Bohm criterion, that ions are Maxwellian in their velocity distribution upon entering the sheath, we expect these distributions to change by the time the ions reach the PFC due to the strong electromagnetic forces within the sheath. Hence, the angles of impact are unlikely to be uniformly distributed, and the energy distribution may shift significantly higher compared to the SOL. These incident ion energy and angle distributions (EADs) at the PFC play a key role in physical sputtering, as discussed in Section 3.1.

Recalling the generalized geometry of a sputtering event is shown in Figure 3.1, now our focus will be on the polar (θ) and azimuthal (ϕ) angles of incidence for incoming ions; we will spend the next section detailing the other side of the sputtering event. Without a first-principles theory for calculating incident ion EADs, one approach to estimating them is a Monte Carlo (94) simulation. With this technique, we launch a large number of test particles through the sheath, sampling from a known velocity distribution. Then, each particle is subjected to the electromagnetic sheath forces, updating the particle's velocity and position for the next time step. Finally, when the particle reaches the sheath, we bin and analyze the velocities and positions at the PFC to determine the overall EAD. The PMI field widely uses Monte Carlo techniques to calculate EADs in state-of-the-art PMI codes like ERO (72), but the successful comparison of incident ion EAD codes with experiments is sensitive to the sheath model of choice. Although ERO uses the Brooks model of the sheath, Borodkina noted a 30% improvement in beryllium erosion predictions using her sheath model to predict incident ion EADs (10). Recent works by Chrobak (26; 27) and Abe (1; 2) have also found success implementing the Borodkina sheath model for incident ion EAD predictions of aluminum, silicon, and carbon PFC experiments using an original IDL code ieadrk3.

Because of the excellent results being attained with ieadrk3, we would like to use this code to calculate incident ion EADs in this work. However, we note two drawbacks to this model: (1) the necessity of an IDL license, which limits the accessibility of ieadrk3 to a subset of the scientific community and (2) the lack

of parallel processing within ieadrk3, which reduces the computational speed to one particle at a time. For these reasons, we have rewritten the physics model implemented by ieadrk3 into Python, with the Monte Carlo portion parallelized for speed. This new code is the PYthon Energy and Angle Distribution (PYEAD) model. Because PYEAD is a code original to this work, we will use this section to explicitly detail its method and provide the code itself in Appendix A.

PYEAD is structured so that all angles and energies are easily computed with one functional wrapper ***mps_dist***(...), the general workflow of which may be seen in Figure 3.8. This function is the analog of the function with the same name in ieadrk3. The input parameters in ***mps_dist***(...), with default values, are given as follows:

$$\begin{aligned}\textbf{mps_dist}(\textbf{alphadeg} = 5.0, \textbf{B} = 2.0, \textbf{ne} = 1.0e19, \textbf{Te} = 25.0, \textbf{Ti} = Te,\\ \textbf{mip_amu} = 2.016, \textbf{Zip} = 1.0, \textbf{mnp} = 1.0, \textbf{mii_amu} = mip_amu, \textbf{Zii} = Zip,\\ \textbf{mni} = 1.0, \textbf{n_ions} = 500, \textbf{out} = None, \textbf{name} = None,\\ \textbf{forceds} = None, \textbf{noe} = None, \textbf{lmps} = 2.0, \textbf{pal} = 2) \quad (3.8)\end{aligned}$$

Here, ***alphadeg*** $= \alpha$ in degrees, ***B*** $= |\vec{B}|$ is the toroidal $\vec{B}$-field in T, ***ne*** $= n_e$ at the sheath entrance in m^{-3}, ***Te*** $= T_e$ in eV, ***Ti*** $= T_{ip}$ in eV, ***mip_amu*** $= m_{ip}$ in amu, ***mii_amu*** $= m_{ii}$ in amu as in i of Figure 3.1, ***Zip*** (***Zii***) is the background plasma (incident) ion's charge state, ***mnp*** (***mni***) is the mach number of the background plasma (incident) ion, ***n_ions*** is the number of Monte Carlo test particles desired, ***out*** is a flag for whether to save the outputs, ***name*** is a string for the file name of the output, ***forceds*** manually sets the DS electric field if desired for debugging purposes, ***noe*** is a flag for specifying no electric field in the sheath if desired for debugging purposes, ***lmps*** $= k$, and ***pal*** is the number of parallel processors used for computation. Careful selection of ***n_ions*** is needed to balance good statistics with runtime; ***n_ions*** ≥ 200 is artificially required for the script to run. If ***out*** $\neq None$, the outputs are saved in .txt and .h5 file formats.

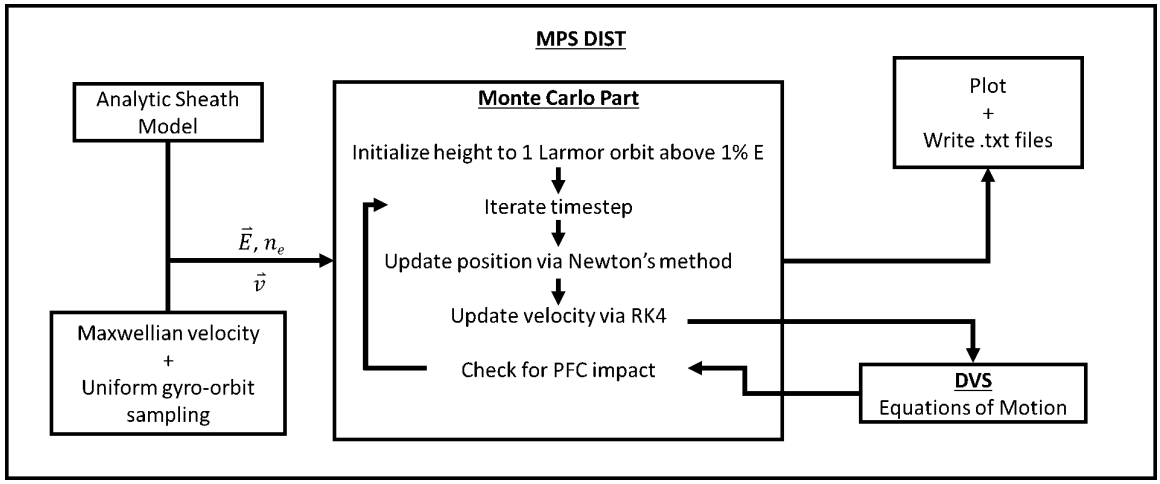

Figure 3.8: Workflow of core functions within PYEAD.

Now, for a discretization of 50000 numerical subdivisions of ξ, PYEAD computes the electric field and density fall-off through the sheath using the Borodkina sheath model in Section 2.3. Next, the code initializes bins to zero for the initial and final histograms of kinetic energy E_{ii}, angles θ and ϕ, perpendicular velocity $v_{\perp}$, and parallel velocity $v_{||}$ (that is, parallel to the toroidal $\vec{B}$-field); we designate 180 numerical subdivisions for each of these histograms. Then, PYEAD initializes the gyro phase angle Ω of all incident ions at the sheath entrance using a uniform random variable bounded by the minimum and maximum gyro phase angles; here, we set the Ω range to 0-2π, but it may be hard-coded to a narrower window if desired (103). As a final step of the initialization, we treat the parallel and perpendicular velocity distributions as Maxwellian with an average velocity equal to the thermal ion speed (109):

$$c_{th} = \sqrt{\frac{2k_B T_{ip}}{m_{ii}}} \tag{3.9}$$

To reduce wasted computational runtime, we clip the parallel velocity to a minimum of $0.01c_s$ in order to ignore ions travelling away from the PFC. We take both $v_{||}$ and $v_{\perp}$ samples from their respective distributions to initialize each particle; we bin these values accordingly in the initial $v_{||}$ and $v_{\perp}$ histograms. The code computes and bins the initial E_{ii} histogram using the usual definition:

$$E_{ii} = \frac{1}{2} m_{ii} \frac{(v_{||} + v_{\perp})^2}{k_B} \tag{3.10}$$

This choice results in a so-called Thompson energy distribution (119).

Assuming a $\pi/180$ toroidal field radial pitch angle, we determine the Cartesian components of the toroidal magnetic field. Then, we pass the above information (E_{ii}, $v_{||}$, $v_{\perp}$, Ω) for each particle and the sheath conditions (α, $\vec{B}$, $\vec{E}$, $n_e(z)$) into the subroutine ***monte_carlo_part***(...), which, as implied, governs the parallelized, Monte Carlo portion of the code. To start, PYEAD breaks the initial velocity of a

given test particle into Cartesian components based on that particle's Ω, $v_{||}$, and $v_{\perp}$:

$$\begin{cases} v_x = v_{||}\cos(\alpha) - v_{\perp}\sin(\Omega)\sin(\alpha) \\ v_y = v_{\perp}\cos(\Omega) \\ v_z = v_{||}\sin(\alpha) - v_{\perp}\sin(\Omega)\cos(\alpha) \end{cases} \tag{3.11}$$

Then, we interpolate the height above the PFC where $|\vec{E}|$ is 1% of its maximum value. The code initially places all test particles one Larmor radius above this height so that the ion dips into the MPS during its first gyro-orbit. The x and y components are initially 0.

Now, we refine the standard timestep τ in PYEAD with z so that:

$$\tau = \begin{cases} \frac{0.01(2\pi)\rho_{ii}}{50000|\vec{v}|} & z > 4\rho_{ii} \\ \frac{10\lambda_D}{|\vec{v}|} & 5\lambda_D \leq z \leq 4\rho_{ii} \\ \frac{0.25\lambda_D}{|\vec{v}|} & z < 5\lambda_D \end{cases} \tag{3.12}$$

where ρ_{ii} is the Larmor radius of the impinging ion. In other words, we refine τ when the height of the particle is $< 4\rho_{ii}$ (i.e. within 2 gyro-orbits) from the PFC and again when the height of the particle is $< 5\lambda_D$ from the PFC. With the appropriate definition of τ chosen, PYEAD updates the Cartesian position of the particle using Newton's method. Then, 4th order Runge-Kutta methods update the velocity with another subroutine $\boldsymbol{DVS}(...)$ of Lorentz force equations:

$$\begin{cases} \frac{dv_x}{dt} = \frac{q_e Z_{ii}}{m_{ii}}[v_y B_z - v_z B_y] \\ \frac{dv_y}{dt} = \frac{q_e Z_{ii}}{m_{ii}}[v_z B_x - v_x B_z] \\ \frac{dv_z}{dt} = \frac{q_e Z_{ii}}{m_{ii}}[v_x B_y - v_y B_x + E_z] \end{cases} \tag{3.13}$$

At this point, we check to see if the particle has hit the PFC ($z = 0$). If the particle does not hit the PFC, the loop begins again with determining τ. We allow a maximum

number of 50000 iterations for the particle to connect with the PFC (matching the number of z subdivisions used in the Borodkina derivation of $\vec{E}$). If the particle does not hit the PFC within this timeline or leaves the sheath entrance ($z > 10L_{MPS}$), then we treat the particle as lost and bin it as 0 for all parameters in the final histogram. Otherwise, when the particle strikes the PFC surface, PYEAD calculates the particle's final E_{ii} via Equation 3.10 using the final $v_{||}$ and $v_{\perp}$ value. Then, θ and ϕ are calculated using:

$$\theta = 90^{\circ} - \arctan\left[\frac{v_z}{\sqrt{v_x^2 + v_y^2}}\right] \tag{3.14}$$

$$\phi = \arctan\left[\frac{v_y}{v_x}\right] \tag{3.15}$$

With the ***monte_carlo_part***(...) concluded, the last step is binning the final E_{ii}, θ, ϕ, $v_{||}$, $v_{\perp}$, x, y, and z histograms. If desired, PYEAD outputs the initial and final histograms as .txt and .h5 files. Table 3.1 outlines the information in each of these main output files. In addition, figures are generated by default when ***monte_carlo_part***(...) ends, consisting of the following: (1) the normalized potential drop-off through the sheath, (2) the normalized electron density drop-off through the sheath, (3) the normalized velocity distribution histograms, (4) the polar inclination angle distribution histogram, (5) the azimuthal angle distribution histogram, (6) the impact energy distribution histogram, (7) the final energy vs polar angle distribution histogram, (8) the final energy vs azimuthal angle distribution histogram, and (9) the azimuthal vs polar angle distribution histogram. Figure 3.9 shows an example of each of these plots. These plots are not intended to be "publication quality" but rather provide the user with rough, instantaneous feedback on the simulation. Instead, it is recommended that the output files delineated in Table 3.1 be used directly to generate figures for publication (see Chapter 5). The plots in Figure 3.9 also allow direct comparison with the analogous plots in ieadrk3. A comparison is shown in Figure 3.10, demonstrating the excellent agreement obtained between these two codes for the final θ, ϕ, and E_{ii} histograms; differences between these histograms are merely

Table 3.1: Table of PYEAD output files for .txt file format.

Name	Contents
'name_comments.txt'	***mps_dist***(...) inputs
'name_distributions.txt'	initial and final EADs
'name_mps.txt'	sheath parameters (i.e. $\vec{E}$, n_e, etc.)
'name_positiondist.txt'	final cartesian location of each particle
'name_particles.txt'	energy and angles for each particle

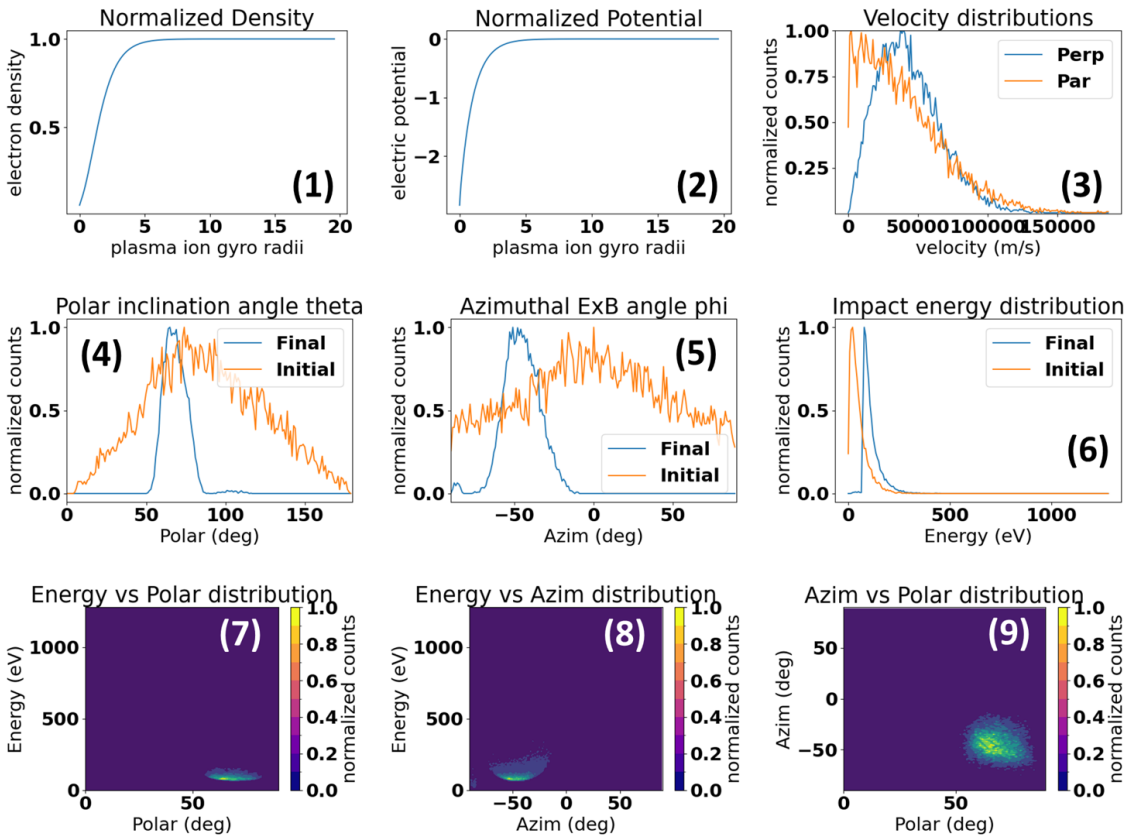

Figure 3.9: Auto-generated figures from PYEAD using the default inputs with 10000 test particles. The subfigure numbers refer to the individualized figure descriptions in the text.

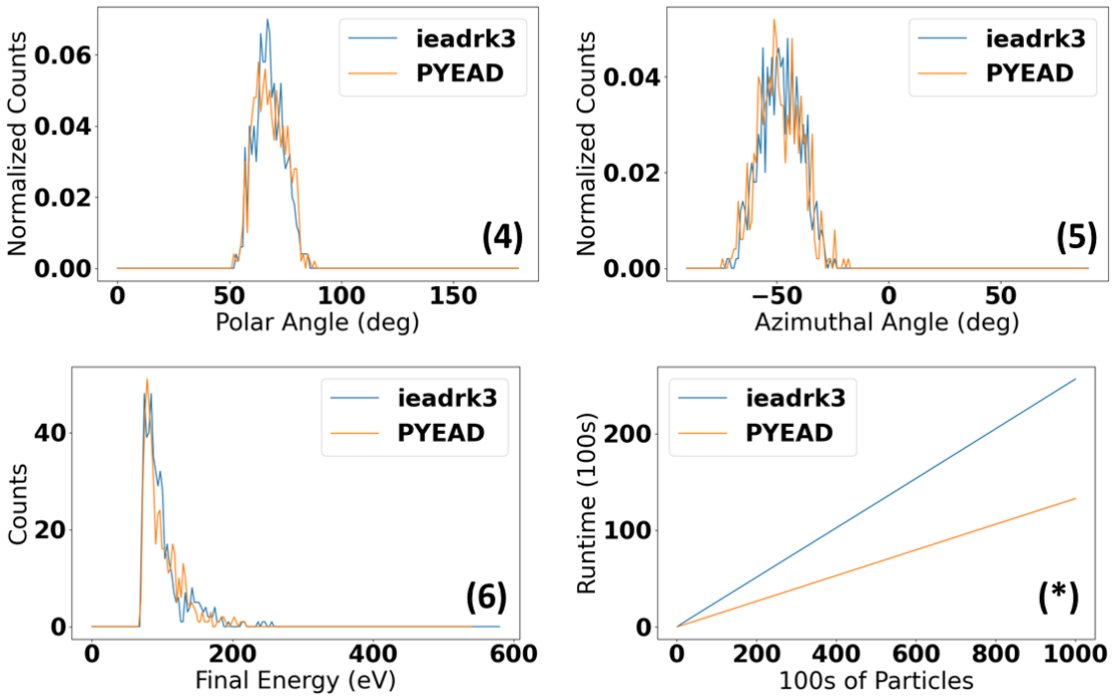

Figure 3.10: Comparison of PYEAD (Python) and ieadrk3 (IDL) default input calculations for subfigures (4), (5), and (6) in Figure 3.9, as well as computational runtime (*) using ***pal***=10.

the result of underlying differences in the random variable algorithms between Python and IDL. Moreover, despite the fact that Python restricts the RK4 computation speed with a much-slower, open-source differential equation solver, Figure 3.10 also shows that the parallelization in PYEAD increases the speed over the IDL code by a factor of 2 with as few as 10 parallel processors.

3.4 Neutral Energy and Angle Distributions and RustBCA

With our discussion of incident ion energy and angle distributions (EADs) now concluded, we turn our attention to the calculation of the resultant sputtered neutral EADs. While the Bohdansky formulation discussed in Section 3.1 is useful for building a generalized understanding of physical sputtering trends, the polar incidence angle θ is often oblique; as a physically relevant example, we can quite clearly see that $\theta \gg 0$ on average in the fourth output of Figure 3.9, which uses the default parameters of Equation 3.8. As discussed in Section 3.1, corrections to semi-empirical formulations like the Bohdansky formula can be made, but binary collision approximation codes provide a much more rigorous treatment of physical sputtering in these oblique instances. Of especial interest to this work, these codes often also provide sputtered neutral EADs for free. It is conventionally assumed in many high-Z redeposition models (see Chapter 4) that such sputtered neutrals obey a Thompson (119) energy distribution (energy noted E_s for sputtered neutral s in Figure 3.1), a cosine forward-scattering angle δ distribution (see Figure 3.1), and a uniform polar angle distribution (not pictured). The BCA-generated EADs allow us to test these assumptions while providing the other benefits of BCA codes. Here, we will briefly discuss the generalizable features of BCA models before discussing the BCA code used in the rest of this work: RustBCA.

The binary collision approximation exploits that standard two-body scattering problem in classical physics that we may generally describe as follows (99; 51); a generalized binary inter-atomic collision is shown in Figure 3.11. The incident ion i begins at position P_o, mass m_{ii}, and energy E_{ii}, taken from within the incident ion EAD at the PFC in Section 3.3. The hypothetically sputtered neutral begins at position T_o with mass m_s and energy $E_s = 0$. The two particles begin and end at a separation of length L between initial points P_o and T_o and respective final points P_f and T_f, beyond which inter-atomic interaction may be ignored.

At each evaluation of particle interaction for inter-atomic distance $r < L$, we use the following parameters to update the particle conditions: the time integral τ (different from the timestep τ in Section 3.3), the impact parameter b (the perpendicular distance between the incident ion and the center of the neutral's inter-atomic potential field $V(r)$), the mass ratio $A = m_s/m_{ii}$, and the barycentric scattering angle χ. At the apsis, given by respective positions P_a and T_a, an inelastic energy loss Q (not to be confused with the Q in Section 3.1) from electron stopping occurs; otherwise, we assume the collision is elastic. The χ and τ variables require complex integrals to define, and the particulars of these integrations vary across BCA codes. Using expression simplifying definitions:

$$v(r) = \frac{(1+A)V(r)}{AE_{ii}} \tag{3.16}$$

and

$$g(r) = \sqrt{1 - \left(v(r) + \left(\frac{b}{r}\right)^2\right)} \tag{3.17}$$

we may define the barycentric scattering angle and time integral as:

$$\chi = \pi - b\left(2\int_a^\infty (r^2 g(r))^{-1} dr\right) = \pi - bI_1 \tag{3.18}$$

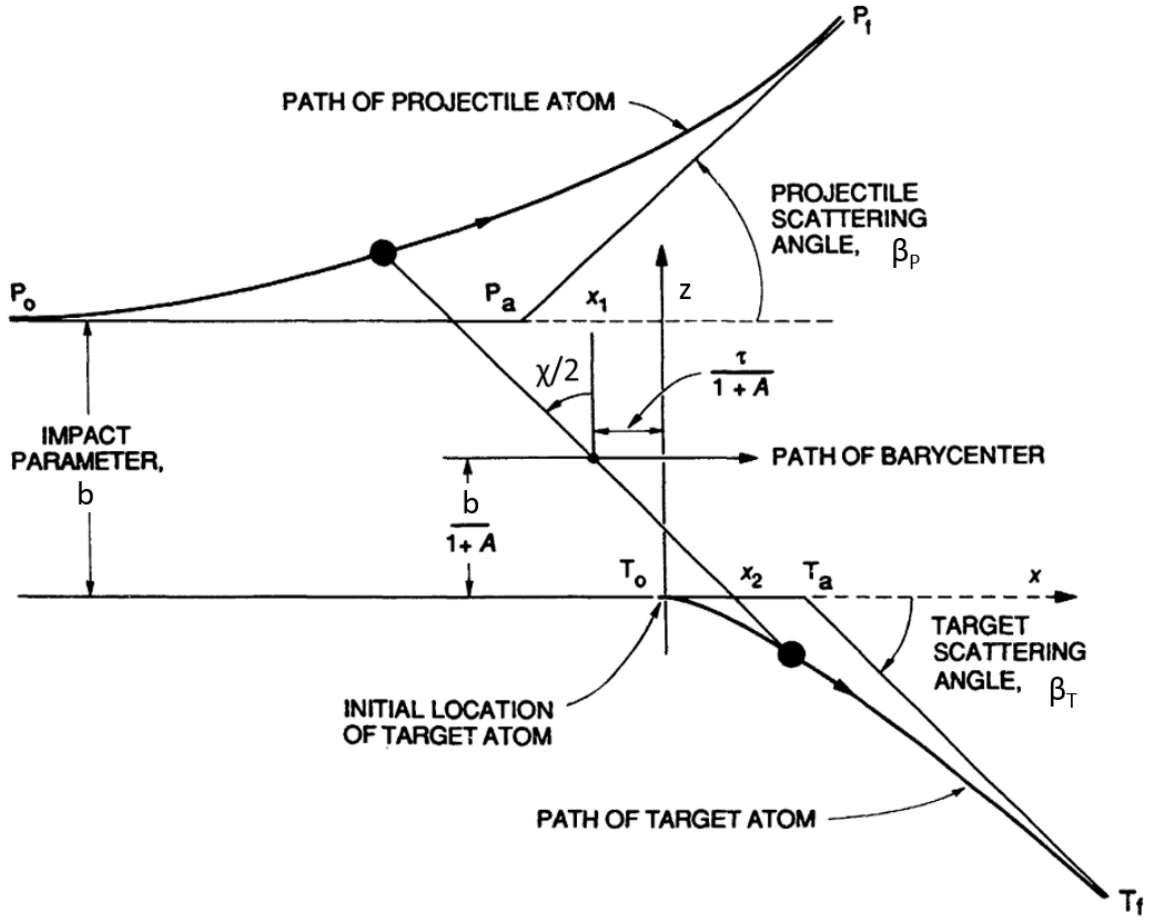

Figure 3.11: Generalized scattering event (99), with labeled parameters highlighted in the text.

and

$$\tau = \sqrt{a^2 - b^2} - \int_a^\infty \left[\frac{1}{g(r)} - \frac{1}{\sqrt{1 - (p/a)^2}} \right] dr = \sqrt{a^2 - b^2} - I_2 \tag{3.19}$$

where a is the inter-atomic separation at the apsis of the collision. We may estimate I_1 and I_2 through different forms of quadrature, such as Gauss-Legendre or Gauss-Mehler. Meanwhile, there are many ways of prescribing the inter-atomic potential $V(r)$ and inelastic energy loss Q. We will not go into these here as they tend to differ across various BCA models; if the reader is interested, please consult the book by Eckstein (43).

The overarching commonality between BCA approaches is the calculation (99) of post-scattering angles and energies; to simplify the calculation, it is common to model the interaction via changes to the barycenter motion. As the particles move from their origins to their apsis positions, the barycenter moves with a velocity inherited from the incident ion. After traveling a time

$$t_i = \frac{\sqrt{L^2 - b^2} - \tau}{\sqrt{2E_{ii}/m_{ii}}} \tag{3.20}$$

the particles reach the apsis, and the inelastic energy loss event occurs. This event increases the duration of travel as the particles recoil away from each other (i.e. $r \nearrow L$ again) by a factor of f^{-1} (e.g. $f = \sqrt{1 - (1 + A)Q/AE_{ii}}$ in (99)). Beyond the apsis, the barycenter moves with time

$$t_a = \frac{f\sqrt{L^2 - b^2} + [b \tan(\chi/2) - \tau(1 + f)]}{f\sqrt{2E_{ii}/m_{ii}}} \tag{3.21}$$

All that remains is calculating the exact apsis positions.

To calculate these apsis positions P_a and T_a, we note that the respective barycentric scattering angles β_P and β_T are uniquely determined from the above

parameters by

$$\beta_P = \arctan\left(\frac{Af\sin(\chi)}{1 + Af\cos(\chi)}\right) \tag{3.22}$$

and

$$\beta_T = \arctan\left(\frac{f\sin(\chi)}{1 - f\cos(\chi)}\right) \tag{3.23}$$

These angles intersect the P_o and T_o planes at distances $\sqrt{x_1^2 + b^2}$ and x_2 from the T_o position (see Figure 3.11), where

$$x_1 = \frac{\tau(1+f) + b(fA-1)\tan(\chi/2)}{f(1+A)} \tag{3.24}$$

and

$$x_2 = b\tan(\chi/2) - x_1 \tag{3.25}$$

Using x_1 and x_2, we determine P_a and T_a. The barycenter motion continues past this point with each particle travelling with updated energy:

$$E_{ri} = \frac{E_{ii}[(1-fA)^2 + 4fA\cos^2(\chi/2)]}{(1+A)^2} \tag{3.26}$$

$$E_s = \frac{E_{ii}[(1-f)^2 A + 4fA\sin^2(\chi/2)]}{(1+A)^2} - E_B \tag{3.27}$$

where E_{ri} is the reflected energy of the initially incident ion and E_B is the binding energy discussed in Section 3.1.

Now, the preceding discussion (99) has outlined a general approach to calculating binary collisions under the classical treatment. To model sputtering, we employ a Monte Carlo approach. For a given test particle representing an incident ion i, we model that ion's interactions through the PFC as a series of these binary collisions. This particle exchanges energy over the course of its collisions. If the particle makes its way back to the PFC surface plane with positive velocity in the z-direction (i.e. away from the PFC), it represents a reflected particle as in (a) of Figure 3.2. If

the particle attains rest ($E_{ri} = 0$) or continues to exhibit negative velocity in the z-direction (i.e. into the PFC) beyond a maximal timestep, it represents an embedded particle as in (b) of Figure 3.2. Meanwhile, the collisions with s particles may result in nonzero E_s, depending on the energy of the ion and the strength of the binding energy. If so, we treat these particles as sputtered as in (c) of Figure 3.2. Then, we may calculate the sputtering yield as the ratio of the sputtered particles to the number of test particles. Similarly, we may determine the overall sputtered neutral EAD by binning the sputtered energy and angles relative to the global reference frame in Figure 3.1 of all sputtered test particles.

While there are many BCA codes designed to study PMI physical sputtering, RustBCA (37) uniquely provides a high-performance model that is open source. Most widely-used codes for PMI sputtering are proprietary and hail from the TRIM-style family of codes such as TRIM.SP (7), TRIDYN (88), and F-TYIDYN (38). The developer of F-TYIDYN developed RustBCA as an open source, robust continuation of the TRIM tradition. As can be seen in Figure 3.12, RustBCA is in excellent agreement with the other TRIM-like codes as well as semi-empirical formulas like the Yamamura corrections (130) to the Bohdansky formula in Equation 3.7. In addition to reproducing TRIM-like models, RustBCA improves upon these models by including diverse algorithms for calculating I_1 and I_2 quadrature, providing complex treatment of inter-atomic potentials $V(r)$, and including high flexibility for complex PFC composition (37). For these reasons, we will use RustBCA, coupled to PYEAD, to model the full picture of gross erosion physics throughout the remainder of this dissertation. We will provide more discussion on this coupling in Chapter 5.

At this point, we will conclude our discussion of gross erosion, the first half of the net erosion process. We have restricted our study to physical sputtering regimes and discussed two codes, PYEAD and RustBCA, that allow us to study these regimes throughout the rest of this work. Already, we may note that gross erosion seems sensitive to sheath conditions; the sheath determines the energy and angle distributions of incident ion fluxes, which in turn determine the sputtered neutral

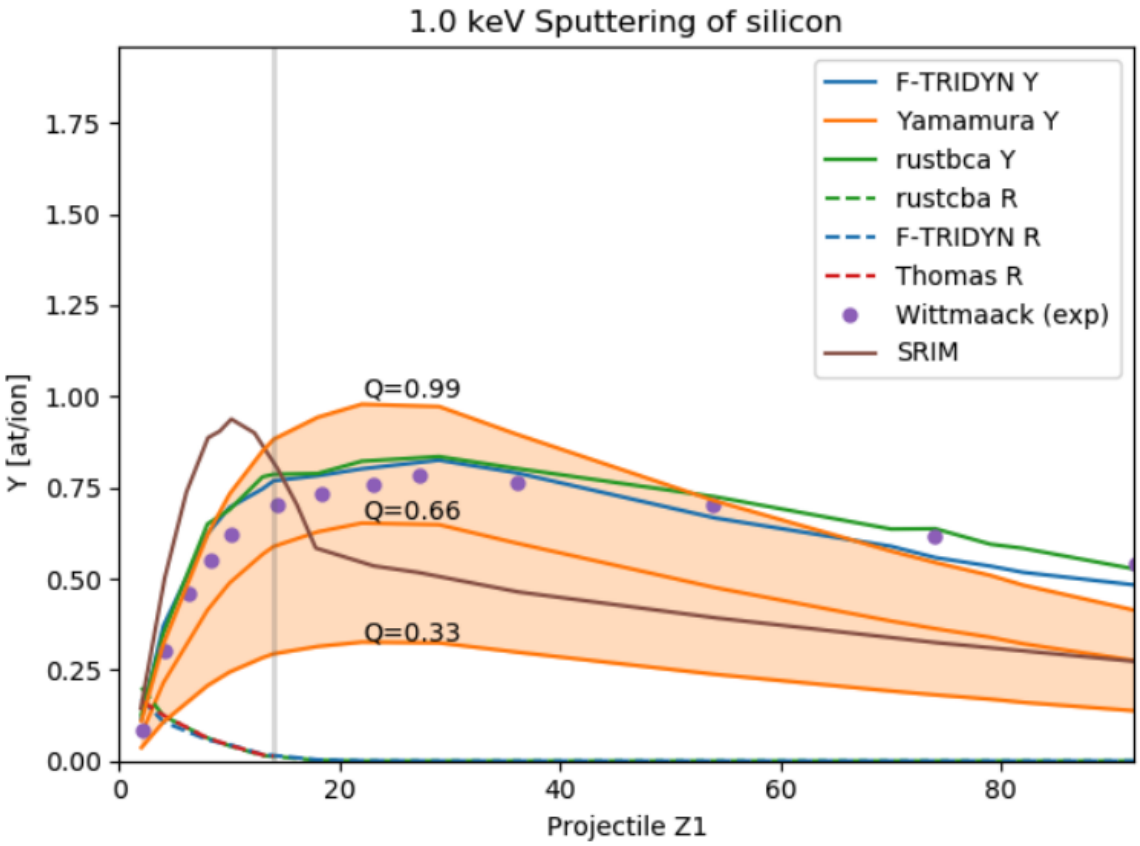

Figure 3.12: Benchmark study comparing silicon sputtering yields in RustBCA to other TRIM-style codes F-TRIDYN and SRIM as well as empirical Yamamura and Thomas formulations and experimental results (37).

energy and forward-scattering angle distributions. This observation will be explored further in Chapter 5. Next, we will turn our attention to PFC redeposition.

3.5 Executive Summary

- The energy and angle distribution of incident ion species (driven by the sheath) and the material properties of the target material determine the gross erosion of the first wall.
- PYEAD, a newly developed Monte Carlo code, calculates incident ion energy and angle distributions using the Borodkina sheath model.
- RustBCA, a binary collision approximation code, calculates physically sputtered energy and angle distributions from incident ion fluxes.
- The coupled model PYEAD-RustBCA provides a Monte Carlo estimation of overall gross erosion.

Chapter 4

Model of Redeposition

4.1 Current Models of High-Z Redeposition

At last, we turn our attention to the other half of net erosion PMI: redeposition. At this stage of the dissertation, we will largely be unable to discuss redeposition with generality. Light ions have relatively low redeposition due to their low inertia, small gyro-orbits, relatively high sputtered velocities, and long ionization lengths (53); as will be seen, these parameters critically set the redeposition fraction. Hence, we cannot apply most of the redeposition mechanisms we will discuss in this chapter to low-Z species in a meaningful way and restrict ourselves to discussing high-Z PFCs, using W as a representative case. In this section we will provide a brief overview of high-Z redeposition from the existing literature at time of writing.

While there are many diverse, fascinating studies of high-Z redeposition throughout the history of PMI research, a handful of seminal papers have dramatically advanced the field. Before we discuss these, it is useful to refer back to Figure 1.12 and note that a redeposition event may occur from either "surface-scale" or "global-scale" pathways. We will emphasize surface-scale (i.e. sheath-scale) pathways here. Global-scale pathways to redeposition eventually require SOL transport dynamics to reach the surface. Impurities in charge state $Z+$ entering the SOL incur a total force

F_Z parallel to the $\vec{B}$-field (109):

$$F_Z \approx -\frac{1}{n_Z}\frac{dp_Z}{ds} + m_Z\frac{v_i - v_Z}{\tau_s} + Zq_eE + \alpha_e\frac{kdT_e}{ds} + \beta_e\frac{kdT_{ip}}{ds} \tag{4.1}$$

where n_Z is the ionized impurity's density, p_Z is the partial pressure of the ionized impurity, s is the distance parallel from the target in the upstream direction of the SOL, m_Z is the mass of the ionized impurity, v_i is the velocity of the plasma ion fluid, v_Z is the velocity of the ionized impurity (both velocities in the parallel-to-$\vec{B}$ direction), τ_s is the stopping time, E is the electric field component in the parallel-to-$\vec{B}$ direction, and both α_e and β_i are coefficients. The five terms in the net force respectively represent (1) the impurity pressure gradient force, (2) the frictional force, (3) the electrostatic force, (4) the electron temperature gradient force, and (5) the ion temperature gradient force (109). If the complex interplay between (1)-(5) are favorable, then a redeposition event will occur. The careful reader should note that these terms are embedded within Equations 1.7-1.10 in OEDGE (see Chapter 1).

Equation 4.1 summarizes a lot of the important components of impurity transport in the SOL; however, other properties like collisionality/charge exchange are important as well. Overall, comprehensive impurity modeling in the SOL quickly becomes complicated; meanwhile, as we have already noted and will continue to see, the surface-scale physics of the sheath affect net erosion in intricate ways. These facts motivate limiting our scope to scrutinizing global or surface scale redeposition with high fidelity. Here, we choose to study redeposition mechanisms at the surface scale; the findings of this work should be refined with complex SOL analysis as future work. The next section will provide more discussion on this topic.

The classical approach to surface-scale redeposition was pioneered by Fussmann and Naujoks (48; 90). This model first assumes that magnetic field lines are mostly parallel to the PFC (48). As a sputtered neutral leaves the PFC surface, we first need to estimate the characteristic length this neutral may travel before becoming ionized. Consequently, we define the first-ionization mean-free path λ_{s+} to first order

as (90; 109):

$$\lambda_{s+} = \frac{v_s}{n_e S_i[n_e, T_e]} \tag{4.2}$$

Here, v_s is the sputtered neutral ballistic speed normal to the PFC surface (hence ∼normal to the $\vec{B}$-field) and S_i, a function of n_e and T_e, is the ionization rate coefficient. In actuality, the first-ionization length depends on the Boltzmann factor for $n_e(z)$ in Equation 2.2 so is sensitive to the $\psi(z)$ distribution throughout the sheath (54); Chapter 5 contains more discussion about the effect of $\psi(z)$ on λ_{s+}. Once the neutral ionizes, it begins a gyro-orbit around the local magnetic field lines with a first-ionization Larmor radius given by:

$$\rho_{s+} = \frac{m_s v_s}{|q_e||\vec{B}|} \tag{4.3}$$

If the Larmor radius is greater than the ionization length, the particle trajectory may subtend the PFC surface within its first gyro-orbit as illustrated in the Figure 4.1 cartoon. We formalize this behavior by introducing a parameter p (90):

$$p = \frac{\lambda_{s+}}{\rho_{s+}} = \frac{q_e|\vec{B}|}{m_s n_e S_i} \tag{4.4}$$

Note that, all else being fixed by facility operations, p is primarily a function of $n_e(z)$. Conversely, if the plasma conditions and PFC material are fixed, p changes only across facilities' $\vec{B}$ magnitudes. In other words, p is independent of velocity; impurities of the same mass nominally have the same redeposition dependency regardless of their sputtered energy (48). Furthermore, it is worth emphasizing that not all singly ionized particles are redeposited (right half-space of Figure 4.1); only those with favorable forward scattering angles redeposit (left half-space of Figure 4.1). For example, when p is unity as in Figure 4.1 and a cosine distribution of forward-scattering angle δ is assumed (i.e. probability $\sim \sin(2\delta)$) , we may estimate 50% redeposition (48; 90). An general estimation of the redeposition fraction f_{red} for a cosine δ distribution

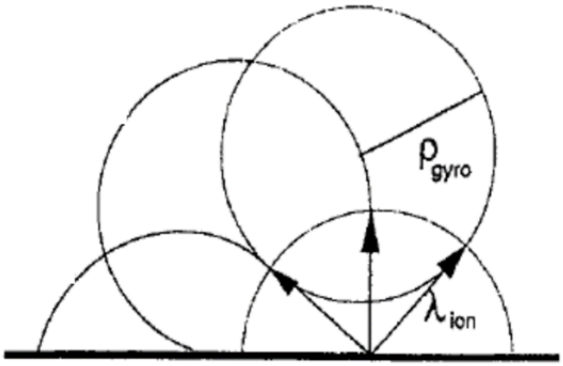

Figure 4.1: The original cartoon (90) of the prompt redeposition process when p is unity, emphasizing the geometric interplay between λ_{s+} and ρ_{s+}.

assumption is (90):

$$f_{red} = \frac{1}{2}\left[1 + \text{sgn}\,(1-p)\left(1 + \frac{4p^2}{(1-p^2)^2}\right)^{-(1/2)}\right] \tag{4.5}$$

Alternatively, the averaged value $\langle f_{red} \rangle$ is represented by (90):

$$\langle f_{red} \rangle = \int_0^\infty f_\lambda(z)\frac{e^{-(z/p)}}{p}dz \tag{4.6}$$

Here, $f_\lambda(z)$ is the ionization length distribution via the Boltzmann factor. Because of the velocity independence of p, Equation 4.6 explicitly expects the same f_{red} value regardless of impurity sputtering energy. Contour plots of p and f_{red} for W PFCs are shown in Figure 4.2, demonstrating the dependency of these parameters on density and temperature.

Importantly, this model asserts that (a) electric fields and (b) multiple ionizations do not significantly contribute to the surface-scale redeposition. We justify assumption (a) by noting that, while electric fields in the sheath will redirect ions toward the surface, dilution of electrons within the Debye sheath model of Section 2.1 works against this effect by reducing the ionization probability (48). Meanwhile, we justify assumption (b) by noting that, for higher charge states, the q_e term in Equation 4.3 is replaced with Zq_e, where Z is the ionization number. Consequently, the Larmor radius shrinks so that intersection with the surface is geometrically improbable if not impossible within the first singly-ionized gyro-orbit, as shown in Figure 4.3. Early simulations using the impurity transport code ERO support these assumptions (48; 90). Thus, this model allows us to solely use the concentration of W^+ to approximate the surface-scale redeposition of W PFCs.

In contrast to the surface-scale redeposition model asserted by Fussmann and Naujoks, work by Chankin suggests that electric fields and multiple ionizations in tandem may have a significant contribution to the surface-scale redeposition (23). This study was able to simulate W redeposition under a broader range of parameters,

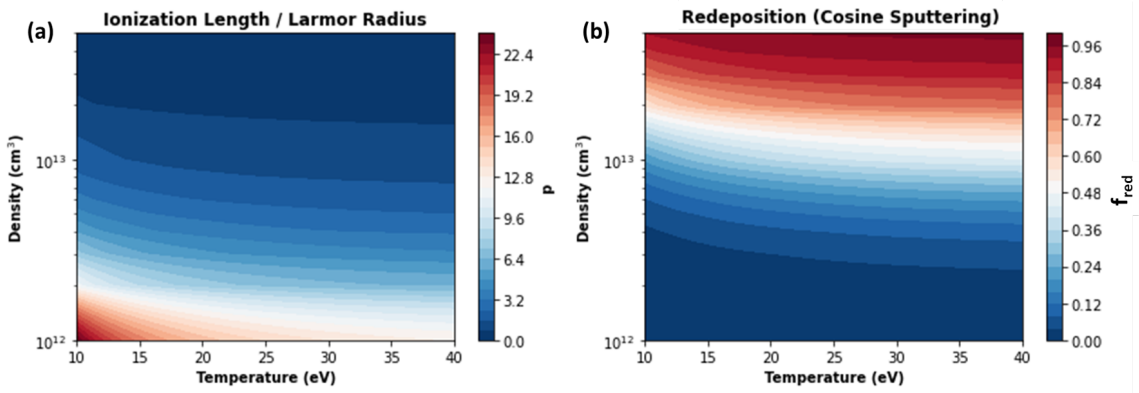

Figure 4.2: Contour plots of p (a) and f_{red} (b) as a function of sheath-entrance density and temperature, held constant throughout the sheath here for illustrative purposes.

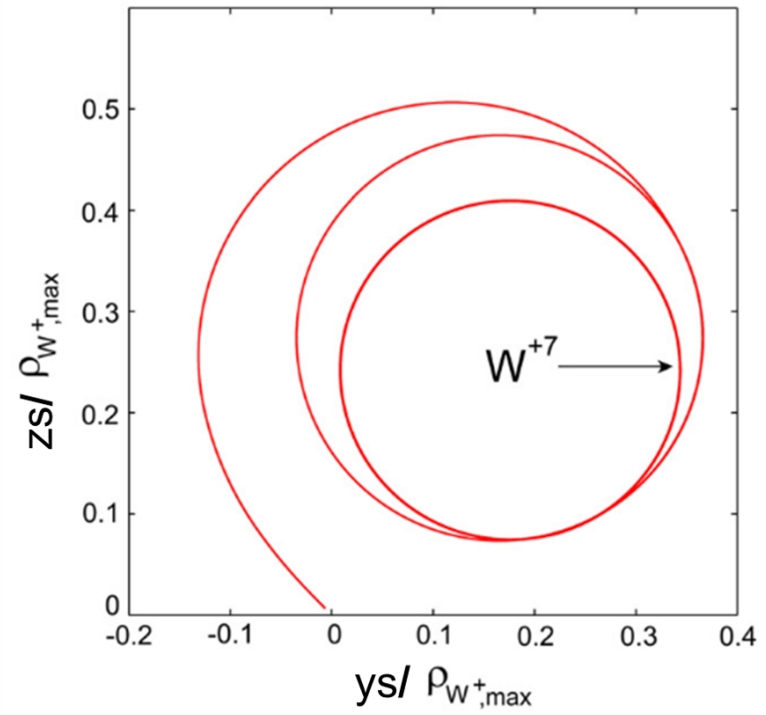

Figure 4.3: Simulated orbit of multiply-ionized W impurity, with distances above and along the surface in relative units to the singly-ionized W Larmor radius. Note that multiply-ionized W does not geometrically intersect with the PFC surface (23).

including ELM-like environments and new values of p. The implications for multiple ionizations as in the Fussmann paper were reproduced in the absence of electric fields, resulting in Figure 4.3 above. Additionally, Equation 4.5 is algebraically simplified and redefined as the non-redeposition fraction (i.e. non-redepositing at the surface-scale) f_{non} (23):

$$f_{non} = 1 - f_{red} = \frac{p^2}{1+p^2} \tag{4.7}$$

Using this equation, f_{non} is tabulated in Table 4.1 for the case with no electric fields but including multiple ionizations. Note that p has a much stronger effect on f_{non} than does T_e alone and that high values of p (i.e. highly ionized W) correspond to high values of f_{non}, as expected.

New to the Chankin study was accounting for the effect of the magnetic pre-sheath at oblique angles. As discussed in Chapter 2, the formula for total potential difference ψ_w is unchanged by introducing the $\vec{B}$-to-PFC pitch angle α, but the angle does change the distribution of the total ψ_w between ψ_{MPS} and ψ_{DS} components. At very shallow angles (e.g. $\alpha \leq 5°$), the Debye sheath component (where $n_e < n_{ip}$) disappears and the magnetic pre-sheath component (where $n_e \approx n_{ip}$) dominates (see Section 2.3). Because the work by Fussmann and Naujoks intrinsically assumed the dominance of the Debye sheath, it was concluded that effects from high electrostatic fields and weak electron densities would cancel each other out. However, if the magnetic pre-sheath indeed dominates, the electron density near the PFC surface may actually enhance the electrostatic redeposition of multiply-ionized W impurities (23).

Consequently, the Chankin paper shows that exit velocities of W neutrals becomes an important component to the surface-scale redeposition model. Here, the exiting W neutral energy is normalized to the ion thermal energy of the magnetic pre-sheath ($R_E = E_s/(3/2kT_{ip})$) for convenience. Hence, the refined redeposition model accounts for the force balance between R_E and electrostatic forces across the sheath in addition to the geometric effects discussed above. Moreover, the work takes a conservative assumption of no collisions between W and D ions. A representative orbit is plotted

Table 4.1: Table of f_{non} values from ERO, not including sheath electric fields but including multiple ionizations (23).

$p \rightarrow T_e$ (eV) $\downarrow$	0.01	0.03	0.1	0.3	1.0	3.0	10.0
3.0	0.1569	0.2970	0.3099	0.2457	0.5313	0.9011	0.9909
10.0	0.3194	0.3721	0.4176	0.5255	0.6516	0.9095	0.9910
30.0	0.3198	0.4255	0.5347	0.6117	0.7260	0.9169	0.9912
100.0	0.3838	0.4588	0.5677	0.6495	0.7577	0.9209	0.9913
300.0	0.4278	0.4686	0.5724	0.6620	0.7716	0.9228	0.9914
1000.0	0.4709	0.4743	0.5690	0.6681	0.7810	0.9246	0.9915

in Figure 4.4. Note that the original trajectory of non-redeposited, multiply-ionized W (shown in red as in Figure 4.3) is now redeposited (shown in blue) within the first gyro-orbit of singly-ionized W (shown in black). As may be seen from this example, sheath electric field effects indeed contribute to total redeposition as a surface-scale effect.

To be more explicit, we may see in Table 4.2 f_{non} values over the same p and T_e grid as Table 4.1 but now including electrostatic effects from the sheath; it is assumed that R_E=0.3 and $\alpha = 3°$ as a representative case. Note that the same scaling with p and T_e occurs as in the Fussmann reproduction of Table 4.1, but the f_{non} values themselves are significantly diminished, sometimes by orders of magnitude. Note also that the simulation producing Table 4.2 assumes that a multiply-ionized W ion escapes the sheath if it is unable to intersect the PFC surface within its first gyro-orbit. If the simulation is extended to allow these ions to have multiple gyro-orbits before intersecting the PFC under ExB drifts within the sheath, the f_{non} values only continue to decrease, as shown in Table 4.3.

Note that an almost insignificant amount of W escapes surface-scale redeposition for the left half of the table in Table 4.3; this fact speaks highly of the ability of W PFCs to survive long-term in fusion reactor environments. However, we note that later simulations for the all-W PFC device WEST comparing the Fussmann and Chankin models emphasize that, while the Chankin results appear promising, the presence of light impurities may diminish the contribution of the sheath to surface-scale redeposition by imparting higher R_E to sputtered neutrals during gross erosion (83).

Later, work across two papers by Mellet demonstrated some general trends of f_{non} with sheath conditions using particle-in-cell or PIC codes to model the sheath as opposed to the analytic models of Chapter 2. This modeling shows a significant disparity in the redistribution of particles across the surface between those that redeposit as a result of surface-scale vs global-scale processes, as shown in Figure 4.5. Here, we see that surface-scale processes dominate as n_e increases and that T_e seems

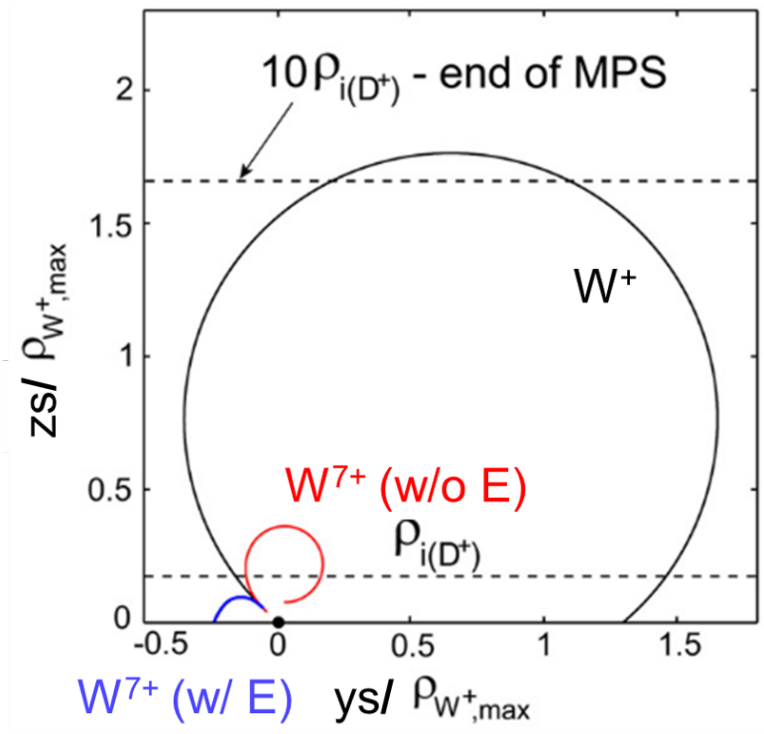

Figure 4.4: Simulated orbit of multiply-ionized W redeposition as a refinement of Figure 4.3 including Chodura sheath electric fields (23).

Table 4.2: Table of f_{non} values from ERO including both sheath electric fields and multiple ionizations but only accounting for the material redepositing within the first gyro-orbit (23).

$p \rightarrow T_e$ (eV) $\downarrow$	0.01	0.03	0.1	0.3	1.0	3.0	10.0
3.0	0.0	$<10^{-4}$	0.0092	0.0532	0.2212	0.5287	0.8023
10.0	0.0	$<10^{-4}$	0.0118	0.1154	0.3145	0.5609	0.8073
30.0	0.0	$<10^{-4}$	0.0191	0.1431	0.3674	0.5853	0.8124
100.0	0.0	$<10^{-4}$	0.0220	0.1583	0.3921	0.5983	0.8140
300.0	0.0	$<10^{-4}$	0.0226	0.1620	0.4011	0.6060	0.8151
1000.0	0.0	$<10^{-4}$	0.0220	0.1632	0.4074	0.6111	0.8174

Table 4.3: Table of f_{non} values from ERO including both sheath electric fields and multiple ionizations and allowing the material requiring multiple gyro-orbits within the sheath to redeposit (23).

$p \rightarrow T_e$ (eV) $\downarrow$	0.01	0.03	0.1	0.3	1.0	3.0	10.0
3.0	0.0	0.0	1.4×10^{-4}	0.0108	0.1326	0.4457	0.7620
10.0	0.0	0.0	8.7×10^{-5}	0.0203	0.1819	0.4689	0.7654
30.0	0.0	0.0	4.1×10^{-5}	0.0213	0.2086	0.4860	0.7691
100.0	0.0	0.0	2.5×10^{-5}	0.0207	0.2188	0.4964	0.7694
300.0	0.0	0.0	1.0×10^{-5}	0.0201	0.2229	0.5012	0.7721
1000.0	0.0	0.0	1.3×10^{-5}	0.0198	0.2255	0.5049	0.7721

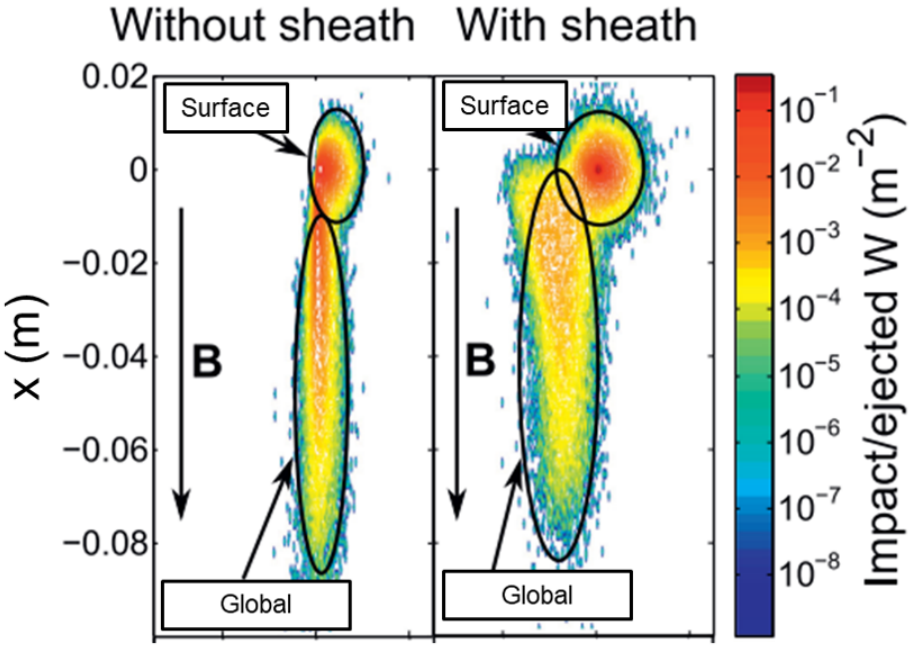

Figure 4.5: Redeposition geometric redistribution for surface-scale and global-scale redeposition processes (84).

to have an effect on the drift direction of redeposited particles: overall towards or away from the ExB drift direction (84). Accounting for 3D effects within the sheath potential, it is proposed that higher temperatures result in higher redeposition fractions due to overall shorter ionization lengths (84). Meanwhile, further PIC-studies emphasize the impact of incident ion type and charge on f_{non} for W by accounting for the full net erosion picture (85); this study results in a figure of merit for key impurities shown in Figure 4.6. We observe that T_e has a greater impact on f_{non} as incident ion m_{ii} increases. Moreover, the $\vec{B}$-to-PFC pitch angle α is scanned from $\alpha = 1 - 4°$, showing that the impact angles are effected by even these slight changes to the localized sheath distribution (85). On the other hand, ERO modeling and experimentation in the mixed-material environment of DIII-D shows that increasing C impurity concentration nonetheless decreases W net erosion due to PFC surface dilution by C embedments reducing the gross erosion (33). In other words, surface composition effects can have a nontrivial impact on these trends and should be considered more closely as this field of study progresses.

Lastly, the work by Guterl (53) considers surface-scale redeposition physics under a broader range of parameters while maintaining the shallow $\alpha < 5°$ assumption. Using a wide range of sheath-entrance n_e and T_e values and the corresponding ionization lengths tabulated in a separate study (54), this paper uses ERO to consider the full effect of the sheath on f_{non} under single-effect changes to the magnetic pre-sheath distribution and total potential drop, PFC surface material, magnetic field, ionization time distribution, and cut-off incident ion energy. Ultimately, f_{non} appears invariant with most of these parameters and driven solely by density and temperature effects using a different parameter than p as the independent variable, $\hat{\lambda}$:

$$\hat{\lambda} = \frac{\lambda_{s+}}{L_{MPS}} \tag{4.8}$$

Note that, under constant plasma parameters, this term now scales with both the $\vec{B}$-field strength and the cosine of the $\vec{B}$-to-PFC pitch angle α (see Equation 2.21).

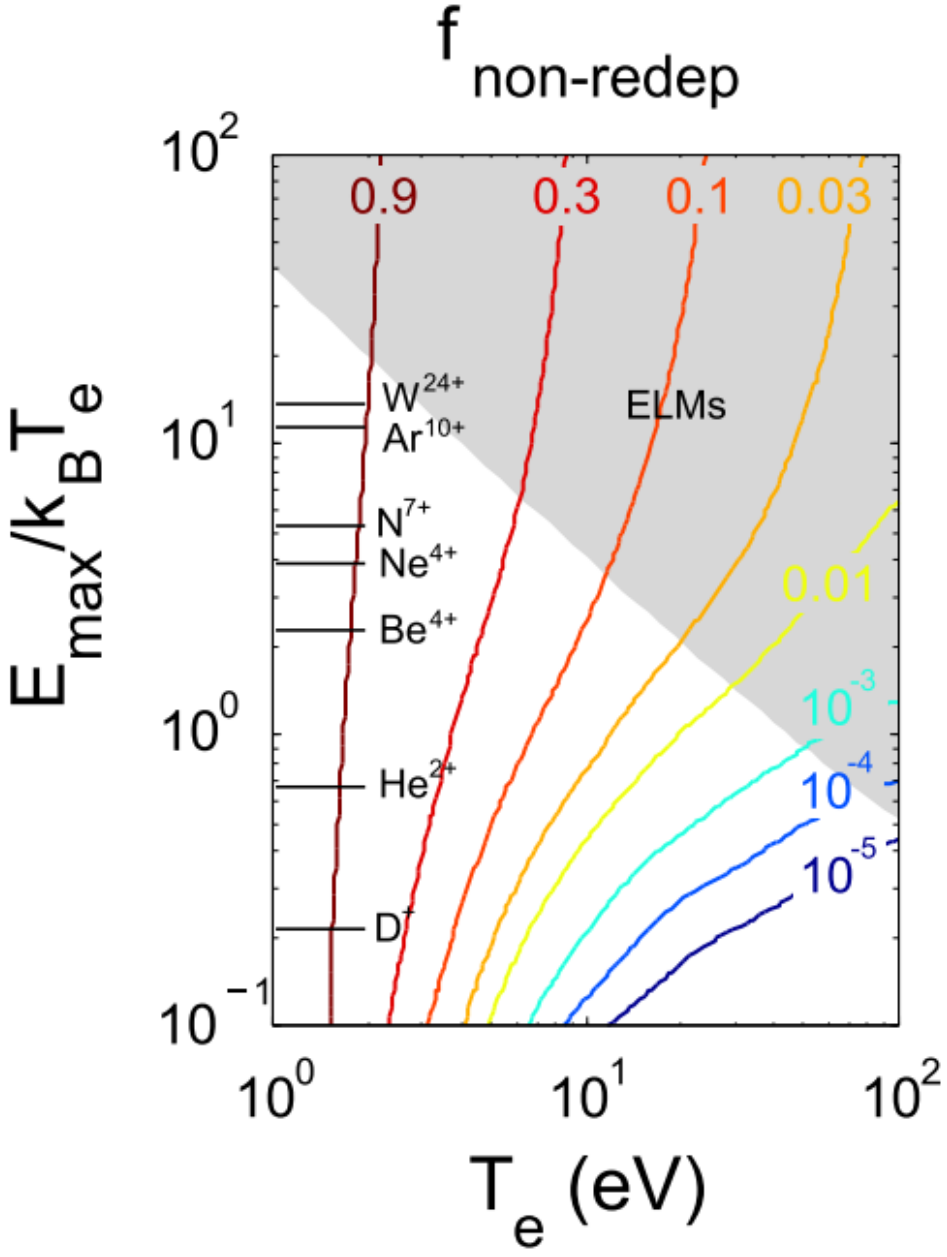

Figure 4.6: Figure of merit for non-redeposition fraction against T_e and maximum normalized sputtering ion energy $\sim R_E$ (85).

The lone exception to this trend invariance is the cut-off energy for the Thompson E_s assumption in this model; a cosine distribution of δ is assumed as in the Fussmann and Chankin papers. Figure 4.7 shows the $\hat{\lambda}$ trend for f_{non} against different charge fractions of W given by

$$X_{W^{i+}} = \#W^{i+}/\#W^0 \tag{4.9}$$

Using this approach, Guterl was able to link dominate charge states $n+$ to the surface-scale redeposition fraction under different regimes of $\hat{\lambda}$ (53).

At this point we have discussed several important papers characterizing high-Z (i.e. W) redeposition within the modeling literature to date. These works have been impactful for setting predictions towards fusion pilot plant designs and regimes of operation. With no intended discredit to the excellent work of these authors, we would like to reframe their findings under a new paradigm for further study, which we will discuss in the next section.

4.2 A Model Refinement of High-Z Redeposition

Stepping back from Section 4.1, two variables have shown overall good predictability for surface-scale redeposition trends of high-Z PFCs: (1) the ratio of the first-ionization length to the first-ionization Larmor radius, denoted p in Equation 4.4, and (2) the ratio of the first-ionization length to the magnetic pre-sheath thickness, denoted $\hat{\lambda}$ in Equation 4.8. Importantly, p emphasizes the importance of the PFC material properties in driving the redeposition fraction but does not emphasize the importance of the sheath. Conversely, $\hat{\lambda}$ emphasizes the importance of plasma sheath conditions, which have a significant effect on both aspects of net erosion, but largely reframes the physics away from the PFC composition. Both of these variables are nominally meant to account for the total effect of all surface-scale redeposition physics. However, the careful reader will note that two distinct mechanisms occur at the surface scale.

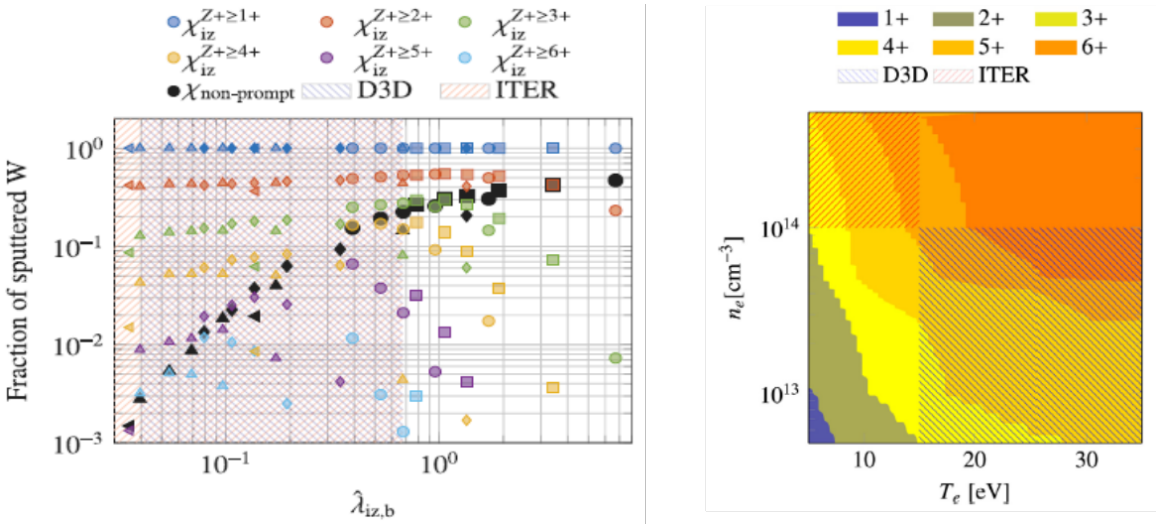

Figure 4.7: Simulated figures of merit for approximating surface-scale redeposition by the concentration of sputtered, multiply-ionized W ions (53). On the left, sputtered fractions of W charge states are compared with the fraction of non-promptly deposited W ($\chi_{non-prompt} = f_{non}$ above). On the right, the charge state of W that best approximates f_{non} is plotted against T_e and n_e. Characteristic regions for DIII-D and predicted regions for ITER are highlighted.

1. Recapping from Section 4.1, singly-ionized high-Z material has a high likelihood of subtending the PFC surface during its first gyro-orbit (90) because the first ionization mean-free path is much smaller typically than the first ionization Larmor radius; in other words, usually $p \ll 1$ in fusion-relevant conditions. Note that this kind of redeposition would occur regardless of the strength of the electrostatic forces within the sheath. On the other hand, multiply-ionized material have increasingly smaller Larmor radii and longer cumulative ionization lengths, so it is unlikely that their overall gyro-orbits can geometrically intersect the PFC surface. Consequently, this geometric-driven mechanism is dominated by 1+ ions (48).

2. On the other hand, multiply-ionized PFC material can make its way back to the surface from within the sheath, depending on the strength of the electric field. As the Coulombic force $\propto Zq_e$, higher charge states are increasingly sensitive to the electrostatic attraction back to the surface; however, their ability to be pushed back to the surface by this force depends on both their sputtered ballistic energy E_s relative to the electric potential energy and the rate of ionization within the sheath (23). Conversely, while a small amount of singly-ionized material would require assistance from electrostatic forces to redeposit, the majority of this material would typically redeposit from the first mechanism, regardless of the electric field strength. In this way, higher charge states from 2+ up to some maximal charge state n+ will predominantly redeposit by this sheath-driven mechanism (53).

Historically, both mechanisms of surface-scale redeposition have been grouped under the term "prompt redeposition"; in fact, all of the surface-scale physics discussed in Section 4.1 are called prompt redeposition in their original papers. However, there are major drawbacks to grouping these mechanisms together, which we will spend the rest of this dissertation exploring. To briefly motivate the need for heuristic separation, consider the total redeposition flux of high-Z material (e.g. W):

$$\Phi_{redep} = \Phi_{W^+} f_{W^+} + \sum_{i=2}^{n} \Phi_{W^{i+}} f_{W^{i+}} + \sum_{j=n+1}^{74} \Phi_{W^{j+}} f_{W^{j+}} \tag{4.10}$$

where Φ represents the flux and f represents the redeposition fraction of each ion species. We separate W^+ as being dominated by geometric-driven redeposition and W^{2-n+} as being dominated by sheath-driven redeposition; we consider $W^{(n+1)-74+}$ redeposition to be dominated by global-scale, SOL-driven physics. The maximal charge state $n+$ depends on the sensitivity of the fusion experiment being modeled, but represents the point at which either $\Phi_{W^{(n+1)+}}$ or $f_{W^{(n+1)+}}$ may be considered insignificant at the surface scale.

Grouping the first two terms in Equation 4.10 as the definition of "prompt redeposition" generates a couple of unnecessary complications. For one thing, this grouping obscures, for a given set of sheath conditions, whether geometric- or sheath-driven physics dominates the overall surface-scale redeposition. Such conflation limits our ability to engineer optimized redeposition fractions across the poloidal distribution of first-wall material. As we will show in Chapters 5 and 6, the trade-off between these two mechanisms varies substantially across sheath conditions. For another thing, grouping confuses the experimental assessment of redeposition. As we will see in Chapter 7, different diagnostic choices are needed to assess net erosion depending on the value of $n+$, but it has been common in experimental measurements to assume $n+ \approx 1+$ based on only the geometric-driven mechanism (93; 13; 123; 14), which Section 4.1 shows is incomplete (53).

For these reasons, we propose reframing high-Z redeposition into three categories: geometric-driven, sheath-driven, and SOL-driven redeposition. We refer to geometric-driven redeposition exclusively as **prompt** redeposition, in the original style of the Fussmann and Naujoks papers. Meanwhile, we refer to sheath-driven redeposition as **local** redeposition instead, repurposing the term from Mellet's work and Stangeby's paper on Chodura sheaths (110). Lastly, we refer to SOL-driven redeposition as **far** redeposition. Cartoons to reinforce these definitions are provided in Figure 4.8, summarizing the discussion within this section. In the next section, we will discuss an approach to redeposition modeling that is capable of distinguishing these mechanisms.

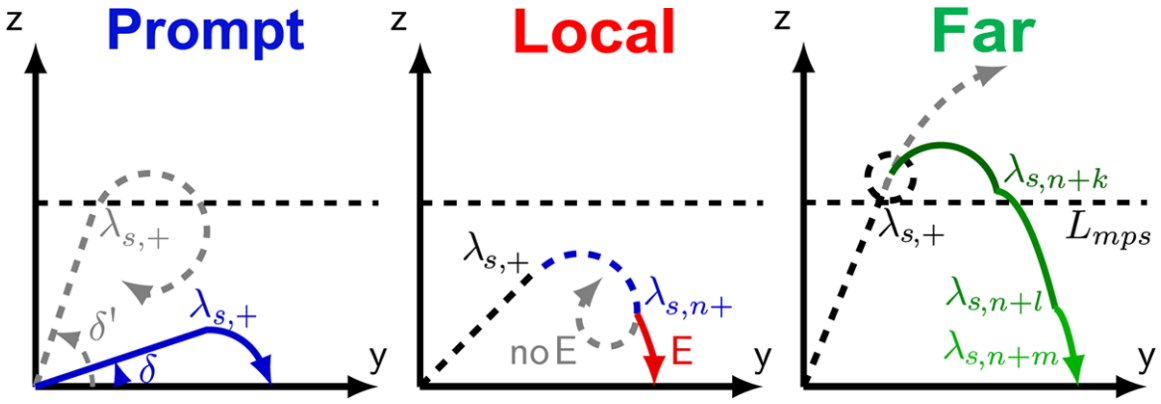

Figure 4.8: Cartoons of prompt (geometric-driven), local (sheath-driven), and far (SOL-driven) redeposition, with trajectories avoiding each redeposition mechanism in gray for comparison.

4.3 Discrimination of High-Z Redeposition Mechanisms and GITR

To complete our modeling workflow of net erosion, we need a final Monte Carlo code capable of modeling redeposition while simultaneously discriminating between prompt, local, and far redeposition trends. The Global Impurity TRansport (GITR) code (131) was selected for this purpose due to its excellent validation for high-Z PFCs at the PISCES-A experiment (132). We will conclude this chapter here with a brief overview of GITR's methodology and the unique modifications made within this model to discriminate among the redeposition mechanisms of Section 4.2.

In GITR (131) we generate an input source file describing the original location and velocity of each test particle and a geometry source file describing the locations of the PFC surface. In our simulations, particle tracking ends when the test particle intersects the PFC surface. Additionally, we may explicitly set the magnetic field geometry and plasma flow velocities. Above the surface we calculate the potential through the sheath using the Brooks model of Section 2.3. This sheath model is currently the only sheath model available in GITR, though GITR has been coupled to the PIC code hPIC (70) in the past as part of the SciDAC workflow. Erosion calculations are available within GITR using tabulated data for certain PFC species (3; 69), but we will not use them here. Instead, we will couple the PYEAD-RustBCA code from Chapter 3 to generate sputtered neutral EADs.

Under the trace particle assumption, there are no pressure or impurity particle-to-particle interactions included in the test particles' equation of motion. Thus, the total force acting on a test particle reduces to two components (131):

$$\vec{F} = \vec{F_L} + \vec{F_C} \tag{4.11}$$

where F_L is the standard Lorentz force and F_C is the overall force from impurity particle-to-plasma collisions, given as (131):

$$\vec{F_C} = -\nu_{drag} m_s \vec{U} \pm m_s \sqrt{\frac{\nu_\perp}{2\Delta t}} \vec{U_\perp} \pm m_s \sqrt{\frac{\nu_{||}}{\Delta t}} \vec{U_{||}} + \alpha_e \vec{\nabla_{||B}}(k_B T_e) + \beta_i \vec{\nabla_{||B}}(k_B T_{ip}) \quad (4.12)$$

Here, ν is the collision frequency, $\vec{U} = \vec{v_s} - \vec{v_{flow}}$ is the relative velocity of the test particle $\vec{v_s}$ to the plasma flow velocity $\vec{v_{flow}}$, Δt is the time step, and both α_e and β_i are coefficients for the electron and plasma ion temperature gradient forces (see Equation 4.1). All directions are parallel or perpendicular to the $\vec{B}$-field.

Unlike PYEAD, GITR includes collisions and ionizations throughout the sheath. In Equation 4.12 the velocity moments in the Fokker-Planck solution (131; 107) complexly determine the ν terms. To move each particle, the Boris algorithm (Boris) integrates $\vec{F_L}$ in Equation 4.11; then, the collision force provides an additional "kick" to the final velocity (131). Lastly, we use the ADAS database (115) to extract $S_i[n_e, T_e]$ for the particle's current velocity, and the particle tests for ionization with probability $1 - e^{-\Delta t/(n_e S_i)}$ using a uniform random number (131). Here, we use the scd50.dat data file for W ionization rates.

Now, we made several minor changes to the default GITR code that enable us to track the redeposition behavior of every test particle. First, the default code holds the density n_e constant throughout the sheath at the sheath-entrance value; it does not include the Boltzmann factor (see Equation 2.2) for the density drop $n_e(z)$. To increase the accuracy of ionization calculations, we introduce a z call to the Boltzmann-factor n_e value during the S_i interpolation from ADAS. Both n_e and n_{ip} calls use the same parameter by default in GITR; given that the n_{ip} population is significantly different in the sheath (see Chapter 2), we added a separate call to n_{ip}

when determining the drag forces (107):

$$n_{ip}(z) = n_{se}\left(1 - \frac{2q_e(\psi(z) - \psi_{se})}{k_B T_e}\right)^{-1/2} \tag{4.13}$$

Moreover, we bin the maximum height of each particle z_{max} and both calculate and bin the gyro-rotation number Ω (i.e. the number of completed Larmor orbits, different from Ω in Section 3.3); we push these values to the redeposition file output in addition to the final position and velocity of each particle.

Using these changes to the GITR code, we are able to uniquely isolate particles whose redeposition is dominated by prompt, local, or far redeposition. Singly-ionized particles that are dominated by prompt physics cannot attain a z_{max} value greater than $2\rho_{s+}$; otherwise, electrostatic forces are required to close the distance between the minimal z of the gyro-orbit and the PFC surface. Furthermore, the gyro-orbit number $\Omega < 1$ for these particles since the first orbit must be interrupted by the PFC. Meanwhile, particles dominated by local physics fall into two categories: (1) singly-ionized particles having $z_{max} > 2\rho_{s+}$ while maintaining $\Omega < 1$ or (2) multiply-ionized particles having $\Omega < 1$. The second condition follows as a natural consequence of the fact that the electrostatic forces dominate over the gyro-motion. Finally, particles dominated by far physics have $\Omega > 1$. From these prescriptions we may define f_{prompt}, f_{local}, and f_{far} fractions that represent the ratio between the number of particles redepositing via a given mechanism to the number of Monte Carlo test particles:

$$f_{prompt} = \frac{\#\, ions \ni \{(charge < 2+) \wedge (\Omega < 1) \wedge (z_{max} < 2\rho_{s+})\}}{\#\, neutrals} \tag{4.14}$$

$$f_{local} = \frac{\#\, ions \ni \{(\Omega < 1) \wedge ((charge > 1+) \vee ((charge < 2+) \wedge (z_{max} > 2\rho_{s+})))\}}{\#\, neutrals} \tag{4.15}$$

$$f_{far} = \frac{\#\, ions \ni \{\Omega > 1\}}{\#\, neutrals} \tag{4.16}$$

We track every particle until it redeposits within our simulations; hence, we assume that

$$f_{prompt} + f_{local} + f_{far} = 1 \tag{4.17}$$

As a final point, it is worth verifying that these prescribed conditions actually capture different groups of particles. One confirmation of this fact is visually demonstrated in Figure 4.9. Here, we see the probability distributions (PDFs) of the first six ionization states of W as they move throughout the sheath and into the SOL. Subplots (a)-(c) look down onto the PFC surface and show the final location of particles originating from an azimuthally symmetric, 1 mm radius spot size centered at the origin; subplots (d)-(f) show the z_{max} and final radial displacement for the same source. Encouragingly, we see good agreement between these kinds of plots and Figure 4.5. The reader should note the change in PDF shape as f_{far} particles escape the sheath in (f) and incur non-sheath plasma conditions and gradients, resulting in the long-range transport seen in (c). On the other hand, the increased z_{max} of f_{local} particles in (b) still stay ∼within the L_{MPS} sheath entrance estimation of Equation 2.21. We see similar profiles (a) and (b) hold for both types of redeposition within the sheath.

Over the past two chapters, we have explained the physics of both gross erosion and redeposition and discussed three models (PYEAD, RustBCA, and GITR) that may be coupled to study the overall net erosion process. We have also provided a refined model of redeposition that discriminates between geometric-driven vs. sheath-driven processes within surface-scale redeposition. Now, we will largely conclude any background discussion of the tools and physics under consideration within this dissertation. In the next chapter, we begin to assess the sensitivity of prompt vs. local vs. far redeposition trends to changes to the sheath thickness L_{MPS}.

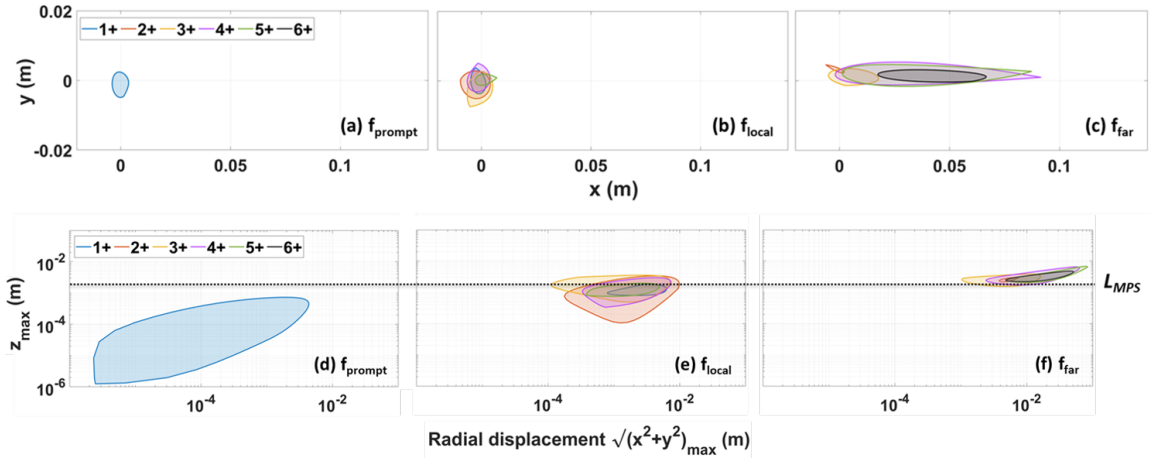

Figure 4.9: Example PDF contours of (a) f_{prompt}, (b) f_{local}, and (c) f_{far} onto the PFC surface for a 1 mm radius source spot centered at the origin, assuming $\alpha = 3°$, $B = 2.25$ T, and D plasma at $\approx 4.5 \times 10^{19}$ m^{-3} density and ≈ 19 eV temperature. The PDF of the maximum displacement above vs. along the PFC surface is respectively shown in (d), (e), and (f).

4.4 Executive Summary

- The current variables associated with predicting high-Z redeposition trends are (1) the ratio between the first-ionization mean-free-path and the first-ionization Larmor radius and (2) the ratio between the first-ionization mean-free-path and the magnetic pre-sheath thickness.
- Different physical processes motivate a heuristic refinement of high-Z redeposition mechanisms:
  - Prompt redeposition is geometric-driven redeposition of singly ionized impurities due to their large Larmor radii and proximity to the material surface.
  - Local redeposition is sheath-driven redeposition of multiply ionized impurities due to strong electrostatic forces within the sheath.
  - Far redeposition is scrape-off layer driven redeposition of impurities exiting the sheath but encountering favorable gradients redirecting their trajectory back to the material surface.
- GITR, a Monte Carlo code using the Brooks sheath model, calculates high-Z redeposition with mechanistic distinction.
- The PYEAD-RustBCA-GITR coupled workflow provides a Monte Carlo estimation of high-Z net erosion.

Chapter 5

Importance of the $\vec{B}$-to-PFC Pitch Angle in Net Erosion

Note: *The content of this chapter is the primary basis of a publication in Physics of Plasmas (42). Here, we reproduce the salient points of that paper in an expanded and revised form to provide greater detail on the methods and techniques used to obtain the published results.*

5.1 Motivation and Methodology

At this stage of the dissertation, it is perhaps beneficial to recap the physics we have discussed so far. In Chapter 1 we introduced the concept of fusion energy and showed the complex PMI impurity pathway between the surface and the core plasma. Then, in Chapter 2 we discussed the physics of the sheath: a thin region of strong electrostatic forces at the PFC surface that insulates the bulk plasma from the PFC. Next, in Chapter 3 we showed the importance of the sheath in setting the incident ion energy and angle distributions onto the PFC surface, which critically determines gross erosion. Finally, in Chapter 4 we examined the sheath's role in determining

redeposition: the density drop sets first-ionization mean-free paths and the potential drop sets electrostatic field strengths.

Overall, the sheath conditions form the first line of defense in mitigating high-Z net erosion. For particles escaping the sheath, we must rely on SOL dynamics to prevent leakage into the core; however, there are major drawbacks to depending on the SOL for leakage mitigation. For example, the SOL contribution to redeposition is less ubiquitous across devices compared to sheath contributions; while the same generalized physics is present across magnetic confinement devices, plasma and divertor geometries set very different edge-SOL integrated conditions (31; 124; 74; 79; 111; 80). At present, we do not completely understand all of the dependencies and consequences of these integrated conditions (i.e. the ITEP gap). Additionally, there is a higher probability of self-sputtering for high-Z ions returning to the PFC surface from the main plasma due to the increased energy gained from the SOL (or potentially core) transport; nonetheless, clever SOL engineering can increase the far redeposition fraction in certain tokamak configurations (120). We have seen examples of large far redeposition in Figure 4.9, in agreement with the global-scale redeposition seen in other studies (84).

The fundamental question is this: **What are the optimal PMI parameters that maximize high-Z redeposition within the sheath (i.e. surface-scale PMI) and minimize reactors' dependence on SOL processes (i.e. global-scale PMI) to reduce high-Z net erosion?** In other words, what PMI regimes minimize gross erosion (the amount of PFC material initially leaving the first wall) and maximize prompt + local redeposition (the amount of PFC material immediately returning to the first wall from within the sheath)? At present, we have seen this question partially answered by the redeposition work surveyed in Section 4.1; for instance, the work by Guterl shows a strong dependence on sheath-entrance electron density and temperature (53). However, one parameter has been minimally varied throughout the current literature: the $\vec{B}$-to-PFC pitch angle, α. We intentionally engineer shallow values of $\alpha < 5°$ in fusion experiments to reduce PMI heat fluxes;

hence, redeposition modeling has not traditionally considered α variation beyond this range, as noted throughout Section 4.1. However, our concern is that evolving PFC surfaces from net erosion and material migration may change the localized value of α, particularly over reactor-relevant PFC lifetimes. Experiments show that, over extended durations of reactor-relevant plasma exposure, structural deformations of the PFC surface increase on both the micro-structural (104; 103) and macro-structural (60; 20) levels. Tile misalignment and other engineering or manufacturing errors can also compound these changes to the idealized PFC geometry, inevitably increasing the local $\vec{B}$-to-PFC pitch angle.

It is worth highlighting that changes to α affect the entire net erosion problem. As discussed extensively in Chapter 2 and shown in Figure 5.1, α has a dramatic impact on the sheath's potential distribution, setting the magnetic pre-sheath to Debye sheath ratio and the magnetic pre-sheath thickness. These changes will clearly affect sheath-driven redeposition (i.e. the local redeposition mechanism) through changes to the electric field structure within the sheath. Moreover, the potential distribution changes the incident ion energy and angle distributions (EADs) onto the surface, which in turn affects the sputtered neutral yield and the EADs of the gross eroded flux (see Chapter 3). Consequently, these changes to the neutral EADs, in combination with the new electron density drop through the sheath via the Boltzmann factor (Equation 2.2), will set new ionization lengths that affect both geometric-driven (i.e. the prompt redeposition mechanism) and sheath-driven redeposition rates. This observation motivates considering the independent effects of α on prompt, local, and far redeposition fractions.

In order now to observe the impact of α on net erosion, we first note that α is intrinsically incorporated into the definition of $\hat{\lambda}$ seen in Equation 4.8. However, α was never varied explicitly in the original Guterl study, though other components of L_{MPS} were. Thus, in order to facilitate comparison with the findings in Section 4.1, we would like to consider any change to α within the context of other variables affecting the pre-sheath thickness. When we consider the definition of L_{MPS} found in Equation 2.21, we

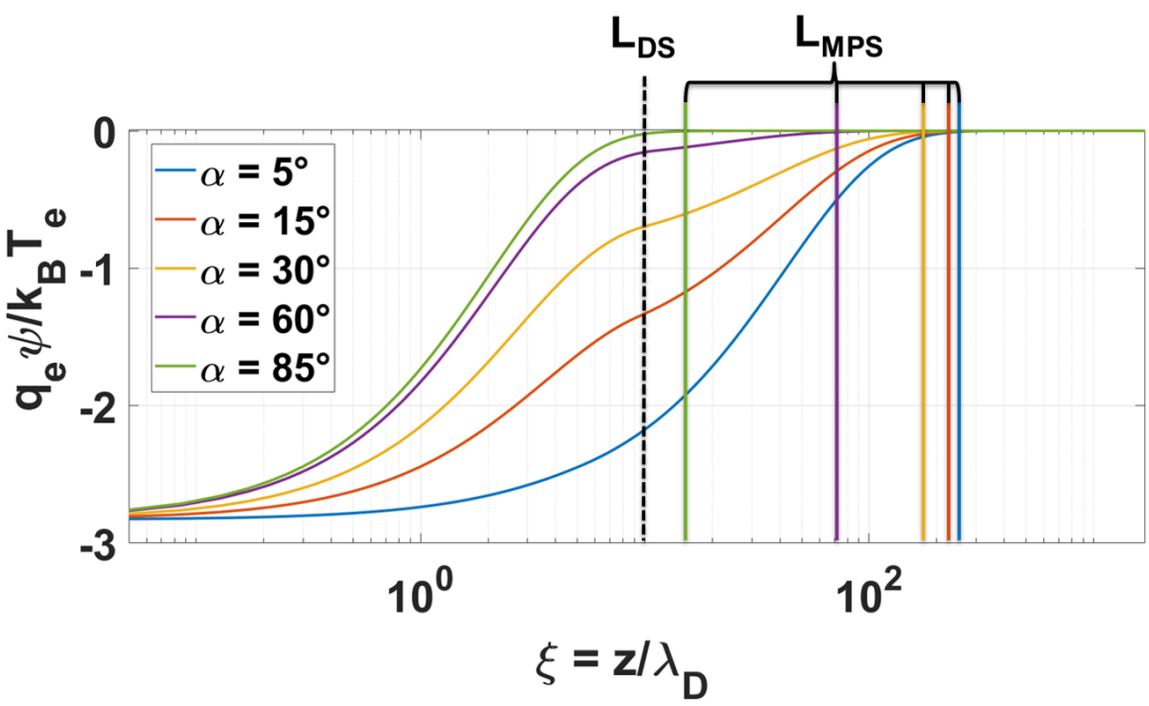

Figure 5.1: Potential distribution through the sheath as a function of above-PFC height using the Borodkina sheath model (see Section 2.3). The impact to the L_{MPS} thickness is noted, with $L_{DS} = 10\lambda_D$ held fixed.

note that the primary PMI parameters of interest, under constant plasma conditions at the sheath entrance, are the following: the plasma ion species, the magnetic field magnitude, and the $\vec{B}$-to-PFC pitch angle. To study the effect of changing these parameters on high-Z net erosion, we consider the workflow diagrammed in Figure 5.2.

We start with the simulation of a SOL plasma background, provided by OEDGE (Section 1.4). For this study, we wish to model plasma discharge conditions representative of standard, repeatable discharges at DIII-D, given its importance as an operating facility at time of writing; that is, we want to consider deuterium plasma in lower-single-null, reverse $\vec{B}_T$, L-mode conditions. To this end, we adopted OEDGE modeling work by Nichols (91) for DIII-D discharges #167192-167220. Here, the outer strike point is roughly centered on the W ring at the upper divertor shelf and approximately 60 cm from the center of the Divertor Materials Evaluation System (DiMES) (128), which we will discuss further in Chapter 7. The work by Nichols used experimental data from divertor Thomson scattering and Langmuir probe measurements as electron density and temperature constraints to the onion-skin model (91), with diagnostic locations against the OEDGE grid readily seen in Figure 1.8. Table 5.1 shows important discharge parameters from this dataset. Critically, we extract the electron and ion densities and temperatures as well as the incident carbon flux at DiMES from the OEDGE model for further use; these moderate plasma conditions include $n_e = 4.68 \times 10^{19}$ m^{-3} and $T_e = 18.58$ eV.

Next, we simulate incident ion EADs from carbon fluxes onto the DiMES target by coupling OEDGE conditions to PYEAD (Section 3.3). Since DIII-D is a graphite-wall device, we treat C as the dominate sputtering ion; PYEAD is an appropriate choice of modeling the C-EADs given the ieadrk3 parent code's excellent agreement with experimental data for light ions. From Table 5.1 we note that C^{1-2+} fluxes are roughly an order of magnitude greater than those for the C^{3-6+} charge states in the OEDGE calculation. To account for the ionization distribution, we first calculate the EADs of each C ionization individually, then create the total C-EAD by weighing the contribution from each charge state by its fractional abundance. Given the abundance

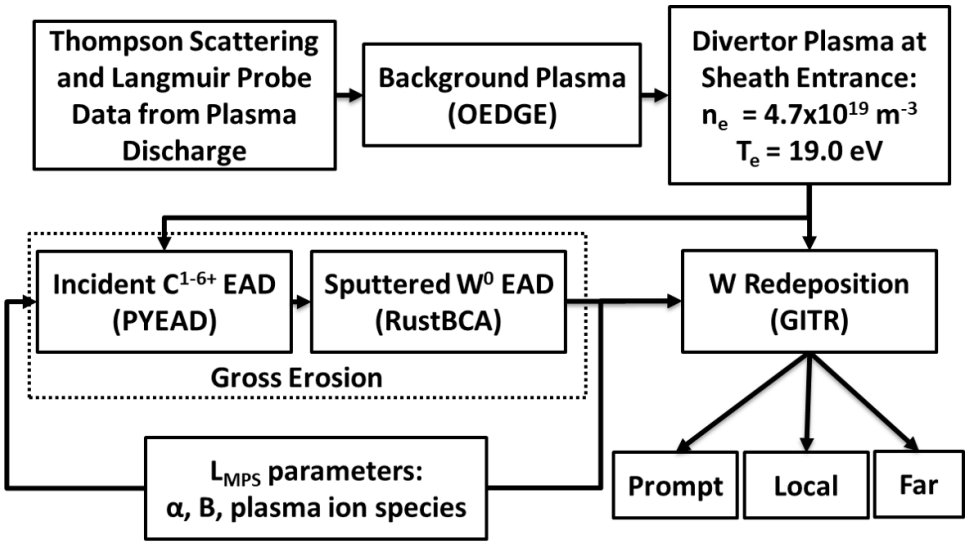

Figure 5.2: Workflow diagram of physics model coupling used to study the entire net erosion physics of high-Z PFCs.

Table 5.1: Table of important OEDGE parameters used for the net erosion simulations in this chapter (91)

Plasma current	1.2 MA
Line-averaged electron density	3×10^{19} m^{-3}
Average injected neutral beam power	3 MW
Toroidal magnetic field (reverse direction)	2.25 T
DiMES n_e	4.68×10^{19} m^{-3}
DiMES T_e	18.58 eV
DiMES C$^+$ flux	2.9×10^{19} m^{-2}s^{-1}
DiMES C^{2+} flux	2.5×10^{19} m^{-2}s^{-1}
DiMES C^{3-6+} flux	4.0×10^{18} m^{-2}s^{-1}

of C^{1-2+}, we expect and find that the overall C-EAD is dominated by the contribution from these charge states.

Then, we simulate the sputtered neutral EADs from the C-eroded PFC surface, using W as a representative high-Z material, by coupling the PYEAD distribution to RustBCA (Section 3.4). To facilitate this coupling, we treat the incident C-EADs as probability distribution functions; these probability distribution functions can be converted to cumulative distribution functions through the usual quadrature over the 3D E_{ii}, θ, and ϕ conditions. We assign energy and angle attributes to each RustBCA test particle of incident C by sampling this cumulative distribution with a uniform random variable. In RustBCA we use the default material properties for W: $E_B = 8.79$ eV and lower cutoff energy $E_c = 3.0$ eV with no upper cutoff energy. In this manner, the overall PYEAD-RustBCA coupling completely accounts for the sputtered gross erosion physics discussed in Chapter 3.

Finally, we couple the RustBCA W^0-EAD outputs to GITR (Section 4.3) in order to capture the redeposition physics. Again, we treat the W^0-EAD as a probability distribution and sample the cumulative distribution function (over E_s, δ, and the azimuthal sputtering angle) with a uniform random variable in order to ascribe initial conditions for each GITR test particle leaving the PFC. At the DiMES sample we consider a 1-mm diameter, azimuthally symmetric PFC element with a smooth surface; we use a separate uniform random variable to decide the initial position of each sputtered neutral within that mm-size spot. We have chosen a mm-scale source because this scale is assumed to have negligible redeposition in DIII-D experiments due to this scale being roughly equal to the typical ionization length near DiMES (33). Consequently, we do not consider surface roughness ($\leq$ μm-scale α-variation) in this chapter. We track each particle until it redeposits, with redeposition events discriminated among prompt, local, and far mechanisms (Section 4.2). Meanwhile, we numerically calculate the first-ionization mean-free path λ_{s+} using the particle-averaged ballistic path length before first ionization. Similarly, we numerically calculate the first-ionization Larmor radius ρ_{s+} using the average $v_\perp$ at first ionization.

We apply an *ad hoc* perpendicular diffusion coefficient of 0.1, and calculate the L_{MPS} value according to Equation 2.21.

As noted in Figure 5.2, we are able to independently manipulate the L_{MPS} value at the relevant points in PYEAD and GITR; RustBCA, being a surface model, is sheath-blind in its calculation process. We consider a range of α parameters from 1-85°, avoiding the extremes of the α domain in order to circumvent arithmetic exceptions in the code. Our simulations will weigh greater emphasis on the shallow end of the α domain since these values are more likely to be relevant for the initial $\alpha < 5°$ engineering of PFC components in the divertor; we simulate $\alpha = 1$, 3, 6, 9, 15, 30, 60, and 85°. Each of these simulations are repeated for both D and He plasmas. Since T is a difficult substance to work with given its reactivity and associated health risks, current experiments largely use D-only plasmas as a proxy for research. Repeating our simulations for He plasma provides an obtuse stand-in for the way D experimental results can be expected to scale with D-T fuel. Of course, this crude model overlooks T-driven chemical erosion, but, as discussed in Section 3.2, we will leave such problems to other experts.

Lastly, we repeat each of the above sets of simulations for a range of magnetic field conditions. The chosen $|\vec{B}|$ values represent a range of important fusion devices at time of writing, from academic experiments to next-step facilities. In particular, we simulate a local magnetic field at DiMES for $|\vec{B}| = 0.7$ (CTH (57)), 2.25 (DIII-D), 5.0 (ITER), and 12.0 T (SPARC). Importantly, we should note that by changing the $|\vec{B}|$ and plasma species values, we are no longer considering the same plasma conditions reflected by our OEDGE model. We will continue to use the OEDGE conditions in Table 5.1 for the SOL in our model but with the caveat that these SOL conditions are not self-consistently ascribed. For this reason, we are incompletely modeling far redeposition in these simulations (beyond the specific example shown in Figure 4.9); instead, particles relegated to f_{far} may instead be thought of as far transport, meaning those particles positioned to be far redeposited but not distinguishable from losses into the core at this time. In this way, f_{far} should be comparable with Equation 4.7

and the ERO model of Figure 4.7. Now, we will step through the results of this set of simulations for each component of the net erosion physics.

5.2 Sensitivity of Gross Erosion to Pitch Angle α

Here, we will detail how C-on-W gross erosion is affected by changes to L_{MPS} with fixed plasma parameters, giving especial attention to how α affects the gross erosion outlook. As discussed in Chapter 3 and the previous section, gross erosion physics is captured within our workflow by the coupled PYEAD-RustBCA component.

5.2.1 Incident Ion Energy and Angle Distributions

We begin by discussing the incident C-EADs produced by PYEAD. As previously noted, the C^{1-2+} charge states dominate over the more positive C^{3-6+} abundance, so we expect them to dominate in the C-EAD. Neutral C^0 is present in the OEDGE simulation, but we will neglect its effect on gross erosion for simplicity. The C^0 will be unaffected by the electromagnetic forces within the sheath and simply provide a "floor" of low energetic (around the thermal velocity of Equation 3.9), azimuthally symmetric particles; hence, we do not anticipate C^0 to be affected by changes to α.

In Figure 5.3 we show histograms of the $E_{ii} - \theta$ distribution across changes to α in DIII-D, deuterium conditions. These simulations use $\boldsymbol{n_ions} = 10^5$, which gives good convergence in the distribution. We note that there is a strong two-peak distribution at shallow values of α which begins to fade as $\alpha \nearrow 90°$. At $\alpha = 85°$ we begin to see some of the computational limitations of the PYEAD model. Recall from Section 3.3 that we initialize the particles at 1% of the total $|\vec{E}|$ through the sheath, which at very steep α values means that the particles essentially start at the surface itself. As a direct consequence of this starting position, we are able to perceive individual gyro-orbit trajectories along the surface, which appear as overlapping bands at this

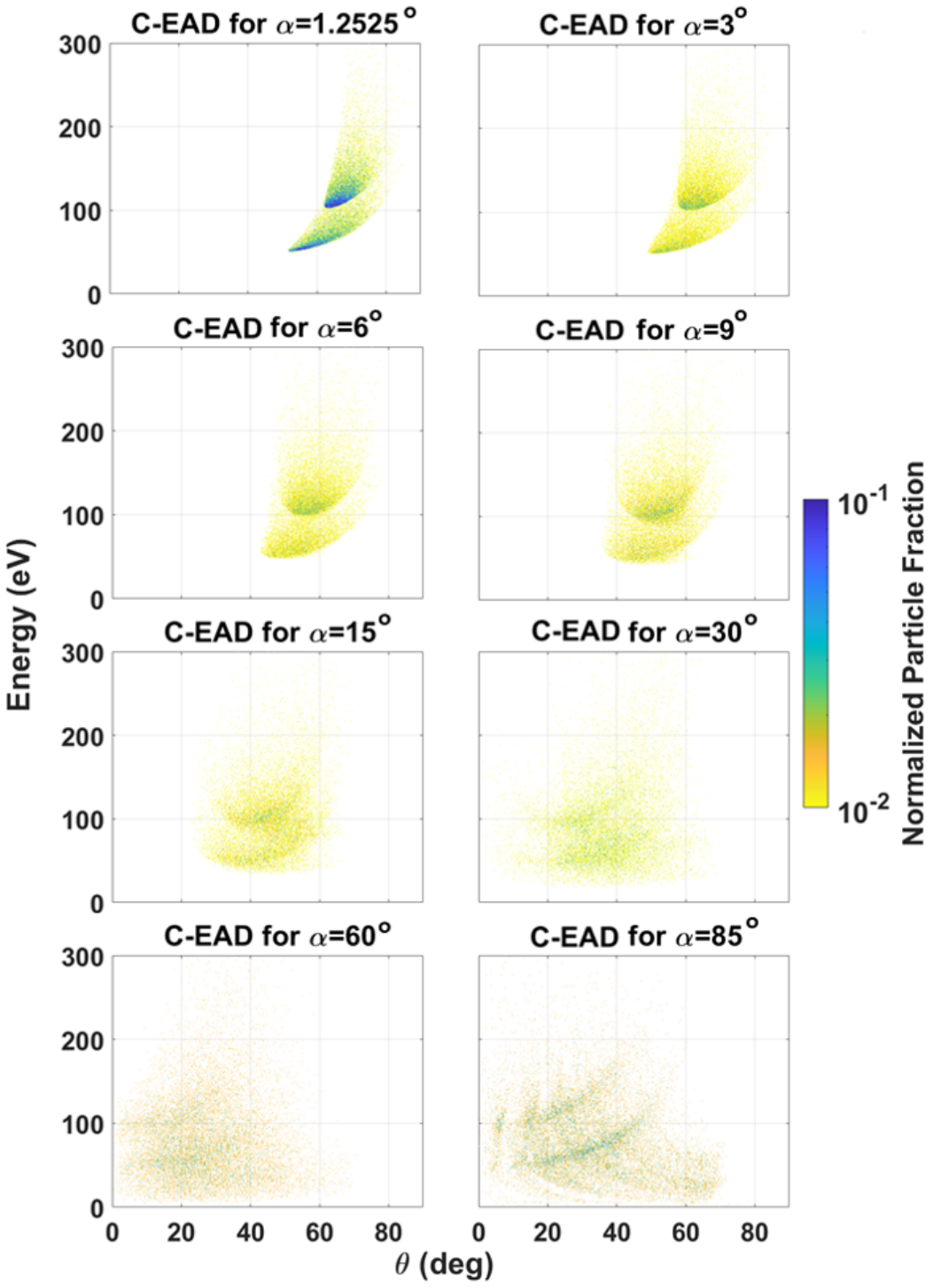

Figure 5.3: Incident C-EAD for $|\vec{B}| = 2.25$ T and D plasma across the full range of simulated α. Normalized particle fraction means particle count normalized to $E_{ii} - \theta$ bin size and total number of particles.

α in Figure 5.3; however, we believe this observation to be largely numerical as the author can find no observation of this phenomenon in literature experiments.

Meanwhile, we may readily explain the α-behavior of the two-peak distribution as a direct consequence of the dominance of C^{1-2+}, as predicted; the remaining charge states fade into the background. The peaks are highly localized where the sheath is thick (e.g. $\alpha = 1°$), which is easily explained by the longer time-of-flight these particles are subject to the strong electromagnetic fields of the sheath. At steeper angles (e.g. $\alpha = 60°$), the sheath is thin, and there is a reduce time-of-flight for electromagnetic forces to dominate the gyro-motion, leading to a more Gaussian particle distribution in $E_{ii} - \theta$ space; in other words, these distributions remain very similar to the initial particle distributions set by PYEAD. Along these lines it is worth noting that the overall C-EADs exhibit Thompson energy distributions that are two-peaked at shallow α and single-peaked at steep α; similarly, the θ distribution becomes more broad as $\alpha \nearrow 90°$. Figure 5.4 shows these 1-D integrated distributions along E_{ii} and θ for different α extremes. Although the $\alpha = 85°$ C-EAD is more noisy for the numerical reason previously discussed, the overall distribution continues these trends in α.

Due to the time-of-flight differences across α, we observe similar trends in the $E_{ii} - \phi$ distribution. Figure 5.5 shows the $E_{ii} - \phi$ histograms across α, which we may immediately note exhibits a similar two-peak distribution at shallow α that broadens and fades as $\alpha \nearrow 90°$. Unlike the θ case the ϕ distribution becomes more uniformly distributed as α becomes steeper, as expected. Overall, the changes to α have the largest effect of all the L_{MPS} variables considered on the various aspects of the C-EADs.

Now, we will briefly discuss the effects of the magnetic field magnitude and the plasma ion species on the C-EAD. The magnetic field magnitude has a slight effect with differing intensity on the C-EAD, depending on the sharpness of the $\vec{B}$-to-PFC pitch angle. At shallow α (e.g. $1°$), where the particles are subjected to sheath electromagnetic fields for the longest duration, the sharpness of the two-peaks

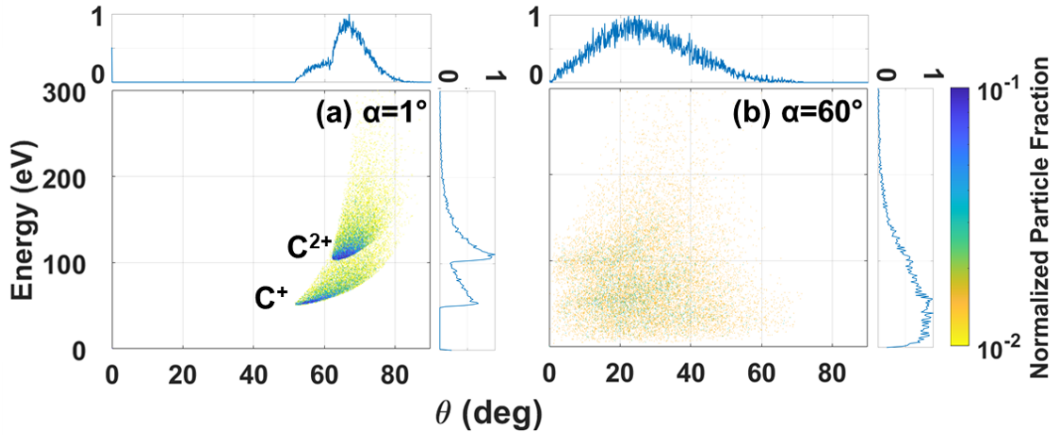

Figure 5.4: Incident C-EAD for $|\vec{B}| = 2.25$ T and D plasma at different α extremes ($\alpha = 1°$ in (a) and $\alpha = 60°$ in (b)), with integrated distributions in E_{ii} (right) and θ (top). Normalized particle fraction means particle count normalized to $E_{ii} - \theta$ bin size and total number of particles.

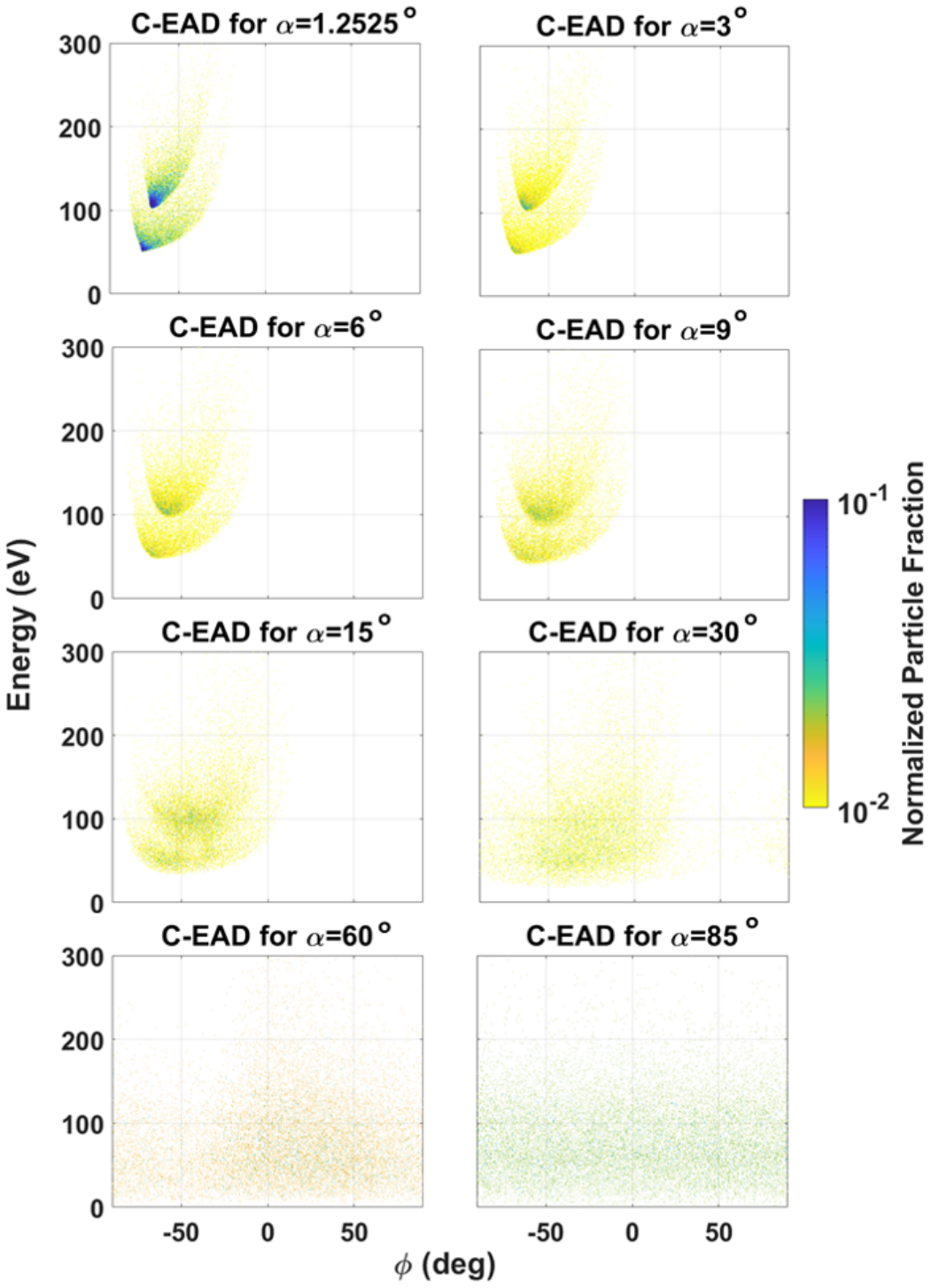

Figure 5.5: Incident C-EAD for $|\vec{B}| = 2.25$ T and D plasma across the full range of simulated α. Normalized particle fraction means particle count normalized to $E_{ii} - \phi$ bin size and total number of particles.

intensifies with the magnetic field strength. We may readily explain this trend with $|\vec{B}|$ by noting that the Larmor radii of these incident ions is inversely proportional to the magnetic field strength, so the particles in higher magnetic fields have a farther extended time-of-flight throughout the sheath. Consequently, the impact angles of the incident ions have a much narrower distribution. Conversely for sharp α (e.g. 60°), the shallowness of the sheath causes the strength of the magnetic field to have minimal impact on the trajectories of incident ions. Figure 5.6 shows the impact of the magnetic field strength on the $E_{ii} - \theta$ C-EAD at different extremes of the α parameter space and (a) 0.7, (b) 2.25, (c) 5.0, and (d) 12.0 T values of $|\vec{B}|$; note the difference between the distributions at (a) vs. (d) for the $\alpha = 1°$ extreme, which becomes inconsequential when $\alpha = 60°$. The trends for the $E_{ii} - \phi$ C-EADs are similar, as shown in Figure 5.7.

Lastly, Figure 5.8 shows the dependence of the C-EAD on the background plasma ion type. As we can see there, the two peaks at shallow α are less sharp in He plasma (b,d) compared to the D plasma (a,c), and there is a slight decrease in the overall θ as well in the He case. We may explain this trend by recalling that the plasma ion mass m_{ip} has an important effect on setting the total potential drop through the sheath (Equation 2.15); as a result, the He plasma has a slightly weaker electric field. The slightly weaker electric field leads to a more glancing θ value onto the surface and a broader peak structure overall for both θ and ϕ angles. On the other hand, there is very little change with the plasma ion species for sharp α values.

From these observations, we should note that the C-EAD is sensitive primarily to the $\vec{B}$-to-PFC pitch angle. There is a slight reduction in energy as $\alpha \nearrow 90°$ given the shortened sheath-duration of these particles' trajectories and a broadened peak in θ and ϕ for the same reason. Given what we have discussed in Chapter 3, we should expect the overall gross erosion to exhibit similar sensitivities across the L_{MPS} parameters considered. We will explore the validity of this claim in the next subsection.

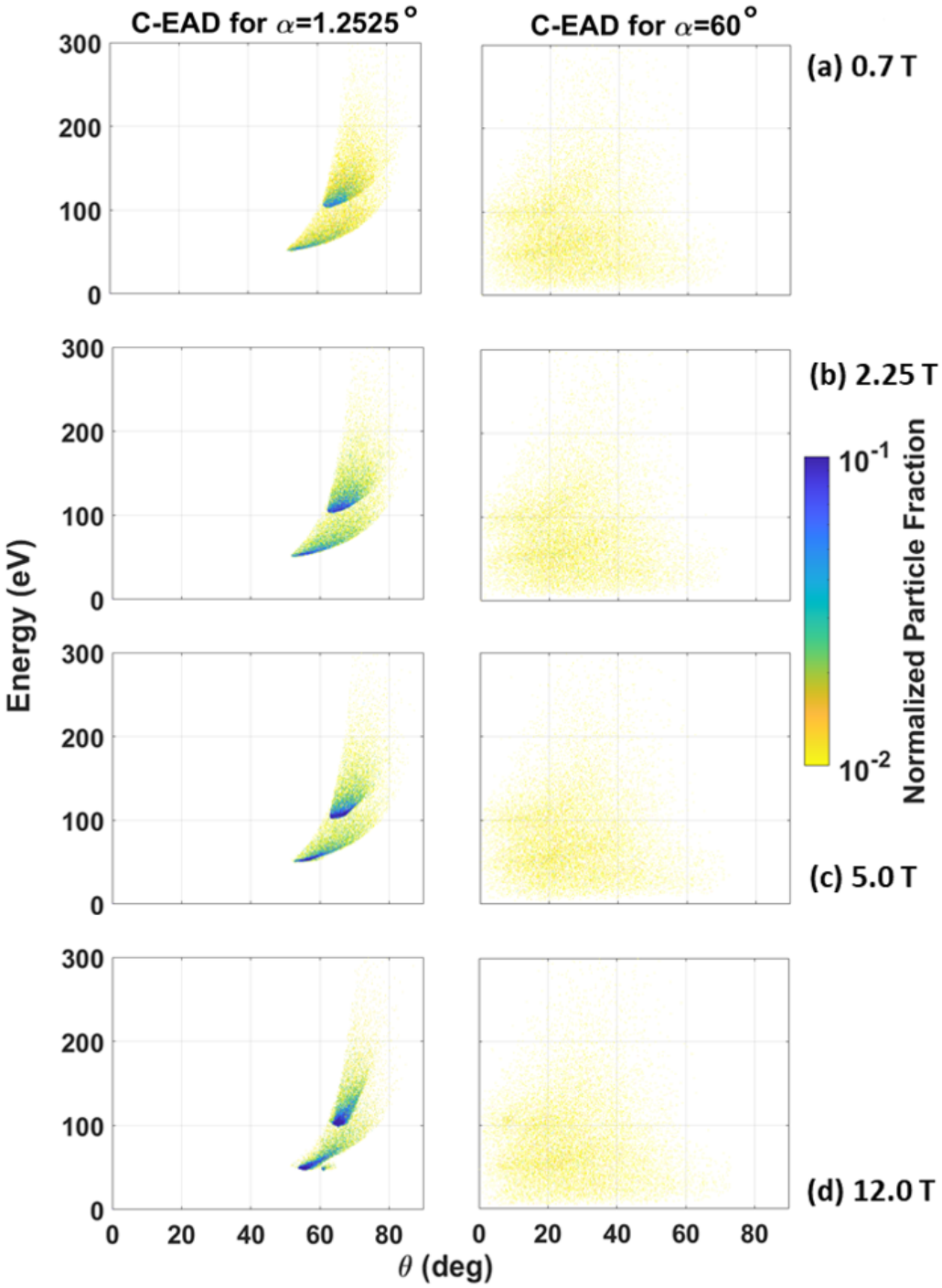

Figure 5.6: Incident C-EAD for D plasma at shallow and steep α across the full range of simulated $|\vec{B}|$. Normalized particle fraction means particle count normalized to $E_{ii} - \theta$ bin size and total number of particles.

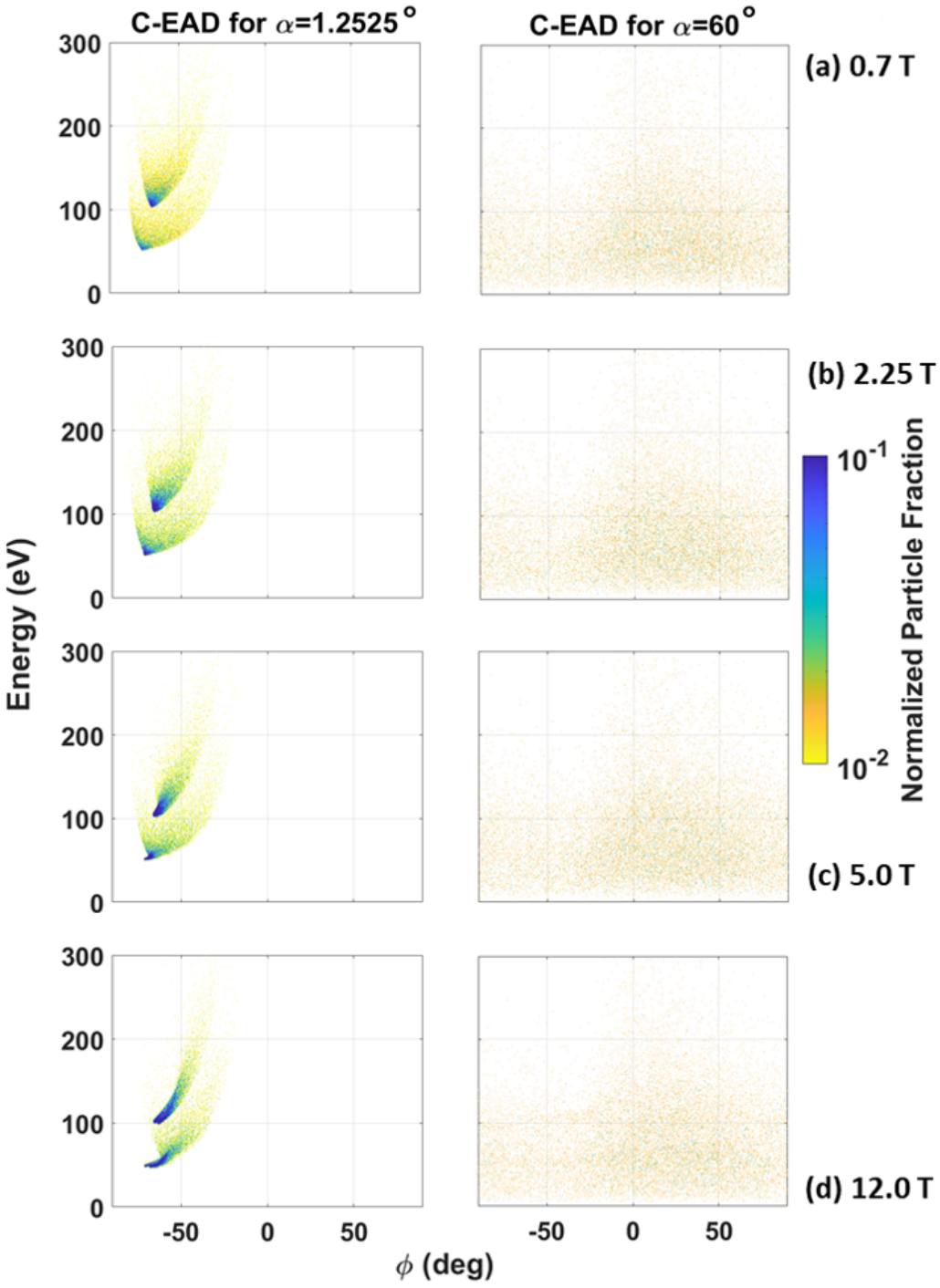

Figure 5.7: Incident C-EAD for D plasma at shallow and steep α across the full range of simulated $|\vec{B}|$. Normalized particle fraction means particle count normalized to $E_{ii} - \phi$ bin size and total number of particles.

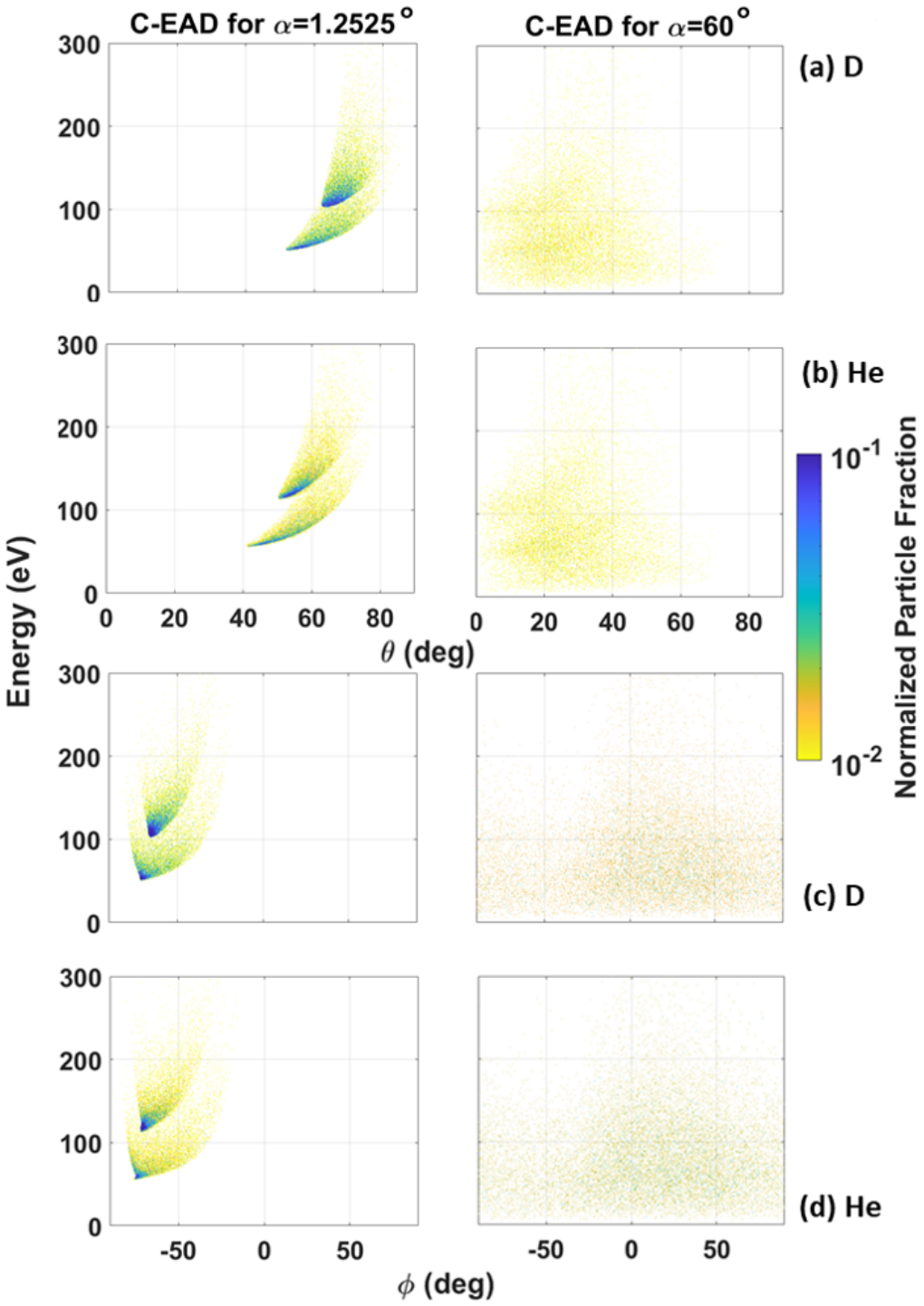

Figure 5.8: Incident C-EADs for D vs He plasma at shallow and steep α and $|\vec{B}| = 2.25$ T. Normalized particle fraction means particle count normalized to $E_{ii} - \theta$ (a-b) or $E_{ii} - \phi$ (c-d) bin size and total number of particles.

5.2.2 Sputtered Neutral Energy and Angle Distributions

Now, we will discuss the neutral tungsten W^0-EADs that we generate in RustBCA as a direct consequence of coupled C-EADs from PYEAD. We observe that the tungsten energy and angle distributions are primarily sensitive to the $\vec{B}$-to-PFC pitch angle, largely inheriting their sensitivity from the C-EAD model. Figure 5.9 shows representative $E_s - \delta$ histograms across the range of α values considered. We observe a Thompson-like distribution in energy across all values of α, as expected; the redeposition literature reviewed in Section 4.1 assumes this E_s distribution. This energy distribution has little, if any, change with the $\vec{B}$-to-PFC pitch angle, which is unsurprising, given the inertia of W compared to C. Nonetheless, our results show a distribution in both δ and the azimuthal sputtering angle that is highly sensitive to α, indicating that the cosine-δ and uniform-azimuthal assumptions in Section 4.1 could be incomplete.

Recall that a cosine-δ distribution has form $\sin(2\delta)$, which visually resembles a Gaussian centered at 45° with truncated tails when plotted. As may be seen in the 1-D integrated distributions of Figure 5.10, this distribution may be approximately correct at steep α, as exemplified by the $\alpha = 60°$ case shown; nevertheless, as $\alpha \searrow 0°$, the calculated δ distribution becomes increasingly skewed to a sub-cosine peak center. This shift corresponds directly with the sharp C-EAD peaks observed in the shallow α regime, which are largely shallow to the surface as well. Overall, the forward-scattering δ is as low as $\approx 25°$ at $\alpha = 1°$ and as high as $\approx 40°$ at $\alpha = 85°$. While a $\sim 15°$ difference may seem slight, it is a significant factor explaining the trend in the prompt-vs-local distribution in the next section.

Similarly, the azimuthal sputtering angle distribution becomes slightly skewed as $\alpha \searrow 0°$. This distribution becomes increasingly perpendicular to the magnetic field as α decreases but not as sharply peaked as the δ distribution. On the other hand, we see a near-uniform distribution in this angle as $\alpha \nearrow 90°$. Figure 5.11 includes example E_s-azimuthal histograms showing these trends; this phenomenon may provide a slight

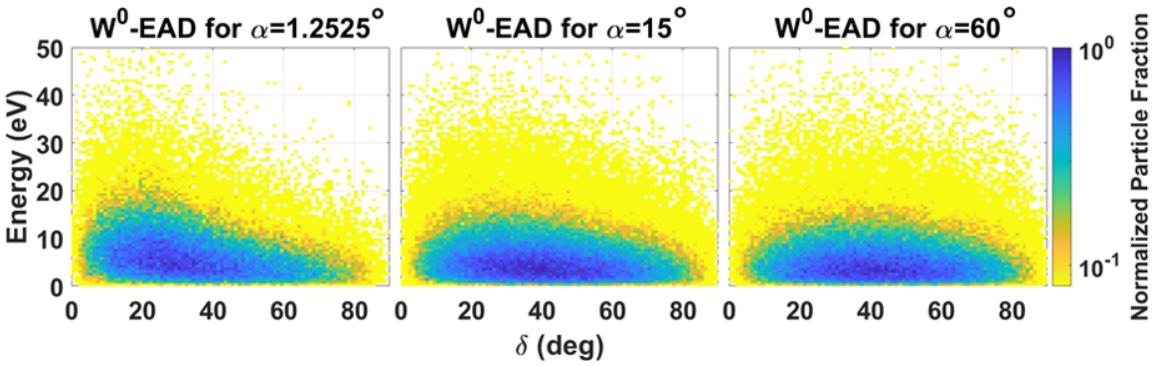

Figure 5.9: Sputtered W^0-EADs for $|\vec{B}| = 2.25$ T and D plasma across a representative subset of simulated α conditions. Normalized particle fraction means particle count normalized to $E_s - \delta$ bin size and total number of particles.

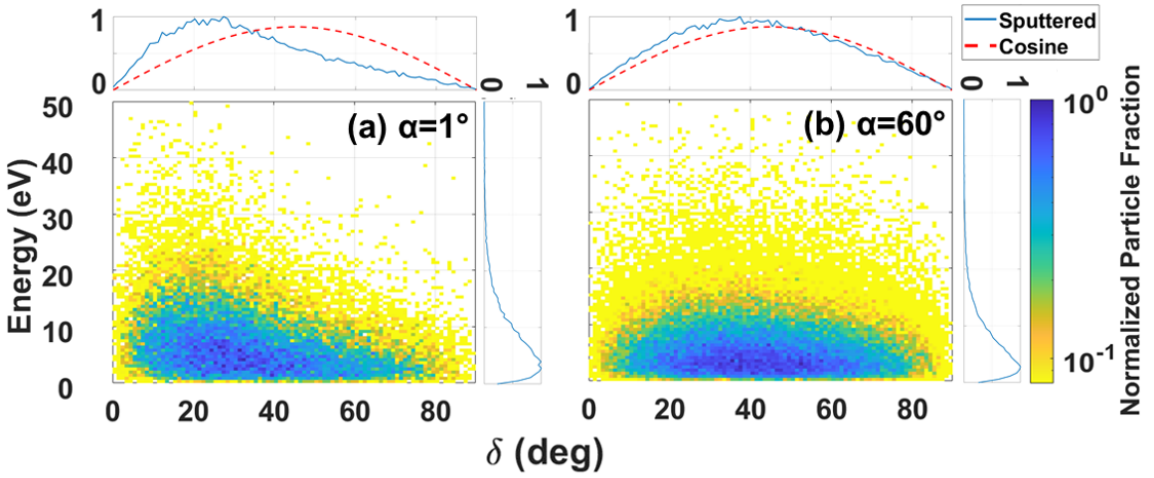

Figure 5.10: Sputtered W^0-EAD for $|\vec{B}| = 2.25$ T and D plasma at different α extremes ($\alpha = 1°$ in (a) and $\alpha = 60°$ in (b)), with integrated distributions in E_s (right) and δ (top). Normalized particle fraction means particle count normalized to $E_s - \delta$ bin size and total number of particles. Also shown is an analytic cosine distribution in δ, for comparison.

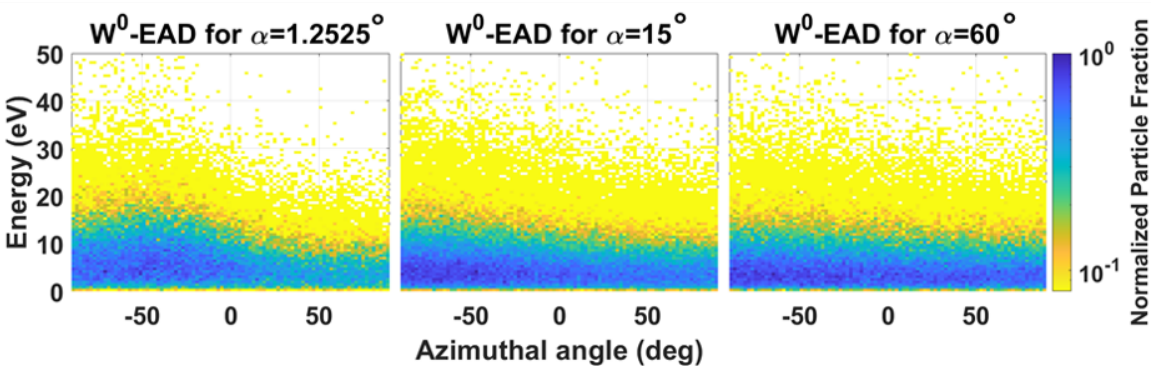

Figure 5.11: Sputtered W^0-EADs for $|\vec{B}| = 2.25$ T and D plasma across a representative subset of simulated α conditions. Normalized particle fraction means particle count normalized to E_s-azimuthal sputtering angle bin size and total number of particles.

increase in surface-scale redeposition, given that the average particle velocity is skewed in the direction of positive-ion gyro-motion (55).

To conclude this subsection, we will discuss the impacts of the magnetic field magnitude and plasma ion species on our W^0-EADs, which are essentially negligible compared to the impact of α. Figure 5.12 shows the changes to the $E_s - \delta$ distributions with $|\vec{B}|$; note that there is very little, if any, difference at either α extreme across the changes to the $\vec{B}$-field magnitude. The particle distribution for the azimuthal sputtering angle is similarly unaffected, as seen in Figure 5.13. This finding aligns with the theory in Chapter 3: Given the inertial difference between C and W, the most important parameters driving the sputtering will be in the high-energy tail of the C-EADs, which does not change significantly with $|\vec{B}|$.

Likewise, there is little change between the W^0-EAD in D vs He background plasma, shown in Figure 5.14. The largest changes (only a few degrees) occur as $\alpha \searrow 0°$ due to a slight shift in the peak centers of the incident C-EAD, as noted in the previous subsection. These shifts are barely noticeable in Figure 5.14 and, we will see, do not contribute much to the distribution of prompt-vs-local redeposition. In general, other factors determined by the two plasma species, such as drag forces partially setting the first-ionization mean-free-path, are probably a larger contributor to any redeposition differences we observe in the next section.

Finally, it is worth noting that there are differences across all changes to L_{MPS} in the sputtered yield, as expected (Chapter 3). However, we are primarily interested in fractional redeposition here, so we will overlook these features for now; we will discuss them in more detail in Chapter 6, where we will treat sputtered yield within a wider context of plasma-material parameters. With our gross erosion component concluded, we will turn our attention to the effect of α on the three mechanisms of redeposition outlined in Section 4.2.

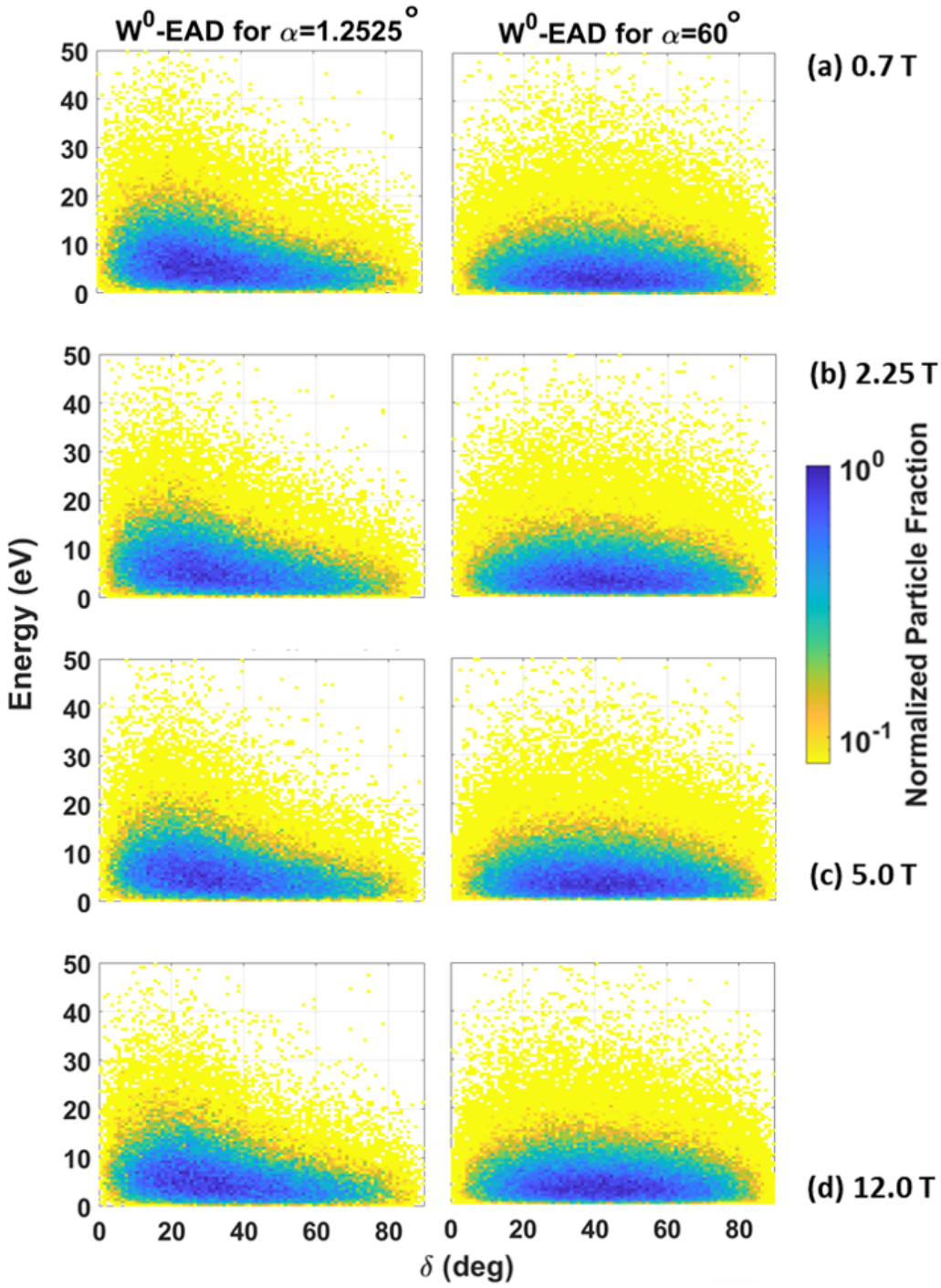

Figure 5.12: Sputtered-W^{0}EAD for D plasma at shallow and steep α across the full range of simulated $|\vec{B}|$, which appear ∼invariant. Normalized particle fraction means particle count normalized to $E_s - \delta$ bin size and total number of particles.

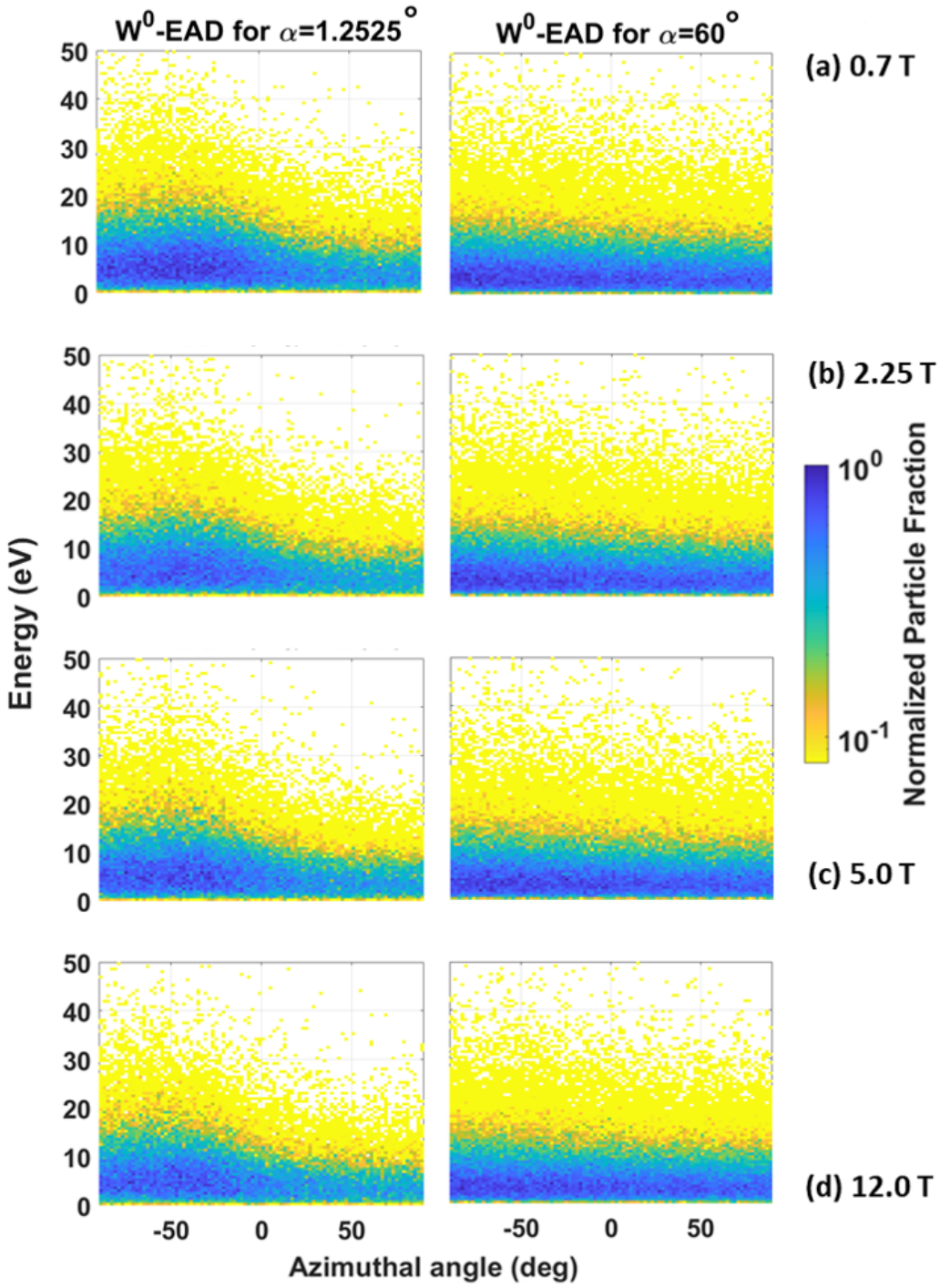

Figure 5.13: Sputtered-W^0EAD for D plasma at shallow and steep α across the full range of simulated $|\vec{B}|$, which appear ∼invariant. Normalized particle fraction means particle count normalized to E_s-azimuthal sputtering angle bin size and total number of particles.

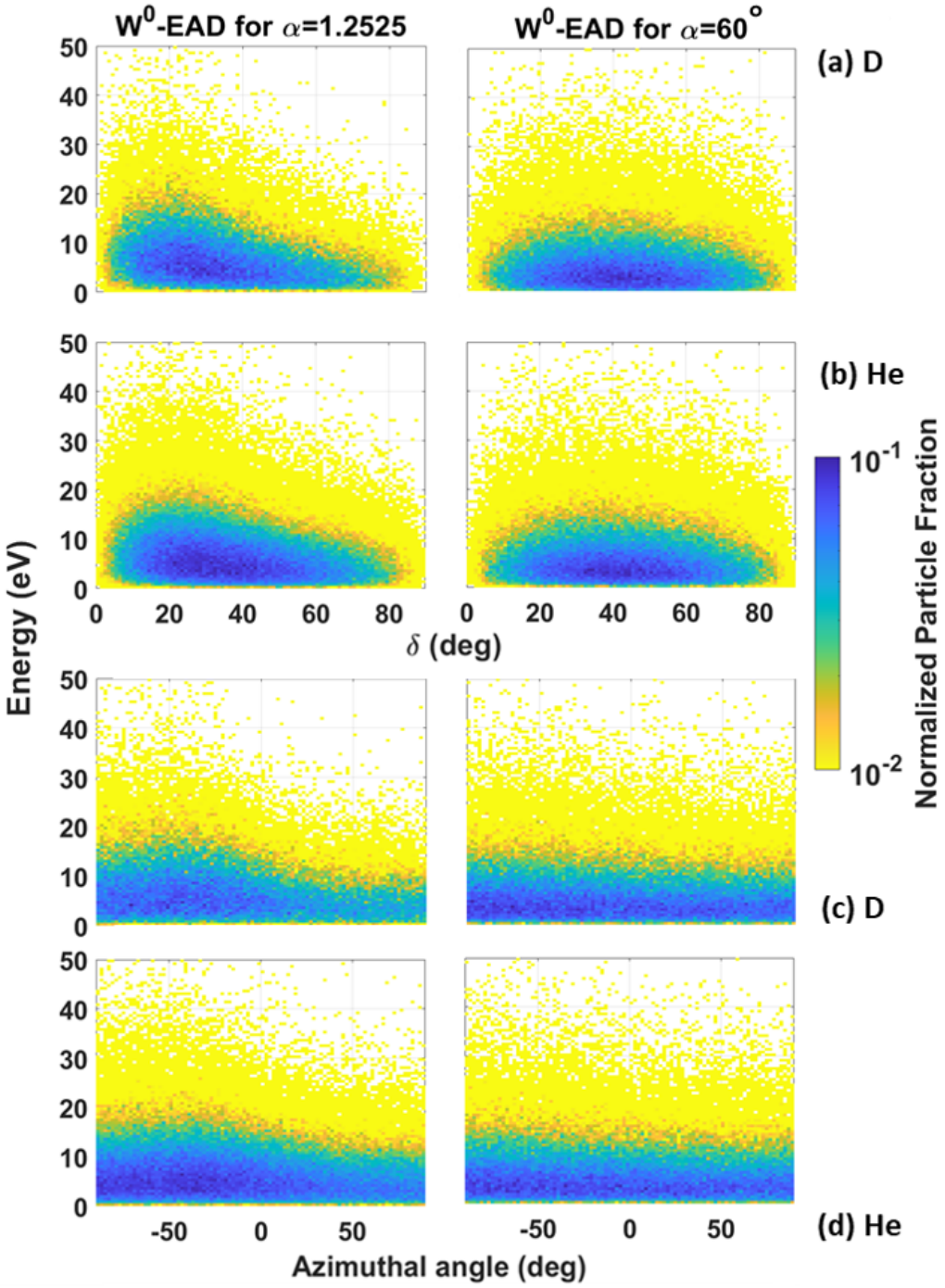

Figure 5.14: Sputtered W^0-EADs for D vs He plasma at shallow and steep α and $|\vec{B}| = 2.25$ T, which appear ∼invariant. Normalized particle fraction means particle count normalized to $E_s - \delta$ (a-b) or E_s-azimuthal sputtering angle (c-d) bin size and total number of particles.

5.3 Sensitivity of Redeposition to Pitch Angle α

We now turn our attention to how W redeposition is affected by changes to L_{MPS} with fixed plasma parameters, giving especial attention to how α affects the redeposition. As discussed in Chapter 4 and Section 5.1, we use GITR to determine the redeposition fractions of f_{prompt}, f_{local}, and f_{far} mechanisms, with f_{far} incompletely ascribing the physical far redeposition as defined in Section 4.2 due to our lack of self-consistent OEDGE simulations; rather, we may here think of the f_{far} delineated in Section 4.3 as far transport, such that these particles are positioned to redeposit, but their redeposition depends entirely on SOL physics that is incomplete in these simulations. In Figure 5.15, we present these redeposition fractions against p (Equation 4.4) as a result of the coupled outputs from RustBCA discussed in Subsection 5.2.2. We will step through the results for each mechanism separately.

5.3.1 Prompt Redeposition Sensitivity to α

Looking at subplot (a) of Figure 5.15, we see that f_{prompt} is fairly insensitive to the particular value of p; more important is the particular α value. As $\alpha \searrow 0°$, the f_{prompt} fraction plateaus to its maximum value for any fixed $|\vec{B}|$ and plasma ion species, which drops by as much as much as 60% as $\alpha \nearrow 90°$. The physics behind this trend is complex; we might first assume that differences in the observed W^0-EAD trends, particularly in forward-scattering δ, explain away the f_{prompt} trend with p, but there is more going on here. At shallow $\alpha \approx 0°$ the sputtered material has a forward scattering angle $\delta \approx 25°$ such that the neutrals travel ballistically very close to the surface at first. However, the gentle n_e gradient in this α regime causes such particles to ionize at a greater height z_{max} above the surface than they would under sharper δ values. Conversely, the ionization length λ_{s+} is shorter in the sharp α regime, where the n_e gradients are stronger. Thus, it is still the case that $z_{max} < 2\rho_{s+}$ for the majority of particles avoiding prompt redeposition in the sharp α limit; in other

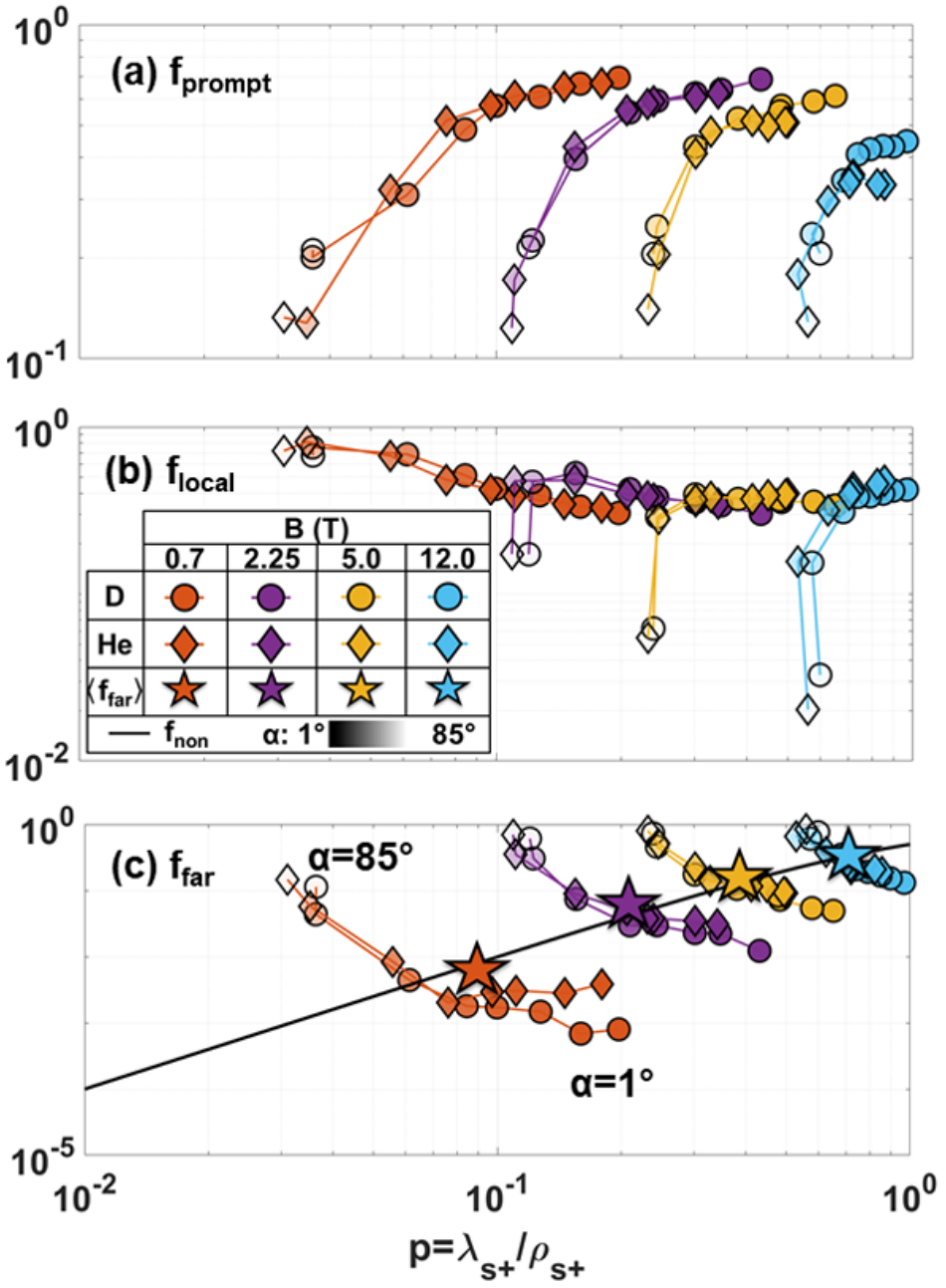

Figure 5.15: Prompt (a), local (b), and far (c) particle fractions as a function of p. In (c), α- and plasma-ion-averaged f_{far} ($\langle f_{far} \rangle$) is compared with f_{non} in Eq. 4.7.

words, trigonometric intuition from the δ distribution with α cannot explain away the decrease in prompt redeposition as $\alpha \nearrow 90°$.

To fully explain the f_{prompt} trend with α, we must recognize something that was overlooked in Chapter 4 and Section 5.1 about how changing the $\vec{B}$-to-PFC pitch angle affects the redeposition physics in Chapter 4. When $\alpha < 5°$, as engineered, the $\vec{B}$-field lines are roughly parallel to the PFC surface, meaning that the majority of the gyro-motion of W^+ is in the plane of the surface normal. However, if α is closer to 90°, the same gyro-motion is now mostly parallel to the PFC surface, meaning that the prompt mechanism is significantly less effective at returning these impurities. In fact, we would expect f_{prompt} to asymptote to 0 as $\alpha \nearrow 90°$, which we see in (a) of Figure 5.15. We illustrate this effect in Figure 5.16, where we show that δ and the L_{MPS} thickness also vary with α; the combination of all three variables drives the prompt redeposition trend in p.

On the other hand, there is very little variation in f_{prompt} against changes in $|\vec{B}|$ or the plasma ion species. With the magnetic field strength, we see a near-superficial shift in $p \propto |\vec{B}|$ that becomes more relevant in the $p \nearrow 1$ extreme. We may easily explain this phenomenon by noting that, although the Larmor radius ρ_{s+} decreases with increasing $\vec{B}$-field magnitude, a $p < 1$ implies that the majority of particles are still ionizing with $\lambda_{s+} < \rho_{s+}$. Thus, we expect to find the general invariance with p demonstrated by (a) in Figure 5.15. Only at very high $|\vec{B}| = 12$ T do we see a slight decrease in f_{prompt} with p as the Larmor radius becomes so small that a significant fraction of ionization events occur at a height incapable of geometric redeposition within a particle's first gyro-orbit. Recalling the invariance of the W^0-EAD with magnetic field strength, we do not expect gross erosion conditions to contribute to the f_{prompt} trend.

Similarly, we see that He plasmas have slightly shifted p values compared to D plasma, which likely result from changes in the ionization length caused to differences in the drag force and n_e drop. The slight increase in δ for He plasmas in Subsection 5.2.2 may also contribute to a shorter λ_{s+}. Regardless, there are few

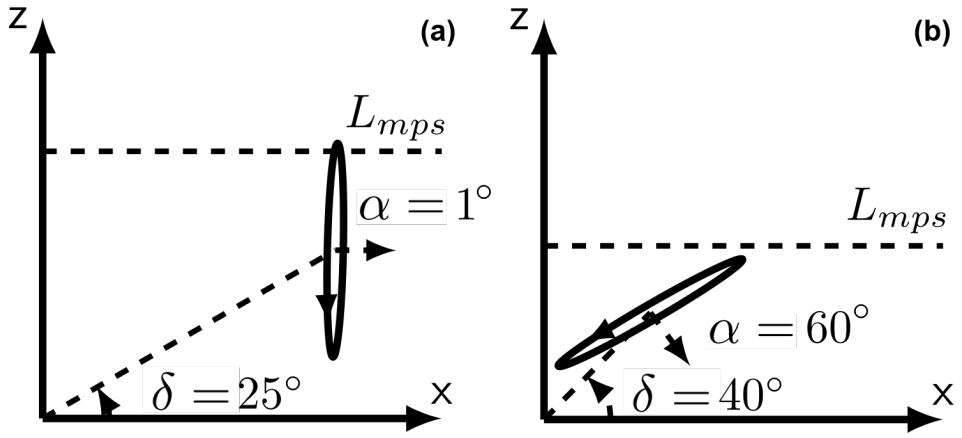

Figure 5.16: Illustrations (not to scale) of gyro-orbits avoiding prompt re- deposition for different α values and otherwise identical conditions. Shallow α conditions favor sheath escape (a), while sharp α conditions favor sheath containment (b), so long as magnetic field conditions yield sufficient L_{MPS} thickness.

changes to the f_{prompt} fraction besides these superficial ones to the p values. As $\alpha \nearrow 90°$, the differences between He and D plasmas become more noticeable due to the reduced Larmor radius in He plasma; here, W particles have a more difficult time redepositing in their first gyro-orbit, further lowering the prompt redeposition fraction at this α extreme. This problem compounds in the high magnetic field limit, resulting in a greater separation between D and He trends.

5.3.2 Local Redeposition Sensitivity to α

Looking at subplot (b) of Figure 5.15, we see that f_{local} produces an almost linear trend across p with some important exceptions. The general trend is largely affected by both the $\vec{B}$-to-PFC pitch angle and the magnetic field strength as the result of a complex interplay of physics. When α is shallow, the f_{local} fraction is generally at its lowest value for fixed $|\vec{B}|$ and plasma ion conditions, and the f_{local} fraction generally increases with few exceptions as α increases. The exceptions to this trend occur as α nears 90°, with a turnaround point that scales with the strength of the magnetic field. We may explain this phenomenon by considering three key components of the local redeposition physics. First, recall that, as noted in the previous subsection, the sub-cosine δ and weak n_e gradients as $\alpha \searrow 0°$ result in a longer ionization length for the average sputtered particle; importantly, this fact results in more neutrals ionizing closer to the sheath entrance than they otherwise would. As a result the particles not redepositing through the prompt mechanism are much more likely to escape into the SOL before they can be dramatically affected by sheath electrodynamics.

Next, as α increases, the forward-scattering angle increases, the n_e gradients increase, the ionization lengths shorten, and the plane of gyro-rotation becomes near-parallel to the PFC surface in accordance with Figure 5.16. Overall, these changes extend particles' duration within the sheath while decreasing the likelihood of prompt redeposition, as discussed in Subsection 5.3.1; these conditions cause the noted increase in local redeposition with α. Lastly, the sheath thickness L_{MPS}

decreases with increasing $|\vec{B}|$ (Equation 2.21) and α; at a point dependent on both of these variables, the sheath becomes so thin that $L_{MPS} < \lambda_{s+}$, meaning particles simply cannot ionize quickly enough to be affected by local redeposition physics. Consequently, we see turnaround points with α, dependent on the $|\vec{B}|$ strength, where the local redeposition now begins to drop significantly as the $\vec{B}$-to-PFC pitch angle increases.

With f_{local} interdependence on α and $|\vec{B}|$ explained, we last consider the effect of plasma ion species on local redeposition. In general, there is perhaps even less dependence between D and He plasmas across p for fixed α and $|\vec{B}|$ conditions. The largest differences manifest at sharp α and high $|\vec{B}|$, where an already thin sheath is even further reduced by shorter ρ_{ip} in He plasma.

5.3.3 Far Transport Sensitivity to α

Finally, looking at the whole of Figure 5.15, we see in subfigure (c) that the losses into the SOL directly correspond to the trade-off between prompt and local redeposition mechanisms. Recall that, because all particles are tracked until redeposition, $f_{far} = 1 - (f_{prompt} - f_{local})$. Hence, the sensitivities of f_{far} across L_{MPS} parameters are directly inherited from their f_{prompt} and f_{local} components. In particular, there is very little change with α in the $\alpha \searrow 0°$ limit under fixed $\vec{B}$ and plasma ion conditions, largely due to the invariance of f_{prompt}. However, as $\alpha \nearrow 90°$, the shortening of the ionization length and the rotation of the gyro-orbit plane result in an increase in particle losses to the far mechanism.

To summarize, particles are well positioned to redeposit through the prompt mechanism near $\alpha \approx 0°$ because the gyro-orbit plane is favorable for geometric intersection with the PFC surface. The particles that escape prompt redeposition are less likely to redeposit via the local mechanism because extended ionization lengths position them relatively close to the sheath entrance; they are more likely to be lost to the SOL and rely on the far mechanism to redeposit. As α increases, the

likelihood of prompt redeposition decreases with the rotation of the plane of gyro-orbit; nonetheless, this increased motion parallel to the PFC, in combination with shortening ionization lengths, leads to an increase in local redeposition. The decrease in f_{prompt} and increase in f_{local} are not perfectly balanced, resulting in a slight increase in far losses; this effect is exacerbated when the sheath becomes too thin for any local contribution. The exact α where f_{local} diminishes depends strongly on $|\vec{B}|$, but the regime is typically present by the time $\alpha \approx 90°$ in our scan. Meanwhile, although α and $\vec{B}$ have a strong, interdependent effect on the prompt-vs-local trade-off, the relevant range of plasma ion species has a minimal effect on the f_{far} fraction. Although we have used a very crude model of D+T conditions, this result continues to suggest that discoveries about high-Z net erosion in D conditions should be good predictors of D+T net erosion under identical plasma regimes.

In subfigure (c) of Figure 5.15, we also compare f_{far} with the theoretical non-redeposited fraction f_{non}, defined with respect to p in Equation 4.7. We can readily see that there is significant deviation from this trend at the extremes of α; nevertheless, the f_{far} average over both α and plasma ion species at fixed $|\vec{B}|$, designated $\langle f_{far} \rangle$, agrees strongly with the f_{non} prediction. The agreement speaks highly of p as an important metric for predicting redeposition trends, despite the fact that f_{non} is a relatively simple model with incomplete sheath physics. Conversely, the deviations from this analytic trend are as high as two orders of magnitude, which could be devastating to reactor performance. Therefore, we need a revised prediction of f_{far} losses that better accounts for the α-driven physics of net erosion. We will make our first attempt to do so in the next section.

5.4 Refinement of Predictive Net Erosion

In Section 4.1 we presented two redeposition predictions of emerging interest in the current literature: a prediction against $p = \lambda_{s+}/\rho_{s+}$ and a prediction against $\hat{\lambda} = \lambda_{s+}/L_{MPS}$. We have already seen that the trend in $p \propto |\vec{B}|$, while surprisingly

useful, needs further corrections to account for the full α-driven physics of net erosion. As a first attempt to include these effects, we might consider $\hat{\lambda} \propto |\vec{B}|/\cos(\alpha)$.

In Figure 5.17 we show a comparison of our f_{far} results from Section 5.3 with the ERO trend with $\hat{\lambda}$ from Section 4.1. We first try to recapture the ERO dataset using our GITR model. In subfigure (a), we show a new simulation dataset using only GITR; this simulation removes the PYEAD-RustBCA component from the Figure 5.2 workflow and replaces it with uniform sampling of an analytic Thompson-E_s, cosine-δ, and uniform azimuthal sputtered angle W^0-EAD, as assumed in the original work by Guterl (53). As shown we are able to get good agreement with the ERO model data, but only in the sharp α limit. The residual between our data and ERO depends on the L_{MPS} parameter but may be as large as two orders of magnitude in some cases at the $\alpha \approx 0°$ extreme. Here, f_{far} variation with α is exclusively limited to the effect of the rotation of the gyro-orbit plane.

Given that the original work assumed a small $\vec{B}$-to-PFC pitch angle, it is surprising at first that we should find stronger agreement in the sharp angle regime. Nonetheless, the ERO paper notes that its $\hat{\lambda}$ trend is sensitive to the choice of upper cut-off energy used when sampling the Thompson distribution in that work (53). Here, in order to facilitate direct comparison with our numerical W^0-EAD results, we have used a Thompson model that is similar to the full PYEAD-RustBCA-GITR energy profile found in Section 5.3. Theoretically, the ERO simulation could be reworked to match these cut-off energies and find better agreement with our data in the $\alpha \searrow 0°$ limit; however, any such agreement would only cause the large residual to shift to the sharp α extreme. Ultimately, the α regime where we have good agreement with the ERO model is not critical for this level of comparison. Much more important are the facts that (1) we are able to reproduce the ERO result in some α limit and that (2) we see a deviation of up to two orders of magnitude from the $\hat{\lambda}$ trend when accounting for the interdependent effects of α.

Meanwhile, in subfigure (b) we show our simulation results from Section 5.3 against the $\hat{\lambda}$ parameter; these simulations reintroduce the PYEAD-RustBCA

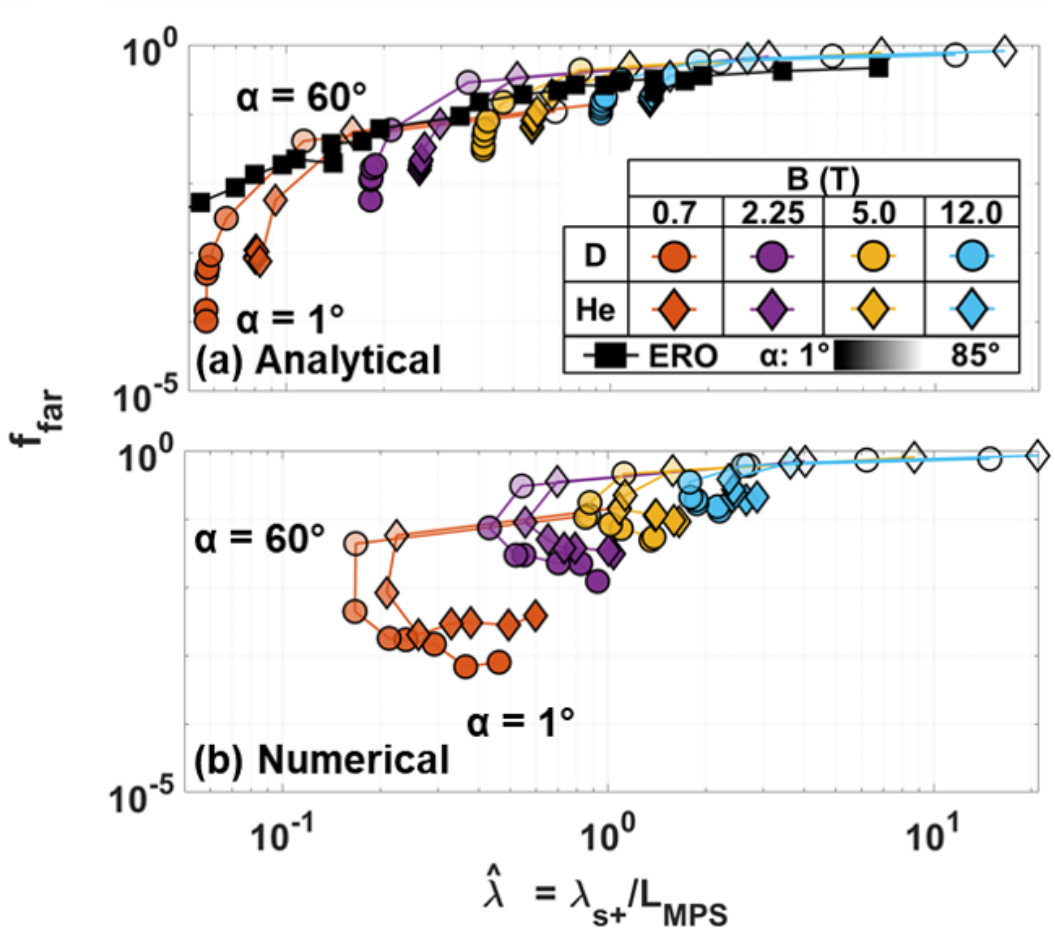

Figure 5.17: Far transport fraction vs $\hat{\lambda}$, with comparisons to the ERO model in $\hat{\lambda}$ shown in Figure 4.7. We show results for the analytic (a) and numerical (b) treatments of W^0-EADs, as discussed in the text.

coupling. As we can see by comparing this data with subfigure (a), the α-driven impact on gross erosion and underlying W^0-EAD has a large impact on both the $\hat{\lambda}$ value and the f_{far} contribution to net erosion. This effect is particularly important as $\alpha \searrow 0°$, where the λ_{s+} elongation results in ∼stagnant f_{far} against $\hat{\lambda}$. Interestingly, the $\hat{\lambda}$ framing offers a clear view of the prompt-vs-local redeposition trade-off discussed in Subsection 5.3.3: Under fixed $|\vec{B}|$, the f_{far} trends begin to wrap around themselves as prompt redeposition decreases and local redeposition increases then decreases for sharper $\vec{B}$-to-PFC pitch angles. While the clearer trade-off is nice in this representation, the over-plotting of our dataset shows that $\hat{\lambda}$ is also incomplete as a predictor of net erosion.

As an important aside, our calculation of λ_{s+} is entirely numerical; we track a subset of neutrals and bin their traveled distance when they first ionize. On the other hand, the simulations in Section 4.1 typically use lookup tables of λ_{s+} based on sheath-entrance n_e and T_e conditions, which assume Thompson-E_s, cosine-δ, and uniform azimuthal sputtering angle distributions. For example, the ERO study with which we are contrasting our results defines a characteristic velocity $v_b = \sqrt{2E_B/m_s}$ and assumes $\lambda_{s+} = v_b \tau_{iz}$, where τ_{iz} is the tabluated ionization time (53). By comparing the subfigures of Figure 5.17, we may readily see that fine structure in sputtered neutral EADs can have a significant effect on λ_{s+}. In principle, the numerical approach we employ here is a refined estimate of overall λ_{s+} values.

Now, we have shown that, while a step in the right direction, $\hat{\lambda}$ is as incomplete as p for a metric of redeposition; these models do not include the effects of α on gross erosion, and, even when these contributions are ignored, they do not fully account for effects such as rotation of the gyro-orbit plane when sharper α are present. These discrepancies are significant within the range of L_{MPS} parameters considered, causing up to two orders of magnitude difference from current predictive models. A refined redeposition model needs to account for the complex interplay between the magnetic field and the $\vec{B}$-to-PFC pitch angle; it should also keep prompt, local,

and far redeposition mechanisms heuristically distinct because the prompt-vs-local trade-off sets the f_{far} contribution and is driven by these α-vs-$|\vec{B}|$ conditions.

As a first attempt to incorporate all of these physics considerations, we show a two-variable refinement of f_{far} predictions using the p and α parameters in Figure 5.18. We choose p as a metric rather than $\hat{\lambda}$ because, although both variables contain a hidden α dependence within λ_{s+} (Equation 2.2), L_{MPS} is more explicitly dependent on α and we do not want to double-count its contribution. As shown slices along α reveal the different sensitivities of f_{prompt} and f_{local} fractions to $\vec{B}$ and α, which together determine the f_{far} fraction. To summarize, prompt redeposition is most dependent on the $\vec{B}$-to-PFC pitch angle only; local redeposition is most dependent on both the $\vec{B}$-to-PFC pitch angle and the $\vec{B}$-field magnitude; and far transport inherits each of these dependencies through the prompt-vs-local trade-off. In this way, α is the most important parameter (among the varied parameters setting the sheath thickness) in determining sheath particle losses.

To conclude this section, we have considered the total, interdependent effect of α, $|\vec{B}|$, and the plasma ion species in determining the prompt, local, and far redeposition fraction. We have seen that a refined model, such as the one shown in Figure 5.18, is needed to completely capture these dependencies. While this refinement is an improvement, it is important to emphasize that our workflow has only considered three of the many plasma and material parameters that determine net erosion. Our next step will be to contextualize these results within the full set of PMI parameters, which we will undertake in the next chapter.

5.5 Executive Summary

- Experimental evidence suggests that the magnetic-field-to-first-wall pitch angle, α, could vary significantly at the micro (nm-μm) and macro (mm-cm) scale over reactor-relevant lifetimes.

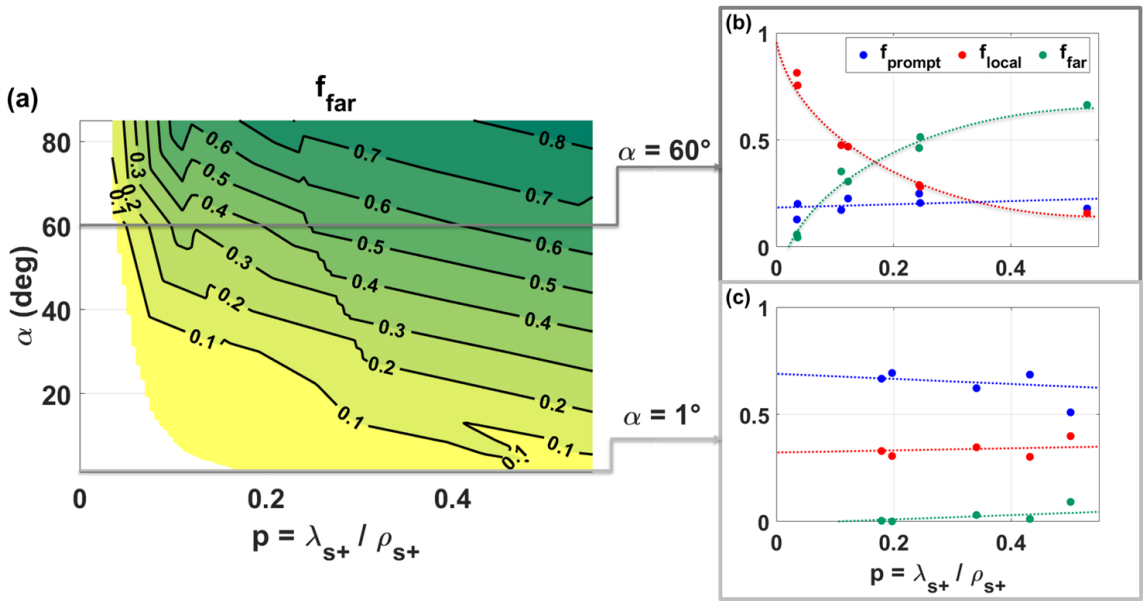

Figure 5.18: Far transport fraction as function of p and α (a). Slices $\alpha = 60°$ (b) and $\alpha = 1°$ (c) are shown, showing different f_{prompt} vs f_{local} scaling.

- Changes to α affect the sheath, which affects the entire net erosion process for high-Z materials.
- A coupled workflow using PYEAD-RustBCA-GITR determines the importance of α to net erosion in the context of other sheath parameters (i.e. the magnetic field magnitude and the plasma ion species) while holding the background plasma fixed.
- The distribution of the sputtered forward-scattering angle, δ, is over-predicted by a cosine model at shallow α.
- The δ distribution, the plane of gyro-rotation relative to the material surface, and the sheath thickness complexly determine the prompt-vs-local redepositon fraction:
  - Prompt redeposition is determined by α.
  - Local redeposition is determined first by α and then by the magnetic field strength.
  - Far transport inherits the above dependencies from the prompt-vs-local trade-off.
- The pitch angle α is the most important parameter determining redeposition fractions of the variables considered, particularly at steep pitch angles.

Chapter 6

An Uncertainty Quantification of Net Erosion Trends

6.1 Motivation and Methodology

In the previous chapter, we observed that model refinement of the working redeposition theory is necessary in order to incorporate the $\vec{B}$-to-PFC pitch angle's effect on net erosion; these angles could evolve significantly over reactor relevant lifetimes through heat damage and other stresses at both the micro-structural and macro-structural levels. The $\vec{B}$-to-PFC pitch angle α primarily influences net erosion physics through changes to the sheath structure; for this reason Chapter 5 examined the influence of various parameters determining sheath structure on net erosion, holding plasma conditions constant at the sheath entrance. From this study we found that α was the most important parameter in determining prompt-vs-local redepositon and setting material losses into the SOL.

While the work in Chapter 5 is a great first step, we have only found α to be so important within the context of one model and three PMI parameters of interest; even though α, $|\vec{B}|$, and the plasma ion species are each important parameters to consider, Chapters 3 and 4 show that a much wider range of parameters affect

both gross erosion and redeposition. This contextualization brings us back to the fundamental question of this dissertation (Section 5.1): **What are the optimal PMI parameters that maximize high-Z redeposition within the sheath (i.e. surface-scale PMI) and minimize reactors' dependence on SOL processes (i.e. global-scale PMI) to reduce high-Z net erosion?** To answer this question we need to understand the interdependent sensitivity of the results we have already shown, reframed within a broader PMI context.

One approach to assessing the sensitivity of the Chapter 5 results could be interchanging components of the workflow with new modules and seeing if the net erosion dramatically differs overall. We have already seen such an example in Section 5.4, when we replaced the PYEAD-RustBCA component with commonly assumed analytic distributions; in doing so, we saw that our numerically generated W^0-EADs, which in theory are a refinement on the analytic approximations, result in dramatically different far transport. As another example of this technique, we show a reproduction of the Figure 5.15 simulations in Figure 6.1, now using a different, incorrect density model. We erroneously generated this dataset early in the work of this dissertation while working on the GITR modifications discussed further in Section 4.3; there, we accidentally fit both the electron and ion densities to a linear drop through the sheath:

$$n_e(z) = n_{ip}(z) = n_{se}\left(\frac{\psi(z)}{\psi_w}\right) \tag{6.1}$$

Of course, the accepted density drops are actually exponential (Equation 2.2) and rational (Equation 4.13), respectively, which are represented in the datasets discussed in Chapter 5. We see that, although the physics processes and trends discussed throughout that chapter are largely the same, the p parameter range compresses and the redeposition fractions themselves differ by up to an additional order of magnitude from the f_{non} fraction with this incorrect model. This example demonstrates some of

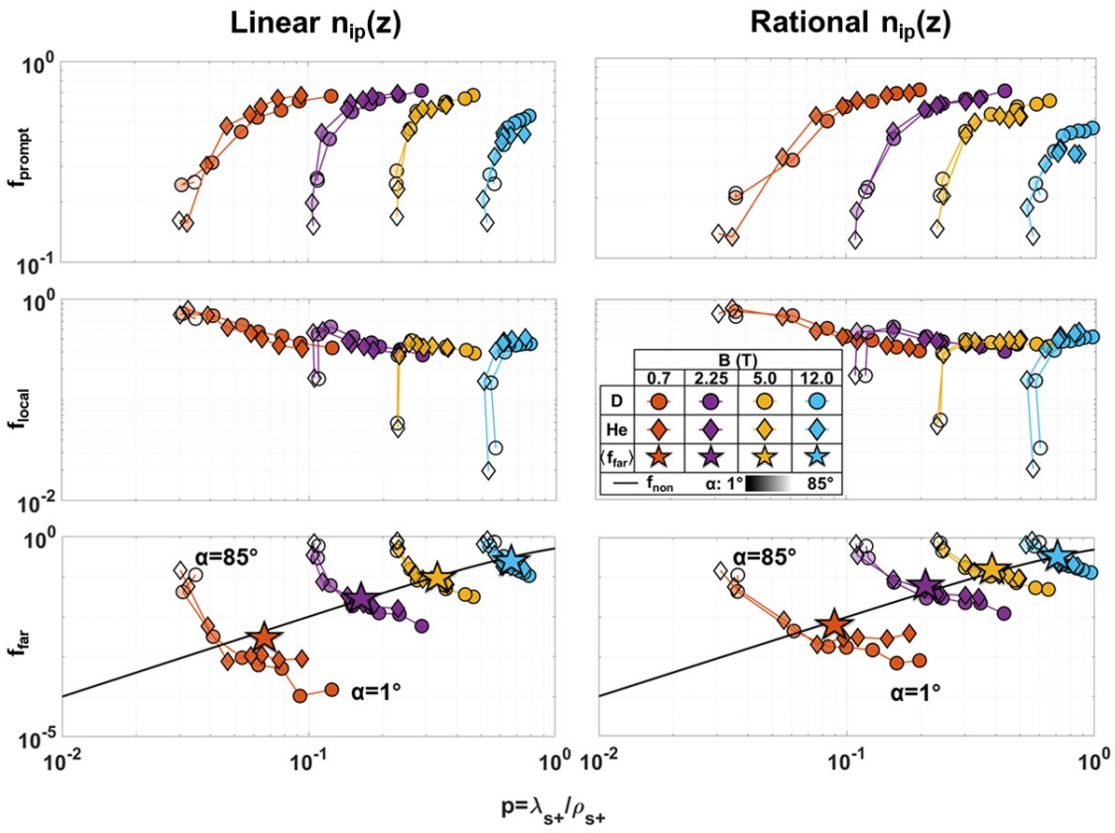

Figure 6.1: Prompt, local, and far particle fractions as a function of p with an incorrect (linear) density model, discussed further in the text, in comparison with the correct (rational) density model. For the far fraction, α- and plasma-ion-averaged f_{far} ($\langle f_{far} \rangle$) is compared with f_{non} in Eq. 4.7. Note that the subfigures associated with the rational model are a direct reproduction of Figure 5.15, provided again here to facilitate comparison with the linear model.

the impacts that sheath model assumptions have on our ability to predict redeposition physics.

Although iteratively changing components of our model can illuminate the ways assumptions influence our conclusions, we have justified throughout this dissertation that our overall workflow represents an up-to-date understanding of the relevant PMI processes. We have good agreement with pre-existing theory (23; 84; 53), and our new contributions provide a clear underlying physics narrative, suggesting an incremental improvement on previous work (Section 4.1). For these reasons we are more interested in the sensitivity of our workflow to itself rather than to the introduction of new components; that is, we will instead assess sensitivity by holding our full model as fixed and varying its input conditions. This technique more readily lends itself to applying our results towards experimental validation and engineering optimization, which we will discuss further in Chapter 7. As an aside we will further discuss exploring model sensitivity through workflow modification in Chapter 9.

Here, we hope to understand two questions: how chaotic is our PYEAD-RustBCA-GITR model and which parameters drive net erosion trends? By the first question we are asking whether we can make reasonable predictions with our workflow towards real-world experiments or if small changes to input conditions result in major changes to net erosion. By the second question we are asking which PMI parameters have the greatest influence over net erosion overall, assuming that our model is reliable for physics predictions. One approach to answering these questions is the use of Sobol' sensitivity indices (106; 114; 59). This technique is a variance-based method of uncertainty quantification, meaning it rigorously decomposes the variance in each output parameter into dependencies upon the variance in each input parameter; for example, we can use it to quantify the impact of α-variation on net erosion in comparison with more-studied PMI parameters like n_e and T_e. Indeed, this standard approach is already applied to net erosion codes (98), including GITR (132).

The general approach to Sobol' indices is as follows (106). We begin with a generic, N-dimensional variable $\vec{X}$, normalized to be within the hypercube $[0,1]^N$,

and a dependent variable $g(\vec{X})$ for some integrable functional process g. Note that $g(\vec{X})$ may be decomposed into:

$$g(\vec{X}) = g_0 + \sum_{i=1}^{N} g_i(X_i) + \sum_{i=1}^{N}\sum_{j=1}^{i-1} g_{ij}(X_i, X_j) + ... + g_{123...N}(X_1, X_2, X_3, ..., X_N) \quad (6.2)$$

where each g_ξ is a function of $\vec{X}$ index X_ξ. We may freely assume an ANOVA decomposition, here meaning that each $\int_0^1 g_{i_1..i_s}(X_{i_1}, ..., X_{i_s})dX_k = 0$ for all $k = i_1, ..., i_s$; so that the variance in g is well-defined, we will further assume without proof that g is square integrable. The first condition further implies that each component is orthogonal over the unit hypercube; hence, we have:

$$\begin{aligned}
\mathrm{Var}(g(\vec{X})) = \mathbb{E}[(g(\vec{X}) - \mathbb{E}[g(\vec{X})])^2] = \mathbb{E}[(g^2(\vec{X})] - \mathbb{E}[g(\vec{X})]^2 = \\
\int_0^1 g^2(\vec{X})d\vec{X} - g_0^2 = \int_0^1 \left[g_0 g(\vec{X}) + \left(\sum_i^N g_i(X_i) \right) g(\vec{X}) + ... + \right. \\
\left. g_{123...N}(X_1, X_2, X_3, ..., X_N) g(\vec{X}) \right] d\vec{X} - g_0^2 = \\
\int_0^1 g_0^2 d\vec{X} + \int_0^1 g_1^2(X_1)d\vec{X} + ... + \int_0^1 g_{123...N}^2(X_1, X_2, X_3, ..., X_N)d\vec{X} - g_0^2 = \\
\sum_{s=1}^{N} \sum_{i_1<i_2<...<i_s}^{N} \int_0^1 g_{i_1...i_s}^2(X_{i_1}, ..., X_{i_s})dX_{i_1}...dX_{i_s} \quad (6.3)
\end{aligned}$$

Thus, we may recall the assumptions of an ANOVA decomposition and note that we have decomposed the variance of g into the sum of each of its components' partial variances. The ratio of each component to the total variance is called that component's global sensitivity index.

We can use this decomposition to further define two important Sobol' indices that ascribe g's sensitivity on a given X_i input (114). The first is the first-order sensitivity index S_i, defined as

$$S_i = \frac{\int_0^1 g_i^2(X_i)dX_i}{\mathrm{Var}\left(g(\vec{X})\right)} \quad (6.4)$$

which isolates the model sensitivity to the X_i variable taken alone. Note that this definition is just the global sensitivity index of the g_i terms. While this information is useful, it is often the case that X_i's interdependent contribution with other variables is also important; we have already seen an example of this concern in practice when discussing the interdependent effects of α and $|\vec{B}|$. Consequently, we will not use the first-order sensitivity index here.

The second important Sobol' index is the total-effect sensitivity index S_{Ti}, defined as

$$S_{Ti} = 1 - S_{\sim i} \tag{6.5}$$

where $S_{\sim i}$ is the sum of all global sensitivity indices that are not indexed to variable X_i. In other words, S_{Ti} is the sum of S_i as well as all other global sensitivity indices for X_i; therefore, while $\sum_i S_i \leq 1$, $\sum_i S_{Ti} \geq 1$ because this sum double-counts the mixed terms. To emphasize, S_{Ti} includes the interdependent contributions of X_i with other variables; for our purposes the total-effect index is the correct choice.

While Sobol' indices are useful to our problem, it is not obvious how to derive an ANOVA functional form like Equation 6.2 for our coupled workflow. Thankfully, we may estimate S_{Ti} using Monte Carlo techniques (114); for two M-sized simulation samples (denoted A and B) we estimate

$$S_{Ti} \approx 1 - \frac{\sum_{m=1}^{M} g(X_1^{m,A}, ..., X_i^{m,A}, ..., X_N^{m,A}) g(X_1^{m,A}, ..., X_i^{m,B}, ..., X_N^{m,A}) - \left(\sum_{m=1}^{M} g(\vec{X}^{m,A})\right)^2}{\sum_{m=1}^{M} g^2(\vec{X}^{m,A}) - \left(\sum_{m=1}^{M} g(\vec{X}^{m,A})\right)^2} \tag{6.6}$$

where $X^{m,*}$ denotes the mth data point in sample $*$. As usual the error of this approximation is the size of the $M+1$ term. Note that we need a large number M of data points in order to have S_{Ti} convergence; moreover, we need $M(N+2)$ simulations to make the S_{Ti} calculation.

Because of the large number of required simulations, we must be clever about how we sample the parameter space of our PMI workflow. Blindly sampling M total data points for the whole workflow may miss key physics regimes; on the other hand, brute forcing one sample from each of D subdivisions across each of N parameters results in $M = D^N$ required simulations per dataset, and N is already quite large. Reviewing the entirety of the discussion so far, we have mentioned a large number of PMI parameters that contribute to net erosion; although probably not exhaustive, this list at least includes the following: the sheath-entrance electron density n_e, the sheath-entrance electron temperature T_e, the sheath-entrance ion density n_{ip}, the sheath-entrance ion temperature T_{ip}, the magnetic field magnitude $|\vec{B}|$, the $\vec{B}$-to-PFC pitch angle α, the PFC atomic mass m_s, the PFC binding energy E_B, the plasma ion mass m_{ip}, the main sputtering ion mass m_{ii}, and the main sputtering ion charge Z_{ii}. For even as few as 2 sampling subdivisions for each of these parameters, we quickly realize that $2^{11}(11 + 2) = 26,624$ simulations are needed. Generously assuming each PYEAD-RustBCA-GITR simulation takes only 15 minutes to generate, this number converts to over 277 days of computational runtime. Worse, many more subdivisions are needed for model accuracy.

This runtime is unreasonable. We can start simplifying by restricting our field of interest and making a few sensible assumptions. First, we will have to restrict our interest again to W as a representative high-Z PFC; restricting further to the most abundant isotope, ^{184}W, eliminates the need to vary m_s and E_B. Second, we restrict our plasma to deuterium ion species, since these plasmas are the focus in fusion energy for the present; in so doing, we remove m_{ip} from the parameter short list and can assume $n_{ip} = n_e$. Third, we will assume isothermal conditions at the sheath entrance; as discussed in Chapter 1, this condition is a common approximation in plasma physics, and we will exploit it to set $T_{ip} = T_e$. In summary, these simplifications bring our number of PMI parameters down to six: n_e, T_e, $|\vec{B}|$, α, m_{ii}, and Z_{ii}. Nonetheless, we estimate an unwieldy 5.3×10^6 days of computational runtime for as few as $D = 20$ subdivisions, which is still very low.

To make our runtime more realistic, our problem is going to require an extremely sparse sampling of our parameter space. The accepted approach in such cases is Latin hypercube (LHC) sampling (94). In LHC sampling we divide our full parameter space into D^N total subdivisions as before. Next, we randomly choose a cell in that space as a first data point; when we go to choose our next data point, we remove any cell with a matching index to our first data point from the options. This process continues until we have selected only D data points to represent the entire parameter space. The benefit of this approach is that it guarantees a uniform sampling of our entire space while keeping the number of data points as low as possible; that is, each data point represents a unique regime of every parameter, and all regimes of all parameters are covered somewhere in the data. To guide the understanding, we show a simple, 2D LHC of D=8 in Figure 6.2. With this approach we are able to limit our dataset to 95(6+2) = 760 simulations for $D = 95$ or about 8 days of runtime, which is finally feasible; even if each simulation takes an hour to run, the dataset will be finished after about a month of runtime, which is still reasonable.

With our procedure finalized at last, we will conclude this section with a discussion of our parameter ranges of interest. We choose to consider a wide range of PMI conditions that covers the scope of research interests at time of writing; we summarize this list in Table 6.1. We choose a range of n_e and T_e that represents tabletop experiments like RF PIE (22) at ORNL up to worst-case SPARC divertor conditions (100); similarly, we have a range of $|\vec{B}|$ magnitudes for the same devices. We consider α across the same range as in Chapter 5 to assess engineered vs worst-case scenarios. Lastly, m_{ii} and Z_{ii} are discrete, dependent parameters, so we must give special consideration to minimize any differences in their sensitivity compared with the continuous, independent ones. We are limited in our m_{ii} options to those ion species available within RustBCA; we show this list in Table 6.1. Conveniently, these ion species cover a wide range in m_{ii}. We can limit $Z_{ii} \leq 30$ here using bounds placed by our n_e and T_e range using collisional radiative modeling with ColRadPy (see Section 7.2). Furthermore, to make Z_{ii} as independent as possible, we only consider

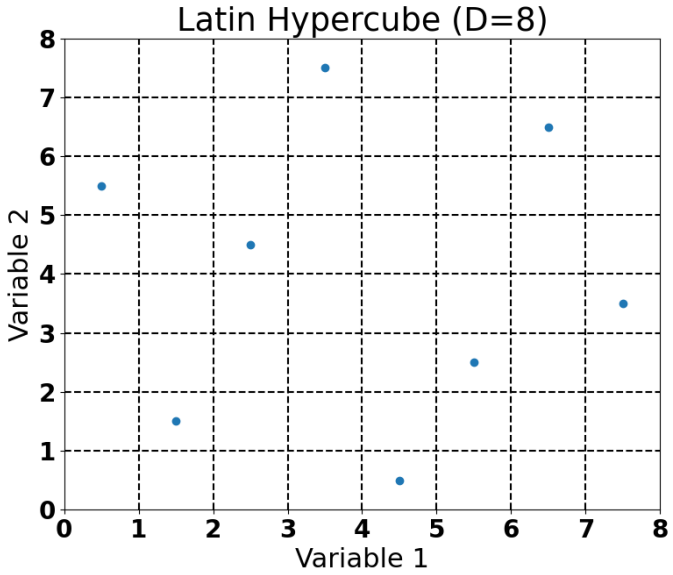

Figure 6.2: An example 2D LHC with D=8 parameter subdivisions of generic Variables 1 and 2.

Table 6.1: Range of values considered for each PMI parameter studied. We list the discrete range of impacting ions available in RustBCA as *ii*.

Parameter of Interest	**Minimal Value**	**Maximum Value**
n_e	5×10^{17} m^{-3}	5×10^{20} m^{-3}
T_e	5 eV	500 eV
$\vec{B}$	0.5 T	12.0 T
α	1°	85°
ii $\in$ {Li, Be, B, C, N, O, Ne, Al, Si, Ar, Ti, Ni, Cu, As, Kr, Xe, Cs, Yb, W}		

three categories of low, middle, or high ionization: low will mean $Z_{ii} = 1$, middle will mean $Z_{ii} = \lceil Z_{max}/2 \rceil$, and high will mean $Z_{ii} = Z_{max}$, where Z_{max} is either Z or 30 depending on the size of the atom; these categories will be treated as 1, 2, and 3 numerically within our Sobol' analysis before normalization to the unit hypercube.

6.2 Sobol' Sensitivity of PYEAD-RustBCA-GITR

In this section we will step through the Sobol' sensitivity analysis of our PYEAD-RustBCA-GITR workflow. Here, we use the S_{Ti} total-effect index discussed in Section 6.1 to isolate the relative importance of n_e, T_e, $|\vec{B}|$, α, m_{ii}, and Z_{ii} in predicting net erosion conditions. We will begin by demonstrating a few examples of the S_{Ti} index using outputs from our workflow that we can directly compare with analytic formulas: λ_{s+}, ρ_{s+}, and L_{MPS}. Good agreement to analytic expectation for these outputs provides a higher degree of confidence in latter analysis of outputs with no ready-made expectations.

In Figure 6.3 we show the S_{Ti} index for the W first-ionization mean-free path outputted by our workflow. We see that our λ_{s+} parameter is most sensitive to n_e; although numerically calculated, this result is in good agreement with Equation 4.2 in that the analytic expression most explicitly depends on n_e. Recall that n_e refers to the sheath-entrance electron density, that $n_e = n_{ip}$ at the sheath entrance by assumption, and that Equations 2.2 and 4.13 set the respective density drops through the sheath based on the sheath entrance parameter. Moreover, neither PYEAD nor GITR accounts for the influence of the incident sputtering ion particle density n_{ii} or charge density n_Z in setting the sheath potential or collisionality, assuming a trace concentration relative to n_{ip}. This level of analysis does not intend to capture the influence from these other densities in setting λ_{s+}.

As a companion to Figure 6.3, we also show histograms in Figure 6.4 of the raw λ_{s+} values plotted against each of our PMI parameters. To draw the eye to the general trend in each subfigure, we average the λ_{s+} values within regularly spaced

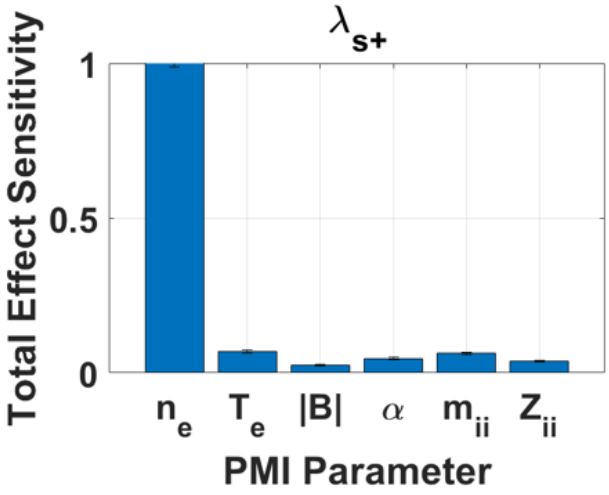

Figure 6.3: Total-effect sensitivity index for the first-ionization mean-free path output λ_{s+} against input PMI parameters n_e, T_e, $|\vec{B}|$, α, m_{ii}, and Z_{ii}.

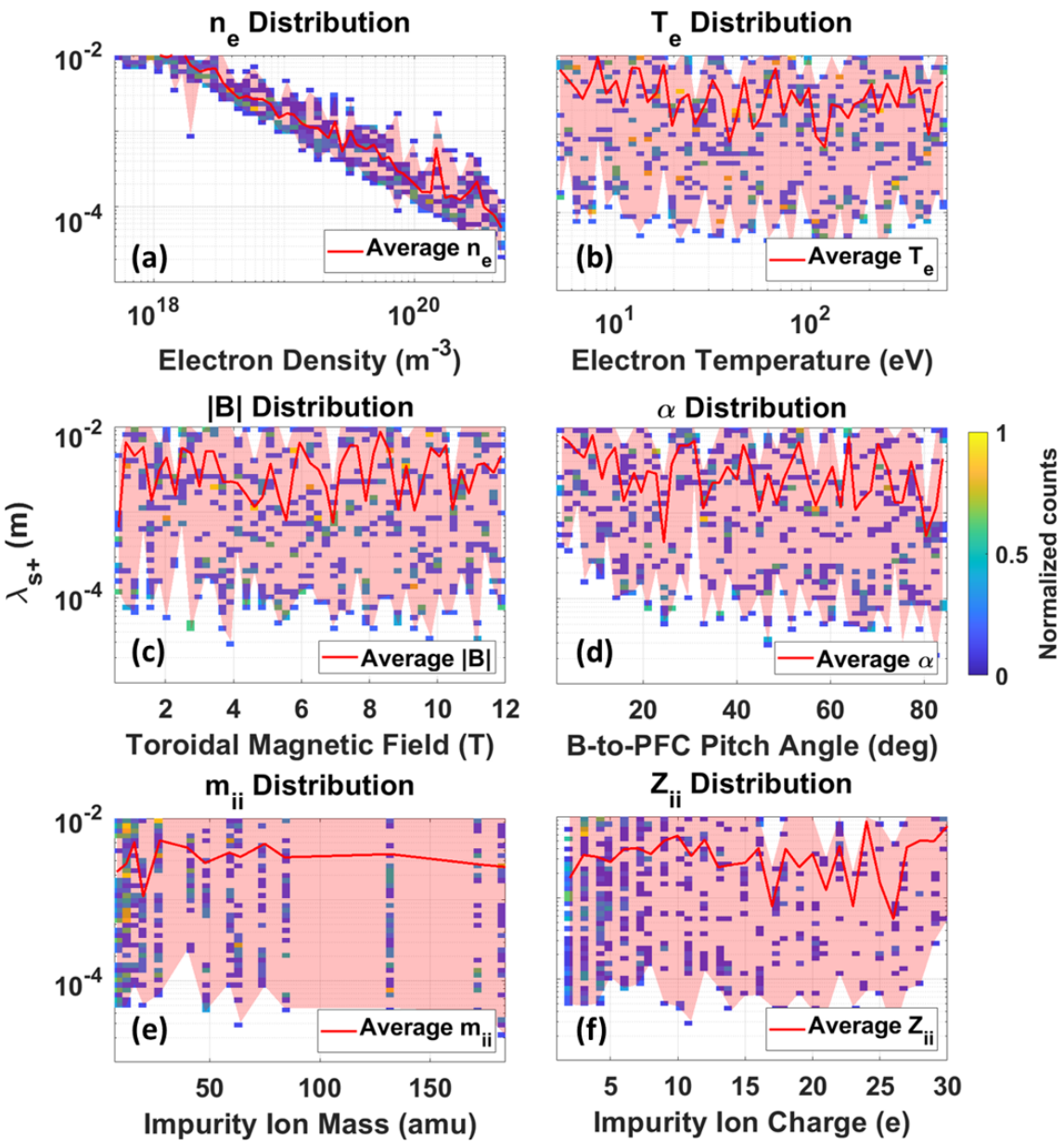

Figure 6.4: Histograms of raw λ_{s+} data (normalized to the maximum bin count) vs input PMI parameters (a) n_e, (b) T_e, (c) $|\vec{B}|$, (d) α, (e) m_{ii}, and (f) Z_{ii}. The bin-averaged trend is shown in red, with the range of averaging shaded in pink for clarity.

bin-widths across the PMI-parameter range; we interpolate an average λ_{s+} curve (red) through these points and shade (pink) the spread of λ_{s+} values included at each bin-averaging for clarity. We may readily see that the n_e term sets a clear trend for λ_{s+} expectations compared to the noisy range of λ_{s+} values for the other parameters. Comparing subfigure (a) in Figure 6.4 to the the S_{Ti} value of n_e in Figure 6.3 provides confirmation that the Sobol' analysis is correctly isolating the most important parameters. We will use the visual language of Figures 6.3 and 6.4 throughout this section to digest the Sobol' analysis.

We show the S_{Ti} indices for the first-ionization Larmor radius ρ_{s+} in Figure 6.5 and corresponding ρ_{s+} histograms for each PMI parameter in Figure 6.6. Again, ρ_{s+} is numerically estimated from the average ρ_{s+} at first-ionization in GITR. Nevertheless, Figure 6.5 shows that this value is strongly dependent on $|\vec{B}|$; that is to say, the Sobol' analysis has isolated the parameter we would expect the strongest ρ_{s+} dependence from based on Equation 4.3. Moreover, we note a ρ_{s+} distribution in $|\vec{B}|$ very similar to the $1/|\vec{B}|$ analytic form in (c) of Figure 6.6.

Lastly, we show the total-effect Sobol' indices for the magnetic pre-sheath thickness L_{MPS} in Figure 6.7 and L_{MPS} histograms in Figure 6.8. Unlike the λ_{s+} and ρ_{s+} outputs, L_{MPS} is entirely generated analytically within our workflow using Equation 2.21. Our Sobol' analysis isolates T_e, $|\vec{B}|$, and α respectively as the most important parameters determining L_{MPS}. Examining Equation 2.21 verifies that this ordering makes sense; L_{MPS} goes like $\sqrt{T_e}$, $1/|\vec{B}|$, and $\cos(\alpha)$ in the analytic form, and we see similar shapes for each of the appropriate subfigures of Figure 6.8. We now have three examples of interpreting S_{Ti} from outputs for which we have a good analytic intuition across the PYEAD-RustBCA-GITR coupling; this fact builds confidence that we have correctly implemented the Equation 6.6 algorithm. Now, we will step through each component of the coupled workflow and isolate the Sobol' indices for important parameters without clear analytic counterparts.

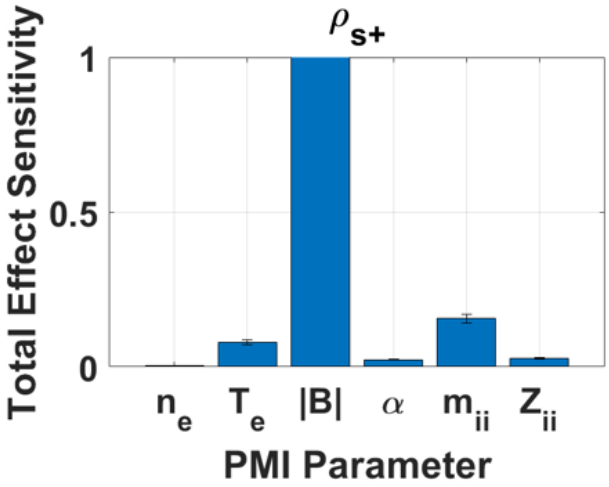

Figure 6.5: Total-effect sensitivity index for the first-ionization Larmor radius output ρ_{s+} against input PMI parameters n_e, T_e, $|\vec{B}|$, α, m_{ii}, and Z_{ii}.

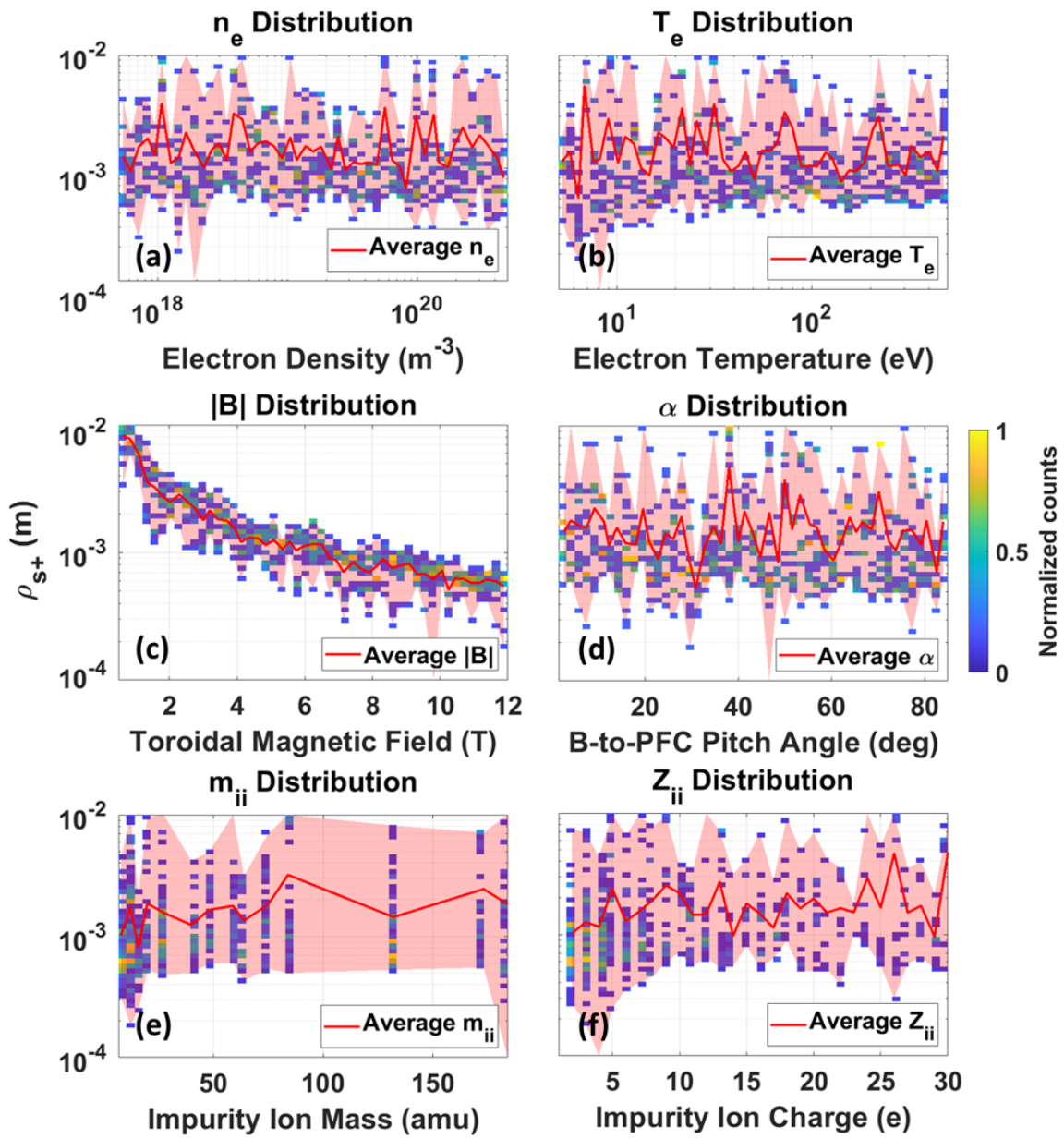

Figure 6.6: Histograms of raw ρ_{s+} data (normalized to the maximum bin count) vs input PMI parameters (a) n_e, (b) T_e, (c) $|\vec{B}|$, (d) α, (e) m_{ii}, and (f) Z_{ii}. The bin-averaged trend is shown in red, with the range of averaging shaded in pink for clarity.

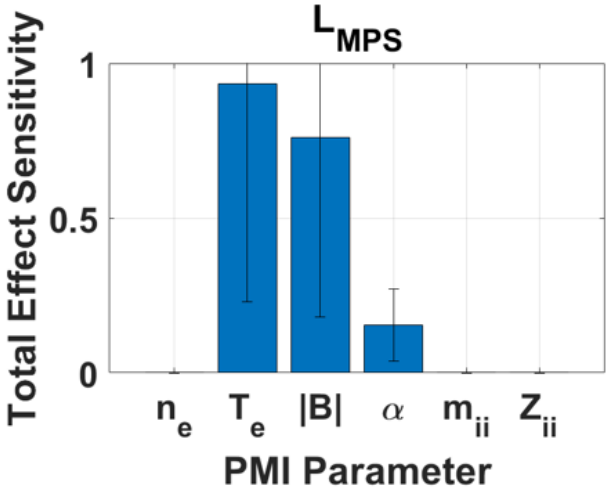

Figure 6.7: Total-effect sensitivity index for the magnetic pre-sheath thickness output L_{MPS} against input PMI parameters n_e, T_e, $|\vec{B}|$, α, m_{ii}, and Z_{ii}.

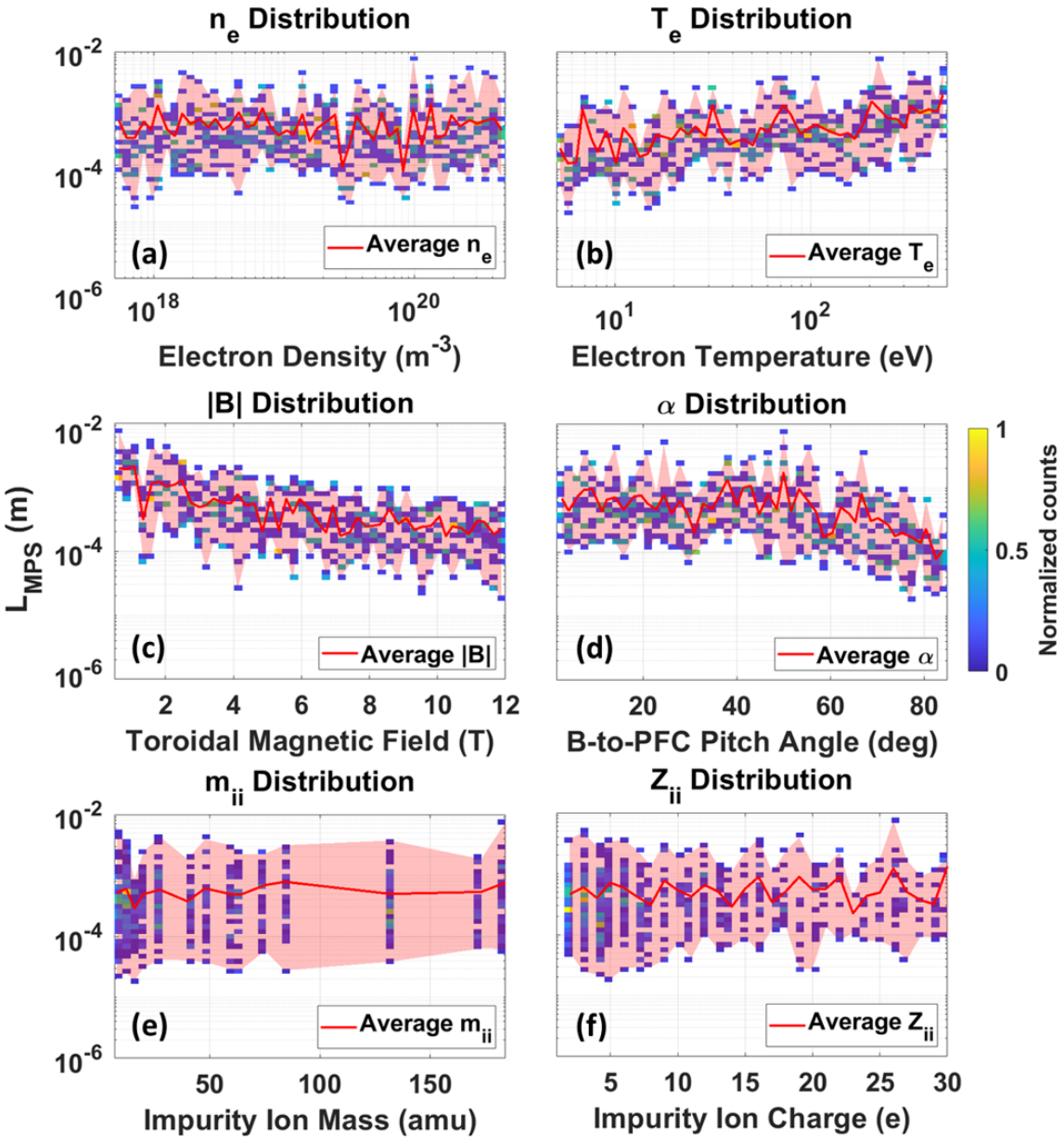

Figure 6.8: Histograms of raw L_{MPS} data (normalized to the maximum bin count) vs input PMI parameters (a) n_e, (b) T_e, (c) $|\vec{B}|$, (d) α, (e) m_{ii}, and (f) Z_{ii}. The bin-averaged trend is shown in red, with the range of averaging shaded in pink for clarity.

6.2.1 Sobol' analysis of PYEAD

From PYEAD we are most interested in the E_{ii}, θ, and ϕ sensitivities to our PMI-parameter inputs. First, we show the Sobol' indices of the particle-averaged sputtering ion impact energy E_{ii} in Figure 6.9. From the analysis we infer that E_{ii} is most strongly predicted by T_e, Z_{ii}, and m_{ii} respectively. We show the histogram trends for E_{ii} in Figure 6.10, which agree with the S_{Ti} intuition. Although we have no analytic expression to validate the physics of this finding, we can justify it with some reasonable observations from Section 3.3. Recall that the initial ion velocity distribution at the sheath entrance is Gaussian about the c_{th} thermal ion speed; Equation 3.9 shows that this speed is proportional to $\sqrt{T_e}$ and inversely proportional to $\sqrt{m_{ii}}$. We know from the analysis in Subsection 5.2.1 that a critical determiner of impinging ion EADs is the time-of-flight during which they may be affected by sheath electrodynamics. Consequently, we expect the PMI parameters setting the initial ion energy and the electrodynamic inertia to have the greatest impact on E_{ii}, which is reflected in the Sobol' indices. Next, the sheath electric field has an important role, represented by n_e and α; finally, the magnetic field, as a conservative field, has comparatively little impact on the average E_{ii}.

Next, we show the S_{Ti} indices for the average incident ion polar inclination angle θ in Figure 6.11 and θ histograms in Figure 6.12. Surprisingly at first, θ seems to be most dependent on α, then Z_{ii}, then m_{ii}; indeed, θ seems almost linear with α in (d) of Figure 6.12. While the sensitivity to m_{ii} and Z_{ii} makes sense given the previous discussion for E_{ii}, the relative independence of the incident ion energy to the $\vec{B}$-to-PFC pitch angle would suggest that α has little impact on the time-of-flight conditions that drive the EAD. However, we must also consider the fact that α sets both the sheath thickness and the rotation of the gyro-orbit plane (Figure 5.16); although the latter has comparatively little impact on the time-of-flight, it does determine the initial angle of the particles' gyro-motion relative to the PFC. Next, the n_e and $|\vec{B}|$ sensitivities follow from the electrodynamic acceleration particles experience within

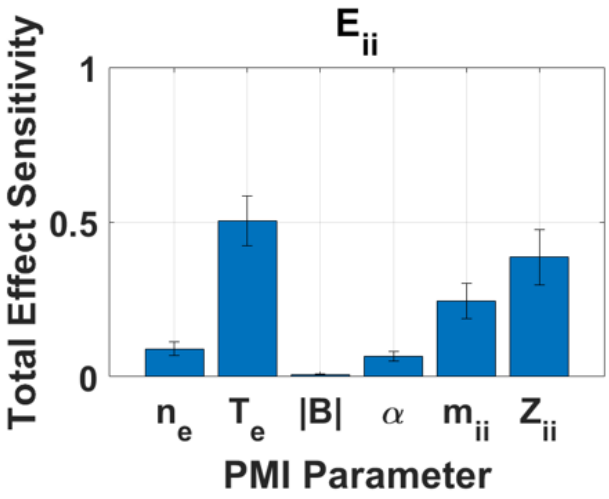

Figure 6.9: Total-effect sensitivity index for the average sputtering ion impact energy output E_{ii} against input PMI parameters n_e, T_e, $|\vec{B}|$, α, m_{ii}, and Z_{ii}.

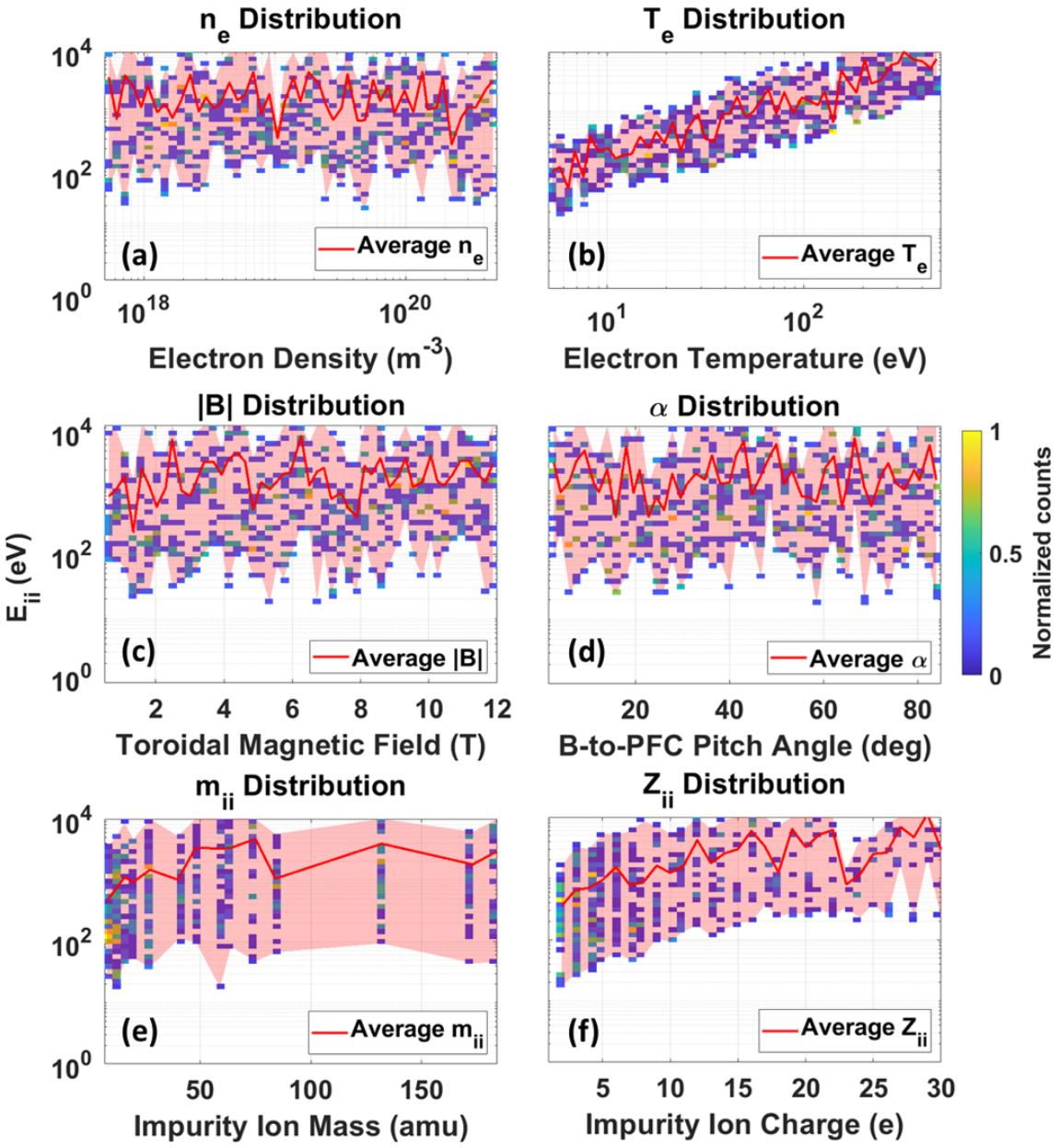

Figure 6.10: Histograms of raw E_{ii} data (normalized to the maximum bin count) vs input PMI parameters (a) n_e, (b) T_e, (c) $|\vec{B}|$, (d) α, (e) m_{ii}, and (f) Z_{ii}. The bin-averaged trend is shown in red, with the range of averaging shaded in pink for clarity.

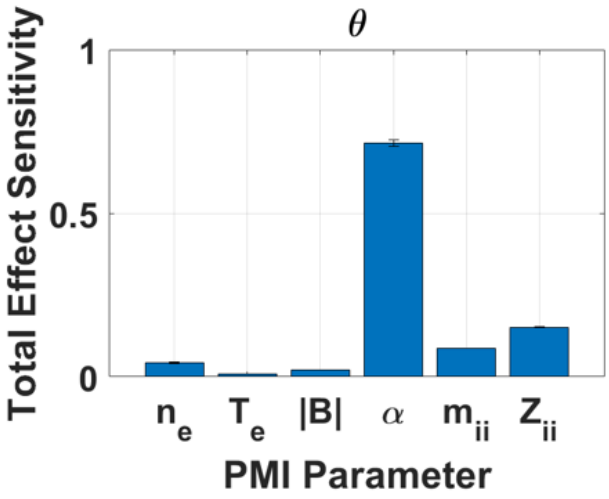

Figure 6.11: Total-effect sensitivity index for the average polar inclination angle output θ against input PMI parameters n_e, T_e, $|\vec{B}|$, α, m_{ii}, and Z_{ii}.

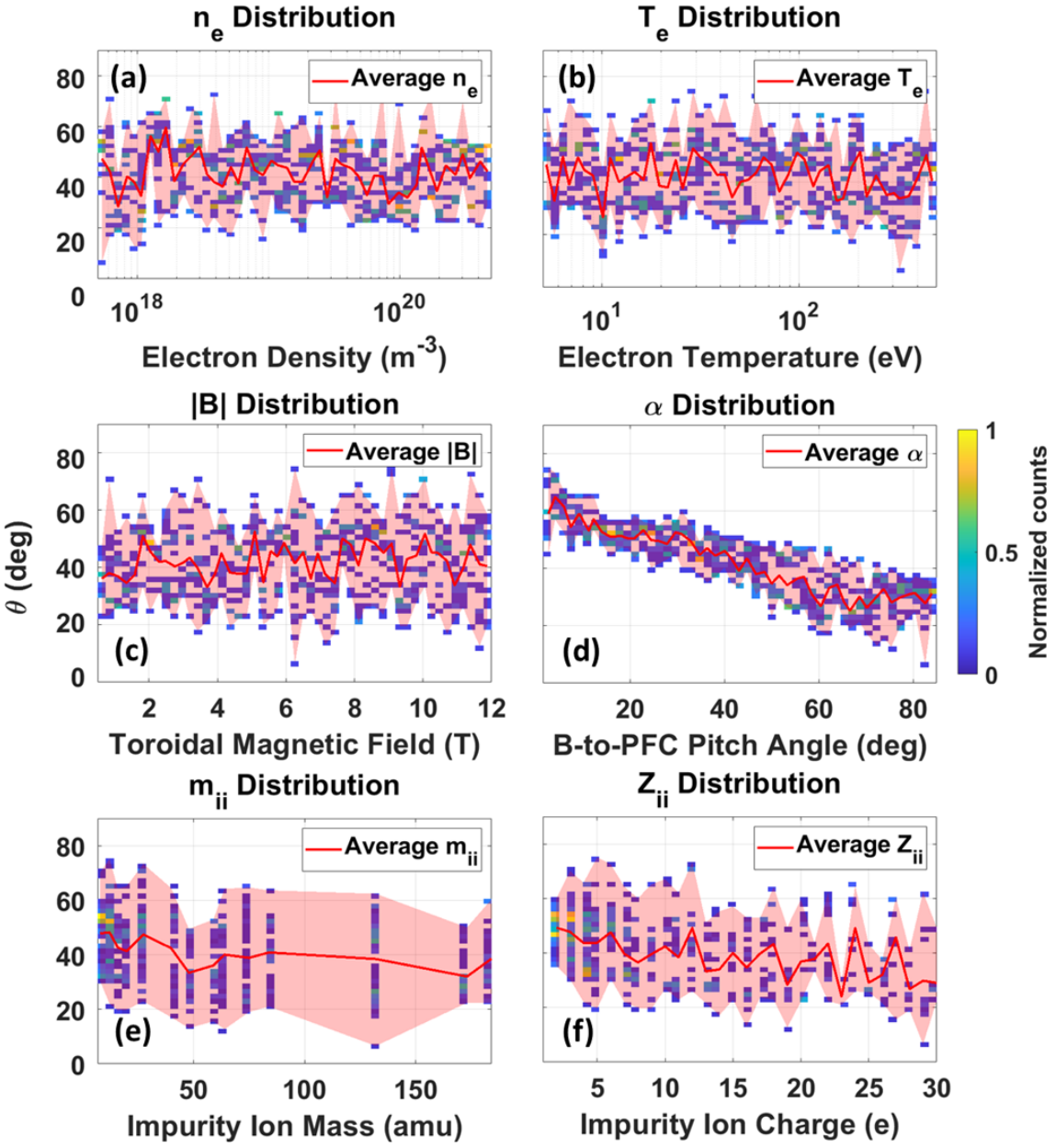

Figure 6.12: Histograms of raw θ data (normalized to the maximum bin count) vs input PMI parameters (a) n_e, (b) T_e, (c) $|\vec{B}|$, (d) α, (e) m_{ii}, and (f) Z_{ii}. The bin-averaged trend is shown in red, with the range of averaging shaded in pink for clarity.

the sheath. Finally, the relatively low θ dependence on T_e is likely due to the Lorentz force; higher velocities are more affected by $\vec{B}$-fields yet have shorter time-of-flights.

Finally, we show the total-effect sensitivities of the average incident azimuthal impact angle ϕ and histograms of this angle against each PMI parameter in Figures 6.13 and 6.14, respectively. Largely, these sensitivities are inherited from the same physical processes as their θ counterparts. Here, there is a marginally higher increase in n_e sensitivity and decrease in T_e sensitivity; while it is difficult to say with certainty, this change might be due to the density's impact on the electric field distribution, which changes the ExB drift forces within the sheath and may, in turn, provide additional changes to the ϕ parameter.

6.2.2 Sobol' analysis of PYEAD-RustBCA

With this next step in our Sobol' analysis, each of the E_{ii}, θ, and ϕ sensitivities from PYEAD will inherently propagate into RustBCA, since PYEAD outputs form the RustBCA inputs during the gross erosion calculation. As we explore the RustBCA sensitivity to underlying PMI parameters, we will be able to qualitatively infer RustBCA's overall sensitivity to PYEAD for free. Here, we are primarily interested in the E_s, Y, and δ outputs.

To start we will consider the sensitivities of the sputtered neutral energy E_s; we show the Sobol' indices for each PMI parameter in Figure 6.15 and histograms for the same parameters in Figure 6.16. Both the parameters isolated by the Sobol' analysis and the underlying parameter trends have overall good agreement with the Chapter 3 theory for physical sputtering, especially when considering the incident ion energy E_{ii} analysis. Here, we find E_s sensitive to T_e, m_{ii}, Z_{ii}, and α. As previously discussed, the first three of these parameters drive the E_{ii} condition, which in turn determines E_s through momentum transfer. Similarly, the α parameter strongly sets the angles of the ion collision, which also plays a role in the momentum transfer of ejected W

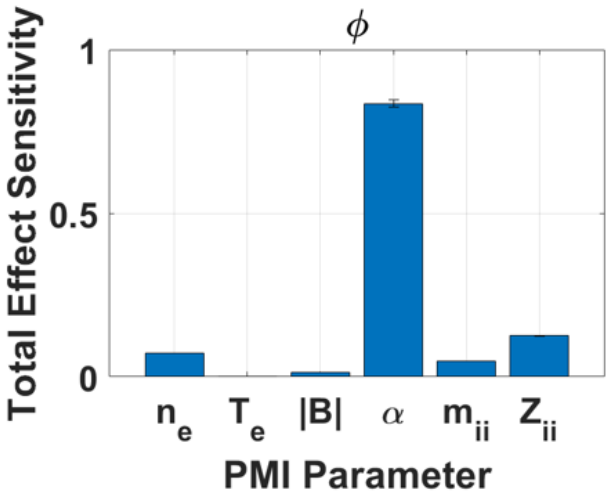

Figure 6.13: Total-effect sensitivity index for the average azimuthal impact angle output ϕ against input PMI parameters n_e, T_e, $|\vec{B}|$, α, m_{ii}, and Z_{ii}.

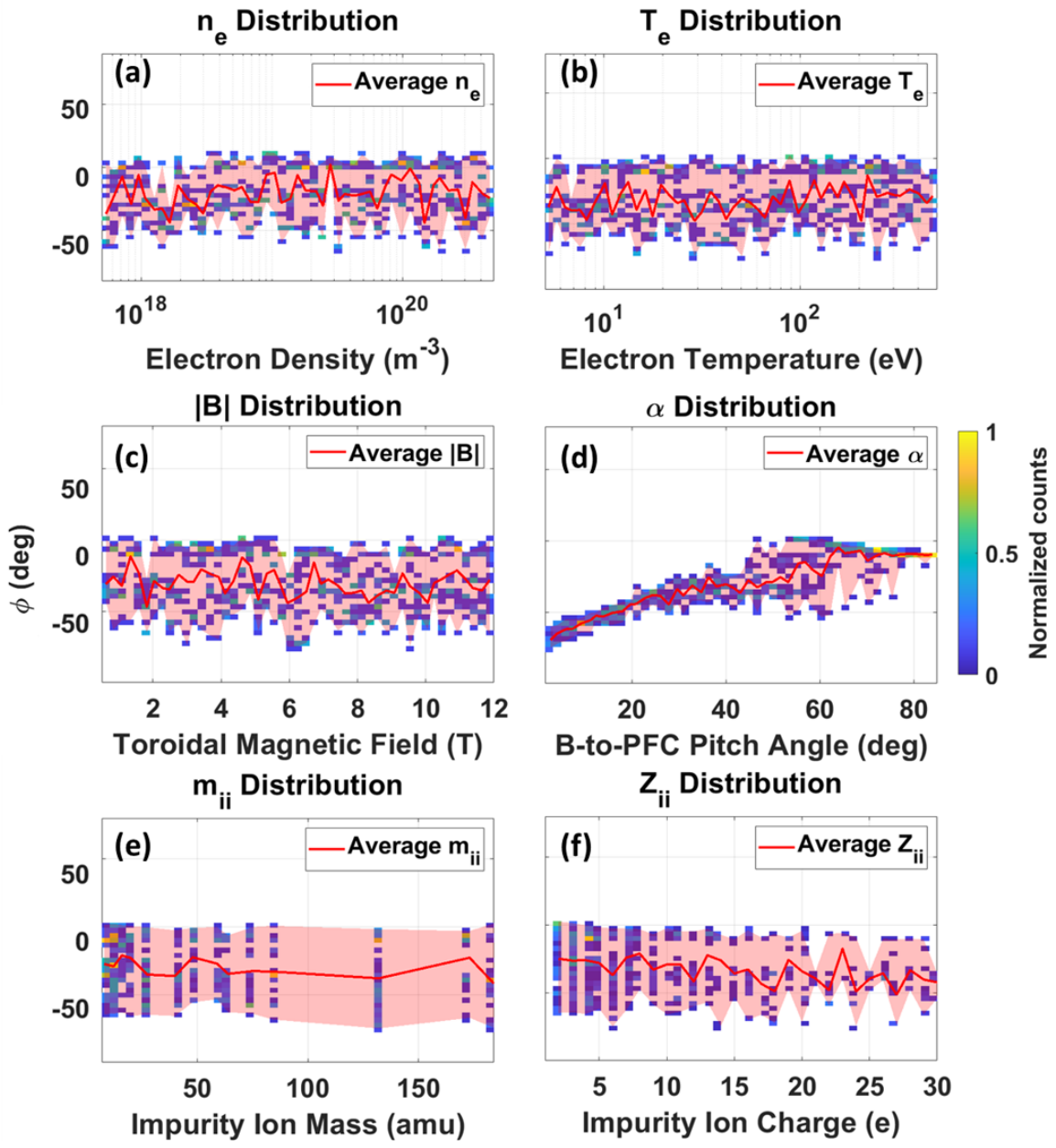

Figure 6.14: Histograms of raw ϕ data (normalized to the maximum bin count) vs input PMI parameters (a) n_e, (b) T_e, (c) $|\vec{B}|$, (d) α, (e) m_{ii}, and (f) Z_{ii}. The bin-averaged trend is shown in red, with the range of averaging shaded in pink for clarity.

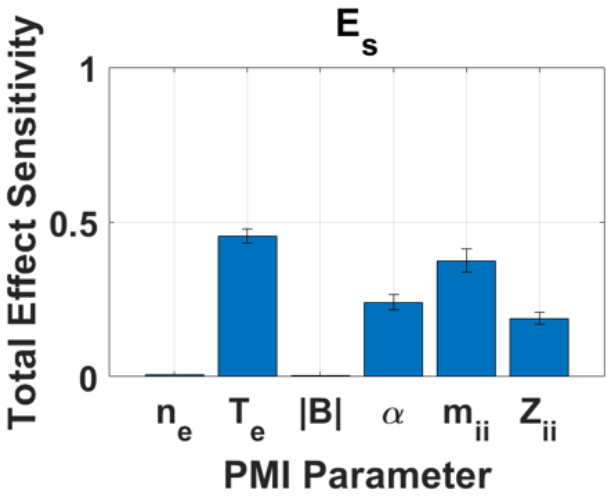

Figure 6.15: Total-effect sensitivity index for the average sputtered neutral energy output E_s against input PMI parameters n_e, T_e, $|\vec{B}|$, α, m_{ii}, and Z_{ii}.

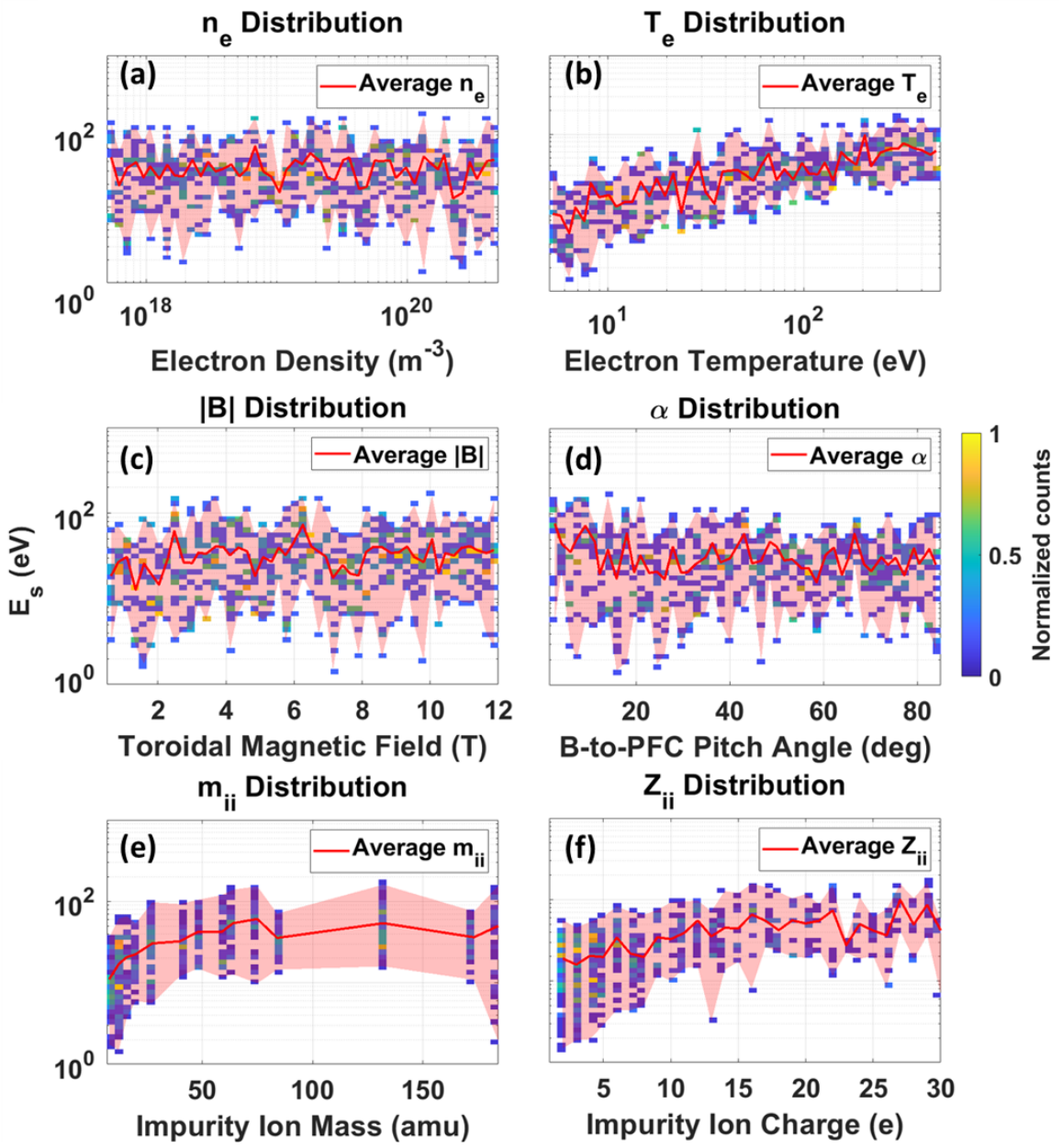

Figure 6.16: Histograms of raw E_s data (normalized to the maximum bin count) vs input PMI parameters (a) n_e, (b) T_e, (c) $|\vec{B}|$, (d) α, (e) m_{ii}, and (f) Z_{ii}. The bin-averaged trend is shown in red, with the range of averaging shaded in pink for clarity.

neutrals (Section 3.1). We see little impact from n_e and $|\vec{B}|$ because these parameters play minor roles in determining the PYEAD outputs.

Meanwhile, we see a similar sensitivity decomposition to E_s in the sputtered yield Y, shown in Figure 6.17. Similar to the definition in Chapter 3, we numerically define Y as:

$$Y = \frac{\#\, W\ neutrals}{\#\, ii\ ions} \tag{6.7}$$

The same four parameters dominate, with a slightly higher dependence on m_{ii} and lower dependence on T_e compared with the E_s indices. The empirical Y in Section 3.1 agrees with this observation, noting that $Y(m_{ii}, E_{ii}, ...)$ in Equation 3.4. Overall, the data in the Figure 6.18 histograms is quite noisy, though there is a slight trend in the interpolated average for each of the noted parameters. These underlying sensitivities generally agree with the low-Z trends from Chrobak's study, though lessened by the greater inertia of W (27).

As an aside, the noisiness of this dataset brings up something that is worth emphasizing about Sobol' indices; while we are able to quantify the relative importance of each parameter in determining an output, we know nothing from S_{Ti} about how deterministic the output itself is. All Sobol' indices are normalized to the output variance, so it is important also to look at the histograms in order to get a sense of what the goodness-of-fit to a given parameter is. Note, for example, subfigure (b) in Figures 6.16 and 6.18; although the S_{Ti} in T_e is quite similar for each case, the spread in Y is very high compared to E_s. Conversely, Figure 6.18 exemplifies the usefulness of Sobol' indices; on the whole, we would have a difficult time determining leading-order parameters amidst such a noisy output without the rigorous decomposition of the output variance provided by S_{T_i}.

Lastly, we are interested in understanding the sensitivity of the average sputtered forward-scattering angle δ. We are primarily interested in this parameter because it had such a large effect on the prompt-vs-local redeposition fraction (Section 5.3). We show the S_{Ti} decomposition in Figure 6.19. Considering momentum transfer, we see

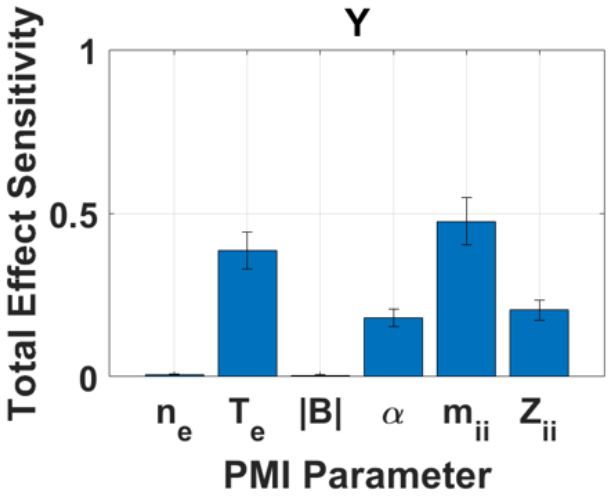

Figure 6.17: Total-effect sensitivity index for the average sputtered yield output Y against input PMI parameters n_e, T_e, $|\vec{B}|$, α, m_{ii}, and Z_{ii}.

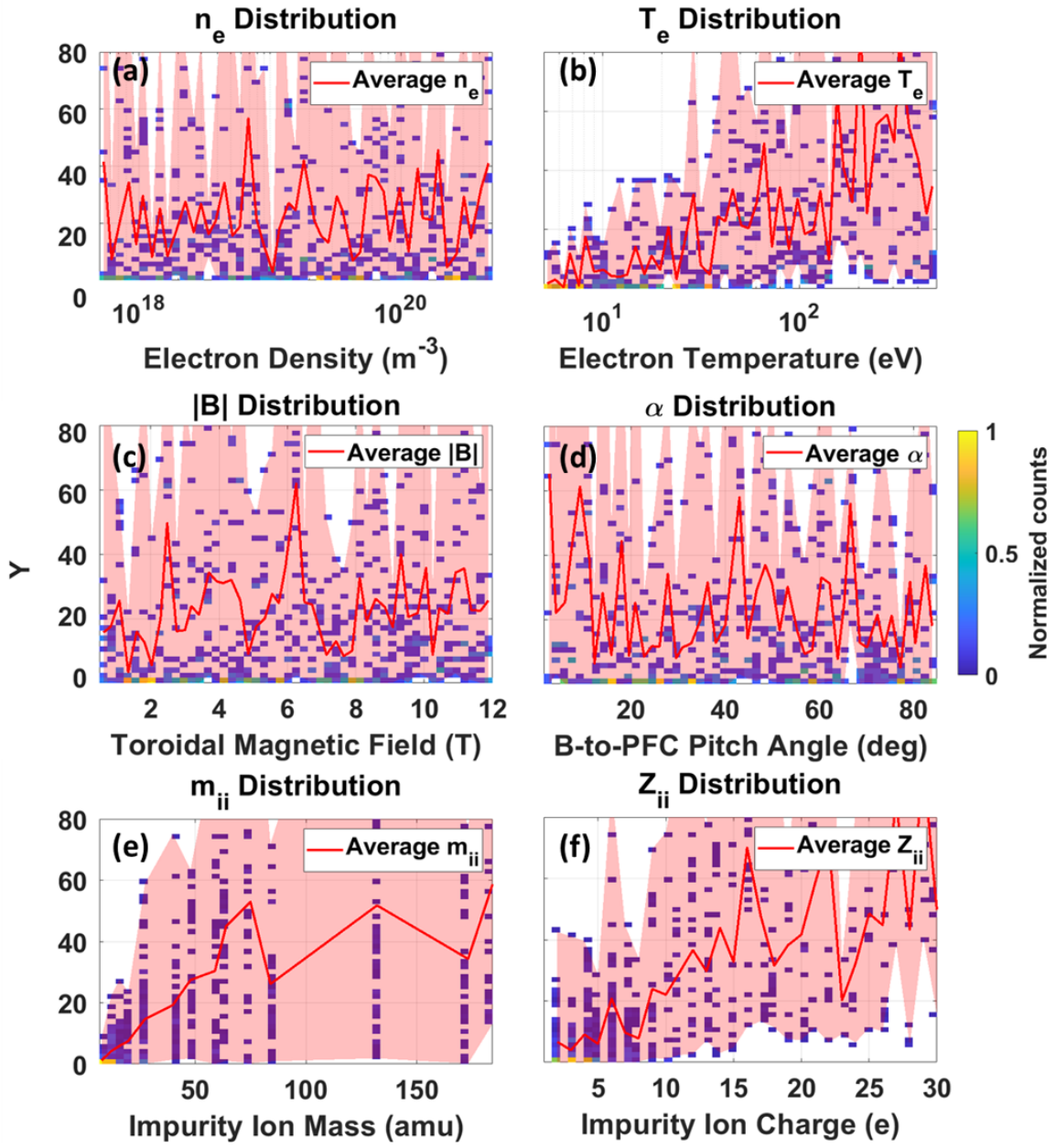

Figure 6.18: Histograms of raw Y data (normalized to the maximum bin count) vs input PMI parameters (a) n_e, (b) T_e, (c) $|\vec{B}|$, (d) α, (e) m_{ii}, and (f) Z_{ii}. The bin-averaged trend is shown in red, with the range of averaging shaded in pink for clarity.

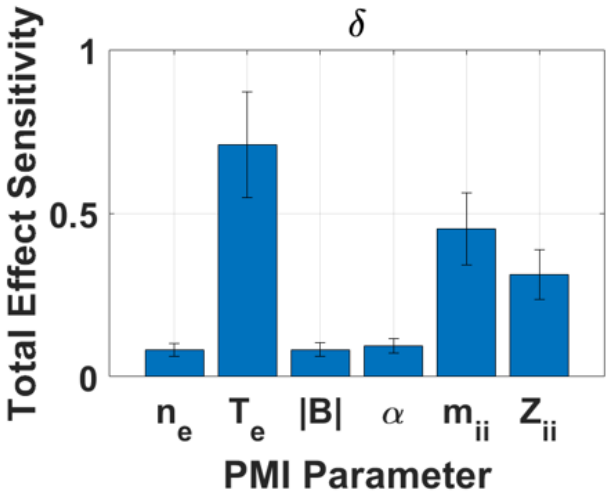

Figure 6.19: Total-effect sensitivity index for the average sputtered forward-scattering angle δ against input PMI parameters n_e, T_e, $|\vec{B}|$, α, m_{ii}, and Z_{ii}.

an unsurprisingly strong dependence on T_e, m_{ii}, and Z_{ii} as the leading-order terms; again, these are the most important parameters determining the incident ion energy.

Somewhat surprising is the relative weakness of the total-effect α index in comparison with those of the other parameters; from a binary-collision intuition, we could naively anticipate a strong α-dependence for the forward-scattering angle, and we saw a strong dependence on α for this output in Section 5.2. This new contextualization suggests that our α-variation only demonstrated a secondary effect determining the forward-scattering angle. Nonetheless, we should further note in Figure 6.20 that the interpolated δ average is fairly constant overall yet increasingly coherent as T_e increases in subfigure (b). In the $T_e \approx 20$ eV range we considered in Chapter 5, we expect more impact from secondary parameters like α in determining the δ distribution. Based on these conclusions and the Chapter 5 results, we should expect T_e to have a large impact on the prompt-vs-local redeposition distribution.

6.2.3 Sobol' analysis of PYEAD-RustBCA-GITR

Ultimately, the motivation behind the Sobol' sensitivity analysis of our PYEAD-RustBCA-GITR workflow has been predicting the most important variables both determining prompt-vs-local redeposition and setting the fraction of SOL losses. We expect the GITR f_{prompt}, f_{local}, and f_{far} fractions to inherit their sensitivities from RustBCA, as these outputs form the GITR inputs. To conclude this chapter, we will step through the total-effect indices of each redeposition fraction and interpret their sensitivities within the context of Subsections 6.2.1 and 6.2.2.

First, we consider the S_{Ti} indices for the prompt redeposition fraction f_{prompt}. Recall that this type of redeposition is defined as redeposition dominated by geometric intersection between large W^+ gyro-motion and the PFC surface; each of E_s, δ, λ_{s+}, and ρ_{s+} is obviously important in setting the prompt fraction, but these variables in turn hinge complexly on the underlying PMI parameter conditions. We show the Sobol' indices for f_{prompt} in Figure 6.21; the most important parameters setting

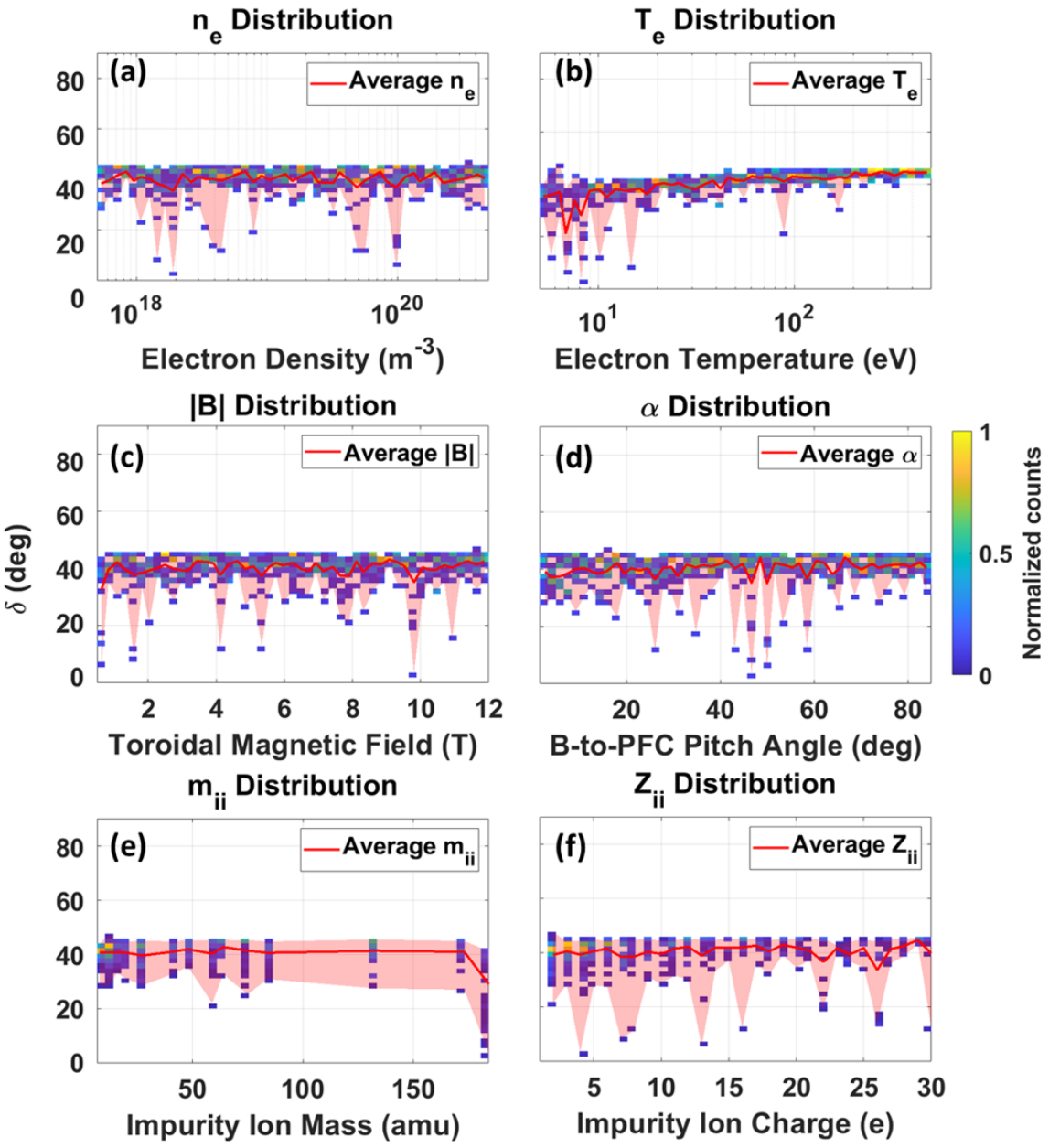

Figure 6.20: Histograms of raw δ data (normalized to the maximum bin count) vs input PMI parameters (a) n_e, (b) T_e, (c) $|\vec{B}|$, (d) α, (e) m_{ii}, and (f) Z_{ii}. The bin-averaged trend is shown in red, with the range of averaging shaded in pink for clarity.

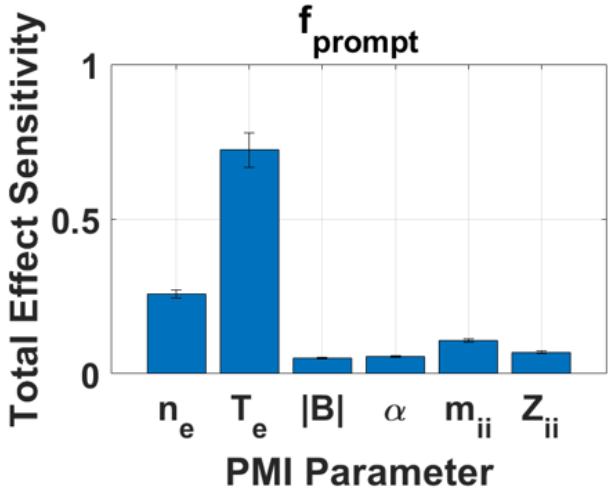

Figure 6.21: Total-effect sensitivity index for the prompt redeposition fraction f_{prompt} against input PMI parameters n_e, T_e, $|\vec{B}|$, α, m_{ii}, and Z_{ii}.

the prompt fraction are the plasma density and, especially, temperature. Next, the incident ion m_{ii} and Z_{ii} conditions are important before magnetic field conditions α and $|\vec{B}|$. The histogram distributions for each PMI parameter are in Figure 6.22. We note that the f_{prompt} trends agree with f_{red} trends discussed in Figure 4.2 for n_e but disagree with the same trends for T_e. We have good reason to believe that we are presenting an improved understanding of the importance of T_e since the original Naujoks work assumed a cosine-δ distribution (90).

We may confirm a few things from the S_{Ti} ordering. Firstly, we recall that the T_e parameter has a strong influence on both the sputtered energy E_s and the forward-scattering angle δ. Secondly, we note that the ionization length is also set to a lesser degree by T_e and primarily by n_e. As T_e increases both the sputtered energy increases and the forward-scattering angle increases, which we saw in Subsection 5.3.1 leads to an increase in f_{prompt}. Similarly, increasing n_e increases the rate of ionization, in turn decreasing the average height of particles at ionization and increasing the prompt fraction for geometric reasons. On the other hand, the f_{prompt} dependence on m_{ii} and Z_{ii} is inherited from the sputtered energy and angle's dependence on those parameters. The magnetic field conditions, which we saw have a large effect on f_{prompt} in Subsection 5.3.1, are the weakest parameters to influence the prompt fraction by comparison; nevertheless, we see the same underlying physics processes discussed in Subsection 5.3.1 determine f_{prompt} overall.

Meanwhile, we present the total-effect sensitivities for the local redeposition fraction in Figure 6.23. Recall that this type of redeposition is defined as redeposition dominated by electrostatic forces pushing $W^{\geq 1+}$ ions within the sheath back to the surface. Here, E_s, δ, λ_{s+}, and ψ are intuitively important to local redeposition but again depend complexly themselves on the underlying PMI parameters. In Figure 6.23 the most sensitive parameters are α, n_e, and T_e respectively. Given the definition of local redeposition, we should not be surprised to see that α and n_e, which set the electric potential and density distributions through the sheath, are the leading order parameters. We show the histograms for f_{local} in Figure 6.24.

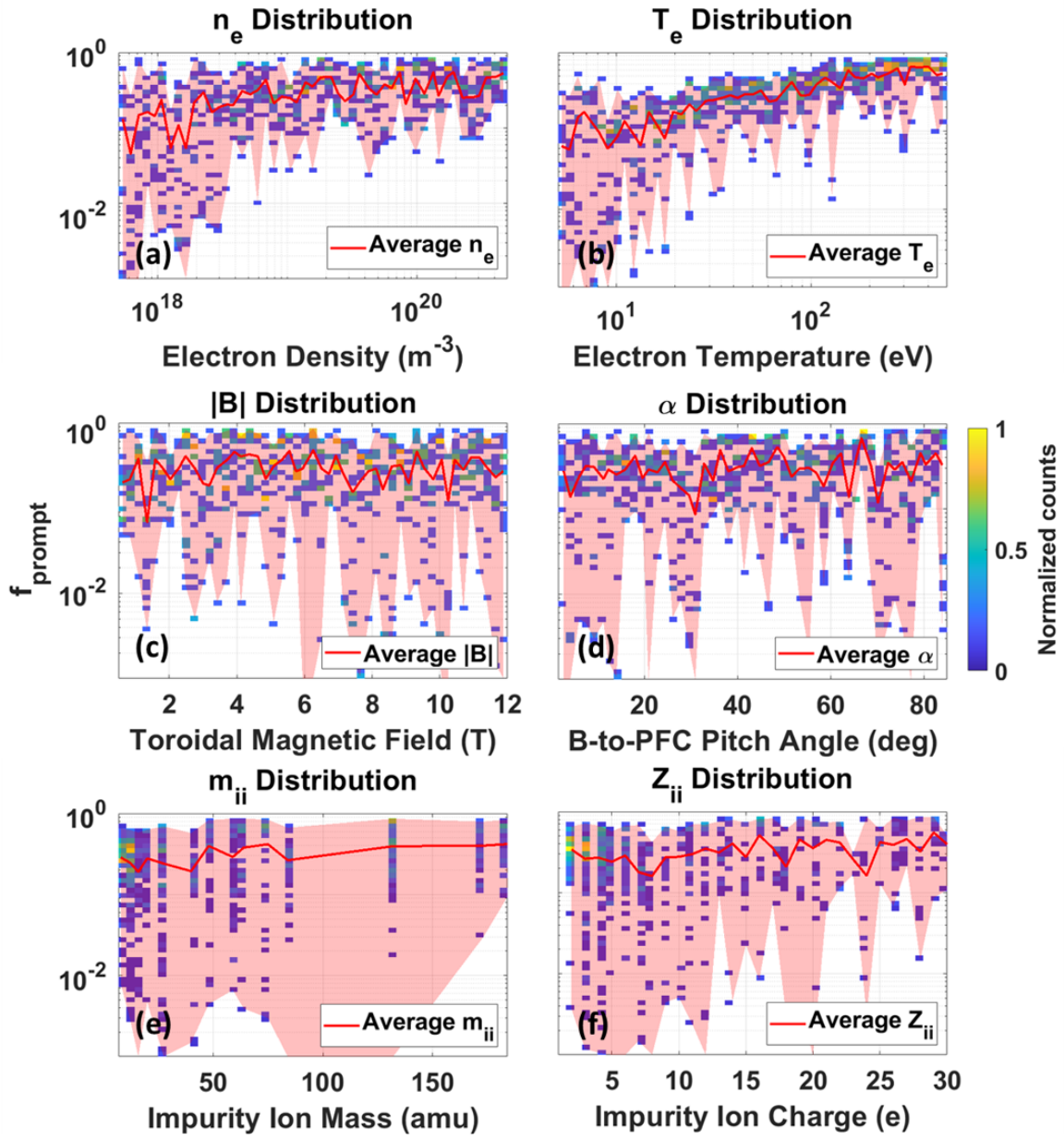

Figure 6.22: Histograms of raw f_{prompt} data (normalized to the maximum bin count) vs input PMI parameters (a) n_e, (b) T_e, (c) $|\vec{B}|$, (d) α, (e) m_{ii}, and (f) Z_{ii}. The bin-averaged trend is shown in red, with the range of averaging shaded in pink for clarity.

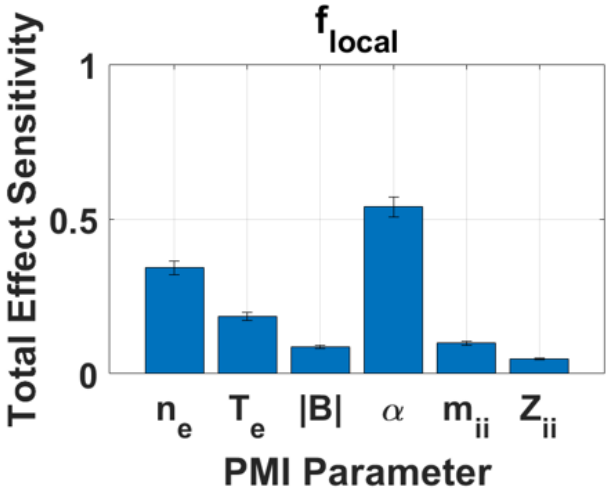

Figure 6.23: Total-effect sensitivity index for the local redeposition fraction f_{local} against input PMI parameters n_e, T_e, $|\vec{B}|$, α, m_{ii}, and Z_{ii}.

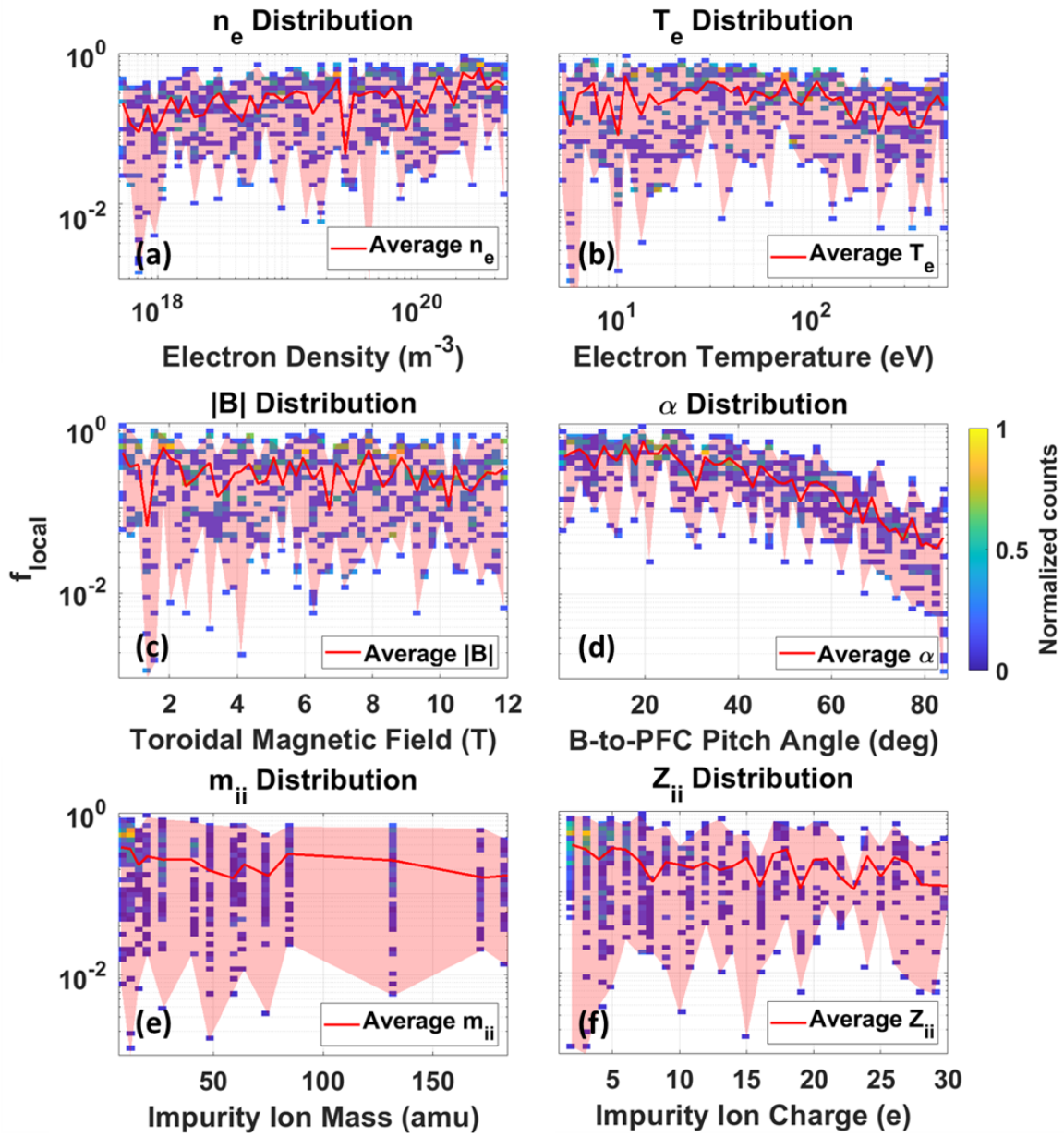

Figure 6.24: Histograms of raw f_{local} data (normalized to the maximum bin count) vs input PMI parameters (a) n_e, (b) T_e, (c) $|\vec{B}|$, (d) α, (e) m_{ii}, and (f) Z_{ii}. The bin-averaged trend is shown in red, with the range of averaging shaded in pink for clarity.

Note that local redeposition increases then decreases with α as before; broadly speaking, the turnaround point seems to be around $\alpha \approx 20 - 25°$ on average. We see an increase in local redeposition with n_e, partially because this parameter increases the rate of ionization so produces greater populations of multiply-ionized W ions in the sheath. On the other hand, increasing T_e results in a slight increase then decrease of f_{local} on average; as in Subsection 5.3.2, we note that the commensurate increase in E_s with T_e places more material closer to the sheath entrance so that the physics determining the T_e trend is similar to that of the α trend.

As a result of both f_{prompt} and f_{local} behavior and sensitivity, we have a good understanding of how trends in the PMI parameters result in PFC material losses into the SOL. We show the far redeposition fraction f_{far}'s Sobol' indices and histogram trends in Figures 6.25 and 6.26, respectively. The most important parameter is the electron density, inheriting its combined sensitivity from prompt and local contributions; this parameter sets the density drop through the sheath and the ionization length. The next most important parameter is the electron temperature, which drives the kinetic energy and angle of the sputtered material. Finally, the $\vec{B}$-to-PFC pitch angle drives the potential distribution in the sheath, which affects both the gross erosion and redeposition components setting far losses. Increasing n_e (a) and T_e (b) reduces while increasing α (d) increases the SOL-dependence on redeposition in Figure 6.26.

At this point, we have separately examined the PMI parameter sensitivity of both gross erosion and redeposition. In particular, the yield Y determines the relative fraction of gross eroded neutrals from incident ion fluxes, and the redeposition fractions $f_{mechanism}$ determine the relative fraction of redeposited material (parsed by mechanism) from eroded neutral fluxes. As previously discussed, the redeposition vs net erosion contribution from the far transport category cannot be distinguished at this time. Moreover, because this workflow couples Monte Carlo codes that require different numbers of test particles in order to optimize statistics versus computational runtime, gross erosion and redeposition have been discussed in fractional forms,

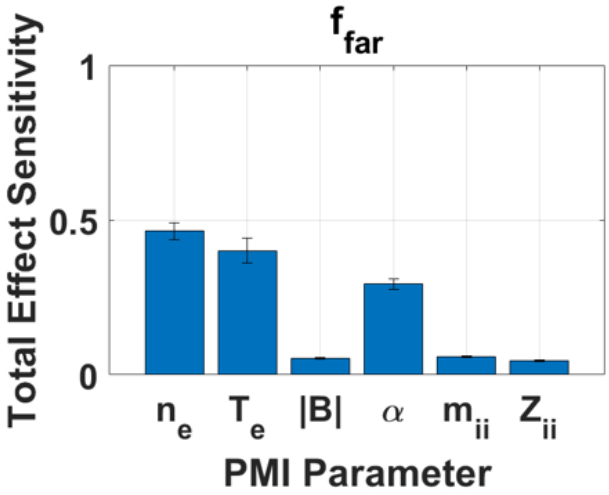

Figure 6.25: Total-effect sensitivity index for the far redeposition fraction f_{far} against input PMI parameters n_e, T_e, $|\vec{B}|$, α, m_{ii}, and Z_{ii}.

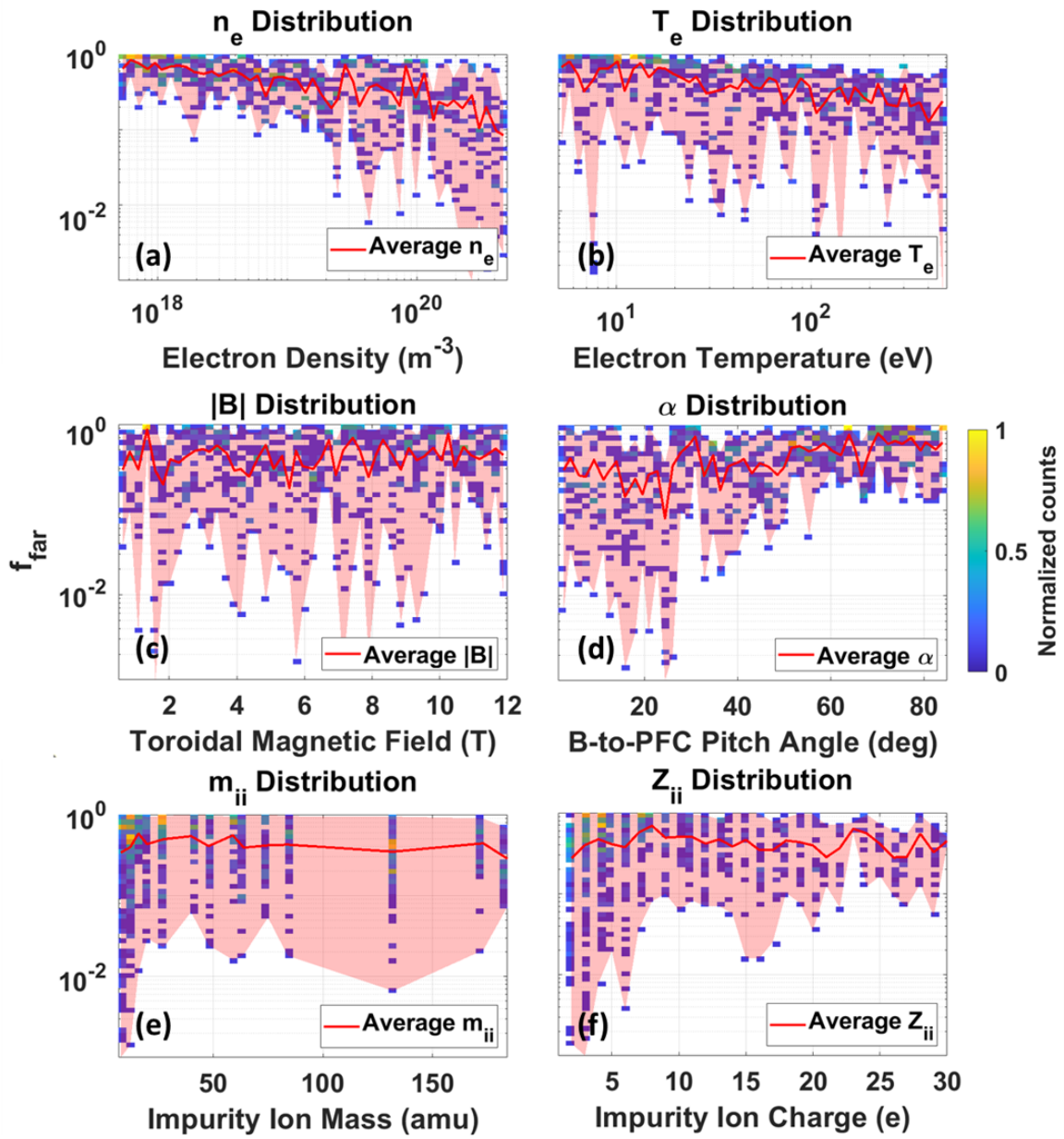

Figure 6.26: Histograms of raw f_{far} data (normalized to the maximum bin count) vs input PMI parameters (a) n_e, (b) T_e, (c) $|\vec{B}|$, (d) α, (e) m_{ii}, and (f) Z_{ii}. The bin-averaged trend is shown in red, with the range of averaging shaded in pink for clarity.

and net erosion has not been directly computed across codes. Nevertheless, we are explicitly interested in net erosion (i.e. gross erosion-redeposition) as the important PMI metric for high-Z PFCs. To provide at least one measure of net erosion, we now consider $Y * f_{mechanism}$ as a tentative output of interest from the PYEAD-RustBCA-GITR workflow. This term is the ratio of the number of particles attributed to a given redeposition mechanism with respect to the number of incident sputtering ions; hence, this term does not take into account the SOL-driven changes in incident sputtering ion flux associated with changing these PMI parameters at the sheath entrance. Future work must further consider these changes in order to provide "real-world" numerical predictions of net erosion from OEDGE experimental discharges.

We show the Sobol' indices for $Y * f_{prompt}$, a measure of global particle count attributed to prompt redeposition, in Figure 6.27 and show the associated histograms for each PMI parameter in Figure 6.28. As expected, inherited sensitivities from both Y and f_{prompt} determine the sensitivity of $Y * f_{prompt}$, but these contributions do not with equal weight. Note that $Y \geq 0$ is not bounded above while $0 \leq f_{mechanism} \leq 1$ is, meaning that Y plays a greater importance in setting the sensitivity of $Y * f_{mechanism}$. As such, $Y * f_{prompt}$ has a strong sensitivity to T_e, m_{ii}, and Z_{ii} because both Y and f_{prompt} generally increase with these terms. Meanwhile, increasing α results in a slight overall decrease in Y but little impact on f_{prompt}, resulting in a $Y * f_{prompt}$ Sobol' index comparable to that of Z_{ii} for this pitch angle. Conversely, increasing n_e results in little impact to Y but a slight increase in f_{prompt}; nevertheless, the S_{Ti} of $Y * f_{prompt}$ is essentially negligible since Y dominates the sensitivity distribution.

Next, we consider a measure of the global particle count attributed to local redeposition, $Y * f_{local}$. We show these Sobol' indices in Figure 6.29 and the associated PMI parameter histograms in Figure 6.30. As before the Y sensitivity dominates the PMI parameter decomposition of $Y * f_{local}$ trends. Because increasing α slightly decreases Y and largely decreases f_{local}, this parameter emerges as the dominant term. Meanwhile, increasing T_e, m_{ii}, and Z_{ii} increases Y but slightly decreases f_{local}; nonetheless, these parameters have high sensitivity measures with overall increasing

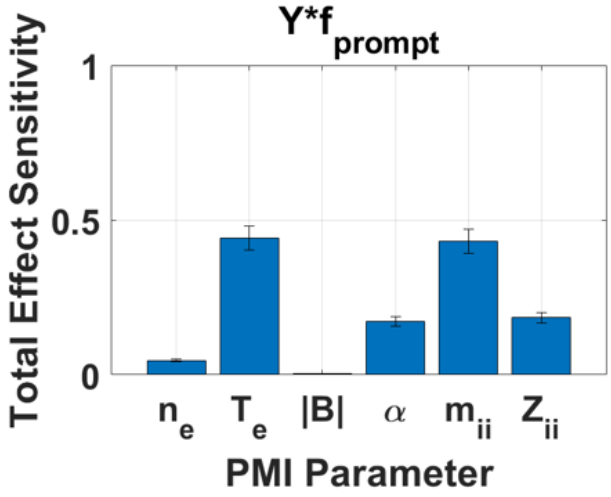

Figure 6.27: Total-effect sensitivity index for $Y * f_{prompt}$ against input PMI parameters n_e, T_e, $|\vec{B}|$, α, m_{ii}, and Z_{ii}.

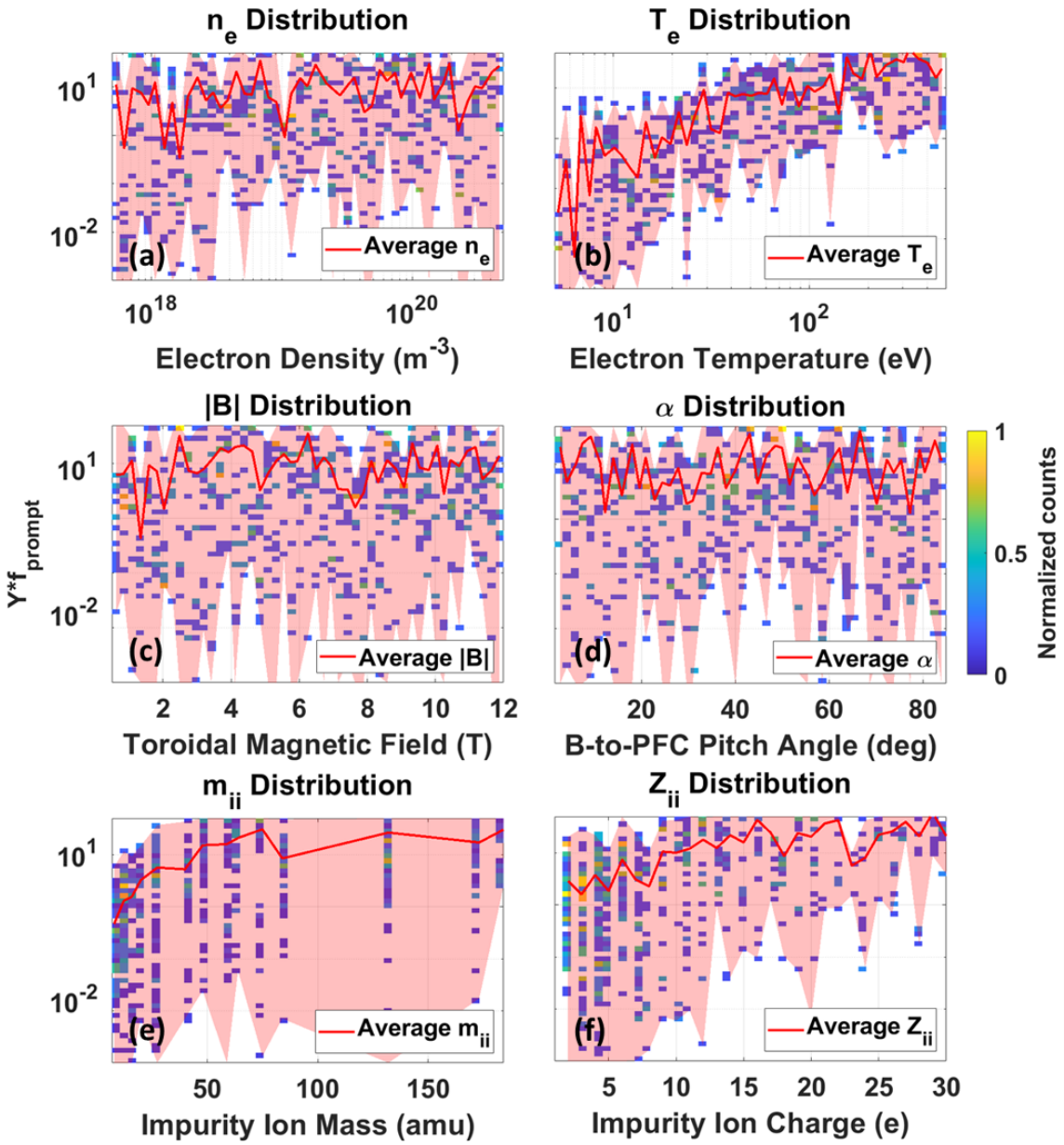

Figure 6.28: Histograms of raw $Y * f_{prompt}$ data (normalized to the maximum bin count) vs input PMI parameters (a) n_e, (b) T_e, (c) $|\vec{B}|$, (d) α, (e) m_{ii}, and (f) Z_{ii}. The bin-averaged trend is shown in red, with the range of averaging shaded in pink for clarity.

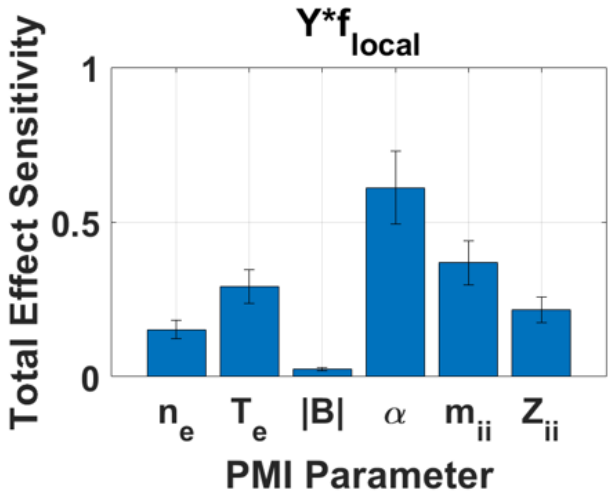

Figure 6.29: Total-effect sensitivity index for $Y * f_{local}$ against input PMI parameters n_e, T_e, $|\vec{B}|$, α, m_{ii}, and Z_{ii}.

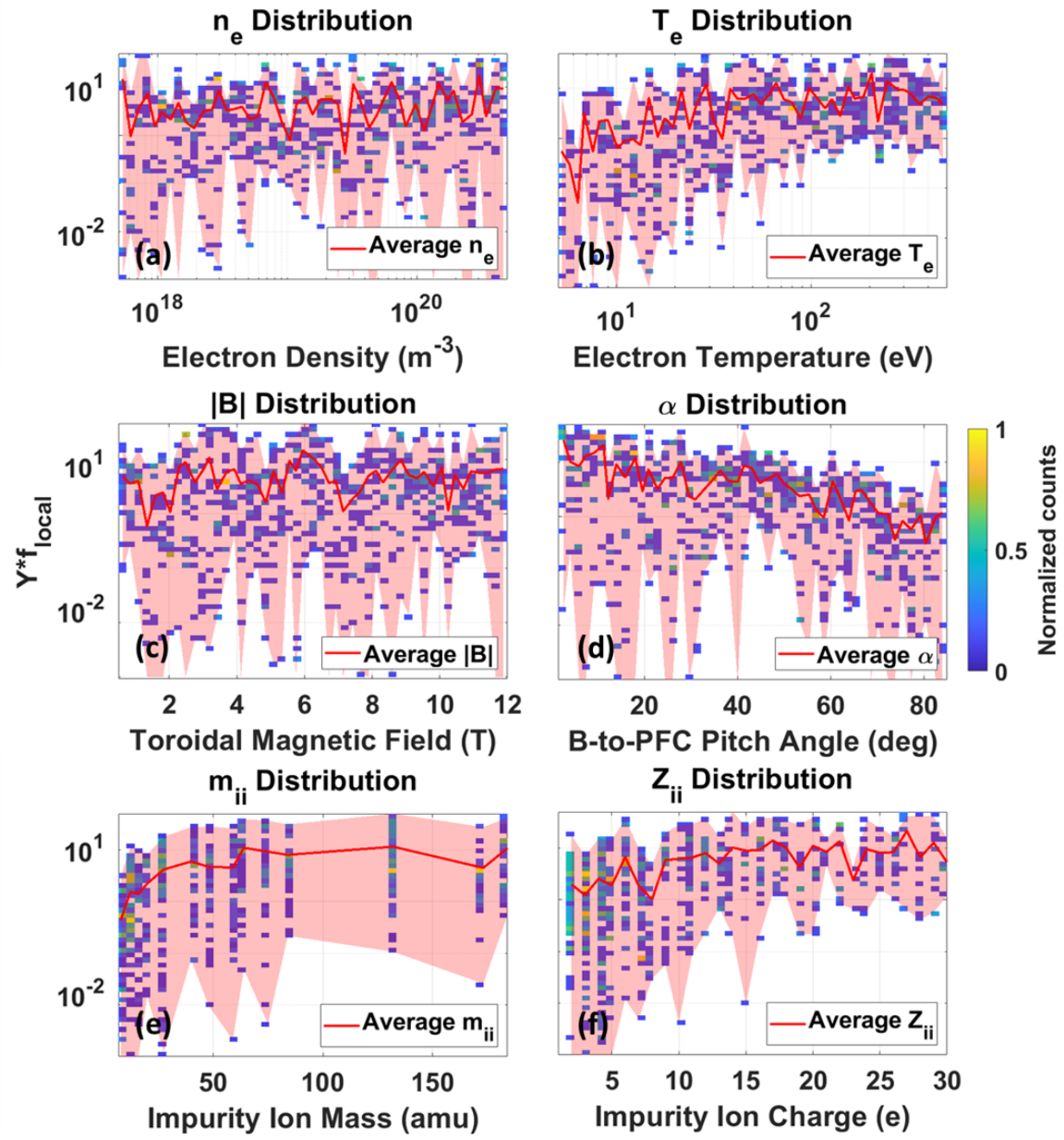

Figure 6.30: Histograms of raw $Y * f_{local}$ data (normalized to the maximum bin count) vs input PMI parameters (a) n_e, (b) T_e, (c) $|\vec{B}|$, (d) α, (e) m_{ii}, and (f) Z_{ii}. The bin-averaged trend is shown in red, with the range of averaging shaded in pink for clarity.

trends in $Y*f_{local}$. Lastly, increasing n_e has a more coherent increase in f_{local} compared to f_{prompt}, so this parameter is slightly more effective than before in driving $Y * f_{local}$ behavior despite the noisy Y distribution in n_e.

Finally, we show the Sobol' indices (Figure 6.31) and PMI parameter histograms (Figure 6.32) for $Y * f_{far}$, a measure of the global particle count attributed to far transport. As with the previous two series of sensitivity analysis, $Y * f_{far}$ inherits its sensitivities from Y and f_{far} but is dominated by Y. Indeed, the $Y * f_{far}$ metric of particle losses into the SOL is most sensitive to n_e, T_e, m_{ii}, and Z_{ii} as a direct inheritance from far transport (in the case of n_e and T_e), and yield (in the case of T_e, m_{ii}, and Z_{ii}) sensitivity. Importantly, the decrease in f_{far} is sufficiently steep and coherent compared to the increase in Y as electron temperature increases that $Y * f_{far}$ has a lower Sobol' index in T_e than might otherwise be expected.

Similarly, the slight increase in f_{far} and slight decrease in Y as α increases commensurately result in little sensitivity of $Y * f_{far}$ to α. This finding may imply that net erosion is actually inert on the whole to changes in the $\vec{B}$-to-PFC pitch angle, which would be significantly beneficial to the longevity of first-wall material in the event of transient-damaged PFCs; nevertheless, it is important to remember that we have considered a wide range of PMI conditions here such that gross erosion (i.e. Y) is highly variational compared to redeposition. Theoretically, the non-α PMI parameters we have considered are stable during L- and inter-ELM H-mode operations, and they may be forced back quickly to ideal conditions after a transient event. Meanwhile, transient events can cause α to remain permanently deformed until the PFC tile may be exchanged during reactor offline maintenance. Thus, even if α is a secondary parameter setting net erosion within the larger PMI parameter space, the relative invariance of the Y-setting PMI parameters during normal operations may exacerbate the importance of α to net erosion over reactor-relevant lifetimes. For these reasons we will set $Y * f_{mechanism}$ metrics of net erosion aside for the remainder of this dissertation, since they may provide a misleading indication of the fully-integrated sensitivity of net erosion to all PMI parameters. In the meantime, we will continue

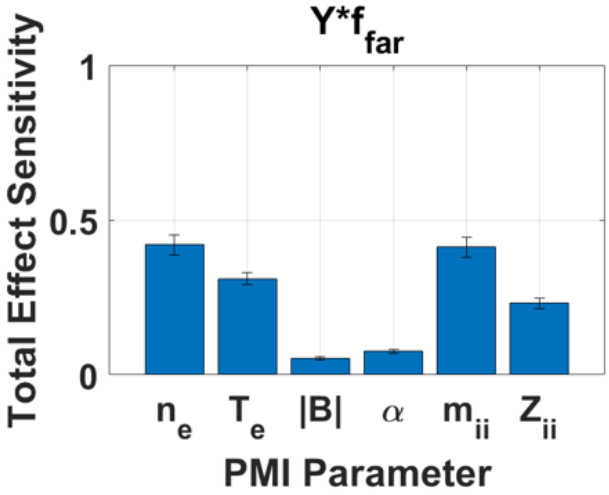

Figure 6.31: Total-effect sensitivity index for $Y * f_{far}$ against input PMI parameters n_e, T_e, $|\vec{B}|$, α, m_{ii}, and Z_{ii}.

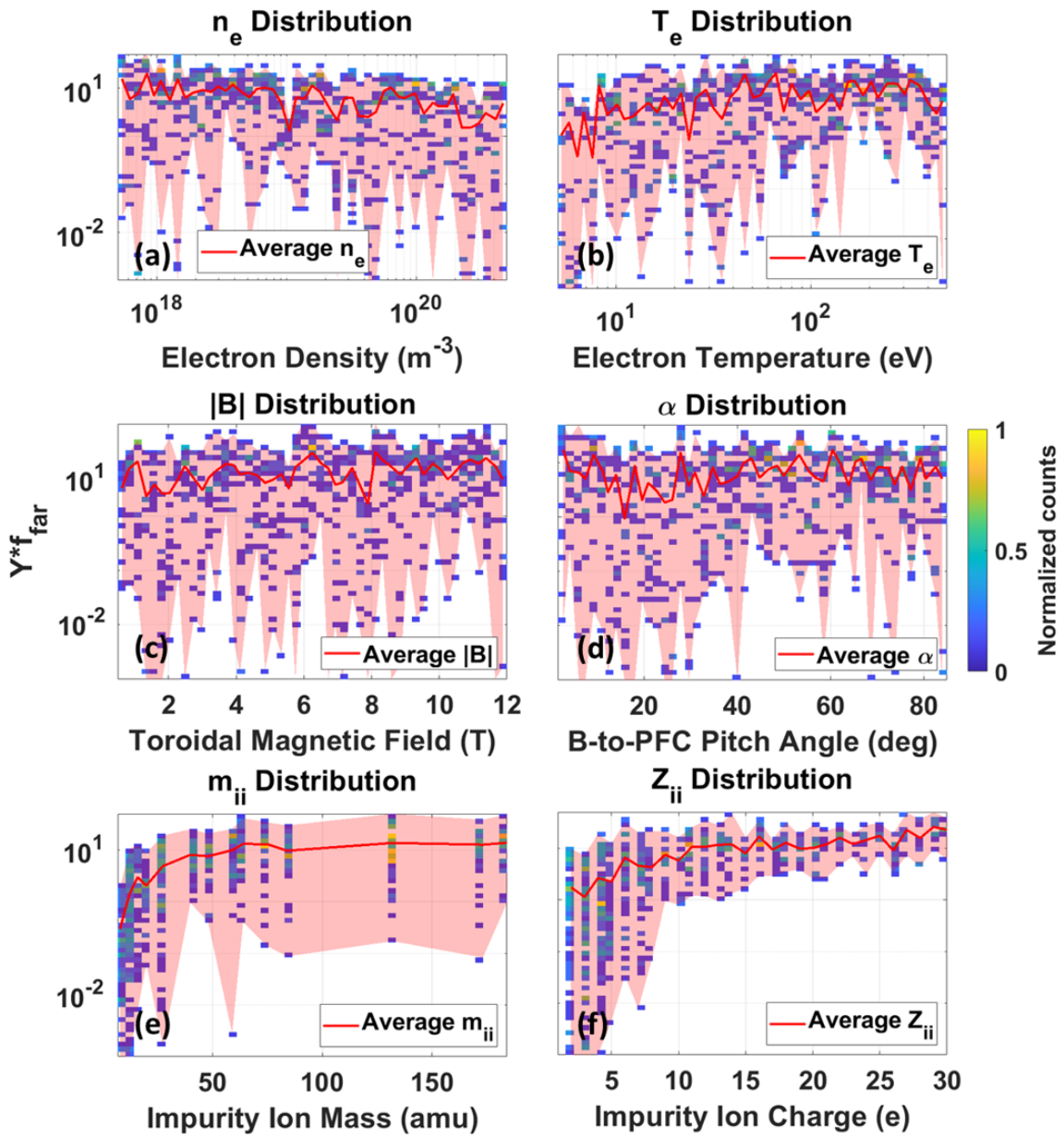

Figure 6.32: Histograms of raw $Y * f_{far}$ data (normalized to the maximum bin count) vs input PMI parameters (a) n_e, (b) T_e, (c) $|\vec{B}|$, (d) α, (e) m_{ii}, and (f) Z_{ii}. The bin-averaged trend is shown in red, with the range of averaging shaded in pink for clarity.

to focus on α's importance to the three redeposition mechanisms and especially the new finding that α is as important as n_e and T_e in setting the fraction of particles entering the SOL, which itself requires rigorous validation (see Chapter 7).

As we conclude this section, we should take a step back from the heavy-handed analysis and interpretation of Sobol' indices and review what we have learned. First, we have recovered f_{far} trends similar to the ERO scan of n_e and T_e discussed in Chapter 4 (53). Second, we have conclusively shown that α is as important of a parameter as the plasma conditions in setting SOL-losses, confirming the implications of our analysis in Chapter 5. This fact dictates that there is a critical need to estimate α evolution across PFCs as we make next-step device projections, especially as ITER switches to being a full W device.

Now, we have assumed throughout this study that our PFCs are in a sputtering-limited regime (i.e. no PFC melting is modeled). One of the implications from subfigure (b) of Figure 6.26 is that increasing the temperature necessarily reduces net erosion, but this statement is not true in all likelihood because of thermal processes. Meanwhile, increased n_e will eventually enter collisional sheath regimes, which require better sheath models (i.e. particle-in-cell codes like hPIC (70)) to simulate accurately. Our model has pushed the limits of the acceptable regimes of application to numerically generate a wide range of conditions; better models should be applied in the high n_e (i.e. collisional) and high T_e (i.e. thermal) cases to improve this work. Nonetheless, we expect the α sensitivity of f_{far} to only increase in each of those cases due to the stronger potential gradients and/or thermal fluxes at steep α.

Lastly, we present a refinement of Figure 5.18 using the entirety of the Sobol' analysis dataset in Figure 6.33. We generated this figure by applying a simple curve fit to the dataset used throughout Chapter 6. This fit is not intended to be predictive and indeed has a large ($\leq 5\times$) residual; rather it is qualitatively illustrative of the combined effect of n_e, T_e, and α in setting the f_{far} fraction. We note that next step devices like ITER are intended to sit comfortably in the $p \ll 1$ parameter space, where α is less likely to change the far fraction dramatically even at $\sim$normal

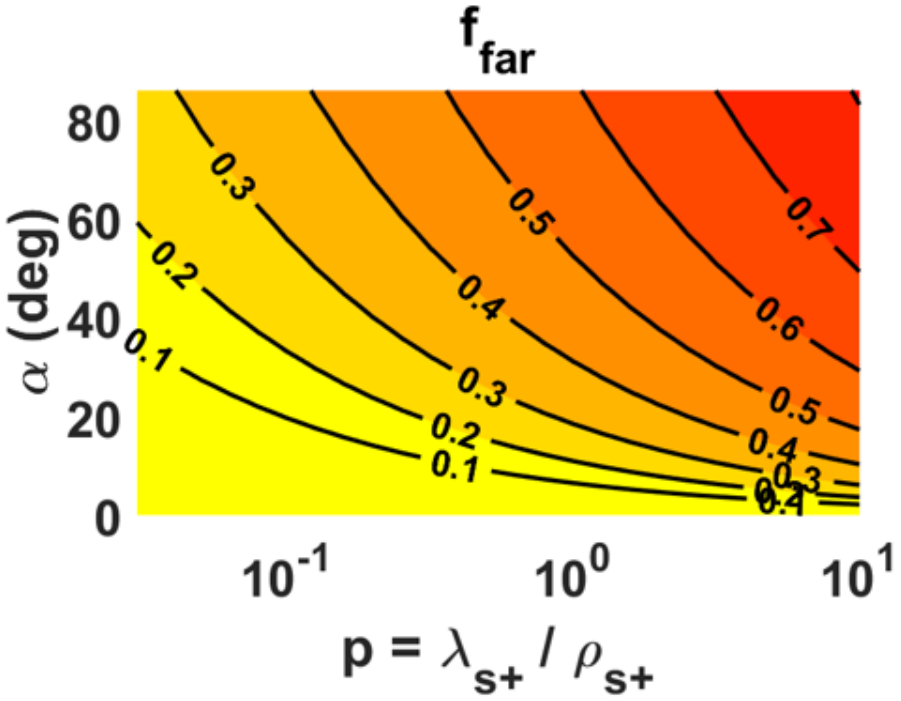

Figure 6.33: Far redeposition fraction as function of p and α, using a simple curve fit to the entire Sobol' analysis dataset.

incidence. Even so, other effects at sharp α (e.g. melting, etc.) could exacerbate its importance even in the small p regime; again, this curve fit has large residual, so the exact f_{far} magnitudes may be under-predicted in this p regime as well. The critical takeaway here is that our early modeling workflow predicts a heretofore unexplored dependence in redeposition on the $\vec{B}$-to-PFC pitch angle through prompt-vs-local redeposition trade-off; these implications must be measured experimentally to test their validity and to refine future modeling efforts.

6.3 Executive Summary

- Sobol' indices determine leading-order parameters in a model by quantifying the fractional dependence of output variance on input variances.
- A Latin hypercube sampling of important plasma-material interaction parameters enables Sobol' analysis of the entire PYEAD-RustBCA-GITR coupled workflow.
- The leading-order parameters determining PYEAD outputs are the electron temperature, the incident ion mass, the incident ion charge, and the magnetic-field-to-material pitch angle, α.
- The leading-order parameters determining PYEAD-RustBCA outputs (i.e. gross erosion) are the same parameters isolated in just the PYEAD code.
- The leading-order parameters determining PYEAD-RustBCA-GITR outputs (i.e. redeposition) are the electron temperature, the electron density, and α.
  - Prompt redeposition is most sensitive to electron density and temperature.
  - Local redeposition is most sensitive to α.
  - Far transport is sensitive to the inherited parameters from prompt-vs-local trade-off.

- The pitch angle α is as important as the commonly studied plasma parameters (i.e. electron density and temperature) in setting the fraction of high-Z material entering the SOL.

Chapter 7

A "Design-of-Experiment" for Assessing Net Erosion

7.1 Motivation and Methodology

In Chapter 5 we demonstrated the importance of the $\vec{B}$-to-PFC pitch angle α in affecting the entirety of high-Z net erosion: not only gross erosion through a change to the incident and sputtered EADs but also redeposition through a change to the prompt-vs-local trade-off. In Chapter 6 we reanalyzed the importance of α within the context of a broad range of PMI parameters and conditions, finding that α is as important as n_e and T_e in determining material losses into the SOL. As we discussed in Section 5.1, there is some experimental evidence to suggest that α may locally evolve over reactor-relevant lifetimes at both the nm-μm and mm-cm scale levels due to material cracking, melting events, etc. If the PYEAD-RustBCA-GITR workflow is indeed accurate, this fact suggests that it is critical to quantify the average α evolution in next-step devices in order to anticipate redeposition fractions and extend PFC lifetimes.

Without next-step devices readily present to test these concerns, the recommended path forward is a two-pronged approach for experimentally estimating α's importance

to the net erosion problem. The first approach is analyzing PFC testbeds exposed to either campaign-long, integrated conditions at current facilities or extended, extreme environments at specialized devices (e.g. MPEX (97)). Experiments along these lines improve our understanding of whether α varies significantly over reactor-relevant lifetimes. We have seen a few examples of these techniques in the papers discussed in Section 5.1, yet similar experiments could better estimate lifetime α-evolution as fusion technology improves. Unfortunately, this technique is necessarily slow moving and cannot completely incorporate all relevant PMI parameters (i.e. the ITEP gap). These efforts should be continually pursued but are fundamentally incomplete on their own.

The second approach is validating the α-dependence of net erosion from our model through dedicated experiments at current operational regimes; then, our refined model can be projected into reactor-relevant conditions, with appropriate improvements to the workflow for those n_e and T_e regimes. This approach has been the workhorse of fusion research for decades but is similarly limited in its utility (i.e. the ITEP gap). At present, the research in this dissertation is better suited to propose experiments in this second category. That is, we will use this final chapter to discuss and design hypothetical experiments to test the claims of our work. In this way we round out a comprehensive look at VVUQ (Verification, Validation, and Uncertainty Quantification) analysis of our PMI workflow: We have explored mathematical verification and Sobol' index uncertainty quantification in Chapter 6; now, we push forward towards experimental validation of our model, all within the context of the research question (Sections 5.1 and 6.1): **What are the optimal PMI parameters that maximize high-Z redeposition within the sheath (i.e. surface-scale PMI) and minimize reactors' dependence on SOL processes (i.e. global- scale PMI) to reduce high-Z net erosion?**.

Our general approach will be the following. DIII-D has a dedicated station for *in situ* and *ex situ* analysis of small PFC samples in its lower divertor; this station is called the Divertor Material Evaluation System or DiMES (128), which

we showed in Figure 1.8, and is generally well-diagnosed for PMI studies. We will use this configuration as a basis for our experimental proposal, but nothing about the experimental pathway we will outline in the subsequent sections is inherently unique to DIII-D. Here, we are interested in validating the effect of α at two scale lengths: μm- and mm-scale deformation. As previously mentioned our workflow is designed to study mm-scale deformation, so these experiments will be our primary focus. Although there is precedent for using analytic sheath models at the μm-scale (103), rigorously improving our model for these regimes is a major overhaul; we will only be able to make tentative predictions for surface-roughness experiments at this time.

Here, we suggest experiments using the DiMES-head design sketched in Figure 7.1. The idea here is to provide as many points of diagnostic coverage as possible for net erosion measurements; we will discuss these diagnostics in greater detail in the subsequent sections. First, we want a graphite probe casing in order to minimize the introduction of new elements into DIII-D; recall that DIII-D has a graphite first wall. We fit this probe casing to allow interchange of removable W samples and ideally to include a Langmuir probe (LP) for measuring localized n_e and T_e conditions. Next, we implement an isotopic approach: We design our W samples to include a large ($\sim$cm) spot of one isotope and a nested small ($\sim$mm) spot of a different isotope. The purpose of this design is twofold. First, the large spot of W enables line-of-sight resolution from the divertor UV-spectroscopy diagnostics at DIII-D; we will discuss spectroscopy in greater detail in Section 7.2, but in short this diagnostic provides an *in situ* estimation of both gross erosion and redeposition. Second, the small spot of W enables resolution of *ex situ* surface characterization diagnostics measuring redeposition within the same field-of-view as the spectroscopy; we will discuss these techniques in Section 7.4. Finally, we embed a microtrench within the small spot of W; this technique enables measurement of both the gross erosion and the sheath thickness, and we will discuss this technique further in Section 7.3. We show an early test of a microtrench design for this purpose in an insert of subfigure (a) of

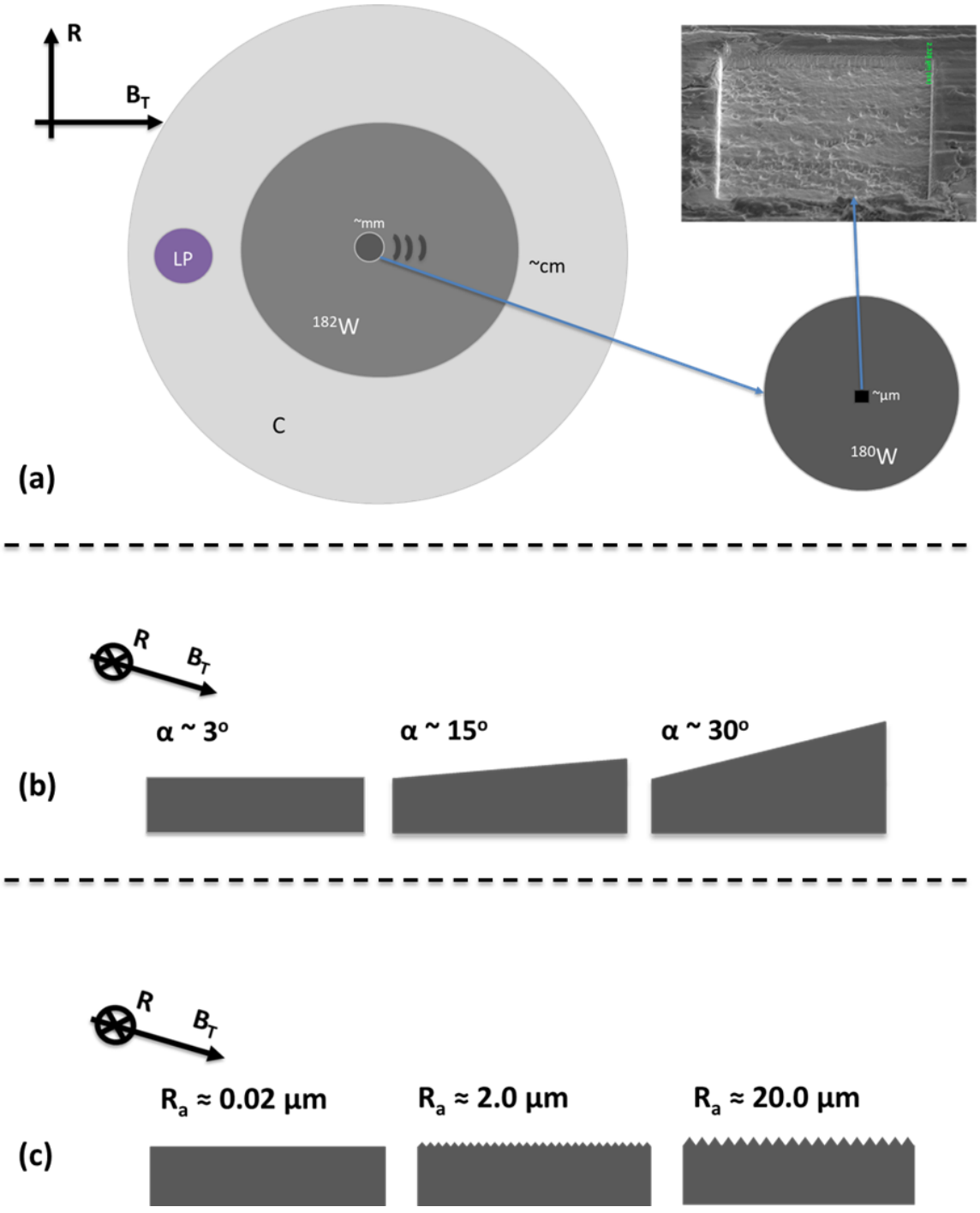

Figure 7.1: Cartoon of idealized DiMES head design. (a) shows the isotopic probe surface with SEM imaging close-ups of early bench-testing of the microtrench design. (b) shows the probe side-view for the mm-scale experiment (not to scale). (c) shows the probe side-view for the μm-scale experiment (not to scale).

Figure 7.1; we used focused ion beam (FIB) instrumentation and SEM imaging to make this design on the bench top at the LAMDA facility at ORNL.

Consistently using the surface design shown in Figure 7.1, we would engineer the W samples themselves in two different categories to test α-variation at different scales of surface deformation. Six samples would be needed in total. First, we would machine three smooth probe surfaces to be at three different degrees of α, as shown in subfigure (b). Exposure and analysis of these probes will provide insight into the importance of the $\vec{B}$-to-PFC pitch angle at the mm scale. Similarly, three flat probes would be engineered at various degrees of surface roughness, shown in subfigure (c), to test the importance of α at the μm scale.

Predictive measurements for these experiments is possible through the use of so-called synthetic diagnostics. Synthetic diagnostics are computational packages that model fundamental physics processes in order to emulate measurement data attached to simulated conditions. Here, synthetic diagnostics will be used to predict the measurability of net erosion trends using our probe design; if these experiments are eventually carried out, this synthetic data can be directly compared with real-world data to aid the interpretation of experimental results. We outline the connection between a physical experiment and its synthetic analog in Figure 7.2. Here, we use ColRadPy (67) to generate synthetic spectroscopy data, MPR to generate synthetic microtrench data, and an analysis routine of our GITR profiles in Figure 4.9 to generate synthetic surface analysis data. We will step through the details and roles of each of these codes in the subsequent sections before analyzing the results from our synthetic experiments.

7.2 Spectroscopic Diagnostics and ColRadPy

To first order, the theoretic principles behind standard line-radiation spectroscopy are relatively simple. Electron transitions between unique, quantized energy levels of an atom, ion, or molecule result in electromagnetic radiation with uniquely

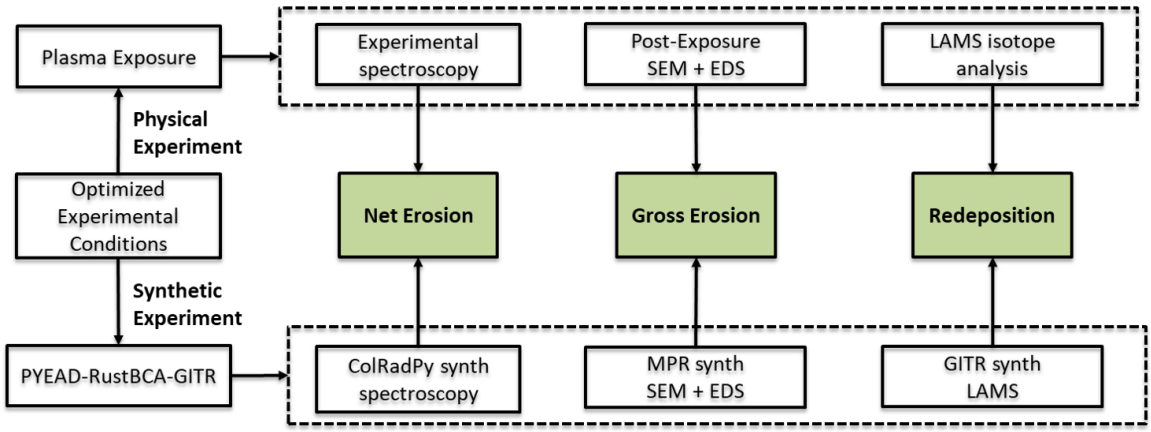

Figure 7.2: Workflow diagram of the connection between the real-world experimental data and the synthetic data we model in this dissertation.

identifiable wavelengths. Measuring these radiations' wavelengths and intensities with a spectrometer (combined with some knowledge about the species in the observed system) allows one to extrapolate information about the physics of the observed matter; note this ability requires quantum-mechanical knowledge of the energy levels associated with the measurement. Note also that radiation in line-radiation spectroscopy is distinct from continuum radiation such as blackbody radiation or bremsstrahlung (63). While such spectroscopy in a vacuum is almost this simple, performing this spectroscopy in a laboratory plasma environment can quickly become complicated. Before discussing these complications, let us start by formalizing the transition of electrons between atomic energy levels.

For simplicity we consider two discrete energy levels $E(i)$ and $E(j)$ and an electron transition from the upper level $E(j)$ to the lower level $E(i)$ (formalized hereafter as $j \to i$). For convenience we will work temporarily in a formalization of frequency instead of wavelength spectroscopy, but the two may be easily converted via proportionality to the speed of light, c. Using the treatment formalized in (76), the frequency ν_{ji} of such a transition is given by:

$$\nu_{ji} = \frac{E(j) - E(i)}{h} \tag{7.1}$$

Here, h is the Planck constant. This transition may occur by two possible means: a spontaneous emission or a stimulated emission. The spontaneous emission corresponds to a relaxation of the electron to a lower energy level. The corresponding change in electron population density n_j at level $E(j)$ may be given proportionally by:

$$-\frac{dn_j}{dt}\bigg|_{j\to i} = A_{j\to i} n_j \tag{7.2}$$

Note that $A_{j\to i}$ is the so-called Einstein spontaneous emission coefficient and represents the $j \to i$ spontaneous transition probability. The corresponding emission

coefficient $\epsilon_{A_{j\to i}}$ for photons emitted for this line is:

$$\epsilon_{A_{j\to i}} = \frac{h\nu_{ji}}{4\pi} A_{j\to i} n_j \tag{7.3}$$

Note that this emission coefficient corresponds to the energy emitted by the radiation per infinitesimal volume, time, and solid angle. Additionally, we emphasize that the measured emission coefficient should be this expression multiplied by a line shape distribution (i.e. Gaussian, Lorentzian, etc.) due to thermal, broadening, and/or instrument effects. Meanwhile, a stimulated emission occurs when incident photons interact with the system. Say the photon is of spectral radiant energy density u_ν. We may describe a similar population density change as the $A_{j\to i}$ case via:

$$-\left.\frac{dn_j}{dt}\right|_{j\to i} = B_{j\to i} n_j u_\nu \tag{7.4}$$

Here, $B_{j\to i}$ is the Einstein stimulated emission coefficient, similarly defined to the spontaneous one. Unlike in the spontaneous case, a reverse process exists for the stimulated case: stimulated absorption. In this case, we describe the change in population density analogously as:

$$-\left.\frac{dn_i}{dt}\right|_{i\to j} = B_{i\to j} n_i u_\nu \tag{7.5}$$

Balancing the particle flow between the three population rate equations above reveals (after some algebraic steps) the following conservation relations:

$$g_i B_{i\to j} = g_j B_{j\to i} \tag{7.6}$$

$$A_{j\to i} = \frac{8\pi h\nu_{ji}^3}{c^3} B_{j\to i} \tag{7.7}$$

Here, g_ξ is the degeneracy of energy level ξ.

Continuing the treatment from (76), we next note the so-called "transition rules," which determine whether a particular electron transition is quantum-mechanically favorable or forbidden. We consider the strength of a transition through its oscillator strength f, which determines the fraction to which a given quantum-mechanical transition represents its analogous classical oscillator. In particular, we have:

$$B_{i\to j} = \frac{q_e^2}{4\epsilon_0 m_e}\frac{1}{h\nu_{ji}} f_{i\to j} \tag{7.8}$$

where ϵ_0 is the electrical permittivity and

$$g_i f_{i\to j} = -g_j f_{j\to i} \tag{7.9}$$

Converting at last to wavelength λ_{ji} spectroscopy, we may define the oscillator strength using the expressions above as:

$$f_{i\to j} = \frac{m_e \epsilon_0 c}{2\pi q_e^2}\frac{g_j}{g_i}\lambda_{ji}^2 A_{j\to i} \tag{7.10}$$

Now, two mathematical relations between the f's are particularly important. One, because f represents the fraction of a classical oscillator, we have a sum to one over all the transitions to the ground state g

$$\sum_j f_{j\to g} = 1 \tag{7.11}$$

Moreover, we have the following sum rule for all radiative transitions from $E(i)$, known as the Thomas-Reiche-Kuhn rule:

$$\sum_{j>i} f_{i\to j} + \sum_{k<i} f_{i\to k} = N \tag{7.12}$$

Here, N is the number of electrons involved in transitions. Finally, we define the line strength S, which in quantum-mechanical theory is given symmetrically by:

$$S_(i,j) = S_{i\to j} = S_{j\to i} = |\langle\Psi_i|T^{(n)}|\Psi_j\rangle|^2 \tag{7.13}$$

As usual, Ψ_ξ represents the wave function of energy level ξ. Furthermore, $T^{(n)}$ is the multipole (of order n i.e. 1=dipole, 2=quadrupole, etc.) transition matrix element, of electric (E) or magnetic (M) type. The line strength is related to the oscillator strength via a dependence on $T^{(n)}$ type. For example, in the E1 (electric dipole) case:

$$g_i f_{i\to j} \approx 30.376\frac{S(i,j)}{\lambda_{ji}} \tag{7.14}$$

Here, $S(i,j)$ is in atomic units and λ_{ji} is in nanometers. The transition rules for E1, M1, and E2 are shown in Table 7.1. We will primarily concern ourselves with electric dipole transitions here.

With the basic theory of electron transitions now formalized (76), we turn our attention to an important complexity to performing spectroscopy measurements in a laboratory plasma environment as opposed to the isolated system above. Namely, the above assumes an isolated system of either one particle or a system of particles in complete thermal equilibrium (76). However, the duration of plasma discharges at current experimental devices may not necessarily allow the plasma to reach complete thermal equilibrium or even local thermal equilibrium. Therefore, collisional radiative models are often necessary to solve the plasma kinematics numerically; if no equilibrium is achieved, time-dependent calculations may be necessary (63). We will call out a few key features of these models below.

We may define complete thermal equilibrium as an equilibrium in which (I) all the atoms, ions, etc. have a Boltzmann distribution and (II) all possible electron transitions have a radiating energy density at the blackbody level of the system temperature (63). Local thermal equilibrium relaxes condition (II) above, allowing

Table 7.1: Table of transition (or selection) rules for a few important transition types (76).

E1	$\Delta L = 0, \pm 1$	$\Delta S = 0$	$\Delta J = 0, \pm 1$	$0 \to 0$ forbidden for L and J
M1	$\Delta L = 0$	$\Delta S = 0$	$\Delta J = 0, \pm 1$	$0 \to 0$ forbidden for L and J
E2	$\Delta L = 0, \pm 2$	$\Delta S = 0$	$\Delta J = 0, \pm 1 \pm 2$	$0 \to 0$ forbidden for L and J
				$\frac{1}{2} \to \frac{1}{2}$ forbidden for J
				$0 \to 1$ forbidden for L and J

for non-thermal radiation (63). However, even this regime may still be an invalid assumption at experimental plasma timescales. Typically, achieving local thermal equilibrium requires high densities such that collisional transitions dominate radiative transitions (63); this achievement is usually impossible for low energy levels where the change in energy ΔE is larger. A general guideline for achieving local thermal equilibrium is (63):

$$n_e \gg 10^{19} T_e^{1/2} (\Delta E)^3 \tag{7.15}$$

where T_e and ΔE are in eV and n_e is in m^{-3}.

Consequently, we must consider more than the simple electron/photon interactions above. Indeed, we need to account for five critical electron processes (63): (1) radiative bound-state transitions, (2) radiative ionization/recombination free-bound transitions, (3) collisional electron-impact transitions, (4) collisional ionization/recombination transitions, and (5) collisional dielectronic recombination / autoionization. Note that (1-2) are the spontaneous/photon-induced transitions we have discussed so far and (3-4) are their electron-collisional analogues. The (5) process occurs when an atom captures a free electron into its upper energy levels, forwarding that electron's energy loss into exciting a lower-level electron (or vice-versa) (63). Hence, we must include collisional cross-sections, the analogue of the Einstein coefficients above, into the collisional radiative model. Depending on the timescale, we may further require time-dependent derivations of these cross-sections (and the Einstein coefficients).

A useful piece of information to extract from spectroscopy data (and the reason we are interested in this diagnostic) is the amount of a species that is present in the observed system. This process is particularly useful for determining PFC net erosion yields, exploiting the relationship between photon and particle fluxes. Suppose that the incoming particle flux of W (as the relevant example, but the same analysis holds generally for other species) is given by Φ_W, the density by n_W, the total integrated photon flux by I_{tot} (with branching ratio Γ_B), the ionization rate by $\langle \sigma_I \nu_E \rangle$, and the

excitation rate by $\langle \sigma_{Ex} \nu_E \rangle$, corresponding to a measurement in a plasma over spatial limits r_1 and r_2. Then, the particle flux is related to the other variables by (93):

$$\Phi_W = 4\pi \frac{I_{tot}}{\Gamma_B h\nu} \frac{\int_{r_1}^{r_2} n_W(r) n_e(r) \langle \sigma_I \nu_E \rangle (r) dr}{\int_{r_1}^{r_2} n_W(r) n_e(r) \langle \sigma_{Ex} \nu_E \rangle (r) dr} \tag{7.16}$$

Unfortunately, this expression has little practical use; it requires a higher precision of the particle velocity's radial distribution than can be achieved experimentally (93). Nevertheless, we may solve it under iterations. Assuming a weak spatial dependence for $\langle \sigma_I \nu_E \rangle$ and $\langle \sigma_{Ex} \nu_E \rangle$, the ratio of integrals trends to unity, becoming (93):

$$\Phi_W = 4\pi \frac{I_{tot}}{\Gamma_B h\nu} \frac{\langle \sigma_I \nu_E \rangle}{\langle \sigma_{Ex} \nu_E \rangle} = 4\pi \frac{I_{tot}}{h\nu} \frac{S}{XB} \tag{7.17}$$

These so-called S/XB ratios are obviously temperature and density dependent but form a concrete connection between photon and particle fluxes if well-known. We can use these S/XB ratios to determine (*in situ*) the amount of spatially-localized, net-eroded W material through characteristic W emission lines of gross erosion and redeposition.

The work by Brezinsek (15) experimentally determined such S/XB ratios by seeding WF_6 at the well-diagnosed limiter of the TEXTOR device, validating the computational work by Pospieszczyk (93). A schematic of the experimental setup is shown below in Figure 7.3. The original Pospieszczyk (93) paper proposed several W I (corresponding with neutral W^0) and W II (W^+) emission lines for PFC erosion studies that were prevalent in the experimental spectrum of TEXTOR; the paper calculated the S/XB coefficients for these lines, shown in Table 7.2, using the ATOM collisional radiative model code. Across multiple papers (13; 15), Brezinsek seeded WF_6 because it rapidly dissociates into neutral W^0 and ionizes to W^+; these studies puffed a known amount of WF_6 gas into the device while simultaneously spatially characterizing their spectroscopic emission with a filtered 2D camera. In the more recent study (15), a refined list of the W I and W II lines are called out, owing to their

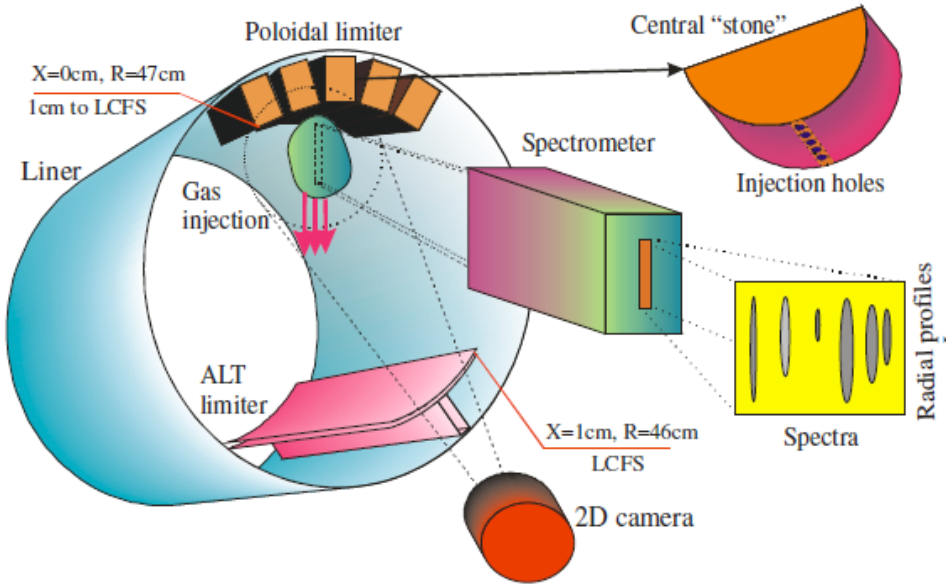

Figure 7.3: TEXTOR experimental setup for measuring S/XB ratios from known fluxes of puffed WF_6 (93).

Table 7.2: Tables of W I and W II lines identified in the TEXTOR spectra, potentially useful for analyzing surface-scale net erosion (93). Table (a) contains spectroscopic identifiers, including quantum configurations and wavelengths. Table (b) contains S/XB values for important W I and W II lines.

Ion	Wavelength (nm)	Rel. Int.	$A_{ki}(s^{-1})$	Configurations			Terms		
W II	276.426 068	182	4.79×10^7	$5d^4(^5D)6s$	–		^6D	–	
W II	361.379 036	133	1.15×10^7	$5d^4(^5D)6s$	–		^4D	–	
W I	361.7522	500	1.1×10^7	$5d^5(^6S)6s$	–	$5d^4 6s(^6D)6p$	^7S	–	$^5P^\circ$
W I	363.1953	200	1.3×10^6	$5d^4 6s^2$	–	$5d^4 6s(^6D)6p$	^5D	–	$^5D^\circ$
W II	364.140 78	113	9.91×10^6	$5d^3 6s^2$	–		^4F	–	
W II	364.559 609	134	1.46×10^6		–	$5d^3(^4F)6s(^5F)6p$		–	$^6G^\circ$
W I	400.8749	1000	1.63×10^7	$5d^5(^6S)6s$	–	$5d^5(^6S)6p$	^7S	–	$^7P^\circ$
W II	434.811 30	109	5.06×10^6	$5d^4(^5D)6s$	–		^4D	–	

(a) ↑

(b) →

	W I		W II	
λ (nm)	400.9	429.5	434.8	364.1
Intensity (au)	2.22×10^4	1.72×10^4	1.92×10^3	4.25×10^3
S/XB at 20 eV $T_W = 4$ eV	60	112	6000	2500
S/XB at 20 eV $T_W = 1$eV	57	106	1423	666
$Flux_{4eV}$	1.33×10^6	1.93×10^6	11.5×10^6	10.6×10^6
$Flux_{1eV}$	1.27×10^6	1.82×10^6	2.73×10^6	2.83×10^6

especial prevalence in the visible and near-UV regions of the spectrum. Modeling of the spectra is in good agreement with the experimental measurements; see Figure 7.4. Here, the S/XB values are compared against the ADAS spectroscopic database, with the W I lines in good agreement and the W II line within a factor of two. We may use W I intensity, combined with S/XB, as a measure of gross erosion and W II, combined with S/XB, as a measure of prompt redeposition (71).

Numerous experiments over the years have taken inspiration from the TEXTOR studies, in particular the choice of wavelengths and corroborated S/XB values. Importantly, the earlier TEXTOR study (13) applied its own findings to the W/C limiter within the device. The line ratio of W II (434.8 nm) to W I (400.9 nm) intensity places a lower bound on surface-scale redeposition at 50%. An earlier study by Dux (41) at ASDEX Upgrade had also used the 400.9 nm W I line in comparison with marker probes to determine that, while the divertor marked the biggest poloidal location of W erosion, the low-field limiters marked the biggest source of W contamination to the core. A JET study in 2013 (123), considered both W I (400.9 nm) and W II (364 nm) emissions at the divertor targets using the S/XB values from TEXTOR. Notably, this study recovered the original assessment made by the TEXTOR team (13) that surface-scale redeposition could be bounded below at 50% via the ratio between S/XB values at different electron densities. In particular, we note that S/XB becomes (S+R)/XB when accounting for redeposition (123), and (for density a and density b):

$$\frac{(\Phi_{WII}/\Phi_{WI})_a}{(\Phi_{WII}/\Phi_{WI})_b} = \frac{S + R_b}{S + R_a} \tag{7.18}$$

Solving for R in terms of S allows for the 50% bound under the a and b considered; they calculated higher redeposition for higher electron temperatures and density, as we demonstrated in Chapter 6.

At time of writing, W I emission lines (especially the 400.9 nm line) are still used for *in situ* gross erosion measurements (14; 71; 73; 52) but campaign-integrated coupons remain the industry standard for monitoring redeposition. W II emission lines

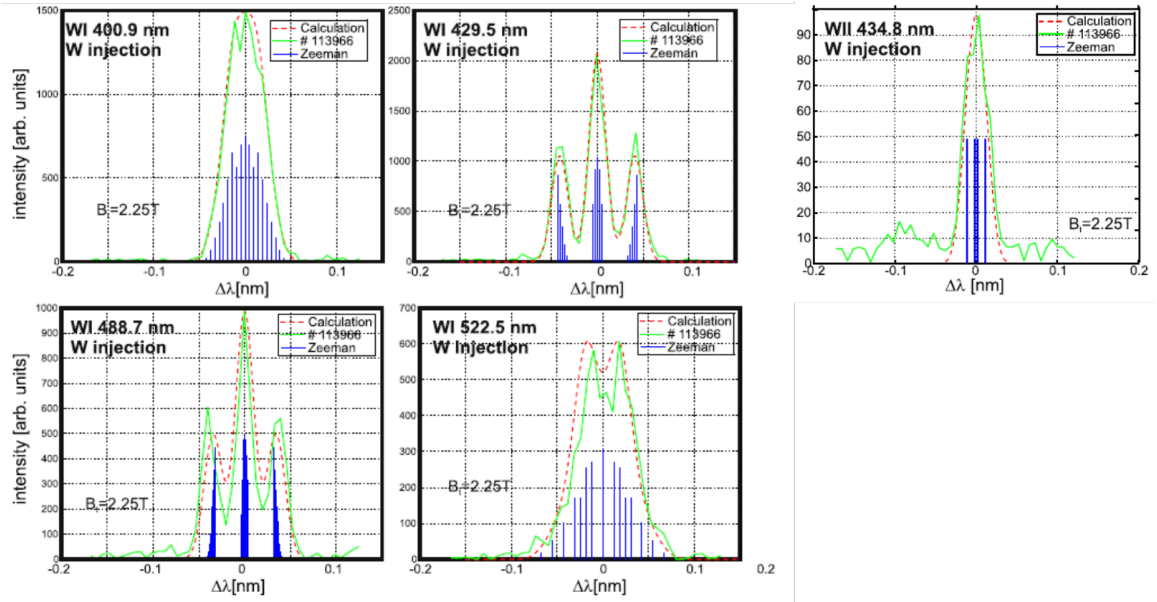

Figure 7.4: Comparisons between simulation and experimental spectroscopy from the TEXTOR study (15), which cross-validates the S/XB results.

have been met with some success as a prompt redeposition diagnostic, but significant local redeposition fractions indicate that many higher charge states of W are needed for accurate spectroscopic measurement of net erosion. To this end the dissertation by Johnson (66) identified some higher charge W emission lines that could be useful as net erosion diagnostics; we tabulate a few of these emission lines of interest in Table 7.3. Research into the practicality of these lines using the UV-spectroscopy system at DIII-D is ongoing to date.

Lastly, we now turn to our synthetic analog of W emission spectroscopy; here, we use ColRadPy (67), which is a collisional radiative code. As with all collisional radiative codes, four processes are critical to understanding population levels. These are electron impact excitations/deexcitations (q), electron impact ionizations (S), electronic recombinations (R), and spontaneous emissions (A) (67). ColRadPy assumes that photon-electron processes are overshadowed by electron-electron processes and ignores them. As an example of the kind of processes considered by ColRadPy, we will reproduce its standard example (67) for a system with two adjacent charge states having both ground and metastable states; metastable states are energy levels through which decay is essentially forbidden by quantum-mechanical transition rules (e.g. Table 7.1). In particular, let the σ_1 subscript represent the lower-charge ground state, σ_2 represent the lower-charge metastable state, ν_1 represent the upper-charge ground state, ν_2 represent the upper-charge metastable state, and i represent the excited levels of the lower charge state. Then, we may solve the following equations for the density n of each level:

$$\frac{dn_{\sigma_1}}{dt} = -n_e \left(\sum_{j \neq 1} q^e_{1 \to j} + S_1 \right) n_1 + \sum_{j \neq 1} (A_{j \to 1} + n_e q_{j \to 1}) n_j + n_e \sum_k R_{\nu_k \to \sigma_1} n_{\nu_k} \quad (7.19)$$

$$\frac{dn_{\sigma_2}}{dt} = -n_e \left(\sum_{j \neq 2} q^e_{2 \to j} + S_2 \right) n_2 + \sum_{j \neq 2} (A_{j \to 2} + n_e q_{j \to 2}) n_j + n_e \sum_k R_{\nu_k \to \sigma_2} n_{\nu_k} \quad (7.20)$$

Table 7.3: Emission lines measured at CTH against the NIST database or identified using ColRadPy without NIST-wavelength correction (66).

Emission Line	**Wavelength (nm)**	**Relative Intensity**	**Energy Transition $E_i - E_k$ (cm^{-1})**
W I	265.65	300	2951.29 - 40583.07
W I	255.13	200	0.00 - 39183.20
W I	400.88	1000	2951.29 - 27889.68
W II	265.80	139	1518.829 - 39129.460
W II	276.43	182	0.00 - 36165.356
W III	224.86		28977.44 - 73289.66
W IV	255.01		46087.55 - 85289.99
W V	77.43		0.00 - 128997.1

$$\frac{dn_i}{dt} = -n_e \left(\sum_{j \neq i} q^e_{i \to j} + S_i \right) n_i + \sum_{j \neq i} (A_{j \to i} + n_e q_{j \to i}) n_j + n_e \sum_k R_{\nu_k \to i} n_{\nu_k} \tag{7.21}$$

$$\frac{dn_{\nu_1}}{dt} = n_e \left(\sum_j S_j n_j \right) - n_e n_{\nu_1} \sum_j R_{\nu_1 \to j} \tag{7.22}$$

$$\frac{dn_{\nu_2}}{dt} = n_e \left(\sum_j S_j n_j \right) - n_e n_{\nu_2} \sum_j R_{\nu_2 \to j} \tag{7.23}$$

Under quasistatic conditions, we assume $(dn_i)/dt = 0$; however, the ground and metastable populations vary with the plasma conditions (67). ColRadPy solves the excited state populations as a matrix inversion (67), where:

$$\begin{bmatrix} n_3 \\ n_4 \\ \vdots \\ n_N \end{bmatrix} = \begin{bmatrix} C_{33} & C_{34} & \dots & C_{3N} \\ \vdots & \vdots & \ddots & \vdots \\ C_{N3} & C_{N4} & \dots & C_{NN} \end{bmatrix}^{-1} \begin{bmatrix} -C_{31} n_{\sigma_1} - C_{32} n_{\sigma_2} - R_3 n_{\nu_1} - R_3 n_{\nu_2} \\ -C_{41} n_{\sigma_1} - C_{42} n_{\sigma_2} - R_4 n_{\nu_1} - R_4 n_{\nu_2} \\ \vdots \\ -C_{N1} n_{\sigma_1} - C_{N2} n_{\sigma_2} - R_N n_{\nu_1} - R_N n_{\nu_2} \end{bmatrix} \tag{7.24}$$

such that we have (67):

$$n_i = \sum_\sigma -n_\sigma \sum_j C'^{-1}_{ij} C_{j\sigma} + \sum_\nu n_\nu \sum_j C'^{-1}_{ij} R_{j\nu} \tag{7.25}$$

where C' is the reduced collisional radiative matrix, having elements that are variable substitutions from the previous five equations. Computing this streamlined linear-algebra expression forms the backbone of the code.

Continuing (67), the script allows the user to select which levels are metastable. ColRadPy treats those non-ground states that are not marked as metastables as excited states: assumed to be in equilibrium with the ground state. Consequently, it sets dn/dt to 0 for metastable levels. From the excited populations, ColRadPy can define extractable coefficients (called GCR coefficients) representing the sum of the possible ways a process can occur. For our purposes of extracting S/XB values, the most important two are SCD (the total ionization from one charge state to another)

and PEC (correlated to the spontaneous emission coefficient); we may define S/XB computationally as SCD/PEC. Explicitly, the metastable-resolved (μ-indexed) S/XB is defined as (68):

$$\frac{S}{XB_{j\to i}} = \frac{\sum_\mu SCD_\mu(n_\mu/n_{tot})}{\sum_\mu PEC_{\mu,j\to i}(n_\mu/n_{tot})} \tag{7.26}$$

Figure 7.5 shows example PEC and SCD values for various W I transitions. Note the high dependence of the total equilibrium temperature dependence (represented by the black dashed line) upon certain metastable population levels for both PEC and SCD values, emphasizing the importance of including metastable populations in the model (68). For example, the total SCD for W I depends most strongly on the $^5D_0$ transition. In some cases, like subfigure (b) of Figure 7.5 at 253.36 nm, the total equilibrium value is almost completely determined by a single metastable. Metastable line identification is an ongoing process; we will not be able to include them in our calculations at present, but these should be included in future work. With the basic theory of spectroscopy and the computational process of ColRadPy now summarized, we turn our attention to the next diagnostic technique: microtrenches.

7.3 Microtrench Diagnostics and MPR

While spectroscopic theory can be complicated to explain and digest, microtrench diagnostics are relatively simple, though brilliant, diagnostic innovations. The functionality relies almost entirely on incident ion energy and angle distributions, which we have comprehensively explained in Section 3.3, and basic geometric principles. Pioneered in the dissertation by Coburn (29), the general principle is that a small (μm-dimensions) trench is etched into the surface of a removable material coupon using FIB or some similar ablative technique. As discussed before, we expect our incident ions to have some angular distribution with a shifting center that depends on sheath conditions. Note that, as these ions enter the trench, they will travel some distance w_{P1} from the leading edge before striking the surface; this distance varies

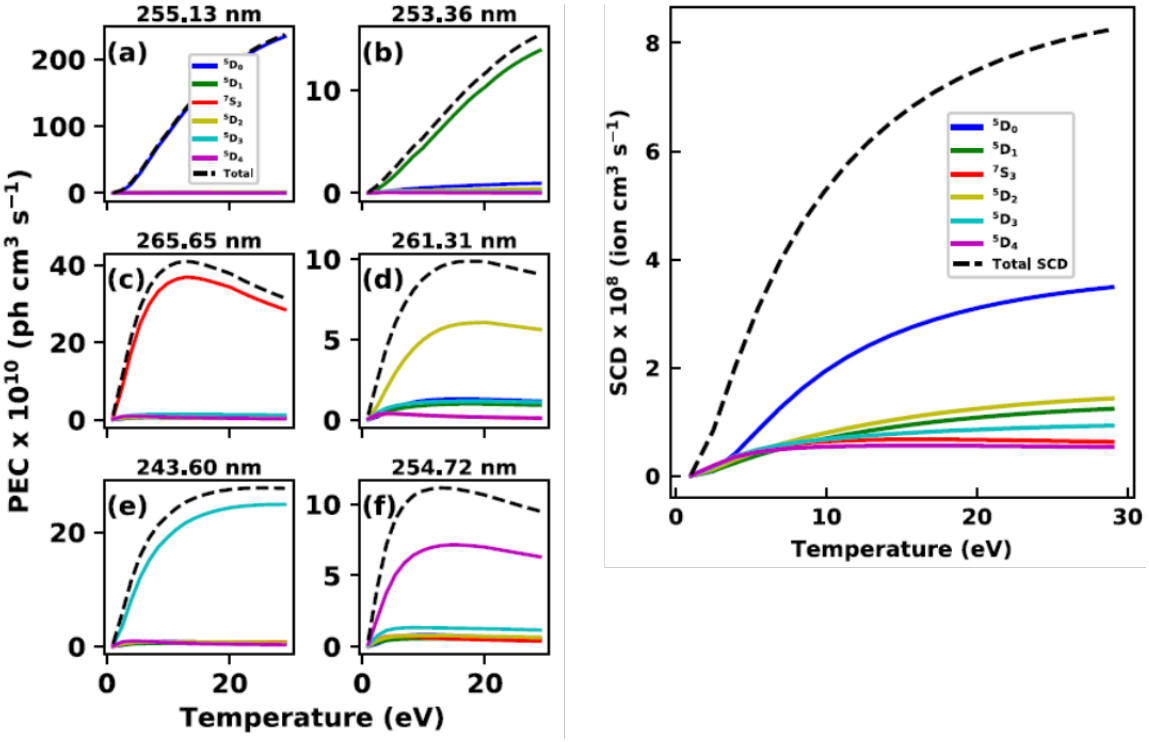

Figure 7.5: ColRadPy-computed PEC and SCD values for some W I emission lines (68).

from ion to ion but is the direct, trigonometric result of the ion's θ value. From the implantation/erosion pattern and the associated shaded region on the microtrench floor, we can perform a geometric backcalculation to determine the average θ. The method for ϕ is essentially the same. We show example data (1) from a microtrench study in Figure 7.6, showcasing the major angles.

Microtrenches provide two important experimental functions for net erosion studies. First, as mentioned, the floor pattern and associated distribution in θ and ϕ is uniquely determined by the sheath conditions (Section 3.3); using a code like PYEAD, we can restrict the inputs of the EAD simulation to match the local conditions at the microtrench and, after iteration of free variables like k, determine the experimental value of L_{MPS}. This approach has been met with success in DIII-D, restricting $k \approx 3$ using PYEAD's IDL forerunner ieadrk3 (2). Second, the microtrench edges will erode slightly over time; using fiducial markers and pre/post-exposure imaging, it is possible to measure gross erosion from the depth change of the downstream edge. To guide the understanding, we show a very extreme example of microtrench erosion in Figure 7.7. We can use this secondary analysis as a means of cross-validating gross erosion measurements from W I spectroscopy.

To aid the analysis of microtrench patterns, Coburn and Lasa devised and modified the MPR code, which analyzes ion impacts for rough surfaces (29; 30). Two branches of this code currently exist at time of writing: one for an analytically described, sinusoidal surface pattern and one for a microtrench structure; Abe further refined this second branch for his L_{MPS} measurements. In both cases, the MPR approach is as follows (77). Before calculation, we describe an analytic surface with surface height:

$$z_s = A_x \sin(x/f_x) + A_y \sin(y/f_y) \tag{7.27}$$

in the sinusoidal case, where z_s is the surface height from its minimum point, A_x/A_y is the surface amplitude in x/y and f_x/f_y is the oscillation frequency in x/y. Alternatively, we may give a microtrench surface with four sides described by height

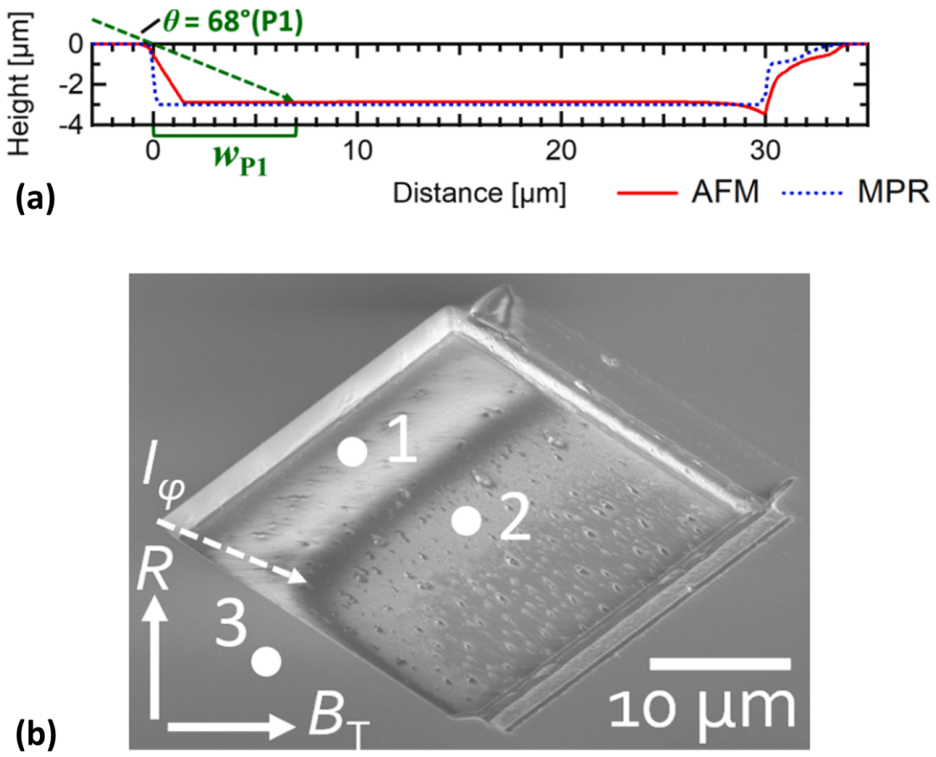

Figure 7.6: Microtrench AFM data (a) and SEM image (b) showcasing the practical uses of microtrenches for determining EADs (1). Note that, here, $\theta = 90° - \theta$ as defined in Figure 3.1 and $I_\phi = \phi$ in the same figure.

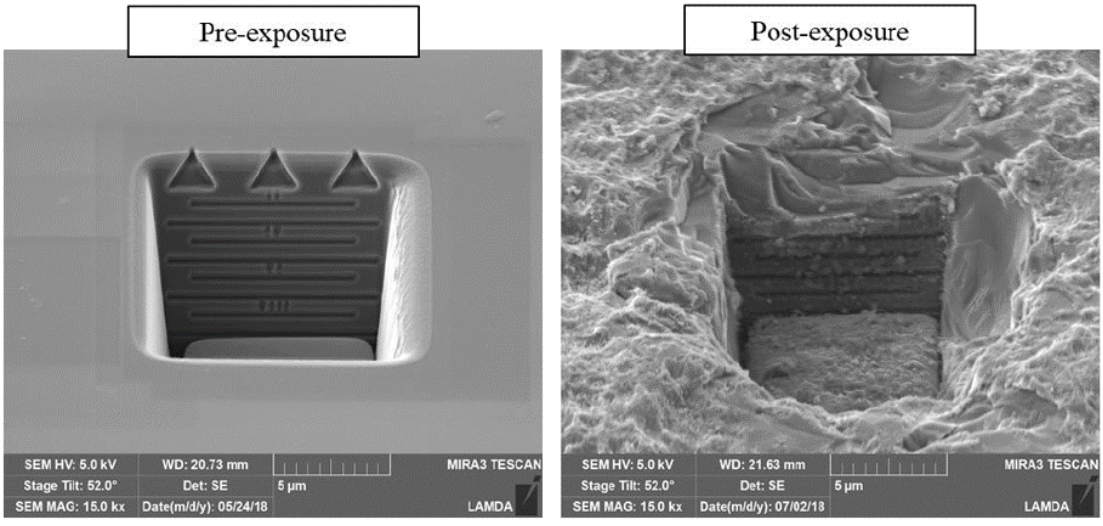

Figure 7.7: SEM images of a Si_3C_2 microtrench pre- and post-exposure, with gross erosion interpretable from fiducial depth markers (29).

z_s of form:

$$z_s = A\tanh(S\xi) + B\tanh(R\xi - C) \tag{7.28}$$

where S and R describe the primary and secondary slope, A and B are constants describing the height with $A < B$, C is an offset where the secondary slope begins, and ξ is either x or y.

From here the Monte Carlo computational steps are the same. We initialize each ion to a random starting position above the surface and set their linear trajectories with initial angle conditions θ_{in} and ϕ_{in}; large, mm-scale gyro-orbits compared to the μm-scale surface variation enables an assumption of straight-line trajectories. Through iteration with Abe, we have been able to directly couple PYEAD distributions to MPR rather than assume constant θ_{in} and ϕ_{in} for each particle. Then, we calculate the surface-modified local θ_{loc} based on the geometric intersection of the particle trajectory and the analytic surface. Next, the code makes a rough approximation of gross erosion yield using Equations 3.4 and 3.7; only certain data tabulations for the free parameters in these equations are available, taken from the book by Eckstein (43): D→W at E_{ii} =250 eV and N→W at E_{ii} =50, 100, 250, or 300 eV. Lastly, the eroded particles sample from a cosine δ, uniform azimuthal distribution; the code determines, again using straight trajectories, if any of these particles geometrically redeposit based on the roughness of the initialized surface. Figure 7.8 provides an illustration of the underlying geometry. We will use the sinusoidal surface to handle surface roughness in the synthetic analog of our μm-scale experiments and use the microtrench surface to predict L_{MPS} estimations. Now, we will switch topics to the final diagnostic of interest: surface analysis techniques.

7.4 Surface Characterization Diagnostics and GITR

Here, we will provide a final bit of diagnostic background for the *ex situ* surface analysis of our idealized DiMES head experiment. Perhaps the most common

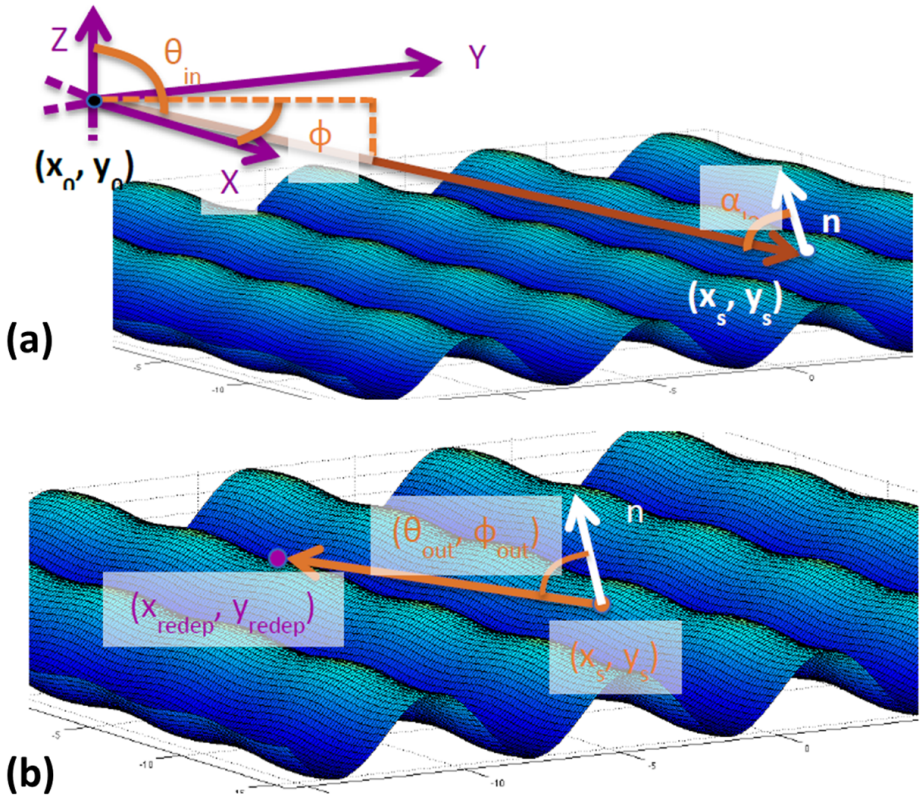

Figure 7.8: Geometry of the incident ion (a) and sputtered neutral (b) angles from the original MPR manual (77). Note the geometry and variables in this figure are different from what was established in Figure 3.1. We will convert all MPR outputs in this dissertation to the Figure 3.1 coordinates before discussing them. Note especially that $\alpha_{in} = \theta_{loc}$ in our formalism.

diagnostic for surface analysis in PMI experiments is Rutherford backscattering spectroscopy (RBS). This technique is only lightly destructive; in principle, we bombard the material surface with a monoenergetic beam of $^4He^+$ ions, and detect the energies of the backscattered ions (96). We may uniquely determine the localized makeup of the material via the cross-sectional energy transfer between its constituent atoms and the incident $^4He^+$. (96). Indeed, the residual energy E_r of the $^4He^+$ (of mass m_{He}) after scattering is uniquely determined by its incident energy E_i, the angle of detection ϕ_d, and the mass of the target particle m_T via (96):

$$E_r = \left(\frac{m_{He} \cos(\phi_d) + \sqrt{m_T^2 - m_{He}^2 \sin^2(\phi_d)}}{m_{He} + m_T} \right)^2 E_i = k_s^2 E_i \tag{7.29}$$

Here, k_s is the so-called scattering parameter. We show a schematic of the definitions in Figure 7.9. The differential cross-section $d\sigma$ represents the probability of the $^4He^+$ ion backscattering after collision with the target atom (96)):

$$\frac{d\sigma}{d\phi_d} = \frac{\left(\cos(\phi_d) + \sqrt{1 - \left(\frac{m_{He}}{m_T} \sin(\phi_d) \right)^2} \right)^2}{\sqrt{1 - \left(\frac{m_{He}}{m_T} \sin(\phi_d) \right)^2}} \tag{7.30}$$

If a $^4He^+$ particle avoids reflection within the first material layer of the target, it will lose energy via collisions as it travels into the target at a rate (96):

$$\Delta E = \Delta t \left(k_s \frac{dE_r}{dx_{in}} + \frac{1}{\cos\phi_d} \frac{dE_r}{dx_{out}} \right) \tag{7.31}$$

Here, Δt is the thickness of the $^4He^+$ penetration and the "in" and "out" subscripts refer to the value at the entrance and exit of the $^4He^+$ particle. Overall, the yield Y_{He} of scattered $^4He^+$ ions is (96):

$$Y = \sigma \Omega Q N \Delta t \tag{7.32}$$

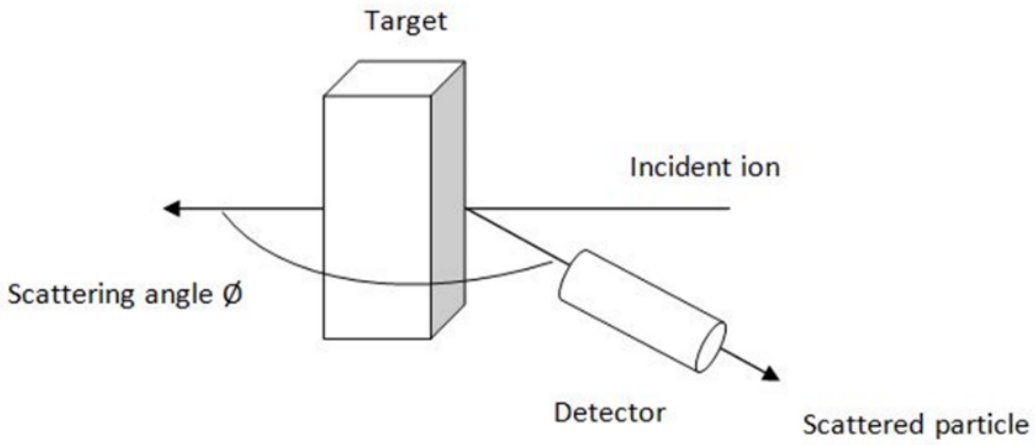

Figure 7.9: Schematic of the basic RBS setup (96).

Here, Ω is the detector solid angle, Q is the number of incident $^4He^+$, and $N\Delta t$ is the number of target atoms. These relationships in conjunction allow us to make a unique determination about the identity of the target atom, since each depends on the target atom's unique mass (96). Note that such a technique can theoretically distinguish isotopes, which our probe design in Figure 7.1 requires.

The fusion community has extensively used RBS analysis in combination with unique designs of removable PFC coupons to determine both gross erosion and redeposition. One example is the Hakola study at ASDEX Upgrade (56), placing coupons at the outer strike point of the divertor as shown in Figure 7.10. The leading edge of the material is made of W, shadowing a region of C. An inclined surface of molybdenum (Mo) begins after the C region. Here, surface-scale W redeposition occurs onto the C surface, where it is shielded from further sputtering. The gross erosion is calculated by adding the redeposition to the net erosion. Meanwhile, the study made a comparison between the net erosion of the high-Z W and Mo surfaces. This procedure compared favorably with gross erosion measurements via S/XB and W I (400.9 nm) spectroscopy. However, it was discovered that, while redeposition was anticipated to be 50-60% of gross erosion by spectroscopy, redeposition only accounted for 30-40% of gross erosion in the coupon sample. This occurrence was explained by the high W environment of ASDEX Upgrade, especially W flux from the main chamber. Consequently, an all-W environment like WEST or the current iteration of ITER may not be as ideally suited as we might expect for *in situ* studies of W net erosion.

As another example, a different style of coupon is shown in Figure 7.11. This study (34) is an example of a coupon used at DIII-D as part of their DiMES diagnostic suite. In this design the study used a larger center ($\sim$1 cm) of W to assess net erosion. Meanwhile, it used a small ($\sim$1 mm) of W is used to assess gross erosion; this assessment assumes the mm size is small enough that surface-scale redeposition may be considered negligible based on estimations of the first-ionization mean-free-path λ_{s+} in DIII-D, but our work in Section 4.3 disagrees with this assumption (Figure 4.9).

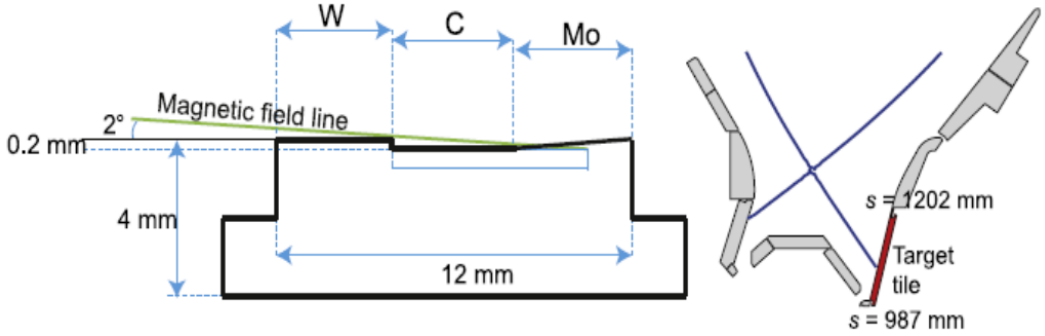

Figure 7.10: Schematic of the PFC coupon used in the Hakola study (left), and its location (highlighted in red) in the divertor (right) (56).

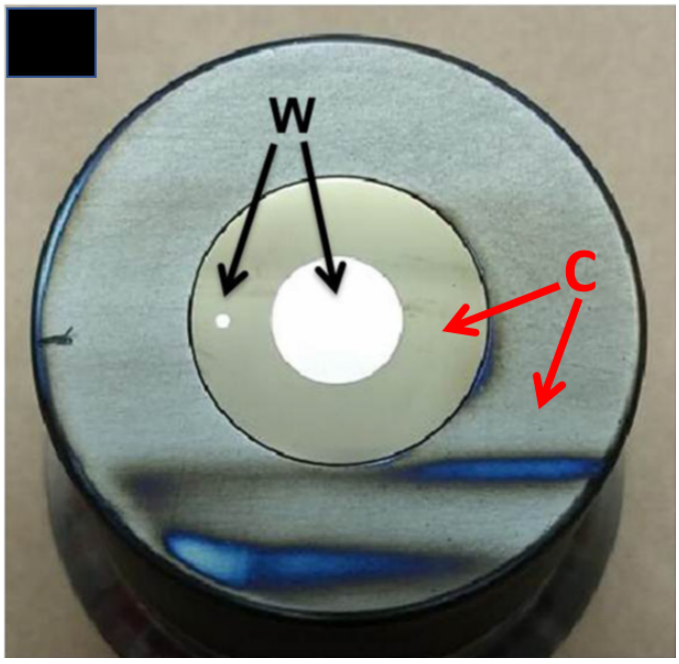

Figure 7.11: Picture of a W/C DiMES head coupon (34).

This study favorably compares, both inter- and intra-ELMs, coupon measurements and ERO impurity simulations with favorable results. A combination of the Ding and Hakola designs forms the inspiration for our probe design in Figure 7.1.

An alternative form of surface analysis used by the fusion community is laser ablation mass spectroscopy (LAMS). Although we noted that the analysis techniques of RBS are theoretically applicable to isotopic discrimination, in practice it is very difficult to make RBS distinctions among high-Z atoms, especially isotopes due to their slight spectral differences relative to their change in mass. Note that both of the coupon examples discussed in this section used RBS to distinguish W on C redeposition, where the spectral distinction is more transparent. As an alternative to RBS, LAMS provides a means of making the same elemental distinctions with improved isotopic discrimination, though at the cost of being a completely destructive technique. We will focus on LAMS diagnostics during the remainder of this section.

Most LAMS systems function on two basic components shown in Figure 7.12: a laser ablative tool and an inductively coupled plasma mass spectrometer (4). The first component scans the material surface with a high-power laser, ablating a set depth and radius of material off the coupon surface. Next, the material enters the second component, consisting of two parts. First, ablated material passes into an inductively coupled plasma (ICP) torch, where it ionizes into its atomic components. Second, the ionized material enters a mass spectrometer (MS), which separates particles by their charge-to-mass ratio using the Lorentz force (4). In principle we may use any MS system, but quadrupole mass analyzers are common for their high resolution (4); these analyzers induce radio-frequency fields that screen material outside of a particular charge-to-mass ratio from passing through to the detector.

An excellent example of this diagnostic comes from the dissertation by Duran (39), which used LAMS and a stable-isotopic mixing model (122) to analyze C and W sourcing and transport in DIII-D. Importantly, this work found excellent agreement between high-resolution RBS measurements and the LAMS tool for W isotopes (40), as needed for our probe design; we show this agreement in Figure 7.13. As our

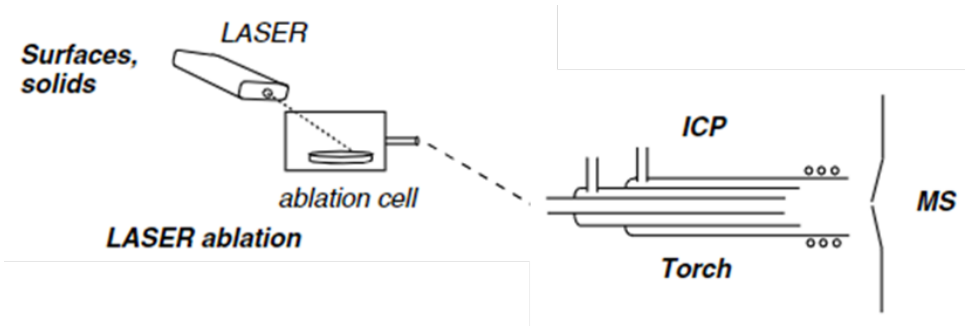

Figure 7.12: Diagram of the major components of a LAMS system (4).

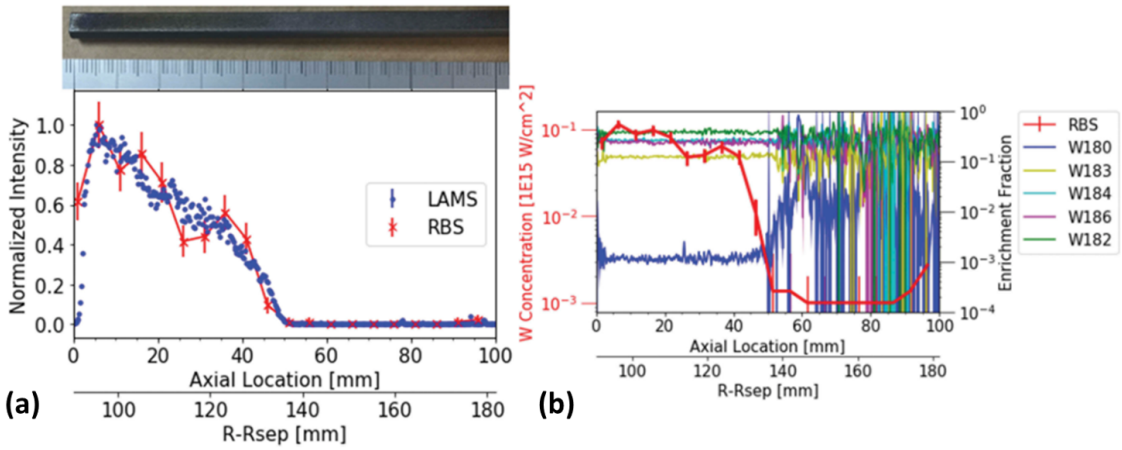

Figure 7.13: Analysis of W deposition on collector probes inserted into the mid-plane of DIII-D (40). (a) shows good agreement between RBS and LAMS data, while (b) shows the decomposition of LAMS data into W isotopes.

synthetic LAMS diagnostic, we will approximate redeposition measurement by taking linear histograms of our GITR redeposition profiles (e.g. Figure 4.9) with bin-width equal to the laser ablation width.

7.5 Experimental Predictions for mm-Scale Deformation

So far, we have discussed three major diagnostics that are theoretically useful, in conjunction with our probe design, to test the α-dependencies of net erosion predicted in Chapters 5 and 6. We have also discussed a series of probes that are machined to vary α on the mm-cm scale (subfigure (b) of Figure 7.1). Here, we will discuss predictions for the data and measurability of such experiments using our synthetic toolkit of ColRadPy, MPR, and GITR analysis on data generated by the PYEAD-RustBCA-GITR coupled workflow.

7.5.1 ColRadPy Spectroscopy Simulations

The first and primary diagnostic of interest is spectroscopy; this diagnostic can distinguish between gross erosion, prompt redeposition, and local redeposition when compared against *ex situ* data by finding the maximal n such that:

$$f_{W^{+}} + f_{W^{2+}} + ... + f_{W^{n+}} \leq f_{redep} \tag{7.33}$$

where f_{redep} is the prompt + local redeposition fraction determined from surface analysis data and $f_{\xi+}$ is determined from the line ratio comparison of W $_{(\xi+1)}$/W I spectroscopy. Assuming W II is dominated by prompt redeposition and the remaining charge states are dominated by local redeposition (up to $n+$), this boundary condition should reveal the prompt-vs-local trade-off with α.

However, before collecting spectroscopic data we must identify plasma conditions (n_e and T_e) that enable the desired measurement. To this end we create an LHC dataset with PYEAD-RustBCA-GITR (Section 6.1) of typical DIII-D divertor conditions: a density range from $8.0 \times 10^{19} \leq n_e \leq 1.0 \times 10^{20}$ m^{-3} and a temperature range from $15.0 \leq T_e \leq 35.0$ eV. We further restrict our α values between $1 \leq \alpha \leq 35°$ to give ourselves a range of prompt-vs-local conditions without introducing too many high-Z impurities into DIII-D from net erosion. We otherwise restrict our PMI parameters to DIII-D relevant values (e.g. $|\vec{B}| = 2.25$ T, C incident ions, D plasma, etc.). From the GITR f_{local} analysis (Section 4.3) of this dataset, we can determine that $n \leq 4$ for this range of conditions, in rough agreement with Figure 4.7. This choice is made using Equation 7.33 for an error bar of 10% agreement with the "true" f_{local} value. We show our analysis of n in subfigure (a) of Figure 7.14.

As shown in subfigure (b) of Figure 7.14, the relative fraction of our largest charge state of interest, $f_{W^{4+}}$, is quite small even at its maximal contribution to f_{local}: at most around 15% of the gross eroded flux is W^{4+}. Ideally, we would like to capture this ionization state across our α range so that we can observe the point at which W^{4+} begins to contribute to the f_{local} redeposition fraction. To compensate for the weak abundance, we need to ensure that our gross erosion yields are producing a large number of particles; we show the yield of our dataset in subfigure (c) of Figure 7.14. Note that a large yield should not contribute too much impurity seeding into the DIII-D SOL so long as our $f_{prompt} + f_{local}$ remains high. Examining the whole of Figure 7.14 with these varied considerations in mind, it seems qualitatively optimal to make our measurements in the $T_e \approx 25-30$ eV range. Based on this choice, we will emulate the DiMES-localized conditions of DIII-D Shot #190453: $n_e = 1.25 \times 10^{19}$ m^{-3} and $T_e = 25.84$ eV.

Having fixed our plasma conditions, we may choose emission lines from Table 7.3 and generate a quasi-static ColRadPy synthetic spectrum for each of our $\alpha = 3$, 15, and 30° probes. Based on their relative intensities and their proximity to visible wavelengths, we choose from Table 7.3 W I at 265.65 nm, W II at 276.43 nm, W III at

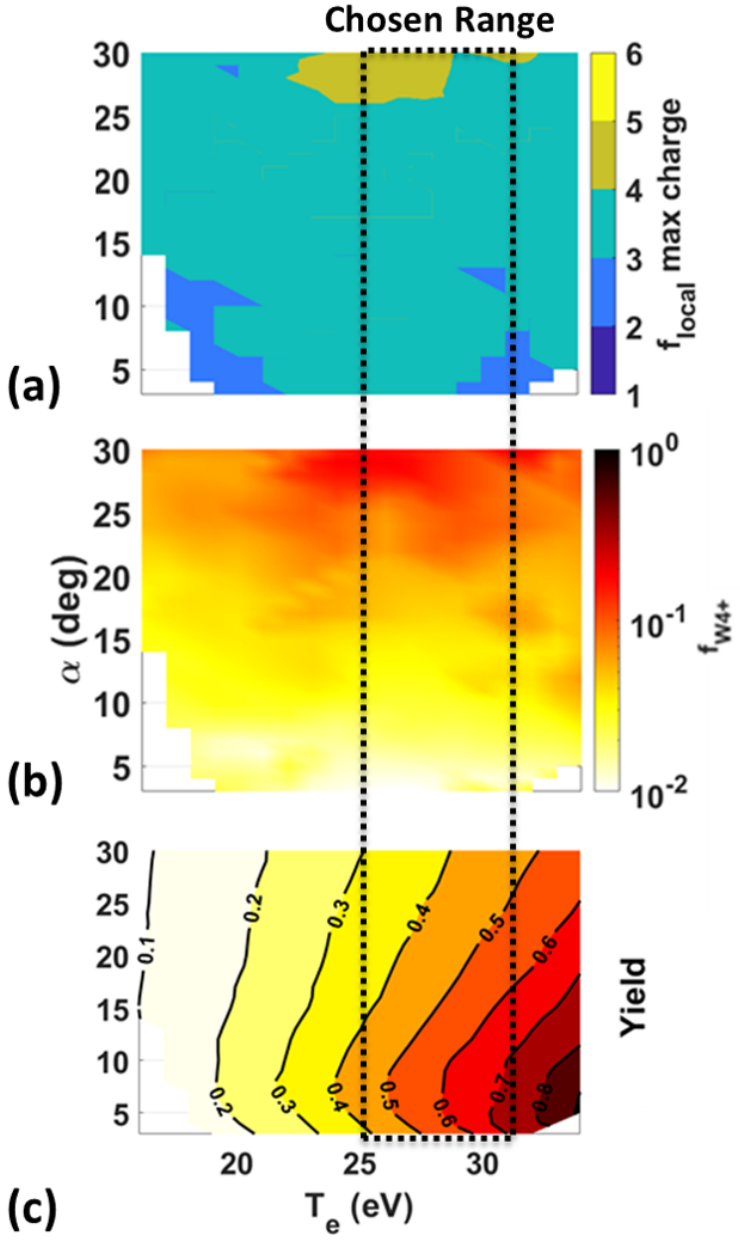

Figure 7.14: Determination of spectroscopic measurability, consisting of (a) maximum f_{local} charge state, (b) $f_{W^{4+}}$ fraction, and (c) overall gross erosion yield. The chosen range of measurement is emphasized in black.

224.86 nm, W IV at 255.01 nm, and W V at 77.81 nm as lines of interest; remember that these wavelengths from ColRadPy are not NIST-corrected at this time. Here, we avoid the W I line at 400.9 nm due to its complex dependence on metastable fractions (68), which we do not model at this level of analysis. We input the final charge-state fractions from PYEAD-RustBCA-GITR as weights to the PEC values in our synthetic spectrum. With these corrections we generate line-ratio comparisons for the emissivity of each charge state against the W I value, which we show in comparison to the "true" charge state fraction from PYEAD-RustBCA-GITR in Figure 7.15. Note that we are successfully able to capture the general trend with α at each charge state using this method.

On the other hand, there are immediate problems with our results. We notice a large residual between the PEC ratio and the "true" charge state fraction for $W^{\geq 2+}$ ions; as a worst-case scenario see W IV/W I in Figure 7.15. These large residuals are primarily caused by the fact that the PECs for these lines are orders-of-magnitude smaller than that of the W I line, so small differences in the emissivity generate large discrepancies in the fractional charge state estimation. Worse, the fractional abundance of W^{3+} is underestimated relative to that of W^{4+} for the same reasons. In summary, our experimental data would dramatically under-measure the fraction of local redeposition if we restricted our focus to these emission lines.

Overall, we can improve our experimental measurement by simply choosing different emission lines with PEC values closer in magnitude to the W I value. However, this change comes at a cost in measurability; the strongest emission lines for higher W charge states sit farther in the UV, where it is significantly more difficult to make spectroscopic measurements. Due to the rapid attenuation of UV signals in standard collection optics, far-UV spectroscopy is less common as a diagnostic on fusion experiments. Nevertheless, Figure 7.15 suggests that some of the identified lines of interest in the VUV can lead to inaccurate information about the relative abundance of W charge states. Choosing instead W III at 178.74 nm, W IV at 151.54 nm, and W V at 81.10 nm (wavelengths not NIST-corrected) results in much closer

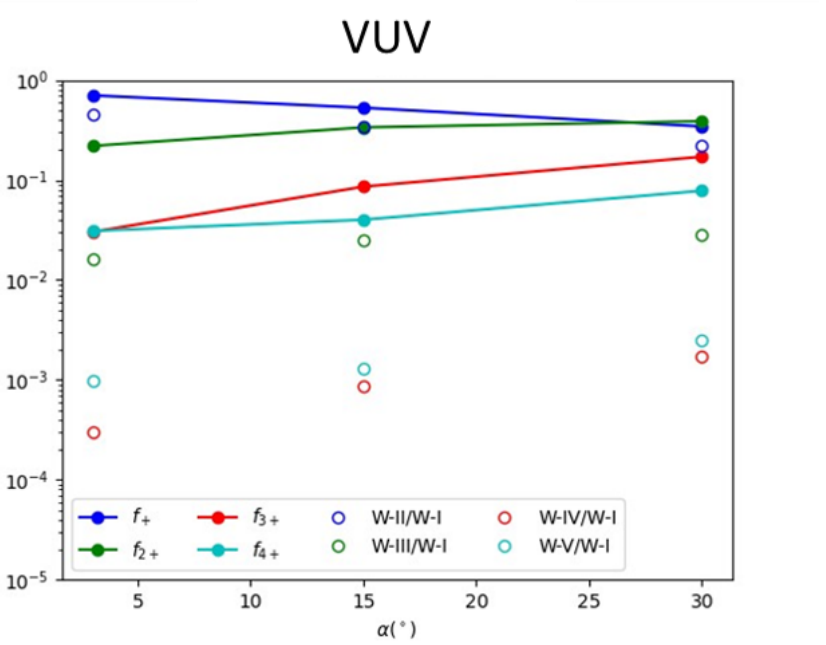

Figure 7.15: Comparison between the PYEAD-RustBCA-GITR charge state fractions f_{charge} and the weighted PEC line ratios from ColRadPy for the VUV lines of interest discussed in Table7.3.

agreement to the expected fractions, as shown in Figure 7.16; we choose these lines due to their predicted PEC intensity in ColRadPy. For the experiment series discussed in Section 7.1, we therefore recommend diagnostic equipment capable of accurate spectroscopic measurement in far-UV wavelengths. We summarize the possible lines of interest for such a measurement in Table 7.4.

7.5.2 GITR LAMS Simulations

Now, we turn our attention to the LAMS diagnostic for our redeposition measurement. Recall from Section 4.3 that we observed a significantly different spatial distribution between prompt + local redeposition, where sheath-driven mechanics dominate, vs far redeposition, where SOL forces determine the particle transport. This feature motivates us to put some radial upper bounds on the redeposited distribution such that the dominate redeposition mechanism transitions from surface-scale to far physics. We start by deriving one such upper bound using a simple-as-possible model. Recall that, under parabolic motion, the maximum radial distance R that a projectile may travel when launched from height h at angle δ with speed $|\vec{v}|$ is

$$R = \frac{|\vec{v}|\cos(\delta)}{a}\left(|\vec{v}|\sin(\delta) + \sqrt{|\vec{v}|^2\sin^2(\delta) + 2ah}\right) \tag{7.34}$$

where a is the acceleration driving the projectile back to the surface. From a simplified perspective, we can treat the guiding center of our gyro-orbiting particle as such a projectile, launched from a height $h = \lambda_{s+}\sin(\delta)$ at its first ionization event; similarly, we can approximate the acceleration the particle experiences as $a \approx q_e|\vec{E}|/m_s$ where $\vec{E}$ is the electrostatic field of the sheath.

Distributing the right hand side and using trigonometric substitution, we can rewrite R as

$$R = \frac{|\vec{v}|^2\sin(2\delta)}{2a} + \sqrt{\left(\frac{|\vec{v}|^2\sin(2\delta)}{2a}\right)^2 + \frac{2h|\vec{v}|^2\cos^2(\delta)}{a}} \tag{7.35}$$

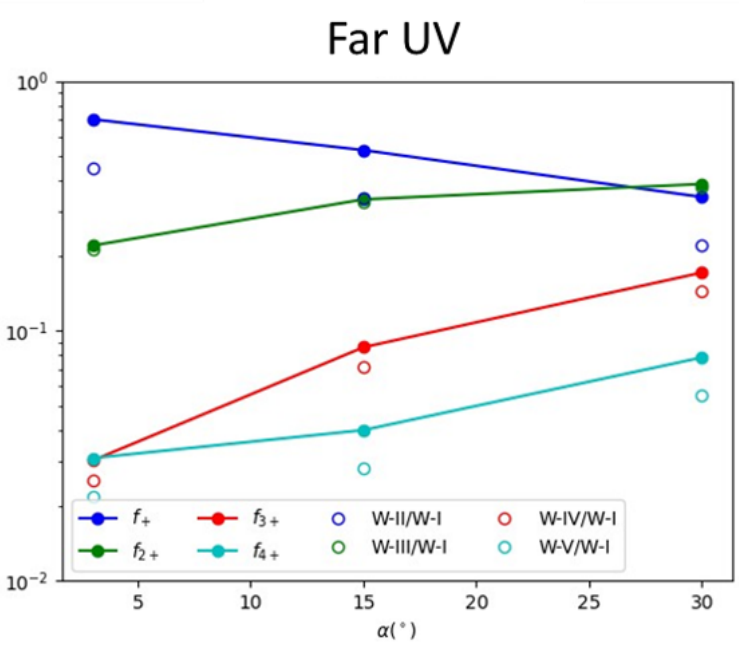

Figure 7.16: Comparison between the PYEAD-RustBCA-GITR charge state fractions f_{charge} and the weighted PEC line ratios from ColRadPy for the revised far-UV lines of interest.

Table 7.4: Emission lines producing good agreement between simulated experimental data and PYEAD-RustBCA-GITR outputs.

Emission Line	**Wavelength (nm)**	**Relative Intensity**	**Energy Transition $E_i - E_k$ (cm^{-1})**
W I	265.65	300	2951.29 - 40583.07
W II	276.43	182	0.00 - 36165.356
W III	178.74		19632.05 - 75697.21
W IV	151.54		43224.40 - 109190.30
W V	81.10		22345.8 - 145767.9

By conservation of energy, particles returning to the surface have less kinetic energy normal to the surface than potential energy, so that

$$|\vec{v}|^2 \leq \frac{2q_e\psi}{m_s \sin^2(\delta)} \tag{7.36}$$

assuming a singly charged ion. Notice that a similar expression holds for increasingly positive charges $W^{\xi \geq 1+}$ but with a weaker restriction on $|\vec{v}| \propto \xi$. Substituting into Equation 7.35 with further trigonometric substitution, we have

$$R \leq \frac{2q_e\psi \cot(\delta)}{m_s a} + \sqrt{\left(\frac{2q_e\psi \cot(\delta)}{ma}\right)^2 + \frac{4q_e\psi h \cot^2(\delta)}{ma}} \tag{7.37}$$

Further substituting our expression for a gives

$$R \leq \frac{2\psi \cot(\delta)}{|\vec{E}|} + \sqrt{\left(\frac{2\psi \cot(\delta)}{|\vec{E}|}\right)^2 + \frac{4\psi h \cot^2(\delta)}{|\vec{E}|}} \tag{7.38}$$

Note that, if we were modeling a higher charge state $W^{\xi \geq 1+}$, both the acceleration and the weaker restriction in Equation 7.36 would still cancel this expression's dependence on charge so that Equation 7.38 still holds. Lastly, we assume that $|\vec{E}| \approx \psi / L_{MPS}$ under a capacitor-like model. Although an oversimplification, this expression should be roughly correct in our small $\alpha \leq 30°$ range where the magnetic pre-sheath is thick (recall Equation 2.22). Making this final substitution, we have

$$R \leq 2L_{MPS} \cot(\delta) + \sqrt{4L_{MPS}^2 \cot^2(\delta) + 4L_{MPS} h \cot^2(\delta)} \tag{7.39}$$

or, further simplifying,

$$R \leq 2L_{MPS} \cot(\delta) \left(1 + \sqrt{1 + h/L_{MPS}}\right) \tag{7.40}$$

Finally, recognizing that $h < L_{MPS}$ is needed for our problem to be relevant at all (i.e. the particle is still inside the sheath), we have

$$R \leq \left(2 + 2\sqrt{2}\right) L_{MPS} \cot(\delta) \tag{7.41}$$

Using this formula, we could crudely approximate $f_{prompt} + f_{local}$ by summing the full distribution of redeposited material measured by the LAMS instrument such that the radial distance from the edge of the small spot is less than this upper bound for R.

Immediately, we see that the precision of δ limits the usefulness of Equation 7.41. As we can see in Figure 7.17, averaging over the RustBCA δ distribution to get an average R value (denoted $\langle R \rangle$) is reasonably accurate at $\alpha = 30°$ but significantly underestimates the surface-scale redeposition when $\alpha = 3°$. Recall that we expect some distribution about δ that is cosine-like as $\alpha \nearrow 90°$ and increasingly skewed sub-cosine as $\alpha \searrow 0°$ (see Subsection 5.2.2); simultaneously, we note that $\cot(\delta) \nearrow \infty$ as $\delta \searrow 0°$. Consequently, we need a better estimator of δ when $\alpha \searrow 0°$ in order to make use of this method. Attempts to use the mode, median, and quantiles of the δ distribution were similarly unsuccessful.

Nevertheless, we should have sufficient knowledge from both our LP-measured plasma parameters and our microtrench-measured deposition pattern (Subsection 7.5.3) such that we can get agreement between our incident ion EADs and PYEAD. Coupling the PYEAD outputs to RustBCA, we can use the full predictive distribution of δ to interpret our R boundary for the LAMS analysis. As one example, we may compute the skewness of our δ distribution and choose a representative upper bound using Equation 7.41 and $\delta_{max} = \text{Mode}(\delta) - \text{Skew}(\delta)\,\text{Mode}(\delta)$, which gives us the redeposition fraction shown in Figure 7.18. Here we get much better agreement at $\alpha = 3$ and $15°$ with the theoretic value, though we significantly overestimate the surface-scale redeposition at $\alpha = 30°$; this overestimation is the result of a greater fraction of f_{far} material that redeposits close to its sourcing as α increases.

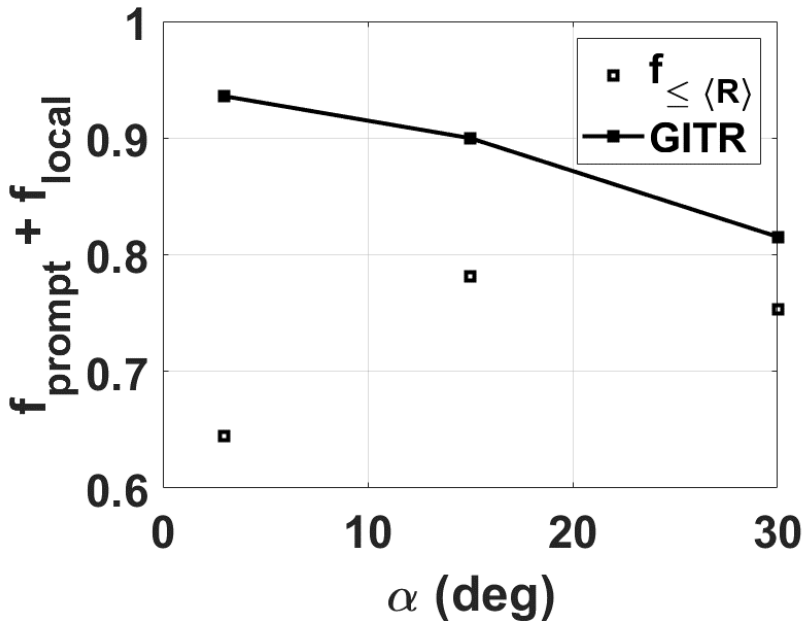

Figure 7.17: Comparison between the PYEAD-RustBCA-GITR charge state fractions $f_{prompt} + f_{local}$ and the fraction of particles within the average radial bound $f_{\leq \langle R \rangle}$.

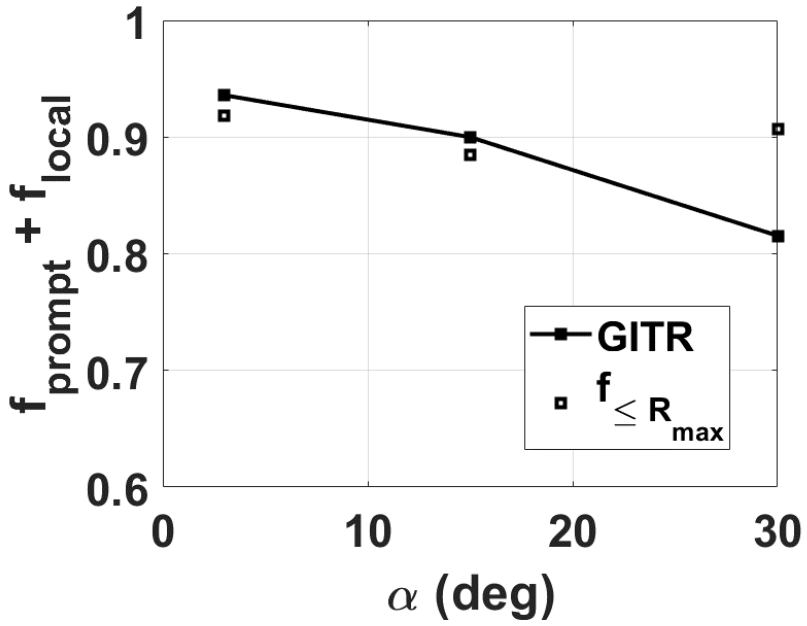

Figure 7.18: Comparison between the PYEAD-RustBCA-GITR charge state fractions $f_{prompt} + f_{local}$ and the fraction of particles within the δ_{max} radial bound $f_{R_{max}}$.

Ultimately, this f_{far} material obscuring the LAMS measurement at $\alpha = 30°$ is material that has just barely made it outside of the sheath before being turned around by the SOL. Although it is possible that we cannot completely screen f_{far} contributions to our LAMS dataset, recall that we can still distinguish between f_{prompt} and $f_{local} + f_{far}$ redeposition via spectroscopy. In other words, we can still observe prompt-vs-local trade-off using Equation 7.33, which is the main experimental goal. Moreover, the sheath edge is an artificial construct at the end of the day used for mathematical convenience; there is no such hard boundary for real-world physics regimes, so the f_{local} overestimation by LAMS is only important in the academic, not utilitarian, sense.

7.5.3 MPR Microtrench Simulations

As the final component of our mm-scale experiment, we discuss MPR simulations optimizing our microtrench measurability. Unlike the previous two diagnostics where we needed to consider the measurability of the prompt-vs-local process in specific, quantified detail, there is much less to say about the microtrench optimization. Here, we mainly need to assess the qualitative clarity of the MPR simulations to determine whether our microtrench geometry captures the relevant EAD angles.

When designing a microtrench, the primary free parameters are aspect ratio and depth. It is typical to use either a square microtrench (1; 2) or a series of differently-oriented rectangular microtrenches (30); square microtrenches seem to give clearer EAD estimations overall. Note that the actual side-length of our microtrench does not matter to our θ and ϕ measurement for geometric reasons beyond giving us more erosion data on the floor. Hence, we will use 30x30 μm side lengths, given the good data attained with these lengths at DIII-D (2).

Thus, we are primarily interested in ensuring that the microtrench depth is neither so shallow that there is no shadowed region on the floor nor so deep that all incident ions miss the floor entirely. We qualitatively check these conditions by varying the

depth d of our trench in Figure 7.19. Based on the contrast between the microtrench floor and the main surface, we can see that $\alpha = 3°$ has a much lower particle count compared to the others due to the more glancing θ in these conditions; too deep of a trench will quickly obscure this measurement. On the other hand, the steep θ at $\alpha = 30°$ results in little contrast between the particle counts of the floor and the surface; too shallow of a trench will offer very little shadowed area with which to geometrically determine the incident ion EADs. As a compromise, we recommend $d = 3$ μm so that both conditions for the measurement can be reasonably met. In combination with the other diagnostic techniques in Subsection 7.5.1 and 7.5.2, we have demonstrated reasonable confidence in our ability to demonstrate prompt-vs-local redeposition sensitivity to α for mm-scale variation in an experimental validation study.

7.6 Experimental Predictions for μm-Scale Deformation

In the previous section we weighed the measurability of a validation study for PYEAD-RustBCA-GITR; this set of experiments varied the surface at the cm-to-mm-scale, which is the intended scale for the model in Chapter 5. Meanwhile, our work in Chapter 6 shows that α is as important of a parameter as n_e and T_e in setting the fraction of high-Z material entering the SOL; this fact naturally calls into question the importance of α-variation at smaller, nm-μm scales. As a companion to the experiments in Section 7.5, it would be interesting to use the same kind of experimental setup for probes that vary surface roughness instead. In subfigure (c) of Figure 7.1, we show a series of such probe designs with different levels of surface roughness from very rough ($R_a \approx 20\mu$m) to mirror-finish ($R_a \approx 0.02\mu$m).

Unfortunately, we are unable to rigorously analyze the expectations for such an experiment using PYEAD-RustBCA-GITR at this time. The major barrier to this

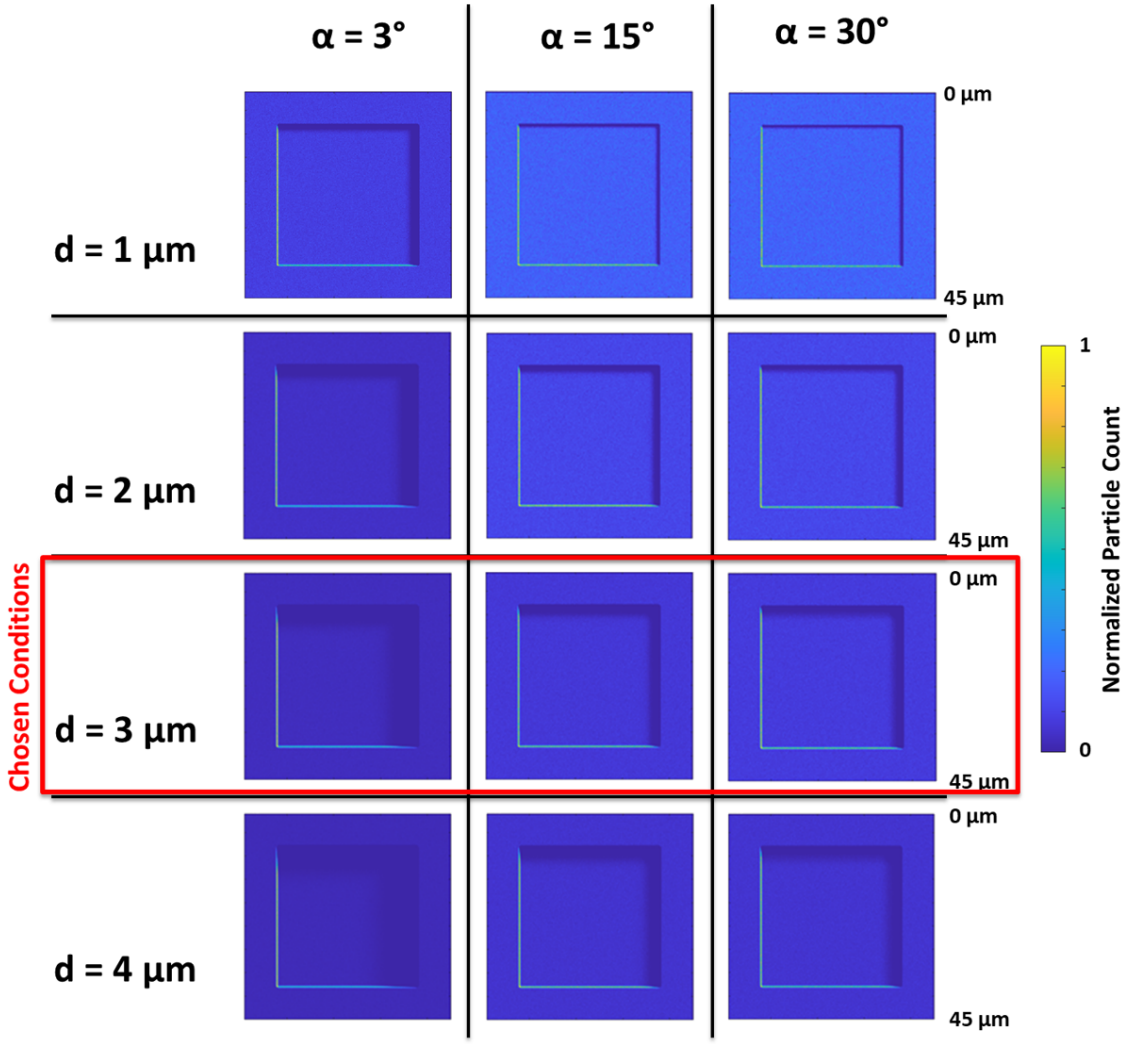

Figure 7.19: MPR simulations varying microtrench depth d at each α of interest. Here, we show the normalized particle fraction (i.e. number of particles normalized to maximum particle count and bin size) of incident ions onto the surface. Little variation is observed in these simulations, and the reader is referred to the digital version of this document for optimal clarity. Our chosen conditions are highlighted in red.

analysis is the need to apply a consistent surface morphology across each module of the workflow. Each "peak" and "valley" along the surface will have its own localized α, needing its own localized incident ion EAD, sputtered neutral EAD, and redeposition distribution; furthermore, those local conditions will each have to be modified according to the "peaks" and "valleys" of the neighboring surface geometry. Similarly, the sheath model of PYEAD and GITR would need a major update into a model that accounts for localized electron and plasma ion populations (i.e. a PIC code), which could vary substantially at this small scale. Although such an undertaking would dramatically improve the utility of our workflow, the undue burden of development relegates this task to future work for now.

Nevertheless, we can reasonably expect the variety of precise $\vec{B}$-to-PFC pitch angles to average out the net erosion dependency on α, as discussed briefly with regards to gross erosion in Chapter 3. We therefore hypothesize that all three surface-roughness probes will have near-identical redeposition fractions to that of $\alpha = 3°$ in our mm-scale experiment. As an additional means of prediction, we can use the surface-roughness branch of the MPR code (Section 7.3) to model the changes to net erosion accrued by rough surfaces. As explained earlier, the MPR code assumes Bohdansky-like erosion and cosine-δ, uniform azimuthal sputtering angle conditions, which Chapter 5 suggests is incomplete. Therefore, instead of predicting our model's expectations for net erosion, this approach instead models what the conventional expectations for net erosion are as a means of experimental comparison.

We show the major outputs from our MPR modeling in Figure 7.20. There is significant variation of θ when $R_a = 20\mu$m but an essentially constant θ flux when $R_a = 0.02\mu$m. In turn, there is a high fraction of both gross erosion and surface-driven, ballistic redeposition for the roughest surfaces; on the other hand, no redeposition is calculated for the mirror-finish surface, so no net erosion figure is generated within MPR. Summarizing, MPR predicts a net erosion fraction of 1, 0.96, and 0.63, respectively, for ascendingly rough surfaces. Note that this code does not account for prompt, local, or far redeposition; MPR only accounts for the ballistic

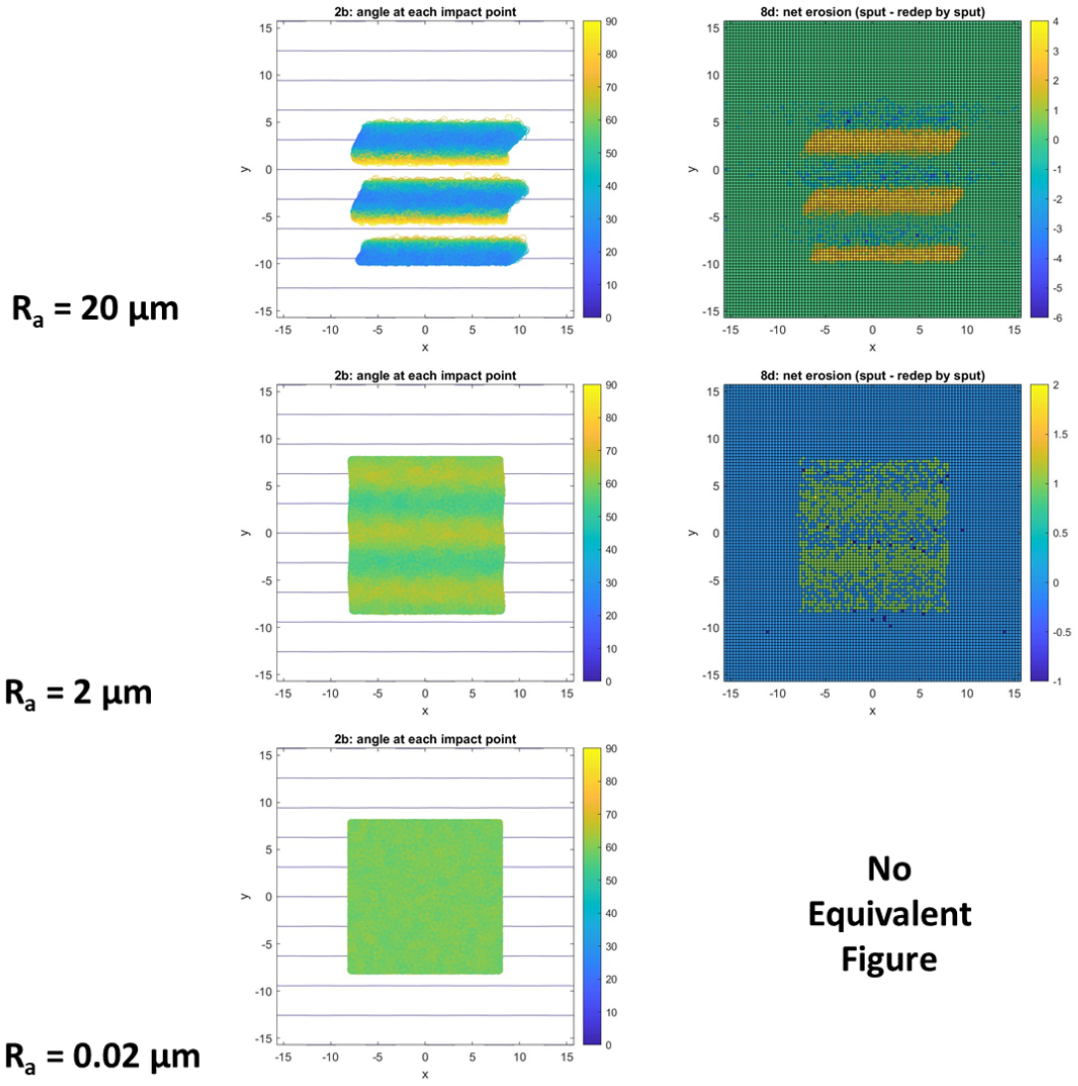

Figure 7.20: Major summary figures generated within MPR, with average impact angle in the left-hand column and net erosion in the right-hand column. No net erosion figure is generated in MPR for $R_a = 0.02$ μm because no redeposition is calculated.

neutral redeposition shown in subfigure (b) of Figure 7.8, which has been ignored in the rest of this dissertation due to only modeling flat surfaces. Thus, we would expect to see significantly reduced erosion yields in the $R_a = 20\mu$m case, which could impact our spectroscopic measurability.

It is unclear if ballistic redeposition would have an impact on the line-ratio analysis discussed in Section 7.2. Naively, there is the possibility that ballistic redeposition could cause us to miss a large fraction of net erosion spectroscopically that would be measured with *ex situ* techniques; consequently, we could overestimate the W^{n+} charge state needed to solve Equation 7.33 and thereby overestimate f_{local}. Conversely, the rapid timescale of this ballistic redeposition could reduce those particles' contribution to the W I line-radiated emissivity to near zero, preserving the measurement. Additionally, changes to the δ distribution will likely require a rework of our boundary method for interpreting $f_{prompt} + f_{local}$ using LAMS, but further updates to our code are needed to improve this interpretation. Indeed, prompt-vs-local trade-off may be impossible to measure for these experiments without the renovations to PYEAD-RustBCA-GITR that we have discussed; even so, simply analyzing net erosion without any mechanistic fidelity to the redeposition measurement can still inform us about the importance of fine-structure α-variation, so these experiments are still recommended. To conclude, we summarize the present technology readiness and theoretic interpretability for both this experiment and the experiment discussed within Section 7.5 in Table 7.5.

7.7 Executive Summary

- Experimental observation of the importance of the magnetic-field-to-surface pitch angle, α, in setting net erosion is critical at this time.

Table 7.5: Current measurability of mm-scale and μm-scale experiments on the grounds of technological readiness and theoretic interpretability. Diagnostics with an experimental readiness in both categories are shaded for emphasis.

Technological Readiness		
	mm-scale	**μm-scale**
VUV Spectroscopy	✓	✓
Far-UV Spectroscopy	×	×
LAMS	✓	✓
RBS	✓	✓
Microtrenches	✓	✓

Theoretical Interpretability		
	mm-scale	**μm-scale**
VUV Spectroscopy	×	×
Far-UV Spectroscopy	✓	✓
LAMS	✓	×
RBS	✓	×
Microtrenches	✓	✓

- A novel, isotopic coupon design (in combination with line-radiative emission spectroscopy, geometrically resolvable surface analysis, and microtrench diagnostics) can experimentally distinguish prompt-vs-local trade-off.
- Synthetic diagnostics coupled to PYEAD-RustBCA-GITR outputs show that experiments with mm-scale α variation are resolvable.
  - Far-UV emission lines may be needed to accurately determine redeposition fractions of multiply charged high-Z ions.
- Experiments with μm-scale α variation require significant sheath and surface model upgrades to the PYEAD-RustBCA-GITR workflow before prompt-vs-local trade-off is resolvable.
  - Experiments without prompt-vs-local distinction can still be useful for determining changes to the overall redeposition fraction for α variation at this scale.

Chapter 8

Discussion of Key Results

Throughout the preceding chapters, we noted the importance of (1) overcoming the ITEP gap in the development of magnetic confinement fusion reactors and (2) minimizing net erosion of high-Z PFCs in the development of ITEP gap solutions. Consequently, we laid out the existing theory of gross erosion and redeposition for high-Z PFCs (especially tungsten) and developed / improved Monte Carlo codes to capture the relevant physics of these phenomenon. Using these tools, as well as refined paradigms of redeposition processes, we have been able to isolate the critical yet often overlooked importance of the $\vec{B}$-to-PFC pitch angle α in net erosion physics. Now, we will take a step back from the detailed analysis of prior chapters to appreciate the implications of our key results.

Throughout this dissertation, we have asked the overarching question: **What are the optimal PMI parameters that maximize high-Z redeposition within the sheath (i.e. surface-scale PMI) and minimize reactors' dependence on SOL processes (i.e. global-scale PMI) to reduce high-Z net erosion?** The first step to tackling this question has been the implementation of a refined paradigm for redeposition mechanisms (Section 4.2). Previously, PMI researchers have typically grouped redeposition under "prompt" and "non-prompt" language, referring to surface- and global-scale processes respectively. However, surface-scale redeposition

includes the cumulative effects of two phenomenon: the geometric-driven intersection of large ion gyro-orbits with PFC surfaces and the sheath-driven acceleration of ionized material back to the first-wall. Different PMI parameters govern the magnitude of these processes such that different parameter conditions can result in a different dominant mechanism, making it more difficult to optimize PFC lifetimes when these mechanisms are grouped. Meanwhile, there is a real need at experimental facilities to capture accurate, *in situ* measurements of surface-scale redeposition, yet these diagnostics (especially the spectroscopy discussed in Section 7.2) require different specifications depending on which redeposition mechanism dominates.

For these reasons we have introduced more precise categories of "prompt" (or geometric-driven), "local" (or sheath-driven), and "far" (or SOL-driven) redeposition. Ultimately, we want to understand how to maximize prompt + local redeposition and minimize a reactor's reliance on far redeposition, which can be more difficult to extrapolate across magnetic confinement facilities. Using this framework, we want to understand PMI parameter sensitivities in order to answer our main research question, but we first considered the (otherwise overlooked) impact of the $\vec{B}$-to-PFC pitch angle parameter α on net erosion; the impact of other PMI parameters are individually more understood across previous net erosion studies (Chapter 4). As shown in Figures 8.1 and 8.2, disruption events over reactor-relevant lifetimes may significantly change localized α values at both the macro (cm-mm) and micro (μm-nm) scale. The research of this dissertation has focused on the impact of majorly transient-damaged tiles (i.e. $0° \leq \alpha \leq 90°$ variation at the mm scale) on redeposition fractions during L-mode and inter-ELM H-mode operation, as opposed to the shallow α assumption held fixed by previous studies. In other words, if a PFC surface is scarred by a transient event and normal operations resume from that point forward, will net erosion assumptions predicting PFC lifetimes significantly change as the result of the newly modified α?

By holding the plasma conditions fixed at the sheath entrance and varying PMI parameters otherwise setting the sheath thickness (i.e. α, $|\vec{B}|$, and plasma ion species), we determined that α can, in fact, have a major impact on both the gross erosion

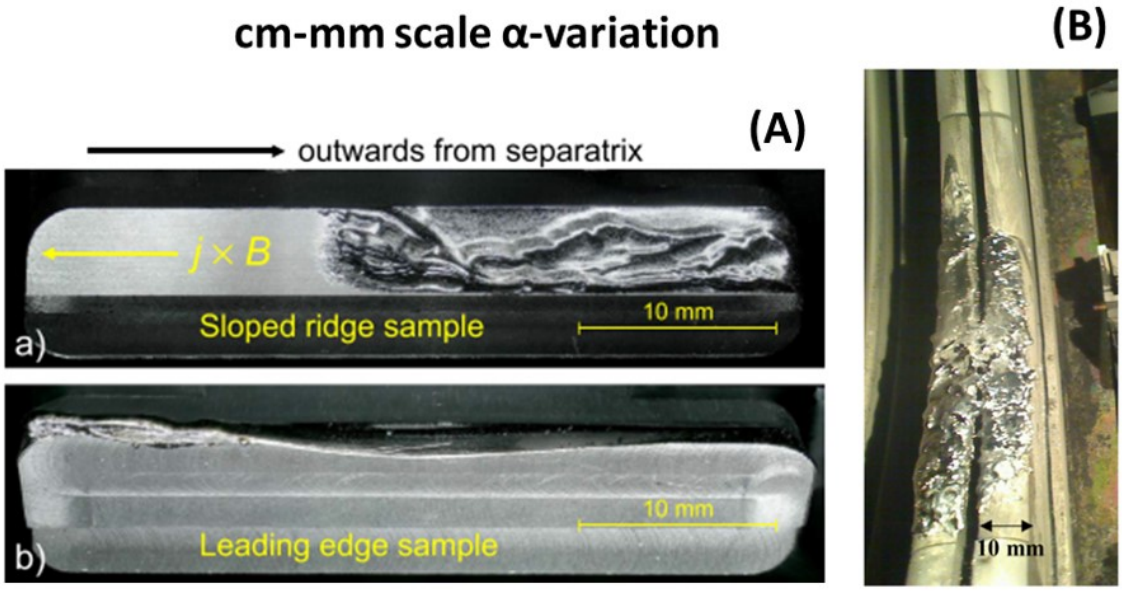

Figure 8.1: Pictures of cm-mm melting deformation to first-wall components during transient emulation studies in the ITER-like divertor at ASDEX Upgrade (75) (Subfigure (A)) and the ITER-like sacrificial limiter at T-10 (20) (Subfigure (B)).

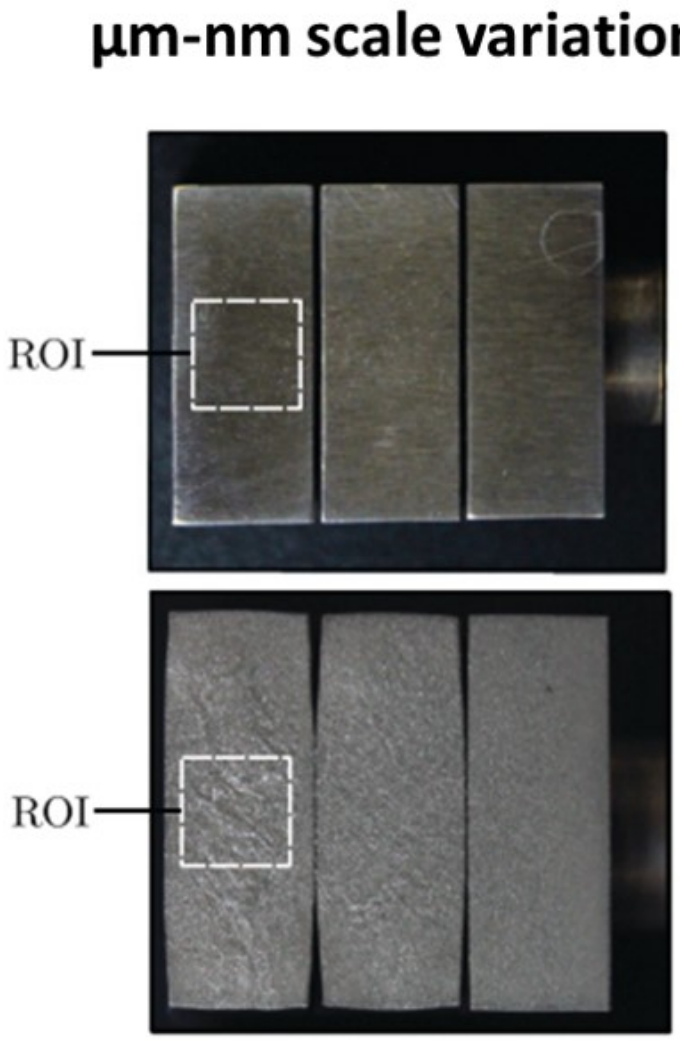

Figure 8.2: Pictures of μm-nm surface morphology changes from melting, cracking, bubbling, etc. of ITER-like W PFCs at the IDTF-Russia facility (104).

and redepositon components of net erosion (Chapter 5). Firstly, we observed that α changes the forward scattering angle δ of sputtered neutrals, which has a significant effect in setting the first-ionization mean-free path and relative maximum height of PFC neutrals to the sheath entrance. Popular convention has presumed that δ exhibits a cosine-like distribution at all α values due to the heavy inertia of high-Z particles; this assumption has led to a continued usage of cosine-δ distributions in simulations of high-Z redeposition at shallow-α. However, through rigorous estimations of incident sputtering ion impact angles, we find that δ is significantly sub-cosine in its distribution at shallow α; moreover, the shift towards an actual cosine-like distribution in δ as $\alpha \nearrow 90°$ has a complex impact on redeposition fractions.

In particular, we noted that, for $\alpha \approx 0°$, prompt redeposition dominates the surface-scale redeposition and that, because material ionizes closer to the sheath entrance due to the shallow δ, material has an increased likelihood to enter the SOL rather than undergo local redeposition. Importantly, this α condition is the normal operational regime intended for first-wall components, especially in the divertor. It is noteworthy that our simulations in this regime agree with net erosion DIII-D measurements (113; 125; 18) and ITER predictions (46) when including our refined δ calculation. It is possible that sub-cosine δ values may not have been observed until now because the ambiguity of the old "prompt" definition and the subsequent ambiguity of which prompt-vs-local pathway is driving the redeposition has circumvented the need to explain rigorously geometric vs sheath contributions. Alternatively, our *ad hoc* sheath diffusion coefficient (Section 5.1) may be significantly underestimated in these codes, such that any δ variation effectively disappears from the *de facto*, cosine distribution of the real world; however, the moderate electron density from our OEDGE plasma would not intuitively indicate that we should expect high collisionality in our sheath. Experimental efforts to distinguish redeposition mechanisms (Chapter 7) can reveal whether variation of δ is needed to explain prompt-vs-local trade-off.

Regardless, the prompt-vs-local ambiguity is less important in normal, steady-state operational conditions; this distinction becomes much more important as α increases. We note that as α increases (driven by transient events not explicitly modeled here), the fraction of prompt redeposition decreases and the fraction of local redeposition increases as the following occur: δ increases, ionization lengths shrink, and the plane of Larmor orbit rotates parallel of the PFC surface; these three conditions serve to decrease the geometric likelihood of prompt redeposition while increasing non-prompt material's time-of-flight within the sheath, hence increasing local redeposition. The trade-off between prompt and local redeposition is imperfectly balanced, leading to an overall increase in the material fraction entering the SOL.

Eventually, the sheath thins ($L_{MPS} \searrow 0$ as $\alpha \nearrow 90°$) to the point where effectively no material can ionize within the sheath, causing the prompt fraction to decrease further and local fraction to begin decreasing. The rate at which the sheath becomes too small is directly driven by the magnetic field strength (i.e. $L_{MPS} \propto 1/|\vec{B}|$), leading to a complex interplay between α and $|\vec{B}|$ that has not been previously observed. In practice, this interplay indicates that α variation may matter less in the high-field environments of pilot plants; on the other hand, the fraction of material entering the SOL is fixed rigidly high in high $\vec{B}$-field regimes of the same plasma conditions (Section 5.3). Fortunately, modifications to the n_e and T_e plasma conditions may be able to outcompete the impact of $|\vec{B}|$ on net erosion (Subsection 6.2.3).

Having built an understanding of the physics effect of varying α, we are then able to return to the framing question of the dissertation. That is, we have used Sobol' analysis (Chapter 6) to isolate the impact on net erosion of a critical subset of PMI parameters (namely, n_e, T_e, $|\vec{B}|$, α, m_{ii}, and Z_{ii}) in order to isolate which parameters are the most important in setting the prompt + local redeposition fraction and to determine what conditions of those isolated parameters minimize the fraction of particles lost to the SOL. We determined that the gross erosion yield is most determined by T_e, m_{ii}, and Z_{ii} due to their impact on the kinetic energy transfer to PFC neutrals during incident ion collisions (Subsection 6.2.2). Similarly, we

determined that the fraction of particles avoiding prompt + local redeposition is most determined by n_e, T_e, and α due to their overall influence on prompt (T_e and n_e) and local (α and n_e) processes (Subsection 6.2.3). The finding that n_e and T_e drive the PFC flux into the SOL is in keeping with previous studies of "prompt"-vs-"non-prompt" redeposition (Section 4.1); however, the discovery that α is roughly as important as these parameters in setting the fraction of eroded particles entering the SOL is new to this study.

One early attempt to compute net erosion across our coupled workflow was to evaluate $Y * f_{far}$, the yield multiplied by the fraction of particles entering the SOL, as a measure of the relative number of particles entering the SOL. Using the same Sobol' analysis, we isolate the most important parameters determining this metric as n_e, T_e, m_{ii}, and Z_{ii}, where the relative importance of α is undercut by the noisy, slight decrease of Y juxtaposed against the increase in f_{far} as $\alpha \nearrow 90°$. It is entirely possible, then, that net erosion is generally invariant to changes in α due to competing gains and losses from different aspects of net erosion with this parameter. However, it is worth noting that, under the steady-state conditions of a reactor's operation, each of n_e, T_e, m_{ii}, and Z_{ii} are minimally varying, meaning that, even if α is a second order parameter, variations of α may become increasingly important to net erosion over reactor-relevant lifetimes. That is, the wide variations in Y that dominate $Y * f_{far}$ sensitivity in our analysis are not necessarily anticipated in standard operations, leaving more room for f_{far} sensitivity to outcompete Y in setting the particle losses into the SOL as α varies over time.

Similarly, while we have good reason to believe that the Monte Carlo workflow in this dissertation accounts for all major physics setting the prompt + local redeposition fractions in the gross erosion regime limited by physical sputtering, a loose coupling between OEDGE and PYEAD-RustBCA-GITR leaves less confidence in our modeling of gross erosion and far redeposition. For example, our workflow uses an arbitrary number of test particles such that we generate sufficient statistics in the outputs of the code components while maintaining a reasonable computational runtime. Important

changes to incident ion fluxes from OEDGE are not accounted for at this time; in other words, while the velocities of incident ions do change at the sheath entrance in our code, their abundance does not change with any PMI parameter variation. See Section 3.2 as an example of how this abundance can be important.

For these reasons, we have focused on PMI parameters and conditions minimizing f_{far} in this document, remaining agnostic to the gross erosion yield. However, two immediate implications are worth noting from the $Y * f_{far}$ results. First, we have overlooked intra-ELM H-mode regimes in our workflow due to the inherent complexities of sheath and SOL collisionality and heat fluxes taking place at the PFC surface during an ELM event; our workflow is not equipped for this regime without significant upgrades to the model. Nevertheless, the clear dominance of Y in setting the net erosion implies that the contribution of α to redeposition will be entirely negligible during an ELM, where yields are increased relative to the inter-ELM case. Now, redeposition during an ELM, regardless of PMI parameter conditions, is likely negligible due to the enormous fluxes of highly kinetic PFC material sputtered from the surface, but any surface-scale contribution to redeposition is much more likely to be dominated by n_e and T_e than α based on this finding. Nonetheless, these ELM events drive an increase in α over time, which may increase the sensitivity of net erosion to α during normal operation as discussed.

Second, the importance of α over long PFC lifetimes may be further exacerbated by commensurate compositional and morphology changes to the PFC surface, which we have neglected for simplicity here. Incident ion embedment (Section 3.1) will increase over the lifetime of a PFC, which will weaken the binding energy of high-Z materials. Consequently, we expect gross yields to increase over the PFC lifetime, which may counteract some mitigating decreases in Y as $\alpha \nearrow 90°$, increasing the net erosion sensitivity to the α parameter. Chemical sputtering from D+T fuel retention may further enlarge these gross yields across the lifetime of PFCs. As discussed in Section 3.1, the WD/W ratio characterizing WD chemical erosion increases away from the strike point due to greater retention in these regions. In the situation where a

PFC tile is damaged by a transient event and the strike point is then swept away from this tile in order to lower localized n_e and T_e conditions (hence lowering net erosion), the increase in chemical sputtering could heighten the importance of sharp α's in the leakage of PFC impurities into the SOL. The fusion community would benefit from more research into the relative rates and sensitivities of chemical erosion for high-Z PFCs in order to better quantify the importance of this issue.

Now, contributions from n_e and T_e (and $|\vec{B}|$, which must be considered when optimizing n_e and T_e for a reactor) are all nicely contained within the standard p parameter, the ratio between the first-ionization length and the first-ionization Larmor radius (Section 4.1). Missing from this parameter is the contribution of α, and existing parameters seemingly accounting for α (i.e. $\hat{\lambda}$, the ratio between the first-ionization length and L_{MPS}) are incomplete (Section 5.3). Thus, we have proposed a 2-variable map of p-vs-α that is better equipped for estimating the fraction of high-Z eroded material entering the SOL over reactor relevant lifetimes. Even over a wide PMI parameter variation, where fits of the modeled SOL-losses are too weak to be "predictive," this p-vs-α contour continues to provide a good, qualitative intuition for the impact of α degradation on net erosion (Subsection 6.2.3). From such a contour we may infer that low p with low α is the optimal regime for reactor operation, which we are already targeting as a fusion community for next-step facilities. What this work now indicates is that the importance of α varies with p, meaning that operation in modes like divertor detachment may be even more important than currently anticipated.

From the large dataset generated in Chapter 6, we are able to note the trade-off between n_e and α, shown in Figure 8.3, as a specific relationship of interest in setting f_{far}. In regimes of divertor detachment, large densities near the PFC targets are engineered in order to lower temperatures near or below the sputtering threshold, hence decreasing PFC gross erosion (79; 111). Not only will this change to the gross yield be significantly efficient in minimizing net erosion based on the discussion throughout this chapter, but also high densities near the sheath entrance

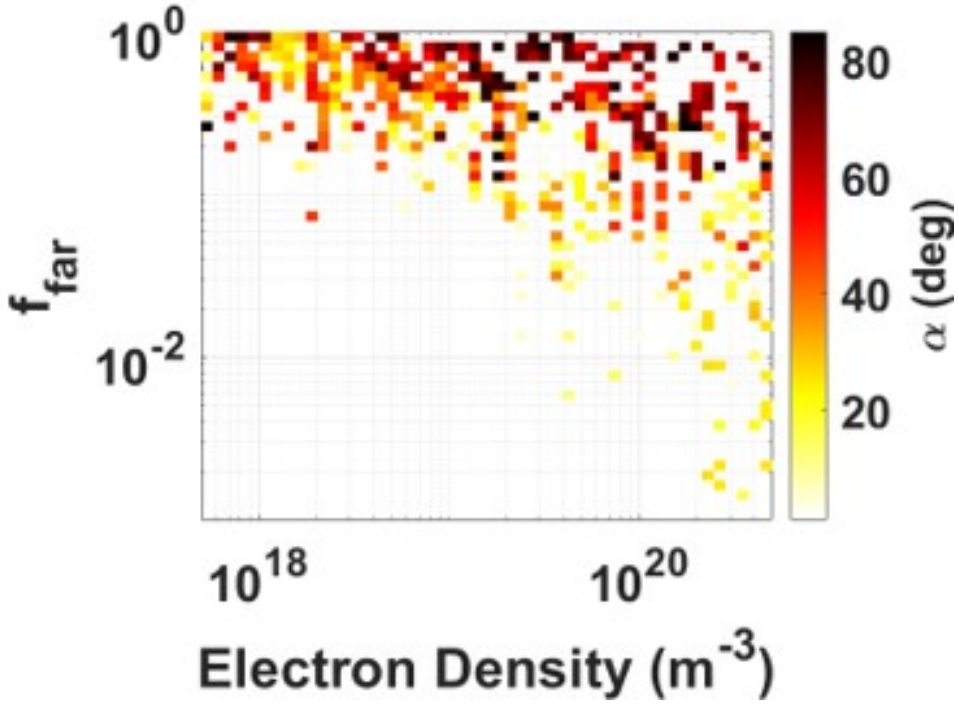

Figure 8.3: Relationship between the electron density and the $\vec{B}$-to-PFC pitch angle in setting the particle fraction entering the SOL, f_{far}.

should significantly increase the fraction of prompt + local redeposition so as to further lowering net erosion. These benefits of high n_e to redeposition are well known (Section 4.1); however, Figure 8.3 shows that the order of magnitude of these benefits depends significantly on the α regime. At intended, engineered $\vec{B}$-to-PFC pitch angles (i.e. $\alpha < 5°$), the particle fraction entering the SOL is as low as $\approx 10^{-3}$ in detached (i.e. $n_e > 10^{20}$ m^{-3}) conditions. In the same density regime, f_{far} increases to ≈ 1 at $\alpha \approx 90°$. Even if the yields are significantly lowered by detached conditions, a three order of magnitude increase in particles entering the SOL can be more than sufficient to undermine any functionality in the core (Section 1.5) if these high-Z impurities are not screened by the SOL. Thankfully, the high collisionality of a detached divertor SOL is likely to increase the fraction of far redeposition, although we are unable to verify this effect with our workflow at present. The integration of all these effects remains important future work.

Another point of interest to conclude from Figure 8.3 has to do with the operation of linear-geometry PMI experiments. In the absence of functional fusion reactors, linear plasma devices emulating divertor plasma conditions at next-step devices have become of increasing interest to the PMI community (e.g. MPEX (97)). However, the standard PFC target design in such facilities is $\alpha = 90°$ based on device geometry. This work suggests that redeposition physics may look considerably different at 90° targets when compared to the $\alpha < 5°$ divertor conditions these linear devices are attempting to emulate. Hence, it is recommended to alter target geometry to shallow α whenever possible during studies specifically examining redeposition at these devices. Otherwise, such studies may significantly overestimate net erosion when extrapolating to the engineered ($\alpha < 5°$) regime of next-step facilities. As an example MPEX is designed with the ability to modify $\alpha \searrow 5°$, and we caution maintaining operation in that regime for all detached divertor studies of high-Z redeposition at this device. Alternatively, this design makes MPEX well suited to study net erosion in the worst-case scenarios of α and to validate experimentally the importance of α to overall net erosion (Chapter 7).

In summary our work shows that, in answer to the fundamental question of this dissertation, n_e, T_e, and α are the most important parameters setting the fraction of eroded high-Z material entering the SOL; at the prefatory level of our analysis, high n_e, high T_e, and low α are needed to maximize high-Z redeposition within the sheath (i.e. surface-scale PMI) and minimize reactors' dependence on SOL processes (i.e. global-scale PMI). However, we qualify this statement with some important caveats. Critically, our workflow has been only designed to look at smooth (mm-scale), high-Z PFCs in L- or inter-ELM H-mode plasmas that are undergoing gross erosion limited to physical sputtering. We have not fully incorporated the transport physics of either the incident sputtering ion (modifying Y) or the sputtered PFC (modifying far redeposition) fluxes from the SOL. Furthermore, we have extended our study into high density and temperature regimes where neglected physics processes may dominate in practice. For example, the work in Chapter 6 implies that increasing T_e results in arbitrarily more prompt redeposition due to an increase in δ and a decrease in the ionization length. Obviously, this line of thinking may be true up to a certain point, but there is some (here undetermined) threshold where melting physics becomes important if not dominant in setting the gross erosion. Similarly, incorporating collisional sheath effects may change the importance of n_e due to changes in the electric potential gradients. Indeed, significant additions to both modeling components and physics validations are need before this workflow will be "predictive" of PFC lifetimes in reactor environments (see Chapter 9). Nonetheless, we have provided within this dissertation both a lengthy defense on the importance of maintaining prompt vs local vs far heuristic refinement within the field and a detailed analysis, for the first time, of the impact of α on redeposition in the basic case of interest. Further model development (e.g. microstructural surface effects) alongside experimental validation of this base case (e.g. Chapter 7) are the critical areas to target next.

Chapter 9

Summary and Future Work

Resolution of the energy-climate crisis will almost certainly require fusion energy as part of the baseload portfolio; however, a variety of factors, both theoretical and practical, currently inhibit reactor readiness. To date the integrated tokamak exhaust and performance (ITEP) gap remains a crucial engineering barrier for magnetic confinement fusion. In this dissertation we have developed new research that may help provide insight into partial ITEP gap solutions: specifically, a model refinement for net erosion (i.e. gross erosion - redeposition) regimes and mechanisms of high-Z plasma facing components (PFCs).

To this end, we discussed a general overview of magnetic confinement fusion in Chapter 1 and showed that redeposition occurs via surface-scale and global-scale plasma-material interaction (PMI) processes. Here, we have focused on surface-scale processes and detail analytic models for this physics regime, called the sheath, in Chapter 2. Afterwards, we showed in Chapter 3 that the sheath affects gross erosion through the manipulation of incident ion energy and angle distributions (EADs), which in turn affect the physically sputtered EADs of PFC neutrals. We developed a new Monte Carlo code, PYEAD, that estimates these incident ion EADs while both (1) maintaining good agreement with similar codes and (2) decreasing computational runtime through streamlining and parallelization. We then coupled PYEAD to

a binary collision approximation code RustBCA to enable estimation of the gross erosion distribution.

Next, we discussed the current models of high-Z redeposition in Chapter 4. There, we noted that these models often conflate distinct mechanisms in a way that obscures the dominate physics process behind redeposition events. As a refinement, we proposed a heuristic separation into geometric-driven (prompt), sheath-driven (local), and scrape-off layer (SOL) driven (far) redeposition; the first two processes are surface-scale processes while the latter is a global-scale process. We modified the Monte Carlo redeposition code GITR to distinguish between these mechanisms and coupled this code to our gross erosion model to create a PYEAD-RustBCA-GITR workflow modeling high-Z net erosion. We demonstrated good agreement with other net erosion studies using this workflow.

In Chapter 5 we noted that the magnetic-field-to-PFC pitch angle α has a profound effect on sheath dynamics and may evolve significantly over reactor-relevant lifetimes. Consequently, we used our workflow to determine the impact of α on W net erosion within the context of other parameters changing the sheath thickness: the magnetic-field magnitude and the plasma ion species. We discovered that α has a significant impact on the forward-scattering angle δ within the W^0-EAD; this observation suggests that the usual cosine-δ distribution assumed in net erosion research may be incomplete. The increasing sharpness of δ, in combination with both the increasing rotation of the W gyro-orbit motion parallel to the surface and the decreasing thickness of the sheath, results in a complex trade-off between prompt vs local redeposition as α increases. As a consequence of this model refinement, we showed that current trend-line estimates may underpredict high-Z net erosion by up to two orders of magnitude if α-driven corrections are not considered. Meanwhile, we demonstrated that some second-order parameters have an impact on net erosion that scales with α; for example, there is little redeposition dependence on the magnetic field at shallow α but a strong dependence at near-normal angles.

We re-contextualized this newly observed α sensitivity within a broader range of PMI parameters in Chapter 6. Using Sobol' sensitivity analysis, we demonstrated that prompt redeposition most strongly depends on plasma parameters like electron density and temperature while local redepositon depends most strongly on α. Hence, we indicate that the $\vec{B}$-to-PFC pitch angle is just as important as the plasma parameters commonly studied with net erosion modeling. In other words, this work suggests that understanding the expected α-evolution across PFC lifetimes may be critical to predicting first-wall longevity.

Lastly, we discussed the importance of validating our PYEAD-RustBCA-GITR code and the Chapter 5-6 results with experimental measurements in Chapter 7. We recommended a combination of spectroscopy, surface analysis, and microtrench diagnostics that, for a specialized coupon of W isotopes, could resolve prompt-vs-local trade-off for α variation at the cm-to-mm scale. Importantly, we showed that far UV emission lines are needed to resolve this measurement due to the relatively low emissivities of VUV lines. We also emphasized the need to make similar measurements for nm-μm scale α variation, though our code is unable to provide predictive synthetic data for such experiments at this time. We collected and discussed the key takeaways of all preceding chapters in Chapter 8.

Moving forward, there are two general categories of next steps critical to the work of this dissertation. First and foremost, we must push for experimental validation studies of both the PYEAD-RustBCA-GITR model and its implications for the importance of α in the net erosion process. Specifically, we recommend the validation steps in Chapter 7 or a similar series of experiments to understand and mitigate the full impact of disruption-driven α evolution on PFC longevity. Although we chose to analyze the measurability of prompt-vs-local trade-off in the environment of DIII-D, MPEX provides a potentially better-diagnosed alternative facility for observing this physics in detached regimes; a reassessment of the Chapter 7 predictions for MPEX plasma conditions would be particularly useful once MPEX comes online and establishes its functional operation space. At time of writing, there are ongoing efforts

to use PYEAD to predict the effect of non-Maxwellian initial distributions on the final incident ion EADs at the MPEX target. Further PYEAD-RustBCA-GITR validation opportunities are readily available from the wealth of global data generated during well-diagnosed PMI experiments; for example, there are also ongoing efforts at time of writing using the RustBCA-GITR coupling to calculate recycled carbon impact angles within the small angle slot divertor of DIII-D. We should continue these types of validation efforts beyond the work of this dissertation, particularly wherever further comparisons with results from the similar code ERO2.0 can be made or the extension of our conclusions into the 3D magnetic fields of stellarators can be cross-validated.

Second, we should refine our PYEAD-RustBCA-GITR workflow to include net erosion physics that we excluded from the focus of this document for conciseness. We have noted surface roughness as a variable of importance, which will likely require the incorporation of high-fidelity sheath models and cross-code surface geometry. Such a workflow would then be equipped to interpret prompt-vs-local trade-off in surface-roughness experiments and verify the Sobol' sensitivity analysis of Chapter 6 at the μm-nm scale. The incorporation of high-fidelity sheath models like hPIC, as well as generally creating a consistent sheath model across the PYEAD and GITR components, will allow us to more rigorously assess the importance of electron density in net erosion into detached divertor regimes. In addition, the inclusion of consistent, complex surface morphology across all three codes would enable us to access the influence of evolving surface composition and roughness on net erosion. Similarly, we should incorporate thermal flux codes (e.g. HEAT (81)) into the PYEAD-RustBCA-GITR workflow in order to better capture the role of temperature in the overall net erosion process and particularly its interplay with α.

Beyond these critical regions of development, further modification to the PYEAD-RustBCA-GITR framework can push the intended envelope of this workflow into other interesting PMI applications. Refining our sheath model to include RF-sheaths would allow an assessment of net erosion sensitivities near antennas and the incorporation of other PMI variables like the frequency of sheath oscillation.

This change could also allow cross-validational studies into explaining observed phenomena like the so-called "impurity problem" of Proto-MPEX, where low-Z impurity production from the helicon window demonstrably drives the net erosion contrary to design (6). Meanwhile, rigorously coupling OEDGE or, as a bigger lift, EPED-SOLPS (Snyder et al.) background plasmas into this workflow could facilitate a more integrated study on the impact of PFC surfaces morphology in setting SOL-impurity sourcing, transport, and redistribution. In particular, an extended-grid EPED-SOLPS coupling to a later version of this workflow could directly facilitate the optimization of ITEP solutions between pedestal, SOL, and PFC requirements.

To conclude, this dissertation has provided a modest step forward on the path to engineering first-wall materials. We have demonstrated the importance of a heuristic refinement to redeposition theory and identified the most important PMI parameters that determine the fraction of high-Z redeposition. In combination with the recommended future work and the other excellent research abundant in the fusion effort, we hope this information will help accelerate gap closure between practical fusion reactors and mid-century energy demands.

Bibliography

[1] Abe, S., Skinner, C. H., Bykov, I., Yeh, Y. W., Lasa, A., Coburn, J., Rudakov, D. L., Lasnier, C. J., Wang, H. Q., McLean, A. G., Abrams, T., and Koel, B. E. (2021). Experimental verification of ion impact angle distribution at divertor surfaces using micro-engineered targets on dimes at diii-d. *Nuclear Materials and Energy*, 27. xxvi, 38, 58, 209, 210, 229

[2] Abe, S., Skinner, C. H., Bykov, I., Yeh, Y. W., Lasa, A., Coburn, J., Rudakov, D. L., Lasnier, C. J., Wang, H. Q., McLean, A. G., Abrams, T., and Koel, B. E. (2022). Determination of the characteristic magnetic pre-sheath length at divertor surfaces using micro-engineered targets on dimes at diii-d. *Nuclear Fusion*, 62(6). 38, 58, 209, 229

[3] Abramov, V. A., Igitkhanov, Y. L., Pistunovich, V. I., and Pozharov, V. A. (1989). First wall and divertor plate sputtering in a tokamak reactor. *Journal of Nuclear Materials*, 162-164:462–466. 92

[4] Ammann, A. A. (2007). Inductively coupled plasma mass spectrometry (icp ms): a versatile tool. *J Mass Spectrom*, 42(4):419–27. Ammann, Adrian A eng Review England 2007/03/28 J Mass Spectrom. 2007 Apr;42(4):419-27. doi: 10.1002/jms.1206. xxvi, 217, 218

[5] ASDEX (1989). The h-mode of asdex. *Nuclear Fusion*, 29:1959–2040. 20

[6] Beers, C. J. (2021). *Impurity Production and Transport in the Prototype Material Plasma Exposure eXperiment*. Thesis. 253

[7] Biersack, J. P. and Haggmark, L. G. (1980). A monte carlo computer program for the transport of energetic ions in amorphous targets. *Nuclear Instruments and Methods*, 174. 50, 71

[8] Bohdansky, J. (1984). A universal relation for the sputtering yield of monatomic solids at normal ion incidence. *Nuclear Instruments and Methods in Physics Research B2*, 1984:587–591. 49

[Boris] Boris, J. P. Relativistic plasma simulation - optimization of a hybrid code. In Boris, J. P., editor, *Fourth Conference on Numerical Simulation of Plasmas*. 93

[10] Borodkina, I., Borodin, D., Kirschner, A., Tsvetkov, I. V., Kurnaev, V. A., Komm, M., Dejarnac, R., and Contributors, J. E. T. (2016). An analytical expression for the electric field and particle tracing in modelling of be erosion experiments at the jet iter-like wall. *Contributions to Plasma Physics*, 56(6-8):640–645. 39, 42, 58

[11] Borodkina, I. E., Komm, M., and Tsvetkov, I. V. (2015). Application of analytical model of the electric potential distribution for calculation of charged particle dynamics in a near-wall layer and sputtering of the plasma facing surfaces. *Russian Physics Journal*, 58(4):438–445. 39

[12] bp (2020). Statistical review of world energy 2020. Report, bp. xv, 2, 3

[13] Brezinsek, S., Borodin, D., Coenen, J. W., Kondratjew, D., Laengner, M., Pospieszczyk, A., and Samm, U. (2011). Quantification of tungsten sputtering at w/c twin limiters in textor with the aid of local wf6injection. *Physica Scripta*, T145. 90, 200, 202

[14] Brezinsek, S., Kirschner, A., Mayer, M., Baron-Wiechec, A., Borodkina, I., Borodin, D., Coffey, I., Coenen, J., den Harder, N., Eksaeva, A., Guillemaut, C., Heinola, K., Huber, A., Huber, V., Imrisek, M., Jachmich, S., Pawelec, E., Rubel, M., Krat, S., Sergienko, G., Matthews, G. F., Meigs, A. G., Wiesen, S., and

Widdowson, A. (2019a). Erosion, screening, and migration of tungsten in the jet divertor. *Nuclear Fusion*, 59(9). 90, 202

[15] Brezinsek, S., Laengner, M., Coenen, J. W., O'Mullane, M. G., Pospieszczyk, A., Sergienko, G., and Samm, U. (2017). Spectroscopic determination of inverse photon efficiencies of w atoms in the scrape-off layer of textor. *Physica Scripta*, T170. xxvi, 200, 203

[16] Brezinsek, S., Pospieszczyk, A., Sergienko, G., Dux, R., Cavedon, M., Faitsch, M., and Krieger, K. (2019b). Chemically assisted physical sputtering of tungsten: Identification via the 6→6+ transition of wd in textor and asdex upgrade plasmas. *Nuclear Materials and Energy*, 18:50–55. xvii, 56, 57

[17] Brooks, J. N. (1990). Near-surface sputtered particle transport for an oblique incidence magnetic field plasma. *Physics of Fluids B: Plasma Physics*, 2(8):1858–1863. 38

[18] Brooks, J. N., Elder, J. D., McLean, A., Rudakov, D. L., Stangeby, P. C., and Wampler, W. R. (2015). Analysis of a tungsten sputtering experiment in diii-d and code/data validation of high redeposition/reduced erosion. *Fusion Engineering and Design*, 94. 241

[19] BU (2022). Does more energy use increase the level of human development? Report, Institute for Global Sustainability: Visualizing Energy. 4, 5

[20] Budaev, V. P., Martynenko, Y. V., Grashin, S. A., Giniyatulin, R. N., Arkhipov, I. I., Karpov, A. V., Savrukhin, P. V., Shestakov, E. A., Solomatin, R. Y., Begrambekov, L. B., Belova, N. E., Fedorovich, S. D., Khimchenko, L. N., and Safronov, V. M. (2017). Tungsten melting and erosion under plasma heat load in tokamak discharges with disruptions. *Nuclear Materials and Energy*, 12:418–422. xxvii, 100, 239

[21] Carter, T., Baalrud, S., Betti, R., Ellis, T., Foster, J., Geddes, C., Gleason, A., Holland, C., Humrickhouse, P., Kessel, C., Lasa, A., Ma, T., Maingi, R., Schaffner, D., Schmitz, O., Shumlak, U., Snead, L., Solomon, W., Trask, E., Waelbroeck, F., White, A., and Rej, D. (2020). Powering the future: Fusion plasmas. 20

[22] Caughman, J. B. O., Butler, K., Curreli, D., Donovan, D., Easley, D. C., Gonzalez-Galvan, A., Johnson, C. A., Meredith, L., and Unterberg, E. A. (2024). Investigation of materials for radio frequency antenna plasma facing components. *IEEE Transactions on Plasma Science*, pages 1–6. 142

[23] Chankin, A. V., Coster, D. P., and Dux, R. (2014). Monte carlo simulations of tungsten redeposition at the divertor target. *Plasma Physics and Controlled Fusion*, 56(2). xvii, xviii, xxix, 52, 53, 78, 79, 80, 81, 83, 84, 89, 138

[24] Chen, F. (2016). *Introduction to Plasma Physics and Controlled Fusion*. Springer, New York, 3rd edition. 9, 10, 12, 14, 27, 28, 30

[25] Chodura, R. (1982). Plasma–wall transition in an oblique magnetic field. *The Physics of Fluids*, 25(9):1628–1633. 38

[26] Chrobak, C. P., Doerner, R. P., Stangeby, P. C., Wampler, W. R., Rudakov, D. L., Wright, G. M., Abrams, T., Ding, R., Elder, J. D., Guterl, J., Guo, H. Y., Lasnier, C., Thomas, D. M., Leonard, A. W., Buchenauer, D. A., McLean, A. G., Watkins, J. G., and Tynan, G. R. (2017). Characterizing low-z erosion and deposition in the diii-d divertor using aluminum. *Nuclear Materials and Energy*, 12:441–446. 58

[27] Chrobak, C. P., Stangeby, P. C., Hollmann, E., Rudakov, D. L., Abrams, T., Ding, R., Elder, J. D., Guterl, J., Hinson, E., Guo, H. Y., Thomas, D. M., Skinner, C. H., McLean, A. G., Wampler, W. R., Buchenauer, D. A., Doerner, R. P., and Tynan, G. R. (2018). Measurement and modeling of aluminum sputtering and

ionization in the diii-d divertor including magnetic pre-sheath effects. *Nuclear Fusion*, 58(10). 38, 58, 162

[28] Ciraolo, G., Thin, A., Bufferand, H., Bucalossi, J., Fedorczak, N., Gunn, J. P., Pascal, J. Y., Tamain, P., Gil, C., Gouin, A., Meyer, O., Devynck, P., Vartanian, S., Klepper, C. C., Serre, E., Nespoli, F., Gallo, A., Marandet, Y., and Rosato, J. (2019). First modeling of strongly radiating west plasmas with soledge-eirene. *Nuclear Materials and Energy*, 20. 52

[29] Coburn, J. (2018). *Erosion Characterization of Advanced Plasma Facing Materials (PFMs) for Magnetic Fusion Reactors*. Thesis. xxvi, 207, 209, 210

[30] Coburn, J., Unterberg, E., Barton, J., Rudakov, D., Bykov, I., Parish, C. M., Wilcox, R., Lasnier, C., Abrams, T., Watkins, J., Hillis, D. L., and Bourham, M. (2019). Erosion characterization of sic and ti3sic2 on diii-d using focused ion beam micro-trenches. *Nuclear Materials and Energy*, 19:316–323. 209, 229

[31] Connor, J. W., Hastie, R. J., Wilson, H. R., and Miller, R. L. (1998). Magnetohydrodynamic stability of tokamak edge plasmas. *Physics of Plasmas*, 5. 99

[32] Craxton, R. S., Anderson, K. S., Boehly, T. R., Goncharov, V. N., Harding, D. R., Knauer, J. P., McCrory, R. L., McKenty, P. W., Meyerhofer, D. D., Myatt, J. F., Schmitt, A. J., Sethian, J. D., Short, R. W., Skupsky, S., Theobald, W., Kruer, W. L., Tanaka, K., Betti, R., Collins, T. J. B., Delettrez, J. A., Hu, S. X., Marozas, J. A., Maximov, A. V., Michel, D. T., Radha, P. B., Regan, S. P., Sangster, T. C., Seka, W., Solodov, A. A., Soures, J. M., Stoeckl, C., and Zuegel, J. D. (2015). Direct-drive inertial confinement fusion: A review. *Physics of Plasmas*, 22(11). 10

[33] Ding, R., Rudakov, D. L., Stangeby, P. C., Wampler, W. R., Abrams, T., Brezinsek, S., Briesemeister, A., Bykov, I., Chan, V. S., Chrobak, C. P., Elder,

J. D., Guo, H. Y., Guterl, J., Kirschner, A., Lasnier, C. J., Leonard, A. W., Makowski, M. A., McLean, A. G., Snyder, P. B., Thomas, D. M., Tskhakaya, D., Unterberg, E. A., Wang, H. Q., and Watkins, J. G. (2017a). Advances in understanding of high-zmaterial erosion and re-deposition in low-zwall environment in diii-d. *Nuclear Fusion*, 57(5). 52, 85, 104

[34] Ding, R., Rudakov, D. L., Stangeby, P. C., Wampler, W. R., Abrams, T., Brezinsek, S., Briesemeister, A., Bykov, I., Chan, V. S., Chrobak, C. P., Elder, J. D., Guo, H. Y., Guterl, J., Kirschner, A., Lasnier, C. J., Leonard, A. W., Makowski, M. A., McLean, A. G., Snyder, P. B., Thomas, D. M., Tskhakaya, D., Unterberg, E. A., Wang, H. Q., and Watkins, J. G. (2017b). High-z material erosion and its control in diii-d carbon divertor. *Nuclear Materials and Energy*, 12:247–252. xxvi, 215, 216

[35] Doerner, R. P., Rudakov, D. L., Chrobak, C. P., Briesemeister, A. R., Corr, C., De Temmerman, G., Kluth, P., Lasnier, C. J., McLean, A. G., Pace, D. C., Pitts, R. A., Schmitz, O., Thompson, M., and Winters, V. (2016). Investigation of he–w interactions using dimes on diii-d. *Physica Scripta*, T167. 54

[36] Dolan, T. (2013). *Magnetic Fusion Technology*, volume 19 of *Lecture Notes in Energy*. Springer, London, 1st edition. xxix, 7, 8, 9, 15, 17, 34

[37] Drobny, J. and Curreli, D. (2021). Rustbca: A high-performance binary-collision-approximation code for ion-material interactions. *Journal of Open Source Software*, 6(64). xviii, 71, 72

[38] Drobny, J., Hayes, A., Curreli, D., and Ruzic, D. N. (2017). F-tridyn: A binary collision approximation code for simulating ion interactions with rough surfaces. *Journal of Nuclear Materials*, 494:278–283. 50, 71

[39] Duran, J. D. (2022). *DETERMINATION OF NEAR-SOL CARBON IMPURITY CONTENT DUE TO DIVERTOR TARGET LEAKAGE USING*

CARBON-13 TRACERS VIA METHANE INJECTION ON THE DIII-D TOKAMAK. Thesis. 217

[40] Duran, J. D., Unterberg, E. A., Zach, M. P., Wampler, W. R., Rudakov, D. L., and Donovan, D. C. (2019). Multiple analytical approach to isotopic transport analysis in magnetic fusion devices. *Fusion Science and Technology*, 75(6):493–498. xxvi, 217, 218

[41] Dux, R., Bobkov, V., Herrmann, A., Janzer, A., Kallenbach, A., Neu, R., Mayer, M., Müller, H. W., Pugno, R., Pütterich, T., Rohde, V., and Sips, A. C. C. (2009). Plasma-wall interaction and plasma behaviour in the non-boronised all tungsten asdex upgrade. *Journal of Nuclear Materials*, 390-391:858–863. 202

[42] Easley, D. C., Diaw, A., Younkin, T. R., Donovan, D. C., Unterberg, E. A., Nichols, J. H., Johnson, C. A., and Kumar, A. (2024). Dependence of high-z redeposition on the field-to-surface pitch angle and other sheath parameters in tokamaks. *Physics of Plasmas*, 31(5). 98

[43] Eckstein, W. (1991). *Computer Simulation of Ion-Solid Interactions*. Springer Series in Material Science. Springer. 69, 211

[44] Eckstein, W., García-Rosales, C., Roth, J., and László, J. (1993). Threshold energy for sputtering and its dependence on angle of incidence. *nuclear Instruments and Methods in Physics Research B2*, 83. 50

[45] EIA (2019). International energy outlook 2019 with projections to 2050. Report, U.S. Energy Information Administration. 3, 4

[46] Eksaeva, A., Kirschner, A., Romazanov, J., Brezinsek, S., Linsmeier, C., Maviglia, F., Siccinio, M., and Ciattaglia, S. (2022). Predictive 3d modelling of erosion and deposition in iter with ero2.0: from beryllium main wall, tungsten divertor to full-tungsten device. *Physica Scripta*, 97(1). 241

[47] Ericsson, G. (2019). Advanced neutron spectroscopy in fusion research. *Journal of Fusion Energy*, 38(3-4):330–355. xv, 8

[48] Fussmann, G., Engelhardt, W., Naujoks, D., Asmussen, K., Deschka, S., Field, A., Fuchs, J., García-Rosales, C., Hirsch, S., Ignacz, P., Lieder, G., Neu, R., Radtke, R., Roth, J., and Wenzel, U. (1995). High-z elements as target materials in fusion devices. 75, 76, 78, 89

[49] Gallo, A., Sepetys, A., Marandet, Y., Bufferand, H., Ciraolo, G., Fedorczak, N., Brezinsek, S., Bucalossi, J., Coenen, J., Clairet, F., Corre, Y., Desgranges, C., Devynck, P., Gaspar, J., Guirlet, R., Gunn, J., Klepper, C. C., Pascal, J. Y., Tamain, P., Tsitrone, E., Unterberg, E. A., and West team, t. (2020). Interpretative transport modeling of the west boundary plasma: main plasma and light impurities. *Nuclear Fusion*, 60(12). 52

[50] García-Rosales, C., Eckstein, W., and Roth, J. (1994). Revised formulae for sputtering data. *Journal of Nuclear Materials*, 218:8–17. 49

[51] Goldstein, H., Poole, C. P., and Safko, J. (2002). *Classical Mechanics*. Pearson, 3rd edition. 67

[52] Grosjean, A., Radenac, T., Fedorczak, N., Donovan, D. C., Guillemaut, C., Johnson, C. A., Gunn, J. P., Ardizzone, P. L., Clairet, F., Easley, D. C., Gil, C., Klepper, C. C., Kosslow, S. R., and Unterberg, E. A. (2022). Development of an integrated multidiagnostic to assess the high-z impurity fluxes in the metallic environment of west using imas. *IEEE Transactions on Plasma Science*, 50(11):4251–4256. 202

[53] Guterl, J., Bykov, I., Ding, R., and Snyder, P. (2021). On the prediction and monitoring of tungsten prompt redeposition in tokamak divertors. *Nuclear Materials and Energy*, 27. xix, 74, 85, 87, 88, 89, 90, 99, 129, 131, 138, 184

[54] Guterl, J., Johnson, C., Ennis, D., Loche, S., and Snyder, P. (2020). Effects ofthe chodura sheath on tungsten ionization and emission in tokamak divertors. *Contributions to Plasma Physics*, 60(5-6). 76, 85

[55] Guterl, J., Wampler, W. R., Rudakov, D., Abrams, T., Wang, H. Q., McLean, A. G., and Snyder, P. (2019). Reduced model of high-z impurity redeposition and erosion in tokamak divertor and its application to diii-d experiments. *Plasma Physics and Controlled Fusion*, 61(12). 118

[56] Hakola, A., Airila, M. I., Karhunen, J., Groth, M., Herrmann, A., Krieger, K., Kurki-Suonio, T., Meisl, G., Oberkofler, M., Neu, R., Potzel, S., and Rohde, V. (2016). Gross and net erosion of tungsten in the outer strike-point region of asdex upgrade. *Physica Scripta*, T167. xxvi, 52, 215, 216

[57] Hartwell, G. J., Knowlton, S. F., Hanson, J. D., Ennis, D. A., and Maurer, D. A. (2017). Design, construction, and operation of the compact toroidal hybrid. *Fusion Science and Technology*, 72(1):76–90. 105

[58] Hays, J., Imbrie, J., and Shackleton, N. (1976). Variations in the earth's orbit: Pacemaker of the ice ages. *Science*, 194(4270):1121–1132. 1

[59] Helton, J. C., Johnson, J. D., Sallaberry, C. J., and Storlie, C. B. (2006). Survey of sampling-based methods for uncertainty and sensitivity analysis. Report, Sandia National Laboratories. 138

[60] Hirai, T., Panayotis, S., Barabash, V., Amzallag, C., Escourbiac, F., Durocher, A., Merola, M., Linke, J., Loewenhoff, T., Pintsuk, G., Wirtz, M., and Uytdenhouwen, I. (2016). Use of tungsten material for the iter divertor. *Nuclear Materials and Energy*, 9:616–622. 100

[61] Hubbard, A. (2000). Physics and scaling of the h-mode pedestal. *Plasma Physics and Controlled Fusion*, 42:A15–A35. 20

[62] Hussein, E. M. A. (2020). Emerging small modular nuclear power reactors: A critical review. *Physics Open*, 5. 3

[63] Hutchinson, I. (2002). *Principles of Plasma Diagnostics*. Cambridge University Press, New York, 2nd edition. 194, 197, 199

[64] IEA (2019). Coal 2019: Analysis and forecasts to 2024. Report, International Energy Agency. 1

[65] Ikeda, K. (2010). Iter on the road to fusion energy. *Nuclear Fusion*, 50(1). xv, 10, 11

[66] Johnson, C. (2020). *Theoretical modeling combined with experimental spectroscopic measurements for the diagnosis of high-Z erosion and transport applications in plasmas*. Thesis. xxx, 204, 205

[67] Johnson, C. A., Loch, S. D., and Ennis, D. A. (2019). Colradpy: A python collisional radiative solver. *Nuclear Materials and Energy*, 20. 192, 204, 206

[68] Johnson, C. A., Loch, S. D., and Ennis, D. A. (2020). The effect of metastable atomic levels in neutral tungsten for erosion and impurity transport applications. *Plasma Physics and Controlled Fusion*, 62(12). xxvi, 207, 208, 222

[69] Khaziev, R. and Curreli, D. (2015). Ion energy-angle distribution functions at the plasma-material interface in oblique magnetic fields. *Physics of Plasmas*, 22(4). 92

[70] Khaziev, R. and Curreli, D. (2018). hpic: A scalable electrostatic particle-in-cell for plasma–material interactions. *Computer Physics Communications*, 229:87–98. 92, 184

[71] Kirschner, A., Brezinsek, S., Huber, A., Meigs, A., Sergienko, G., Tskhakaya, D., Borodin, D., Groth, M., Jachmich, S., Romazanov, J., Wiesen, S., and Linsmeier, C. (2019). Modelling of tungsten erosion and deposition in the divertor of jet-ilw in

comparison to experimental findings. *Nuclear Materials and Energy*, 18:239–244. xvii, 52, 54, 55, 202

[72] Kirschner, A., Tskhakaya, D., Kawamura, G., Borodin, D., Brezinsek, S., Ding, R., Linsmeier, C., and Romazanov, J. (2016). Modelling of impurity transport and plasma-wall interaction in fusion devices with the ero code: Basics of the code and examples of application. *Contributions to Plasma Physics*, 56(6-8):622–627. xvii, 55, 58

[73] Klepper, C. C., Unterberg, E. A., Marandet, Y., Curreli, D., Grosjean, A., Harris, J. H., Johnson, C. A., Gallo, A., Goniche, M., Guillemaut, C., Gunn, J. P., Raghunathan, M., Tsitrone, E., Ciraolo, G., Colas, L., Donovan, D., Ekedahl, A., Easley, D., and Urbanczyk, G. (2022). Characterizing w sources in the all-w wall, all-rf west tokamak environment * , **. *Plasma Physics and Controlled Fusion*, 64(10). 202

[74] Kotschenreuther, M., Liu, X., Hatch, D. R., Mahajan, S., Zheng, L., Diallo, A., Groebner, R., Hillesheim, J. C., Maggi, C. F., Giroud, C., Koechl, F., Parail, V., Saarelma, S., Solano, E. R., and Chankin, A. (2019). Gyrokinetic analysis and simulation of pedestals to identify the culprits for energy losses using 'fingerprints'. *Nuclear Fusion*, 59(9). 99

[75] Krieger, K., Balden, M., Coenen, J. W., Laggner, F., Matthews, G. F., Nille, D., Rohde, V., Sieglin, B., Giannone, L., Göths, B., Herrmann, A., de Marne, P., Pitts, R. A., Potzel, S., and Vondracek, P. (2018). Experiments on transient melting of tungsten by elms in asdex upgrade. *Nuclear Fusion*, 58(2). xxvii, 239

[76] Kunze, H.-J. (2009). *Introduction to Plasma Spectroscopy*. Springer Series on Atomic, Optical, and Plasma Physics. Springer, New York. xxix, 194, 196, 197, 198

[77] Lasa, A. (2017). Documentation of: Scripting for preliminary studies on micro patterning and roughness (mpr). xxvi, 209, 212

[78] Lawson, J. (1957). Some criteria for a useful thermonuclear reactor. 9

[79] Leonard, A. W., McLean, A. G., Makowski, M. A., and Stangeby, P. C. (2017). Compatibility of separatrix density scaling for divertor detachment with h-mode pedestal operation in diii-d. *Nuclear Fusion*, 57. 99, 245

[80] Lipschultz, B., Parra, F. I., and Hutchinson, I. H. (2016). Sensitivity of detachment extent to magnetic configuration and external parameters. *Nuclear Fusion*, 56. 99

[81] Looby, T., Reinke, M., Wingen, A., Menard, J., Gerhardt, S., Gray, T., Donovan, D., Unterberg, E., Klabacha, J., and Messineo, M. (2022). A software package for plasma-facing component analysis and design: The heat flux engineering analysis toolkit (heat). *Fusion Science and Technology*, 78(1):10–27. 252

[82] Manabe, S. and Wetherald, R. (1967). Thermal equilibrium of the atmosphere with a given distribution of relative humidity. *Journal of the Atomospheric Sciences*, 24(3):241–259. 1

[83] Marandet, Y., Bufferand, H., Bucalossi, J., Ciraolo, G., Lisgo, S. W., and Tsitrone, E. (2015). Assessment of tungsten sources in the edge plasma of west. *Journal of Nuclear Materials*, 463:629–633. 82

[84] Mellet, N., Gunn, J. P., Pégourié, B., Hakola, A., Airila, M., Marandet, Y., and Roubin, P. (2017a). Influence of the magnetised sheath on the redeposition location of sputtered tungsten and its effect on the net erosion. *Nuclear Materials and Energy*, 12:488–493. xviii, 84, 85, 99, 138

[85] Mellet, N., Gunn, J. P., Pégourié, B., Marandet, Y., Martin, C., and Roubin, P. (2017b). Tungsten erosion by impurities and redeposition: focus on the magnetised sheath. *Plasma Physics and Controlled Fusion*, 59(3). xviii, 85, 86

[86] Mordijck, S. (2020). Overview of density pedestal structure: role of fueling versus transport. *Nuclear Fusion*, 60. 23

[Mossessian et al.] Mossessian, D., Hughes, J., Hubbard, A., Marmar, E., and Wolfe, S. H-mode pedestal studies in alcator c-mod. In Todd, T. N., editor, *27th European Physical Society*. xvi, 21

[88] Möller, W. and Eckstein, W. (1984). Tridyn - a trim simulation code including dynamic composition changes. *Nuclear Instruments and Methods in Physics Research B2*, 2. 50, 71

[89] NASA (2021). Temperature anomalies over land and over ocean. xv, 2

[90] Naujoks, D., Asmussen, K., Bessenrodt-Weberpals, M., Deschka, S., Dux, R., Engelhardt, W., Field, A., Fussmann, G., Fuchs, J., García-Rosales, C., Hirsch, S., Ignacz, P., Lieder, G., Mast, K., Neu, R., Radtke, R., Roth, J., Wenzel, U., and Team, A. U. (1996). Tungsten as target material in fusion devices. *Nuclear Fusion*, 36(6):671–687. xviii, 75, 76, 77, 78, 89, 169

[91] Nichols, J. H., Abrams, T., Chrobak, C. P., Donovan, D. C., Duran, J. D., Elder, J. D., Rudakov, D. L., Stangeby, P. C., Unterberg, E. A., Wampler, W. R., Watkins, J. G., and Zamperini, S. A. (2021). Modeling of exb effects on tungsten re-deposition and transport in the diii-d divertor. *Nuclear Fusion*, 61(9). xvi, xxix, 17, 19, 102, 103

[92] Pitts, R. A., Bonnin, X., Escourbiac, F., Frerichs, H., Gunn, J. P., Hirai, T., Kukushkin, A. S., Kaveeva, E., Miller, M. A., Moulton, D., Rozhansky, V., Senichenkov, I., Sytova, E., Schmitz, O., Stangeby, P. C., De Temmerman, G., Veselova, I., and Wiesen, S. (2019). Physics basis for the first iter tungsten divertor. *Nuclear Materials and Energy*, 20. 25, 45

[93] Pospieszczyk, A., Borodin, D., Brezinsek, S., Huber, A., Kirschner, A., Mertens, P., Sergienko, G., Schweer, B., Beigman, I. L., and Vainshtein, L. (2010).

Determination of rate coefficients for fusion-relevant atoms and molecules by modelling and measurement in the boundary layer of textor. *Journal of Physics B: Atomic, Molecular and Optical Physics*, 43(14). xxvi, xxx, 90, 200, 201

[94] Press, W. H., Teukolsky, S. A., Vetterling, W. T., and Flannery, B. P. (2007). *Numerical Recipes: The Art of Scientific Computing*. Cambridge University Press, 3rd edition edition. 58, 142

[95] Pütterich, T., Neu, R., Dux, R., Whiteford, A. D., O'Mullane, M. G., and Summers, H. P. (2010). Calculation and experimental test of the cooling factor of tungsten. *Nuclear Fusion*, 50(2). xvi, 23, 24

[96] Raja, P. and Barron, A. (2021). Rutherford backscattering of thin films. xxvi, 213, 214, 215

[97] Rapp, J., Lau, C., Lumsdaine, A., Beers, C. J., Bigelow, T. S., Biewer, T. M., Boyd, T., Caneses, J. F., Caughman, J. B. O., Duckworth, R., Goulding, R. H., Hicks, W. R., Kafle, N., Piotrowicz, P. A., and West, D. (2020). The materials plasma exposure experiment: Status of the physics basis together with the conceptual design and plans forward. *IEEE Transactions on Plasma Science*, 48(6):1439–1445. 189, 247

[98] Robbe, P., Blondel, S., Casey, T. A., Lasa, A., Sargsyan, K., Wirth, B. D., and Najm, H. N. (2023). Global sensitivity analysis of a coupled multiphysics model to predict surface evolution in fusion plasma-surface interactions. *Computational Materials Science*, 226. 138

[99] Robinson, M. T. (1992). The binary collision approximation: Background and introduction. *Radiation Effects and Defects in Solids: Incorporating Plasma Science and Plasma Technology*, null. xviii, 50, 67, 68, 69, 70

[100] Rodriguez-Fernandez, P., Creely, A. J., Greenwald, M. J., Brunner, D., Ballinger, S. B., Chrobak, C. P., Garnier, D. T., Granetz, R., Hartwig, Z. S.,

Howard, N. T., Hughes, J. W., Irby, J. H., Izzo, V. A., Kuang, A. Q., Lin, Y., Marmar, E. S., Mumgaard, R. T., Rea, C., Reinke, M. L., Riccardo, V., Rice, J. E., Scott, S. D., Sorbom, B. N., Stillerman, J. A., Sweeney, R., Tinguely, R. A., Whyte, D. G., Wright, J. C., and Yuryev, D. V. (2022). Overview of the sparc physics basis towards the exploration of burning-plasma regimes in high-field, compact tokamaks. *Nuclear Fusion*, 62. 142

[101] Roth, J., Tsitrone, E., Loarer, T., Philipps, V., Brezinsek, S., Loarte, A., Counsell, G. F., Doerner, R. P., Schmid, K., Ogorodnikova, O. V., and Causey, R. A. (2008). Tritium inventory in iter plasma-facing materials and tritium removal procedures. *Plasma Physics and Controlled Fusion*, 50(10). 23

[102] Schaeffer, B. (2013). Pairing effect on the binding energy curve of n=z atomic nuclei. *World Journal of Nuclear Science and Technology*, 3:79–82. xv, 6

[103] Schmid, K., Mayer, M., Adelhelm, C., Balden, M., and Lindig, S. (2010). Impact of gyro-motion and sheath acceleration on the flux distribution on rough surfaces. *Nuclear Fusion*, 50(10). 34, 61, 100, 190

[104] Shah, V., van Maris, M. P. F. H. L., van Dommelen, J. A. W., and Geers, M. G. D. (2020). Experimental investigation of the microstructural changes of tungsten monoblocks exposed to pulsed high heat loads. *Nuclear Materials and Energy*, 22. xxvii, 100, 240

[Snyder et al.] Snyder, P. B., Canik, J. M., Shafer, M. W., Park, J. M., Park, J. S., Staebler, G. M., Wilcox, R. S., Leonard, A. W., Moser, A. L., Wang, H. Q., McLean, A. G., and Scotti, F. Self-consistent integrated modeling of the pedestal, scrape-off layer, and divertor. In Buttery, R., editor, *29th IAEA Fusion Energy Conference*. 253

[106] Sobol', I. M. (2001). Global sensitivity indices for nonlinear mathematical models and their monte carlo estimates. *Mathematics and Computers in Simulations*, 55(1-3):271–280. 138

[107] Stacey, W. (2005). *Fusion Plasma Physics*. 93, 94

[108] Stacey, W. (2010). *Fusion: An Introduction to the Physics and Technology of Magnetic Confinement Fusion*. Wiley-VCH, Weinheim, 2nd edition. 5, 7, 9, 12, 14

[109] Stangeby, P. (2000). *The Plasma Boundary of Magnetic Fusion Devices*. Plasma Physics Series. Institute of Physics, Bristol. xv, xvi, xvii, 14, 15, 16, 20, 22, 27, 29, 30, 31, 32, 34, 35, 37, 46, 48, 51, 56, 61, 75, 76

[110] Stangeby, P. C. (2012). The chodura sheath for angles of a few degrees between the magnetic field and the surface of divertor targets and limiters. *Nuclear Fusion*, 52(8). 38, 39, 42, 90

[111] Stangeby, P. C. (2018). Basic physical processes and reduced models for plasma detachment. *Plasma Physics and Controlled Fusion*, 60(4). 99, 245

[112] Stangeby, P. C., Elder, J. D., Boedo, J. A., Bray, B., Brooks, N. H., Fenstermacher, M. E., Groth, M., Isler, R. C., Lao, L. L., Lisgo, S., Porter, G. D., Reiter, D., Rudakov, D. L., Watkins, J. G., West, W. P., and Whyte, D. G. (2003). Interpretive modeling of simple-as-possible-plasma discharges on diii-d using the oedge code. *Journal of Nuclear Materials*, 313-316:883–887. 17

[113] Stangeby, P. C., Rudakov, D. L., Wampler, W. R., Brooks, J. N., Brooks, N. H., Buchenauer, D. A., Elder, J. D., Hassanein, A., Leonard, A. W., McLean, A. G., Okamoto, A., Sizyuk, T., Watkins, J. G., and Wong, C. P. C. (2013). An experimental comparison of gross and net erosion of mo in the diii-d divertor. *Journal of Nuclear Materials*, 438:S309–S312. 241

[114] Sudret, B. (2008). Global sensitivity analysis using polynomial chaos expansions. *Reliability Engineering and System Safety*, 93(7):964–979. 138, 139, 140

[115] Summers, H. P. (2004). The adas user manual, version 2.6. 93

[116] Tanga, A., Behringer, K., Costley, A., Brusati, M., Denne, B., Edwards, A., Gibson, A., Gill, R., Gottardi, N., Granetz, R., Harbour, P., Jäckel, H., Keilhacker, M., Lazzaro, E., Malacarne, M., Morgan, P., Noll, P., O'Rourke, J., Stott, P., Summers, D., Tagle, J., and Thomas, P. (1987). Magnetic separatrix experiments in jet. *Nuclear Fusion*, 27:1877–1895. 20

[117] Tester, J., Drake, E., Driscoll, M., Golay, M., and Peters, W. (2012). *Sustainable Energy: Choosing Among Options*. The MIT Press, Cambridge, MA, 2nd edition. 1, 3

[118] Thomas, C. D., Cameron, A., Green, R., Bakkenes, M., Beaumont, L., Collingham, Y., Erasmus, B., Ferreira de Siqueira, M., Grainger, A., Hannah, L., Hughes, L., Huntley, B., van Jaarsveld, A., Midgley, G., Miles, L., Ortega-Huerta, M., Peterson, A., Phillips, O., and Williams, S. (2004). Extinction risk from climate change. *Nature*, 427:145–148. 1

[119] Thompson, M. W. (1967). Ii. the energy spectrum of ejected atoms during the high energy sputtering of gold. *The Philosophical Magazine: A Journal of Theoretical Experimental and Applied Physics*, 18. 61, 66

[120] Tskhakaya, D., Groth, M., and contributors, J. E. (2013). 1d kinetic modelling of the jet sol with tungsten divertor plates. *J Nucl Mater*, 438(Suppl):S522–S525. Tskhakaya, D Groth, M eng Netherlands 2013/07/01 J Nucl Mater. 2013 Jul;438(Suppl):S522-S525. doi: 10.1016/j.jnucmat.2013.01.108. 99

[Unterberg] Unterberg, E. Implications of net erosion and redeposition of solid-surface plasma facing material in long-pulse fusion devices. In *Technical Meeting on Long-Pulse Operation of Fusion Devices*. xvi, 24

[122] Unterberg, E. A., Donovan, D. C., Duran, J. D., Stangeby, P. C., Zamperini, S., Abrams, T., Rudakov, D. L., Wampler, W. R., and Zach, M. P. (2019). Use of isotopic tungsten tracers and a stable-isotope-mixing model to characterize divertor source location in the diii-d metal rings campaign. *Nuclear Materials and Energy*, 19:358–363. 217

[123] van Rooij, G. J., Coenen, J. W., Aho-Mantila, L., Brezinsek, S., Clever, M., Dux, R., Groth, M., Krieger, K., Marsen, S., Matthews, G. F., Meigs, A., Neu, R., Potzel, S., Pütterich, T., Rapp, J., and Stamp, M. F. (2013). Tungsten divertor erosion in all metal devices: Lessons from the iter like wall of jet. *Journal of Nuclear Materials*, 438:S42–S47. 90, 202

[124] Viezzer, E. (2018). Access and sustainment of naturally elm-free and small-elm regimes. *Nuclear Fusion*, 58. 99

[125] Wampler, W. R., Stangeby, P. C., Watkins, J. G., Buchenauer, D. A., Rudakov, D. L., and Wong, C. P. C. (2013). Measurements of net erosion and redeposition of molybdenum in diii-d. *Journal of Nuclear Materials*, 438:S822–S826. 241

[126] Wang, K., Doerner, R. P., Baldwin, M. J., Meyer, F. W., Bannister, M. E., Darbal, A., Stroud, R., and Parish, C. M. (2017). Morphologies of tungsten nanotendrils grown under helium exposure. *Sci Rep*, 7:42315. Wang, Kun Doerner, R P Baldwin, M J Meyer, F W Bannister, M E Darbal, Amith Stroud, Robert Parish, Chad M eng Research Support, U.S. Gov't, Non-P.H.S. England Sci Rep. 2017 Feb 14;7:42315. doi: 10.1038/srep42315. xvii, 54, 55

[127] Wiesen, S., Reiter, D., Kotov, V., Baelmans, M., Dekeyser, W., Kukushkin, A. S., Lisgo, S. W., Pitts, R. A., Rozhansky, V., Saibene, G., Veselova, I., and

Voskoboynikov, S. (2015). The new solps-iter code package. *Journal of Nuclear Materials*, 463:480–484. 17

[128] Wong, C. P. C., Junge, R., Phelps, R. D., Politzer, P., Puhn, F., and West, W. P. (1992). Divertor materials evaluation system at diii-d. *Journal of Nuclear Materials*, 196-198:871–875. 102, 189

[129] Xu, Y. (2016). A general comparison between tokamak and stellarator plasmas. *Matter and Radiation at Extremes*, 1(4):192–200. xv, 12, 13

[130] Yamamura, Y. (1984). A simple analysis of the angular dependence of light-ion sputtering. *Nuclear Instruments and Methods in Physics Research B2*, 2. 49, 71

[131] Younkin, T. R., Green, D. L., Simpson, A. B., and Wirth, B. D. (2021). Gitr: An accelerated global scale particle tracking code for wall material erosion and redistribution in fusion relevant plasma–material interactions. *Computer Physics Communications*, 264. 92, 93

[132] Younkin, T. R., Sargsyan, K., Casey, T., Najm, H. N., Canik, J. M., Green, D. L., Doerner, R. P., Nishijima, D., Baldwin, M., Drobny, J., Curreli, D., and Wirth, B. D. (2022). Quantification of the effect of uncertainty on impurity migration in pisces-a simulated with gitr. *Nuclear Fusion*, 62(5). 92, 138

[133] Zylstra, A. B., Hurricane, O. A., Callahan, D. A., Kritcher, A. L., Ralph, J. E., Robey, H. F., Ross, J. S., Young, C. V., Baker, K. L., Casey, D. T., Doppner, T., Divol, L., Hohenberger, M., Le Pape, S., Pak, A., Patel, P. K., Tommasini, R., Ali, S. J., Amendt, P. A., Atherton, L. J., Bachmann, B., Bailey, D., Benedetti, L. R., Berzak Hopkins, L., Betti, R., Bhandarkar, S. D., Biener, J., Bionta, R. M., Birge, N. W., Bond, E. J., Bradley, D. K., Braun, T., Briggs, T. M., Bruhn, M. W., Celliers, P. M., Chang, B., Chapman, T., Chen, H., Choate, C., Christopherson, A. R., Clark, D. S., Crippen, J. W., Dewald, E. L., Dittrich, T. R., Edwards, M. J., Farmer, W. A., Field, J. E., Fittinghoff, D., Frenje, J., Gaffney, J., Gatu Johnson,

M., Glenzer, S. H., Grim, G. P., Haan, S., Hahn, K. D., Hall, G. N., Hammel, B. A., Harte, J., Hartouni, E., Heebner, J. E., Hernandez, V. J., Herrmann, H., Herrmann, M. C., Hinkel, D. E., Ho, D. D., Holder, J. P., Hsing, W. W., Huang, H., Humbird, K. D., Izumi, N., Jarrott, L. C., Jeet, J., Jones, O., Kerbel, G. D., Kerr, S. M., Khan, S. F., Kilkenny, J., Kim, Y., Geppert Kleinrath, H., Geppert Kleinrath, V., Kong, C., Koning, J. M., Kroll, J. J., Kruse, M. K. G., Kustowski, B., Landen, O. L., Langer, S., Larson, D., Lemos, N. C., Lindl, J. D., Ma, T., MacDonald, M. J., MacGowan, B. J., Mackinnon, A. J., MacLaren, S. A., MacPhee, A. G., Marinak, M. M., Mariscal, D. A., Marley, E. V., Masse, L., et al. (2022). Burning plasma achieved in inertial fusion. *Nature*, 601(7894):542–548. Zylstra, A B Hurricane, O A Callahan, D A Kritcher, A L Ralph, J E Robey, H F Ross, J S Young, C V Baker, K L Casey, D T Doppner, T Divol, L Hohenberger, M Le Pape, S Pak, A Patel, P K Tommasini, R Ali, S J Amendt, P A Atherton, L J Bachmann, B Bailey, D Benedetti, L R Berzak Hopkins, L Betti, R Bhandarkar, S D Biener, J Bionta, R M Birge, N W Bond, E J Bradley, D K Braun, T Briggs, T M Bruhn, M W Celliers, P M Chang, B Chapman, T Chen, H Choate, C Christopherson, A R Clark, D S Crippen, J W Dewald, E L Dittrich, T R Edwards, M J Farmer, W A Field, J E Fittinghoff, D Frenje, J Gaffney, J Gatu Johnson, M Glenzer, S H Grim, G P Haan, S Hahn, K D Hall, G N Hammel, B A Harte, J Hartouni, E Heebner, J E Hernandez, V J Herrmann, H Herrmann, M C Hinkel, D E Ho, D D Holder, J P Hsing, W W Huang, H Humbird, K D Izumi, N Jarrott, L C Jeet, J Jones, O Kerbel, G D Kerr, S M Khan, S F Kilkenny, J Kim, Y Geppert Kleinrath, H Geppert Kleinrath, V Kong, C Koning, J M Kroll, J J Kruse, M K G Kustowski, B Landen, O L Langer, S Larson, D Lemos, N C Lindl, J D Ma, T MacDonald, M J MacGowan, B J Mackinnon, A J MacLaren, S A MacPhee, A G Marinak, M M Mariscal, D A Marley, E V Masse, L Meaney, K Meezan, N B Michel, P A Millot, M Milovich, J L Moody, J D Moore, A S Morton, J W Murphy, T Newman, K Di Nicola, J-M G Nikroo, A Nora, R Patel, M V Pelz, L J Peterson, J L Ping, Y Pollock, B B Ratledge, M Rice, N G Rinderknecht, H Rosen, M Rubery, M S

Salmonson, J D Sater, J Schiaffino, S Schlossberg, D J Schneider, M B Schroeder, C R Scott, H A Sepke, S M Sequoia, K Sherlock, M W Shin, S Smalyuk, V A Spears, B K Springer, P T Stadermann, M Stoupin, S Strozzi, D J Suter, L J Thomas, C A Town, R P J Tubman, E R Trosseille, C Volegov, P L Weber, C R Widmann, K Wild, C Wilde, C H Van Wonterghem, B M Woods, D T Woodworth, B N Yamaguchi, M Yang, S T Zimmerman, G B eng Research Support, Non-U.S. Gov't Research Support, U.S. Gov't, Non-P.H.S. England 2022/01/28 Nature. 2022 Jan;601(7894):542-548. doi: 10.1038/s41586-021-04281-w. Epub 2022 Jan 26. 10

Appendix

A PYEAD Source Code

Here, we reproduce the PYEAD source code that we developed as part of this dissertation research. In this version of PYEAD, the names of the subroutines, names of the output files, and comments throughout are verbatim whenever possible from the ieadrk3 code, in order to facilitate comparison and troubleshooting against ieadrk3.

```
#####################################################
#
# File name: PYEAD.py
#
# Modified by: Davis Easley
#
# Purpose: This program executes ion impact energy and angle
# distribution calculations as a Python conversion from
    existing IDL
# code, written by C. Chrobak and modified by S. Abe, named
    ieadkr3.pro.
# By converting to Python, this code may be more widely and
    easily used
# in the absence of an IDL license. To compensate for the
    longer
# computational runtime associated with open-source
    differential
# equation solvers, the monte carlo process has been isolated
     and
# parallelized (in contrast to the IDL version).
#
# Version: ieadrk3.pro updates through Abe 2022
#
#####################################################

import numpy as np
import math
import matplotlib.pyplot as plt
```

```
from scipy.integrate import solve_ivp
import time
from joblib import Parallel, delayed

def mps_dist(alphadeg=None,mii_amu=None,mip_amu=None,mni=None
    ,mnp=None,Te=None,Ti=None,B=None,Zip=None,Zii=None,ne=None
    ,n_ions=None,out=None,name=None,forceds=None,noe=None,lmps
    =None,pal=None):
        #alphadeg: toroidal pitch angle, degrees from surface
            plane
        #mii_amu: impurity or launched ion mass (amu)
        #mip_amu: background plasma ion mass (amu)
        #mni: mach number of main ions
        #mnp: mach number of impurity ions
        #Te=Ti (default): electron and ion temperature (eV)
        #B: magnetic field strength (T)
        #Zip=Zii (default): plasma and impurity ion charge
            state
        #ne: background plasma elecron desnity (m^-3)
        #n_ions: number of ions to track
        #out: set /output switch to generate output text
            files
        #name: file name for outputs
        #forceds: manually set Debye electric field
            contribution
        #noe: flag no electric field in sheath
        #lmps: sheath thickness = lmps*rho_i*sin(alpha)
        #pal: number of parallel processors
```

```
if alphadeg != None:
        alphadeg = 90.0 - alphadeg

#Set default parameters if none chosen:
if mip_amu == None:
        mip_amu = 2.016
if mni == None:
        mni = 1.0
if mnp == None:
        mnp = 1.0
if alphadeg == None:
        alphadeg = 85.0
if Te == None:
        Te = 25.0
if B == None:
        B = 2.0
if Zip == None:
        Zip = 1.0
if Zii == None:
        Zii = Zip
if ne == None:
        ne = 1.0e19
if n_ions == None:
        n_ions = 500
if mii_amu == None:
        mii_amu = mip_amu
if Ti == None:
```

```
        Ti = Te
if forceds == None:
        forceds = 0.0
if lmps == None:
        lmps = 2.0
if pal == None:
        pal = 2

#Initialize output files if requested:
if out != None:
        if name == None:
                name = 'run'
        commfile = name+'_comments.txt'
        distfile = name+'_distributions.txt'
        #angfile = name+'_angle.inp'
        mpsfile = name+'_mps.txt'
        posfile = name+'_positiondist.txt'
        partfile = name+'_particles.txt'
        comlun = open(commfile,'w')
        dislun = open(distfile,'w')
        #anglun = open(angfile, 'w')
        poslun = open(posfile, 'w')
        mpslun = open(mpsfile, 'w')
        partlun = open(partfile,'w')

        mpslun.write('y[m], y[m/rho_ion], y[m/r_d], E
            [V/m], lambda_norm, ne[E13cm-3], ne[norm],
             lambda_debye, lambda_mps'+'\n')
```

```
            comlun.write('// runid: '+name+'\n')
            comlun.write('// alphadeg_(deg), mii_(amu),
                mip_(amu), Te_(eV), B_(T), zi_plasma,
                zi_ion, ne_(m^-3), n_ions'+'\n')
            comlun.write(str(90.0-alphadeg)+", "+str(
                mii_amu)+", "+str(mip_amu)+", "+str(Te)+",
                 "+str(B)+", "+str(Zip)+", "+str(Zii)+",
                "+str(ne)+", "+str(n_ions)+'\n')

            dislun.write('// runid: '+name+'\n')
            dislun.write('polar_deg, se_polardist,
                surf_polardist, azim_deg, se_azimdist,
                surf_azimdist, eV, se_eVdist, surf_eVdist,
                 vbins, vperpdist, vpardist'+'\n')

            outbins = np.zeros(60)

print(90.0-alphadeg, mip_amu, Te, B, ne)

#Verify precision
mip_amu = np.double(mip_amu)
mni = np.double(mni)
mnp = np.double(mnp)
alphadeg = np.double(alphadeg)
Te = np.double(Te)
B = np.double(B)
Zip = np.double(Zip)
```

```
Zii = np.double(Zii)
ne = np.double(ne)
mii_amu = np.double(mii_amu)
Ti = np.double(Ti)
forceds = np.double(forceds)
lmps = np.double(lmps)

#Set number of numerical divisions for sheath
    distance normal to surface:
ndvis = 50000

#Convert to radians:
alpha = alphadeg*(np.pi/180.0)

#Set constants:
e = np.double(1.602e-19) #Charge per electron in C
Nav = np.double(6.022e23) #Atoms per mol
eps = np.double(8.85e-12) #Vacuum permittivity in F/m
me = np.double(9.109e-31) #Mass of electron in kg
kb = e #Boltzmann's constant for T in eV

mip = mip_amu/Nav/1000.0 #Plasma ion mass in kg
mii = mii_amu/Nav/1000.0 #Impurity ion mass in kg

qi = e*Zip #Plasma ion charge
qii = e*Zii #Impurity ion charge
r_d = np.sqrt(eps*kb*Te/(ne*e**2.0)) #Debye length in
    m
```

```
no = ne #Bulk density
csp = np.sqrt(kb*(Te+Ti)/mip) #Plasma sound speed
    from Stangeby 2000
cip = np.sqrt(kb*Ti/mii) #Ion sound speed from
    Stangeby 2000
cii = np.sqrt(2.0*kb*Ti/mii) #Thermal ion speed

R_ics = mip*csp/(qi*B) #Larmor radius for plasma ion
    at plasma sound speed
R_iimp = mii*cii/(qii*B) #Larmor radius for impurity
    ion at thermal ion speed

################################################
#Analytic expression for electric field in Debye
    sheath:
################################################

Y = np.double(np.linspace(0.0,float(ndvis)-1.0,ndvis)
    /float(ndvis) * 0.010) #0.010 Y vector normal to
    surface, 10mm total length
lamb = np.double(np.linspace(0.0,float(ndvis)-1.0,
    ndvis)) #Electric potential to the same

#Dimensionless parameters
rho_i = R_ics/r_d #Larmor radius with ion speed =
    sound speed
L_mps = lmps*rho_i*np.sin(alpha) #magnetic pre-sheath
     length
```

```
xsi = Y/r_d #dimensionless distance

#Electric field structure solution
lamb_w = 0.5*np.log(2.0*np.pi*(me/mip)*((Te+Ti)/(Te))
    ) #Borodkina eq.21

#Critical angle above which Debye sheath vanishes
alpha_star = np.arccos(np.sqrt(2.0*np.pi*(me/mip)
    *(1.0+(Ti/Te))))*(180.0/np.pi)

print('angle= '+str(90.0-alphadeg)+'\n')
print('critical angle= '+str(alpha_star)+'\n')
if out != None:
        comlun.write('critical angle= '+str(
            alpha_star)+'\n')
        comlun.write('plasma thermal speed cip m/s=
            '+str(cip)+'\n')
        comlun.write('ion thermal speed cii m/s= '+
            str(cii)+'\n')
        comlun.write('plasma sound speed csp m/s= '+
            str(csp)+'\n')

if (alphadeg > alpha_star) and (forceds == 0.0):
        print('alpha greater than critical angle ...
            no DS')
```

```
            lamb = lamb_w*np.exp(-2.0*xsi/L_mps) #
                electric potential across MPS only;
                Chrobak 2018 eq. A.2
            lambdebye = lamb*0.0
            lambmps = lamb
            xsi_mps = 0.0
        else:
            lamb_mps = np.log(np.cos(alpha)) #Chodura
                drop Borodkina eq. 6 / Stangeby eq. 2.109
            if forceds > 0.0:
                    lamb_mps = (1.0-forceds)*lamb_w
            delta_mps = -4.0*np.log(np.cos(alpha))/(lmps*
                rho_i*np.sin(alpha))**2.0 #Borodkina eq.
                12

            C1 = -delta_mps*lamb_mps-6.0*np.cos(alpha)
            a = (np.sqrt(-delta_mps*lamb_mps)-np.sqrt
                (2.0*np.exp(lamb_w)+4.0*np.cos(alpha)*np.
                sqrt(1.0-(lamb_w-lamb_mps))+C1))/(lamb_w-
                lamb_mps)
            Q = (1/a)*np.sqrt(2.0*np.exp(lamb_w)+4.0*np.
                cos(alpha)*np.sqrt(1.0-(lamb_w-lamb_mps))+
                C1)

            #Split the potential into two drops, Debye
                and MPS
            xsi_mps = -(1.0/a)*np.log((lamb_w-lamb_mps+Q)
                /Q)
```

```
            lamb_mps2 = lamb_w + Q - Q*np.exp(a*xsi_mps)
            i_debye = [i for i, j in enumerate(xsi) if j
                >=0.0 and j<=xsi_mps]
            i_mps = [i for i, j in enumerate(xsi) if j>=
                xsi_mps]

            #Debye layer solution
            lamb[i_debye] = lamb_w + Q - Q*np.exp(-a*xsi[
                i_debye])
            #MPS solution
            lamb[i_mps] = lamb_mps*np.exp(-np.sqrt(-(
                delta_mps/lamb_mps))*(xsi[i_mps]-xsi_mps))

            lambdebye = lamb*0.0
            lambdebye[i_debye] = lamb[i_debye]
            lambmps = lamb*0.0
            lambmps[i_mps] = lamb[i_mps]

    lamb_norm = kb*Te/e #Normalization constant for e-
        field strength lambda=e(phi-phi0)/(kb*Te)

    #Stop total electric potential in volts
    lamb_y = lamb*lamb_norm

    #E-field structure, SI units
    E_y = -1.0*der(Y,lamb_y)
    if noe != None:
            E_y = 0.0*lamb_y
```

```
ne_d = np.exp(lamb)

plt.figure()
plt.plot(Y/R_ics,lamb)
plt.xlabel('ion gyro radii r_ion')
plt.ylabel('normalized potential')
plt.show()

plt.figure()
plt.plot(Y/R_ics,ne_d)
plt.xlabel('ion gyro radii r_ion')
plt.ylabel('Electron Density / no')
plt.show()

if out != None:
        mpslun.write('debye-mps-border(m) = '+str(
            xsi_mps*r_d)+'\n')
        for nd in range(int(ndvis/10)):
                nds = nd*10
                denE13cm3 = no*ne_d[nds]/1.0e19
```

```
                mpslun.write('{:0.3e}'.format(Y[nds])
                    +',          '+'{:0.3e}'.format(Y[
                    nds]/R_ics)+',       '+'{:0.3e}'.
                    format(Y[nds]/r_d)+',
                    '+'{:0.3e}'.format(E_y[nds])+',
                    '+'{:0.3e}'.format(lamb[nds])+',
                            '+'{:0.3e}'.format(
                    denE13cm3)+',          '+'{:0.3e}'.
                    format(ne_d[nds])+',
                    '+'{:0.3e}'.format(lambdebye[nds])
                    +',    '+'{:0.3e}'.format(lambmps[
                    nds])+',      \n')

##################################################
#
#Monte Carlo method:
#
##################################################

T_start = time.time()

#Define initial placeholders for calculated 3D angle
    distributions and energy distributions
finale = np.zeros(n_ions,dtype=np.double)
theta = np.zeros(n_ions,dtype=np.double)
se_theta = np.zeros(n_ions,dtype=np.double)
azim = np.zeros(n_ions,dtype=np.double)
se_azim = np.zeros(n_ions,dtype=np.double)
```

```
finalebins = np.zeros(180,dtype=int)
se_ebins = np.zeros(180,dtype=int)
thetabins = np.zeros(180,dtype=int)
se_thetabins = np.zeros(180,dtype=int)
azimbins = np.zeros(180,dtype=int)
se_azimbins = np.zeros(180,dtype=int)

#Velocity bins
vperpbins = np.zeros(180,dtype=int)
vparbins = np.zeros(180,dtype=int)

posbinloc = np.double(0.400*np.linspace
    (0.0,1000.0-1.0,1000)/1000.0 - 0.050) #xz
    distribution bin locations from -50 to 350 (mm)

#Initialize xyz position bins
finalxbins = np.zeros(1000,dtype=int)
finalybins = np.zeros(1000,dtype=int)
finalzbins = np.zeros(1000,dtype=int)

#Particle trajectory information structure
partinfo = {'VPERP' : 0.0, 'VPAR' : 0.0, 'EI' : 0.0,
    'EF' : 0.0, 'POLARI' : 0.0, 'POLARF' : 0.0, 'AZIMI
    ' : 0.0, 'AZIMF' : 0.0, 'DELTAX' : 0.0, 'DELTAY' :
     0.0, 'DELTAZ' : 0.0}
partsum = [partinfo.copy() for k in range(n_ions)]
```

```
#Toroidal field components
By = np.double(-B*np.cos(alpha))
Bz = np.double(B*np.sin(alpha))
Bx = np.double(0.0)
delta = np.double(1.0*np.pi/180.0) #toroidal field
    radial pitch angle
Bx = np.double(-B*np.sin(delta))

################################################
#Define initial velocities:
################################################

#Determine gyro phase angle range of ion entering
    sheath
#Specify a min and max initial gyro phase angle, then
     choose a set of random angles to use in that
    range
#Refer to Schmid 2010 paper to calculate range of
    gyration phase angle for particles entering the
    sheath
bigomega_min = np.double(0.0*np.pi/180.0)
bigomega_max = np.double(360.0*np.pi/180.0)
bigomega_rand = np.double(np.random.RandomState
    (61517).uniform(size=n_ions)*(bigomega_max-
    bigomega_min)+bigomega_min)

#1D maxwellian distrubtion forward direction
```

```
vparvec = np.sqrt((cii*np.double(np.random.
    RandomState(2017).normal(size=n_ions)))**2.0)

#Clip to minimum of mni=0.01 to prevent backward-
    going ions
clipind = [i for i, j in enumerate(vparvec) if j
    <0.01*csp]
vparvec[clipind] = np.double(0.01*csp)

#Maxwellian distribution of perpendicular ion
    velocities
c = np.sqrt(kb*Ti/mii)
vperpvec = np.sqrt((c*np.double(np.random.normal(size
    =n_ions)))**2.0 + (c*np.double(np.random.
    RandomState(1984).normal(size=n_ions)))**2.0)

#Calculate velocity distribution histograms
maxv = max([max(vperpvec),max(vparvec)])
vbinloc = np.double(np.linspace(0.0,180.0-1.0,180))
    /180.0*maxv

#Calculate total kinetic energy of ions entering
    sheath
totale = 0.5*mii*(vparvec**2+vperpvec**2)/kb
maxebin = max(totale)*3.0
ebinloc = np.double(np.linspace(0.0,180.0-1.0,180))
    /180.0*maxebin
```

```
#Fill in particle initial values:
for i in range(len(partsum)):

        partsum[i]['VPERP'] = vperpvec[i]
        partsum[i]['VPAR'] = vparvec[i]
        partsum[i]['EI'] = totale[i]

if n_ions > 200:
        result = Parallel(n_jobs=pal)(delayed(
           monte_carlo_part)(n,n_ions,vperpvec,
           vparvec,vbinloc,vperpbins,vparbins,mii_amu
           ,mii,mip,qi,qii,B,e,bigomega_rand,alpha,Y,
           xsi,lamb,r_d,ndvis,lmps,L_mps,E_y,R_ics,Bx
           ,By,Bz,csp,cip,ebinloc,totale,posbinloc)
           for n in range(n_ions))
        for n in range(n_ions):
                finale[n] = result[n][1]
                partsum[n]['EF'] = result[n][2]
                if result[n][3] != None:
                        finalebins[result[n][3]] += 1
                if result[n][4] != None:
                        se_ebins[result[n][4]] += 1
                partsum[n]['DELTAX'] = result[n][5]
                partsum[n]['DELTAY'] = result[n][6]
                partsum[n]['DELTAZ'] = result[n][7]
                if result[n][8] != None:
                        finalxbins[result[n][8]] += 1
                        finalybins[result[n][9]] += 1
```

```
                finalzbins[result[n][10]] +=
                    1
            se_theta[n] = result[n][11]
            partsum[n]['POLARI'] = result[n][12]
            se_azim[n] = result[n][13]
            partsum[n]['AZIMI'] = result[n][14]
            if result[n][15] != None:
                se_thetabins[result[n][15]]
                    += 1
                se_azimbins[result[n][16]] +=
                    1
            theta[n] = result[n][17]
            partsum[n]['POLARF'] = result[n][18]
            azim[n] = result[n][19]
            partsum[n]['AZIMF'] = result[n][20]
            if result[n][21] != None:
                thetabins[result[n][21]] += 1
                azimbins[result[n][22]] += 1
            if result[n][23] != None:
                vperpbins[result[n][23]] += 1
                vparbins[result[n][24]] += 1
else:
            print('Insufficent n_ions to ensure
                accuracy. n_ions must be >200. \n
                ')

vperpbins = (vperpbins.astype(np.double))/float(
    n_ions)
```

```
vparbins = (vparbins.astype(np.double))/float(n_ions)
finalxbins = (finalxbins.astype(np.double))/float(
    n_ions)
finalybins = (finalybins.astype(np.double))/float(
    n_ions)
finalzbins = (finalzbins.astype(np.double))/float(
    n_ions)

T_end = time.time()-T_start
print('Time elapsed ='+str(T_end)+'\n')

#Output plots
thetabinloc = np.double(np.linspace
    (0.0,180.0-1.0,180))
plt.figure()
plt.plot(thetabinloc,thetabins,label='Final')
plt.xlim(0.0,180.0)
plt.title('Polar inclination angle theta')
plt.plot(thetabinloc,se_thetabins,label='Initial')
print('mean theta= '+str(np.mean(theta))+'\n')
print('stddev theta= '+str(np.std(theta))+'\n')
plt.legend()
plt.show()

azimbinloc = np.double(np.linspace(0.0,180.0-1.0,180)
    )-90.0
plt.figure()
plt.plot(azimbinloc,azimbins,label='Final')
```

```
plt.xlim(-90.0,90.0)
plt.title('Azimuthal ExB angle phi')
plt.plot(azimbinloc,se_azimbins,label='Initial')
print('mean azim= '+str(np.mean(azim))+'\n')
print('stddev azim= '+str(np.std(azim))+'\n')
plt.legend()
plt.show()

plt.figure()
plt.plot(ebinloc,finalebins,label='Final')
plt.title('Impact energy distribution')
plt.plot(ebinloc,se_ebins,label='Initial')
plt.legend()
print('mean finale= '+str(np.mean(finale))+'\n')
print('stddev finale= '+str(np.std(finale))+'\n')
plt.show()

plt.figure()
plt.plot(vbinloc,(vperpbins+0.0001)/max(vperpbins),
    label='Perp')
plt.title('Normalized velocity distributions')
plt.ylim(0.001,1.0)
plt.plot(vbinloc,(vparbins+0.0001)/max(vparbins),
    label='Par')
plt.legend()
plt.show()

plt.figure()
```

```
plt.plot(posbinloc,finalxbins+0.0001,label='x')
plt.title('Final positions x y z')
plt.ylim(0.01,1.0)
plt.plot(posbinloc,finalybins+0.0001,label='y')
plt.plot(posbinloc,finalzbins+0.0001,label='z')
plt.legend()
plt.show()

#Output to files
if out != None:
        dnions = float(n_ions)
        for l in range(180):
                dislun.write(str(thetabinloc[l])+'
                    '+'{:0.4e}'.format(se_thetabins[l
                    ]/dnions)+' '+'{:0.4e}'.format(
                    thetabins[l]/dnions)+' '+str(
                    azimbinloc[l])+' '+'{:0.4e}'.
                    format(se_azimbins[l]/dnions)+'
                    '+'{:0.4e}'.format(azimbins[l]/
                    dnions)+' '+str(ebinloc[l])+'
                    '+'{:0.4e}'.format(se_ebins[l])+'
                    '+'{:0.4e}'.format(finalebins[l])
                    +' '+str(vbinloc[l])+' '+'{:0.4e
                    }'.format(vperpbins[l]/dnions)+'
                    '+'{:0.4e}'.format(vparbins[l]/
                    dnions)+'\n')

        #Write angle.inp file for sdtrim input
```

```
#for l in range(90):
        #anglun.write(str(thetabinloc[l])+'
            '+'{:0.4e}'.format(thetabins[l])
            +'\n')

#Write distribution of final positions file
poslun.write('distance[m],deltax,deltay,
    deltaz'+'\n')
for l in range(1000):
        poslun.write(str(posbinloc[l])+'
            '+'{:0.4e}'.format(finalxbins[l])
            +' '+'{:0.4e}'.format(finalybins[l
            ])+' '+'{:0.4e}'.format(finalzbins
            [l])+'\n')

#Write particle summary file, all summary
    info structure
partlun.write('particle, vperp[m/s], vpar[m/s
    ], par/perp, Ei[eV], Ef[eV], polari[deg],
    polarf[deg], azimi[deg], azimf[deg],
    deltax[m], deltay[m], deltaz[m] \n')
for n in range(n_ions):
```

```
            partlun.write(str(n+1)+'  '+'{:0.4e}'.
                format(partsum[n]['VPERP'])+'
                '+'{:0.4e}'.format(partsum[n]['
                VPAR'])+'  '+str(partsum[n]['VPAR
                ']/partsum[n]['VPERP'])+'  '+'{:0.4
                e}'.format(partsum[n]['EI'])+'
                '+'{:0.4e}'.format(partsum[n]['EF
                '])+'  '+str(partsum[n]['POLARI'])
                +'  '+str(partsum[n]['POLARF'])+'
                '+str(partsum[n]['AZIMI'])+'  '+str
                (partsum[n]['AZIMF'])+'  '+str(
                partsum[n]['DELTAX'])+'  '+str(
                partsum[n]['DELTAY'])+'  '+str(
                partsum[n]['DELTAZ'])+'\n')

comlun.write('L_mps = '+str(L_mps*r_d)+'\n')
comlun.write('r_d = '+str(r_d)+'\n')
comlun.write('mean theta = '+str(np.mean(
    theta))+'\n')
comlun.write('stddev theta = '+str(np.std(
    theta))+'\n')
comlun.write('mean azim = '+str(np.mean(azim)
    )+'\n')
comlun.write('stddev azim = '+str(np.std(azim
    ))+'\n')
comlun.write('mean finale = '+str(np.mean(
    finale))+'\n')
```

```
                comlun.write('stddev finale = '+str(np.std(
                    finale))+'\n')

                dislun.close()
                #anglun.close()
                comlun.close()
                mpslun.close()
                partlun.close()
                poslun.close()

def monte_carlo_part(n,n_ions,vperpvec,vparvec,vbinloc,
    vperpbins,vparbins,mii_amu,mii,mip,qi,qii,B,e,
    bigomega_rand,alpha,Y,xsi,lamb,r_d,ndvis,lmps,L_mps,E_y,
    R_ics,Bx,By,Bz,csp,cip,ebinloc,totale,posbinloc):
        ################################################
        #Loop over all particles in the initial distribution:
        ################################################

        if n % math.floor(0.01*n_ions) == 0:
                print(str(n+1)+'/'+str(n_ions))
        else:
                print(str(n+1)+'/'+str(n_ions))

        v_perp = vperpvec[n]
        v_par = vparvec[n]
        perpind = np.argmin(abs(vbinloc-v_perp))
        parind = np.argmin(abs(vbinloc-v_par))
```

```
if (mii_amu != None) and (mii != mip):
        r_gyro = mii*v_perp/(qii*B)
else:
        r_gyro = mip*v_perp/(qi*B)

vx0 = -v_perp*np.cos(bigomega_rand[n]) #out of B-E
    plane
vy0 = v_perp*np.sin(bigomega_rand[n])*np.sin(alpha)-
    v_par*np.cos(alpha) #in E-direction
vz0 = v_par*np.sin(alpha)-v_perp*np.sin(bigomega_rand
    [n])*np.cos(alpha) #ion sound speed in B-direction

#Split the path into ndvis number of steps
dt = np.zeros(ndvis,dtype=np.double)
vx = np.zeros(ndvis,dtype=np.double)
vy = np.zeros(ndvis,dtype=np.double)
vz = np.zeros(ndvis,dtype=np.double)
ypos = np.zeros(ndvis,dtype=np.double)
xpos = np.zeros(ndvis,dtype=np.double)
zpos = np.zeros(ndvis,dtype=np.double)
speed = np.zeros(ndvis,dtype=np.double)
ke = np.zeros(ndvis,dtype=np.double)
tim = np.zeros(ndvis,dtype=np.double)

vx[0] = vx0 #out of B-E plane
vy[0] = vy0 #in E-direction
vz[0] = vz0 #in B-direction
```

```
#Start particle at position where electric field is
    0.03 (1% of max normalized field of lambda=3)
ypos[0] = (xsi[max([i for i, j in enumerate(lamb) if
    j<-0.03])])*r_d
#Add one orbit diameter above this 1% level so that
    bottom of the orbit just dips into the mpsheath
ypos[0] += 2.0*r_gyro*np.sin(alpha)

speed[0] = np.sqrt(vx0**2.0+vy0**2+vz0**2)
ke[0] = 0.5*mii*speed[0]**2

#Track ion trajectories through layers of the sheath
k=0
dt = np.double(np.array([(0.01*2.0*np.double(np.pi)*
    r_gyro)/np.sqrt(vx0**2.0+vy0**2.0+vz0**2.0)]*ndvis
    ))

while (ypos[k] > 0.0) and (ypos[k] < 10.0*L_mps*r_d
    *3.0/lmps+2.0*r_gyro*np.sin(alpha)) and (k < ndvis
    -2):

        #Update timestep if position is within 2 gyro
            -orbits of surface
        if ypos[k] < 2.0*r_gyro:
                dt[k] = 10.0*r_d/speed[k]
```

```
#If position is less than 5 Debye lengths
    from surface, timestep shrinks to time it
    takes to travel 0.25 Debye lengths
if ypos[k] < 5.0*r_d:
        dt[k] = 0.25*r_d/speed[k]

# Solve E-field at current position
Eind = np.argmin(abs(Y-ypos[k]))
Ey = 1.0*E_y[Eind]

#The following 3 lines are Newton's method
    for calculating next position
xpos[k+1] = xpos[k]+vx[k]*dt[k]+0.5*((qii/mii
    )*(Bz*vy[k]-By*vz[k]))*dt[k]**2.0
ypos[k+1] = ypos[k]+vy[k]*dt[k]+0.5*((qii/mii
    )*(Ey-Bz*vx[k]+Bx*vz[k]))*dt[k]**2.0
zpos[k+1] = zpos[k]+vz[k]*dt[k]+0.5*((qii/mii
    )*(vx[k]*By-vy[k]*Bx))*dt[k]**2.0

#The following are 4th order Runge-Kutta
    method for velocity
H = dt[k] #Step size
t = tim[k] #initial X value
pvx = vx[k] #initial Y values
pvy = vy[k]
pvz = vz[k]
PV = np.array([pvx,pvy,pvz])
```

```
            result = solve_ivp(lambda x, y: DVS(x,y,Bx,By
                ,Bz,Ey,qii,mii),[t,t+2*H],PV,'RK45',t_eval
                =[t+H],first_step=H)

            vx[k+1]=result.y[0][0]
            vy[k+1]=result.y[1][0]
            vz[k+1]=result.y[2][0]

            speed[k+1] = np.sqrt(vx[k+1]**2.0+vy[k
                +1]**2.0+vz[k+1]**2.0)
            ke[k+1] = 0.5*mii*(speed[k+1]**2.0)/e

            tim[k+1] = tim[k]+dt[k]

            k += 1

    if k < ndvis-2:

            #Final Energy
            finale_n = ke[k]
            partsum_EF = finale_n

            #Fill in particle summary info structure

            ebinind = np.argmin(abs(ebinloc-finale_n)) #
                fill in energy distribution

            #Inital Energy
```

```
se_ebinind = np.argmin(abs(ebinloc-totale[n])
    ) #fill in initial energy distribution

partsum_DELTAX = xpos[k]-xpos[0] #This is the
     radial direction
partsum_DELTAY = ypos[k]-ypos[0] #This is the
     normal to surface direction
partsum_DELTAZ = zpos[k]-zpos[0] #This is the
     toroidal field direction

xbinind = np.argmin(abs(posbinloc-xpos[k]))
ybinind = np.argmin(abs(posbinloc-ypos[k]))
zbinind = np.argmin(abs(posbinloc-zpos[k]))

#Sheath Incident Angle
se_theta_n = 90.0 - np.double(np.arctan(-vy0
    /(np.sqrt(vz0**2.0+vx0**2.0))))*180.0/np.
    pi
partsum_POLARI = se_theta_n

se_azim_n = np.double(np.arctan(vx0/vz0))
    *180.0/np.pi
partsum_AZIMI = se_azim_n

se_thetabin = math.floor(se_theta_n)
se_azimbin = 90+math.floor(se_azim_n)

#Final angle
```

```
            theta_n = 90.0-np.double(np.arctan(-vy[k-1]/(
                np.sqrt(vz[k-1]**2.0+vx[k-1]**2.0))))
                *180.0/np.pi
            partsum_POLARF = theta_n
            azim_n = np.double(np.arctan(vx[k-1]/vz[k-1])
                )*180.0/np.pi
            partsum_AZIMF = azim_n

            thetabin = math.floor(theta_n)
            azimbin = 90+math.floor(azim_n)

    else:
            finale_n = 0.
            partsum_EF = 0.
            ebinind = None
            se_ebinind = None
            partsum_DELTAX = 0.
            partsum_DELTAY = 0.
            partsum_DELTAZ = 0.
            xbinind = None
            ybinind = None
            zbinind = None
            se_theta_n = 0.
            partsum_POLARI = 0.
            se_azim_n = 0.
            partsum_AZIMI = 0.
            se_thetabin = None
            se_azimbin = None
```

```
                theta_n = 0.
                partsum_POLARF = 0.
                azim_n = 0.
                partsum_AZIMF = 0.
                thetabin = None
                azimbin = None
                perpind = None
                parind = None

        return n, finale_n, partsum_EF, ebinind, se_ebinind,
            partsum_DELTAX, partsum_DELTAY, partsum_DELTAZ,
            xbinind, ybinind, zbinind, se_theta_n, partsum_POLARI,
            se_azim_n, partsum_AZIMI, se_thetabin, se_azimbin,
            theta_n, partsum_POLARF, azim_n, partsum_AZIMF,
            thetabin, azimbin, perpind, parind

def der(X,x):
        h = np.double(X[1]-X[0])
        N = len(x)
        y = np.double(np.zeros(N))
        y[0] = (-3*x[0]+4*x[1]-x[2])/(2*h)
        y[N-1] = (3*x[N-1]-4*x[N-2]+x[N-3])/(2*h)
        for i in range(N):
                if i!=0 and i!=N-1:
                        y[i] = (x[i+1]-x[i-1])/(2*h)
        return np.double(y)

def DVS(t,PV,Bx,By,Bz,Ey,qii,mii):
```

```
    vx = PV[0]
    vy = PV[1]
    vz = PV[2]
    ax = np.double(qii / mii)*np.double(Bz*vy-By*vz)
    ay = np.double(qii / mii)*np.double(Ey-Bz*vx+Bx*vz)
    az = np.double(qii / mii)*np.double(vx*By-vy*Bx)
    return np.array([ax,ay,az])
```

Vita

Davis was born and raised in Dickson, Tennessee on the western side of Nashville. After graduating valedictorian from Dickson County High School, he attended Sewanee: The University of the South (a liberal arts college just outside of Chattanooga), where he studied mathematics, physics, and chemistry as part of his Bachelor's degree. He graduated *summa cum laude* with honors in both mathematics and physics and immediately pursued his Ph.D. in Energy Science and Engineering at the Bredesen Center of UTK with a focus in fusion energy. He has maintained a long working relationship with Oak Ridge National Laboratory throughout his undergraduate and graduate career, completing five undergraduate internships and winning the prestigious SCGSR fellowship as part of his graduate research. Outside of work, he enjoys adventuring in the Smokies and writing/performing music. He married midway through his graduate school career and now spends his life with his wife, Liz, who is his greatest companion.